Proceedings of

RAGtime 17–19: Workshops on black holes and neutron stars

1–5 November / 17–19 October /
23–26 October '15/'16/'17
Opava, Czech Republic

Editors:
Z. Stuchlík, G. Török,
V. Karas

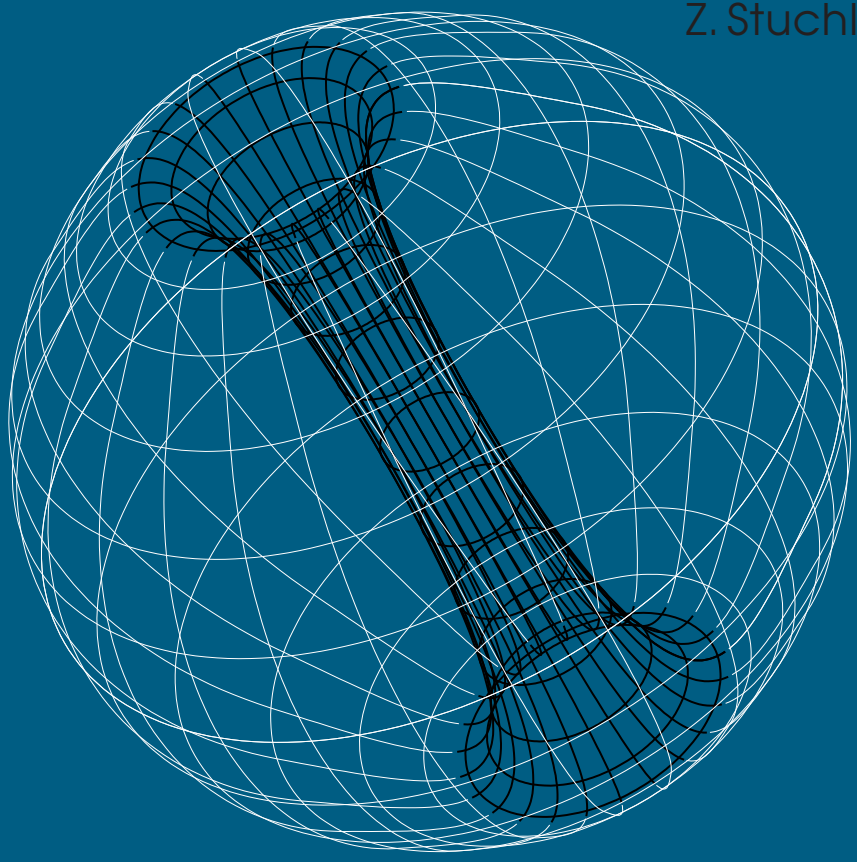

SILESIAN UNIVERSITY IN OPAVA

Publications of the Institute of Physics No. 8

Proceedings of RAGtime 17–19: Workshops on black holes and neutron stars 17–19/23–26 Oct., 1–5 Nov. 2015/2016/2017 Opava Czech Republic

Z. Stuchlík, G. Török and V. Karas, editors

Opava 2017

Annotation: In this Proceedings, the talks presented during workshops *RAGtime 17–19: Workshops on black holes and neutron stars, 17–19/23–26 Oct., 1–5 Nov. 2015/2016/2017, Opava, Czech Republic* are collected.

ISBN 978-80-7510-257-7

PREFACE

RAGtime – the series of the Relativistic Astrophysics Group workshops and proceedings – started in 1999 at Institute of Physics, the Faculty of Philosophy and Science of the Silesian University in Opava, Czech Republic. Almost two decades later, the latest volume presents a new edition of the workshop proceedings related to the triad of annual events organized during years 2015, 2016, and 2017. The progress of research has been outstanding: the period of just three years witnessed celebrations of the Centenary of Einstein's General Theory of Relativity *and* the long-awaited direct detection of gravitational waves, crowned by variety of discoveries on the border-line of modern Theoretical Physics, Astronomy and Astrophysics, and Particle Physics. The yearly gatherings offer an opportunity to discuss efforts and achievements of the workshop participants together with the most recent developments in the field.

Processes near black holes and neutron stars, as well as various types of more exotic compact objects are discussed. Solutions of general relativity are extended to viable alternatives, such as string theories and supersymmetry schemes. Several contributions cover surprising and intricate subtleties of high-frequency oscillations observed in low-mass X-ray binaries and accreting black holes. Astro-particle physics has been represented by the works on acceleration mechanisms in astrophysical shocks and the processes leading to chaos in motion of matter near black holes. The classical theory of figures of equilibria of fluid tori has been elaborated within the analytical framework appropriate for the environment of magnetized compact objects. Optical phenomena connected with the appearance of these structures are examined in strong gravity, where their signatures appear via timing, spectroscopy and polarimetry of the emerging radiation signal. Finally, black holes are considered in the cosmological context. Among the standard variety of works in the field of relativistic physics we also publish in this proceedings a breaking novel fundamental work relating the ideas of supersymmetry theory to the models of genetics.

Most of the presented contributions were obtained by collaborating research groups of the Silesian University in Opava, The Astronomical Institute of the Czech Academy of Science, and the Faculty of Mathematics and Physics of Charles University in Prague. Participants from a wide international community have represented Observatoire de Paris, Joint Institute for Nuclear Research in Dubna, International Space Science Institute in Bern, Osservatorio Astronomico di Roma, University of Cologne, University of Oxford, Ulugh Beg Astronomical Institute in Tashkent and others.

We thank the Editorial Board members for advice and assistance, and all the authors for careful preparation of their contributions. We are also indebted to the Ministry of Education of the Czech Republic and European Social Fund in Czech Republic for providing financial support for the previous workshops in the framework of the Grants No. CZ.1.07/2.3.00/20.0071 (SYNERGY) and CZ.1.07/2.2.00/28.0271 (INAP). Current work is supported by the INTER-EXCELLENCE project No. LTI17018 and the internal grant of Silesian University in Opava No. 07/2015-FPF.

Opava, December 2017

Z. Stuchlík, G. Török and V. Karas
editors

In memory of dr. Jeffrey E. McClintock (1942–2017), a wonderful friend and colleague, an exceptional astrophysicist, and the amiable participant of our meetings.

(Picture credit: David Kofroň)

CONTENTS

A. Araudo, V. Karas
Truncation of AGN jets by their interaction with a passing star cluster 1

M. Bursa
Numerical implementation of equations for photon motion in Kerr spacetime 7

K. Goluchová, G. Török, M. Urbanec, G. Urbancová, E. Šrámková
Innermost stable circular orbits around compact stars:
Terms that are quadratic in spin 23

J. Horák
Wave excitation at Lindblad resonances using the method of multiple scales 33

J. Horák, O. Straub, E. Šramková, K. Goluchová, G. Török
Epicyclic oscillations of thick relativistic disks 47

I. Hubač, M. Švec, S. Wilson
Quantum entanglement and quantum information in biological systems (DNA) 61

P. Jalůvková, E. Kopteva, Z. Stuchlík
The motion of the test particle near the black hole embedded into dust. 85

M. Kološ
Magnetic field generated by current loop in flat spacetime 91

M. Kološ, A. Tursunov
Comparison of charged particle dynamics around compact object immersed
into uniform or dipole magnetic field 99

E. Kopteva, I. Bormotova, M. Korkina
New exact solutions for Schwarzschild-like black holes 111

J. Kovář, P. Slaný, Z. Stuchlík, V. Karas, A. Trova
Analytical solution for charged fluid pressure profiles - circulation
in combined electromagnetic field 119

D. Lančová, P. Bakala, K. Goluchová, M. Falanga, V. De Falco, L. Stella
The study on behaviour of thin accretion disc affected by
Poynting-Robertson effect 127

D. Pugliese, Z. Stuchlík
Constraints on two accretion disks centered on the equatorial plane
of a Kerr SMBH 137

L. Štofanová, M. Zajaček, D. Kunneriath, A. Eckart, V. Karas
Modelling the bow–shock evolution along the DSO/G2 orbit
in the Galactic centre 153

P. Suková
Hysteresis behavior of shocks in low angular momentum flows 163

G. Török, K. Goluchová, E. Šrámková, J. Horák, P. Bakala, M. Urbanec
A one-parametric formula relating the frequencies of twin-peak quasi-periodic oscillations 177

B. Toshmatov, Z. Stuchlík
Note on the character of the generic rotating charged regular black holes in general relativity coupled to nonlinear electrodynamics 195

B. Turimov, J. Rayimbaev, A. Rakhmatov
Gravitational field energy of rotating brany black hole 201

A. Tursunov, M. Kološ
On the synchrotron radiation reaction in external magnetic field 211

J. Vrba, M. Urbanec, Z. Stuchlík
Escape cones of null-geodesics from the interior of rotating compact stars 223

M. Zajaček, V. Karas, E. Hosseini, A. Eckart, B. Shahzamanian, M. Valencia-S., F. Peissker, G. Busch, S. Britzen, J. A. Zensus
Polarization properties of bow shock sources close to the Galactic centre 237

O. Zelenka, G. Lukes-Gerakopoulos
Chaotic motion in the Johannsen-Psaltis spacetime 253

Proceedings of *RAGtime 17–19, 17–19/23–26 Oct., 1–5 Nov., 2015/2016/2017, Opava, Czech Republic*
Z. Stuchlík, G. Török and V. Karas, editors, Silesian University in Opava, 2017, pp. 1–6

Truncation of AGN jets by their interaction with a passing star cluster

Anabella T. Araudo[1,a] and Vladimír Karas[1,b]

[1]Astronomical Institute, Czech Academy of Sciences, Boční II 1401,
CZ-141 00 Prague, Czech Republic
[a]anabella.araudo@asu.cas.cz
[b]vladimir.karas@cuni.cz

ABSTRACT
We are interested in the effects of interaction of jets in Active Galactic Nuclei when they encounter various obstacles, namely, stars in Nuclear Star Cluster surrounding the nucleus and globular clusters passing across the inner jet, as well as dense clouds from the Broad Line Region. The interaction provides a scenario to address non–thermal processes. In jet–star interactions a double bow–shock structure is formed where particles get accelerated via diffusive mechanism. Individual encounters have a limited effect, however, dense clusters of massive stars can truncate the jet as the cluster crosses the jet line near the jet launching region. Much of the jet kinetic energy density is transferred to the shock and it becomes available to accelerate particles. We conclude that the interaction of jets with clusters of massive stars is a promising way to explain detectable levels of gamma rays from Fanaroff–Riley class I of edge–brightened radio galaxies.

Keywords: galaxies: active – galaxies: jets – stars: clusters

1 INTRODUCTION

Active galactic nuclei (AGN) contain an accreting super–massive black hole (SMBH) in the center of a galaxy. In some cases these objects form powerful radio–emitting jets (Begelman et al., 1984). The emission from the jets is non–thermal and generated by a population of relativistic particles accelerated in strong shocks. This non–thermal emission is assumed to be produced by synchrotron and inverse Compton (IC) processes, although hadronic models have been also considered to explain gamma–ray detections.

The interaction of AGN jets with clouds from the Broad Line Region (BLR) was suggested by Blandford and Königl (1979) as a mechanism for knot formation in the M87 radio galaxy jet. Also, the gamma–ray production through the interaction of a cloud from the BLR with the AGN jet was studied by Dar and Laor (1997) and by Araudo et al. (2010). In the latter work, the authors showed that the jet–cloud interactions may generate detectable gamma–rays in non–blazar AGN, of transient nature in nearby low–luminous sources, and steady in the case of powerful objects.

978-80-7510-257-7

Stars surround the central region of AGN. Nuclear star clusters have been detected in majority of galaxies and they represent the densest stellar systems (Neumayer et al., 2011; Schödel et al., 2014). Also, the globular cluster population evolves within the galactic potential and it may provide stars into interaction region of jets (Gnedin et al., 2014; Fragione et al., 2017). Jet–star interactions have been studied as a possible mechanism of jet mass loading and deceleration. In the seminal work of Komissarov (1994), the interaction of low–mass stars with jets was considered to analyse the mass transfer from the former to the latter in elliptical galaxies, concluding that jet–star interactions can significantly affect the jet dynamics and matter composition in low–luminous jets. Later on, and motivated by the detection of gamma–ray emission in misaligned AGN jets, different authors considered jet–star interactions as a possible scenario to produce shocks, accelerate particles, and emit non–thermal photons.

The interaction of AGN jets with massive stars was investigated by a number of authors (see, e.g., Araudo et al. (2013); Wykes et al. (2015); Bednarek and Banasiński (2015), and further references cited therein). Barkov et al. (2010) studied the interaction of AGN jets with red giant stars. In all the cases, the conclusion is that in order to have a detectable level of gamma–ray emission, a large number of stars have to be simultaneously present within the jet. More recently, Vieyro et al. (2017) analyzed the collective non–thermal emission from AGN jets interacting with early–type stars. They conclude that, for the particular case of radio galaxy M87, the gamma–ray emission level produced by jet–star interactions is below the detected flux in the GeV domain.

Hubbard and Blackman (2006) analysed the mass loading and truncation of the jet by interactions with stars, also considering the case of an interposed stellar cluster. Bednarek and Banasiński (2015) investigated the interaction of globular clusters with jets at few kpc from the SMBH. They considered that the power of the collective wind of globular clusters is determined by the relativistic winds of individual milliarcsecond pulsars within the cluster. Even when pulsars have a relativistic wind, the collective wind has a size of $\sim$ 1 pc in the case of Cen A where the jets have a kinetic luminosity $L_{\rm j} \sim 10^{43}$ erg s^{-1} (Wykes et al., 2015). Therefore, the collision of a single globular cluster cannot truncate the jet and about 10 clusters simultaneously within the jet are required to have a detectable level of non–thermal emission.

In the present contribution we study the interaction of AGN jets with a single cluster of massive stars. To this end we consider standard prescriptions for jets and stellar cluster collective winds.

2 JET–STELLAR CLUSTER INTERACTION

Jets from AGN are relativistic, with bulk Lorentz factors reaching $\Gamma \sim 10$ where the terminal velocity is thought to be set by the radiation drag and the ambient medium into which the jet propagates (Abramowicz et al., 1990; Vokrouhlicky and Karas, 1991; Fukue, 2005). The matter composition of these jets is not well known and two different prescriptions are commonly adopted: a jet composed only by electron–positron pairs (e.g. Komissarov (1994)), and a lepto–hadronic jet (e.g. Reynoso et al. 2011) with the same number density of protons and electrons, i.e. $n_e = n_p$.

In the present work we consider a lepto–hadronic jet. Concerning the kinetic luminosity (L_j), jets from type I Faranoff–Riley (FR I) galaxies are less luminous, with $L_j < 10^{44}$ erg s^{-1}, whereas FR II jets have $L_j > 10^{44}$ erg s^{-1}. The jet kinetic pressure is

$$P_j = \frac{L_j}{\sigma_j c} \sim 10^{-8} \left(\frac{R_j}{\mathrm{pc}}\right)^{-2} \left(\frac{L_j}{10^{40}\,\mathrm{erg\,s^{-1}}}\right) \mathrm{erg\,cm^{-3}} \quad (1)$$

where $\sigma_j = \pi R_j^2$ is the jet cross section and R_j is the jet width. The former, less energetic sources are particulary interesting from the viewpoint of our current considerations.

The collective wind (i.e., the superposed wind from cluster members; CW) of a cluster of massive stars interacting with an AGN jet can block a significant fraction of the jet cross section (Hubbard and Blackman, 2006). Cantó et al. (2000) performed a hydrodynamical study of the collective wind of a dense cluster of massive stars. It can be described as a single wind with mass–loss rate $\dot{M}_{cw} \sim 10^{-4}\ M_\odot\ \mathrm{yr}^{-1}$ and velocity $v_{cw} \sim 1000 - 2000$ km s^{-1} (Torres and Domingo-Santamaría, 2007).

The interaction of a stellar cluster with the jet produce a double bow–shock structure as described in e.g. Araudo et al. (2013). The shock in the jet is relativistic whereas the shock in the collective wind is non–relativistic with a velocity $\sim v_{cw}$. The contact discontinuity is located at a distance R_{sp} from the center of the cluster, where the jet and cluster wind $P_{cw} = \dot{M}_{cw} v_{cw}/(\pi R_{sp}^2)$ ram pressures are equated. By equating $P_{cw} = P_j$ we find

$$\frac{R_{sp}}{R_j} = 0.5 \left(\frac{\dot{M}_{cw}}{10^{-4}\,\mathrm{M_\odot yr^{-1}}}\right)^{0.5} \left(\frac{v_{cw}}{2000\,\mathrm{km\,s^{-1}}}\right)^{0.5} \left(\frac{L_j}{10^{40}\,\mathrm{erg\,s^{-1}}}\right)^{-0.5}. \quad (2)$$

We can see that a cluster of massive stars can truncate the jets in FR I radio galaxies (i.e. $R_{sp}/R_j \sim 1$) and therefore most of the jet kinetic luminosity is transferred to the shock and available to accelerate particles, as we discuss in the next section.

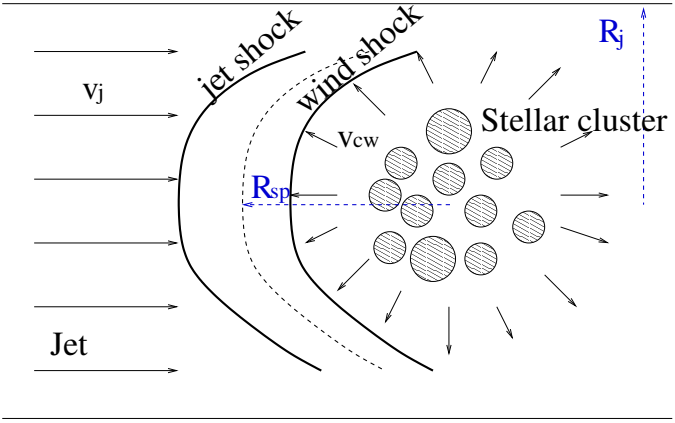

Figure 1. Sketch of the jet-stellar cluster interaction. Two shocks develop and a transition region, as described in the text.

3 PARTICLE ACCELERATION AND NON–THERMAL EMISSION

Particles can be accelerated in both jet and CW shocks, and emit non–thermal emission in the shocked plasma. Diffusive acceleration of particles in relativistic and non–relativistic shocks has been studied by different authors with detailed semi–analytical and numerical approaches (e.g. Kirk et al. (2000); Park et al. (2015)). Here we follow a simple description.

The luminosity of the shock in the jet is $L_{\rm sh,j} = (R_{\rm sp}/R_{\rm j})^2 L_{\rm j}$ giving

$$\left(\frac{L_{\rm sh,j}}{\rm erg\,s^{-1}}\right) = 2.5\times10^{39}\left(\frac{\dot{M}_{\rm cw}}{10^{-4}\,{\rm M_\odot yr^{-1}}}\right)\left(\frac{v_{\rm cw}}{2000\,{\rm km\,s^{-1}}}\right). \quad (3)$$

The shock in the collective wind have a luminosity $L_{\rm sh,cw} \sim L_{\rm cw}$, where

$$\left(\frac{L_{\rm cw}}{\rm erg\,s^{-1}}\right) \sim 10^{38}\left(\frac{\dot{M}_{\rm cw}}{10^{-4}\,{\rm M_\odot yr^{-1}}}\right)\left(\frac{v_{\rm cw}}{2000\,{\rm km\,s^{-1}}}\right)^2. \quad (4)$$

By assuming that a fraction $\zeta_{\rm nt} \sim 0.01 - 0.1$ of $L_{\rm sh,j}$ and $L_{\rm cw}$ goes to non–thermal particles, the luminosity in non thermal electrons (L_e) and protons (L_p) is $L_{\rm nt} = L_e + L_p = \zeta_{\rm nt} L_{\rm sh}$. The magnetic field B plays an important role in the acceleration of particles. By assuming that the magnetic energy density $U_{\rm mag} = B^2/8\pi$ is in equipartition with non–thermal particles, i.e. $U_{\rm mag} = U_{\rm nt}$, where $U_{\rm nt} = L_{\rm nt}/(\pi R_{\rm sp}^2 c)$, we find the upper limit

$$\left(\frac{B_{\rm eq}}{\mu\rm G}\right) = 50\left(\frac{\zeta_{\rm nt}}{0.01}\right)^{0.5}\left(\frac{R_{\rm j}}{\rm pc}\right)^{-1}\left(\frac{L_{\rm j}}{10^{40}\,{\rm erg\,s^{-1}}}\right)^{0.5} \quad (5)$$

in the jet shock downstream region, and

$$\left(\frac{B_{\rm eq,cw}}{\mu\rm G}\right) = 20\left(\frac{\zeta_{\rm nt}}{0.01}\right)^{0.5}\left(\frac{v_{\rm cw}}{2000\,{\rm km\,s^{-1}}}\right)^{0.5}\left(\frac{R_{\rm j}}{\rm pc}\right)^{-1}\left(\frac{L_{\rm j}}{10^{40}\,{\rm erg\,s^{-1}}}\right)^{0.5} \quad (6)$$

in the CW shock downstream region.

Accelerated particles are injected in the shock downstream region following a power–law energy distribution $N_{e,p} \propto E_{e,p}^{-\beta}$, with $\beta \sim 2$ in non–relativistic shocks (i.e. the collective wind) and $\beta \sim 2.2 - 2.4$ in relativistic shocks (i.e. the jet). The energy density in particles with energy $E_{e,p}$ is $U_{e,p} \propto N_{e,p} E_{e,p}^2$, resulting the same amount of energy in every energy decade when $\beta = 2$, whereas most of the energy is concentrated in low–energy particles when $\beta > 2$ (Bell et al., 2018). Therefore, even when the energy budget to accelerate particles in the jet shock is larger than in the collective wind (i.e. $L_{\rm sh,j} > L_{\rm cw}$), the energy density at the highest energies can be comparable.

Gamma–rays can be produced by proton–proton (pp) collisions with a cooling rate $dE_p/dt \propto n_p$ (e.g. Kelner et al. (2006)). Stellar winds are denser that AGN jets where jet–stellar cluster interactions can take place, and therefore, there are more targets for pp collisions in the collective wind than in the jet. A large density contrast, combined with the fact that the spectrum of non–thermal protons accelerated in relativistic shocks is steeper than in non–relativistic shocks, can produce a gamma–ray flux in the shocked collective wind larger than in the shocked jet region.

4 CONCLUSIONS

We study the interaction of a cluster of massive stars with AGN jets as a continuous process that must occur repetitively in galactic nuclei and a promising mechanism that can trigger production of high–energy particles. We show that stellar clusters with mass loss rate $\dot{M}_{\rm cw} \sim 10^{-4} M_{\odot}$ yr^{-1} and velocity $v_{\rm cw} \sim 2000$ km s^{-1} can truncate an AGN jet with kinetic luminosity $L_{\rm j} \sim 10^{40}$ erg s^{-1}. Therefore, this scenario is very promising option for particle acceleration given that most of the jet kinetic luminosity will be transferred to the bow shock and therefore there is sufficient energy budget to accelerate particles and produce detectable levels of non–thermal emission, in particular in the gamma–ray domain.

ACKNOWLEDGEMENTS

The authors acknowledge the Czech Science Foundation (ref. 14-37086G) – "Albert Einstein Center for Gravitation and Astrophysics" in Prague, and the EU COST Action (ref. CA16104) "Gravitational waves, black holes and fundamental physics".

REFERENCES

Abramowicz, M. A., Ellis, G. F. R. and Lanza, A. (1990), Relativistic effects in superluminal jets and neutron star winds, *The Astrophysical Journal* , **361**, pp. 470–482.

Araudo, A. T., Bosch-Ramon, V. and Romero, G. E. (2010), Gamma rays from cloud penetration at the base of AGN jets, *Astronomy and Astrophysics* , **522**, A97, arXiv: 1007.2199.

Araudo, A. T., Bosch-Ramon, V. and Romero, G. E. (2013), Gamma-ray emission from massive stars interacting with active galactic nuclei jets, *Monthly Notices of the Royal Astronomical Society* , **436**, pp. 3626–3639, arXiv: 1309.7114.

Barkov, M. V., Aharonian, F. A. and Bosch-Ramon, V. (2010), Gamma-ray Flares from Red Giant/Jet Interactions in Active Galactic Nuclei, *The Astrophysical Journal* , **724**, pp. 1517–1523, arXiv: 1005.5252.

Bednarek, W. and Banasiński, P. (2015), Non-thermal Radiation from Collisions of Compact Objects with Intermediate-scale Jets in Active Galaxies, *The Astrophysical Journal* , **807**, 168, arXiv: 1506.01181.

Begelman, M. C., Blandford, R. D. and Rees, M. J. (1984), Theory of extragalactic radio sources, *Reviews of Modern Physics*, **56**, pp. 255–351.

Bell, A. R., Araudo, A. T., Matthews, J. H. and Blundell, K. M. (2018), Cosmic-ray acceleration by relativistic shocks: limits and estimates, *Monthly Notices of the Royal Astronomical Society* , **473**, pp. 2364–2371, arXiv: 1709.07793.

Blandford, R. D. and Königl, A. (1979), Relativistic jets as compact radio sources, *The Astrophysical Journal* , **232**, pp. 34–48.

Dar, A. and Laor, A. (1997), Hadronic Production of TeV Gamma-Ray Flares from Blazars, *Astrophysical Journal Letters* , **478**, pp. L5–L8, arXiv: astro-ph/9610252.

Fragione, G., Antonini, F. and Gnedin, O. Y. (2017), Disrupted Globular Clusters and the Gamma-Ray Excess in the Galactic Centre, *ArXiv e-prints*, arXiv: 1709.03534.

Fukue, J. (2005), Terminal Speed of On-Axis Jets from a Supercritical Accretion Disk, *Publications of the Astronomical Society of Japan* , **57**, pp. 691–698.

Gnedin, O. Y., Ostriker, J. P. and Tremaine, S. (2014), Co-evolution of Galactic Nuclei and Globular Cluster Systems, *The Astrophysical Journal* , **785**, 71, arXiv: 1308.0021.

Hubbard, A. and Blackman, E. G. (2006), Active galactic nuclei jet mass loading and truncation by stellar winds, *Monthly Notices of the Royal Astronomical Society* , **371**, pp. 1717–1721, arXiv: astro-ph/0604585.

Kelner, S. R., Aharonian, F. A. and Bugayov, V. V. (2006), Energy spectra of gamma rays, electrons, and neutrinos produced at proton-proton interactions in the very high energy regime, *Phys. Rev. D* , **74**(3), 034018, arXiv: astro-ph/0606058.

Kirk, J. G., Guthmann, A. W., Gallant, Y. A. and Achterberg, A. (2000), Particle Acceleration at Ultrarelativistic Shocks: An Eigenfunction Method, *The Astrophysical Journal* , **542**, pp. 235–242, arXiv: astro-ph/0005222.

Komissarov, S. S. (1994), Mass-Loaded Relativistic Jets, *Monthly Notices of the Royal Astronomical Society* , **269**, p. 394.

Neumayer, N., Walcher, C. J., Andersen, D., Sánchez, S. F., Böker, T. and Rix, H.-W. (2011), Two-dimensional Hα kinematics of bulgeless disc galaxies, *Monthly Notices of the Royal Astronomical Society* , **413**, pp. 1875–1888, arXiv: 1101.5154.

Park, J., Caprioli, D. and Spitkovsky, A. (2015), Simultaneous Acceleration of Protons and Electrons at Nonrelativistic Quasiparallel Collisionless Shocks, *Physical Review Letters*, **114**(8), 085003, arXiv: 1412.0672.

Schödel, R., Feldmeier, A., Kunneriath, D., Stolovy, S., Neumayer, N., Amaro-Seoane, P. and Nishiyama, S. (2014), Surface brightness profile of the Milky Way's nuclear star cluster, *Astronomy and Astrophysics* , **566**, A47, arXiv: 1403.6657.

Torres, D. F. and Domingo-Santamaría, E. (2007), Collective effects of stellar winds and unidentified gamma-ray sources, *Astrophysics and Space Science* , **309**, pp. 345–350, arXiv: astro-ph/0611360.

Vieyro, F. L., Torres-Albà, N. and Bosch-Ramon, V. (2017), Collective non-thermal emission from an extragalactic jet interacting with stars, *Astronomy and Astrophysics* , **604**, A57, arXiv: 1704.01919.

Vokrouhlicky, D. and Karas, V. (1991), General relativistic effects in astrophysical jets, *Astronomy and Astrophysics* , **252**, pp. 835–841.

Wykes, S., Hardcastle, M. J., Karakas, A. I. and Vink, J. S. (2015), Internal entrainment and the origin of jet-related broad-band emission in Centaurus A, *Monthly Notices of the Royal Astronomical Society* , **447**, pp. 1001–1013, arXiv: 1409.5785.

Proceedings of *RAGtime 17–19, 17–19/23–26 Oct., 1–5 Nov., 2015/2016/2017, Opava, Czech Republic*
Z. Stuchlík, G. Török and V. Karas, editors, Silesian University in Opava, 2017, pp. 7–21

Numerical implementation of equations for photon motion in Kerr spacetime

Michal Bursa

Astronomical Institute of the Czech Academy of Sciences
Boční1401, 141 00 Praha 4, Czech Republic
bursa@astro.cas.cz

ABSTRACT
Raytracing is one of the essential tools for accurate modeling of spectra and variability of various astrophysical objects. It has a major importance in relativistic environments, where light endures to a number of relativistic effects. Because the trajectories of light rays in curved spacetimes, and in Kerr spacetime in particular, are highly non-trivial, we summarize the equations governing the motion of photon (or any other zero rest mass particle) and give analytic solution of the equations that can be further used in practical computer implementations.

Keywords: Kerr spacetime – raytracing – photon motion – numerical relativity

1 INTRODUCTION

The continuously increasing sensitivity, resolution (both angular and spectral) and collecting area of telescopes and instruments onboard satellites provide astronomers with constantly better energy spectra and light curves. Those are to be compared with models of our understanding of what processes shape them, for which we need (among other things) tools that will tell us how radiation propagates from the source through a curved spacetime to a distant detector – we need so called raytracing tools.

Raytracing requires fast and accurate computations of photon trajectories through the spacetime. This can be achieved in a number of ways, but the two conceptually distinct methods use either direct numerical integration of geodesic equation or evaluation of an analytic solution. The first method is very general and can be used in any spacetime, on the other hand speed can be a limiting factor in certain applications. The second method obviously relies on the integrability of geodesics and can only be used in spacetimes, which meet this condition such as in Kerr spacetime. Its advantage is speed in case one needs to connect two distant endpoints of the trajectory or access points on the trajectory in some other way than following the path step by step with small increments. The choice between one or the other method depends mainly on the target application or the implementing code design considerations, one is not generally better than the other. Of course, raytracing is only necessary if we deal with a region of spacetime along the line of sight that hosts an extremely gravitating object. This can be a black hole or a neutron star near the the center of

978-80-7510-257-7

the emission or somewhere in between the source and the observer, or simply a sufficiently dense distribution of matter along that path.

This paper summarizes equations for photon trajectories in Kerr spacetime along with their analytic solutions and gives a description for their practical numerical implementation. The equations were derived by Carter (1968) but due to their complexity, a full solution was inaccessible until computers became powerful enough to do the job. Rauch and Blandford (1994) first gave the solutions to Carter's equations in terms of elliptic integrals for the Kerr metric and since then a number of authors have published their ideas about ways of solving them. Particularly good description was given by Čadež et al. (1998); Li et al. (2005); Bozza (2008); Bini et al. (2012) and Yang and Wang (2013). Different authors, however, use different approaches, symbols and different tables of integrals, so it is not always easy to compare the solutions. Moreover, most of the authors employ axial symmetry and only focus on the motion in r-θ plane.

The intention of this paper is to provide a complete description of the problem of photon motion in Kerr spacetime, summarize the original equations and provide formulae for motion in t, r, θ and φ coordinate under a unified notation. We tend to demonstrate not only solutions, but how to use them practically for a numerical implementation of a raytracing algorithm.

2 EQUATIONS OF MOTION IN CURVED SPACETIME

In general relativity, gravity is regarded as a consequence of a curved spacetime geometry, where any source of mass or energy is a source of that curvature. Trajectories of free particles copy the spacetime warp while they connect any two points along the shortest path in accord with the principle of least action. Using that principle, an equation of motion for massive and mass-less particles can be derived that is called geodesic equation

$$\frac{\mathrm{d}^2 x^\mu}{\mathrm{d}\tau^2} = -\Gamma^\mu_{\alpha\beta}\frac{\mathrm{d}x^\alpha}{\mathrm{d}\tau}\frac{\mathrm{d}x^\beta}{\mathrm{d}\tau}\,, \tag{1}$$

where τ is an affine parameter (for a massive particle usually its proper time) and Γ is the connection tensor characterizing the shape of the spacetime. This equation can be of course solved numerically and in some trivial cases also analytically. In case of axially symmetric stationary spacetimes, the analytic solution was discovered long after the equation had been written down.

Kerr spacetime (or any stationary and axisymmetric spacetime for that matter) has two obvious symmetries that arise from the fact that its metric does not explicitly depend on time and azimuthal coordinate. This enables to find two Killing vectors associated with those differentiable symmetries that satisfy Killing equation $\nabla_\mu K_\nu + \nabla_\nu K_\mu = 0$. Kerr solution also admits a hidden symmetry represented mathematically by the existence of a Killing tensor field $K'_{\mu\nu}$ – a symmetric tensor field satisfying condition $\nabla_{(\alpha}K'_{\mu\nu)} = 0$ (that the trace-free part of the symmetrization of $\nabla K'$ vanishes). This third symmetry was first appreciated by Carter (1968), who deduced the existence of an associated conserved quantity Q and demonstrated the separability of Hamilton-Jacobi equation. In addition, Kerr spacetime, as well as other $\{2,2\}$ vacuum spacetimes, posses a conformal Killing

spinor, which helps to determine parallel propagation of vectors that are perpendicular to geodesics and which leads to yet another conserved complex quantity called Walker-Penrose constant (Walker and Penrose, 1970).

According to Noether's theorem (Noether, 1918), all spacetime symmetries are related to conserved quantities. Each Killing vector corresponds to a quantity that is conserved along geodesics, meaning that the product of the Killing vector and the geodesic tangent vector is conserved along the geodesic so that $\frac{d}{d\lambda}(K_\mu \frac{dx^\mu}{d\tau}) = 0$, where τ is an affine parameter of the geodesic. The symmetry associated with Killing tensor is related to Carter's constant $Q = K'_{\mu\nu}u^\mu u^\nu$. Physically, these three constants correspond to the conserved energy, the angular momentum with respect to the symmetry axis of the black hole, and the square of the total angular momentum along the geodesic (Bardeen et al., 1972; Wald, 1984). Beside this, the norm of four-velocity thanks to its parallel propagation is a fourth conserved number.

Carter's discovery of conserved quantity Q allowed him to explicitly demonstrate the separability of Hamilton-Jacobi equation and enabled to solve general geodesic motion in Kerr spacetime analytically (Misner et al., 1973; Chandrasekhar, 1983). Following his approach, the Hamilton-Jacobi equation for the Hamilton's principal function S,

$$2\frac{\partial S}{\partial \tau} = g^{\mu\nu}\frac{\partial S}{\partial x^\mu}\frac{\partial S}{\partial x^\nu}\,, \tag{2}$$

becomes after evaluation of metric coefficients

$$\begin{aligned} 2\frac{\partial S}{\partial \tau} =& \frac{1}{\rho^2\Delta}\left[(r^2+a^2)\frac{\partial S}{\partial t} + a\frac{\partial S}{\partial \varphi}\right]^2 - \frac{1}{\rho^2\sin^2\theta}\left[a\sin\theta\frac{\partial S}{\partial t} + \frac{\partial S}{\partial \varphi}\right]^2 \\ & - \frac{\Delta}{\rho^2}\left(\frac{\partial S}{\partial r}\right)^2 - \frac{1}{\rho^2}\left(\frac{\partial S}{\partial \theta}\right)^2 \end{aligned} \tag{3}$$

and we seek a solution in a form

$$S = \tfrac{1}{2}\delta\tau - Et + L_z\varphi + S_r(r) + S_\theta(\theta)\,, \tag{4}$$

where the negative sign of energy or the factor $1/2$ is chosen for convenience and already anticipates the final solution.

When the Hamilton-Jacobi equation (3) is applied to the anzatz (4) it turns out that the resulting equation can be arranged in such a way that on one side it has terms that only contain explicit dependence on r coordinate and on other side it has terms with θ dependence. Using a separation constant Q, it can thus be split into two equations

$$\left(\frac{dS_r}{dr}\right)^2 = \frac{R(r)}{\Delta^2} \quad \text{and} \quad \left(\frac{dS_\theta}{d\theta}\right)^2 = \Theta(\theta)\,, \tag{5}$$

where

$$R(r) = [(r^2+a^2)E - aL_z]^2 - \Delta[Q + (L_z - aE)^2 + \delta r^2]\,, \tag{6}$$

$$\Theta(\theta) = Q - (L_z^2\sin^{-2}\theta - a^2E^2 + \delta a^2)\cos^2\theta \tag{7}$$

and Q is Carter's separation constant. Details can be found in Chandrasekhar (1983), Chapter 62.

The solution for the principal function S then becomes

$$S = \tfrac{1}{2}\delta\tau - Et + L_z\varphi + \int^r \frac{\sqrt{R(r)}}{\Delta}\,\mathrm{d}r + \int^\theta \sqrt{\Theta(\theta)}\,\mathrm{d}\theta\,. \tag{8}$$

and the basic equations for geodesic motion can be obtained from the solution by calculating the partial derivatives of S with respect to different constants of motion and setting those to zero. Starting with Carter's constant, we find that

$$\frac{\partial S}{\partial Q} = \frac{1}{2}\int \frac{1}{\Delta\sqrt{R}}\frac{\partial R}{\partial Q}\,\mathrm{d}r + \frac{1}{2}\int \frac{1}{\sqrt{\Theta}}\frac{\partial \Theta}{\partial Q}\,\mathrm{d}\theta = 0 \tag{9}$$

that leads to

$$\int^r \frac{1}{\sqrt{R}}\,\mathrm{d}r = \int^\theta \frac{1}{\sqrt{\Theta}}\,\mathrm{d}\theta\,. \tag{10}$$

This frequently used equation describes the geodesic trajectory in $[r,\theta]$ plane, which provides sufficient description of the trajectory shape in applications that have stationary and axially symmetric geometry. For instance, many raytracing applications only use this equation for computing, e.g., an accretion disk image or spectrum, if the disk is assumed to be axially symmetric.

Similarly, we find a relation for photon's affine parameter (what would be the proper time for massive particles)

$$\begin{aligned}\frac{\partial S}{\partial \delta} &= \frac{1}{2}\tau + \frac{1}{2}\int \frac{1}{\Delta\sqrt{R}}\frac{\partial R}{\partial \delta}\,\mathrm{d}r + \frac{1}{2}\int \frac{1}{\sqrt{\Theta}}\frac{\partial \Theta}{\partial \delta}\,\mathrm{d}\theta \\ &= \frac{1}{2}\tau + \frac{1}{2}\int \frac{r^2}{\sqrt{R}}\,\mathrm{d}r + \frac{1}{2}\int \frac{a^2\cos^2\theta}{\sqrt{\Theta}}\,\mathrm{d}\theta = 0\,,\end{aligned} \tag{11}$$

$$\tau = \int^r \frac{r^2}{\sqrt{R}}\,\mathrm{d}r + a^2\int^\theta \frac{\cos^2\theta}{\sqrt{\Theta}}\,\mathrm{d}\theta\,. \tag{12}$$

For energy E as a constant of motion we have

$$\begin{aligned}\frac{\partial S}{\partial E} &= -t + \frac{1}{2}\int \frac{1}{\Delta\sqrt{R}}\frac{\partial R}{\partial E}\,\mathrm{d}r + \frac{1}{2}\int \frac{1}{\sqrt{\Theta}}\frac{\partial \Theta}{\partial E}\,\mathrm{d}\theta \\ &= -t + \int \frac{r^4E + r^2a^2E + 2Ma^2rE - 2MarL_z}{\Delta\sqrt{R}}\,\mathrm{d}r + \\ &\quad + \int \frac{Ea^2\cos^2\theta}{\sqrt{\Theta}}\,\mathrm{d}\theta = 0\,,\end{aligned} \tag{13}$$

which can be expressed after some rearranging with the help of (12) as

$$t = \tau E + 2M\int^r \frac{r^3E - a(L_z - aE)r}{\Delta\sqrt{R}}\,\mathrm{d}r\,. \tag{14}$$

And finally, the derivative of S with respect to L_z gives

$$\begin{aligned}\frac{\partial S}{\partial L_z} &= \varphi + \frac{1}{2}\int \frac{1}{\Delta\sqrt{R}}\frac{\partial R}{\partial L_z}\,\mathrm{d}r + \frac{1}{2}\int \frac{1}{\sqrt{\Theta}}\frac{\partial \Theta}{\partial L_z}\,\mathrm{d}\theta \\ &= \varphi - \int \frac{2MrL_z - 2MarE - r^2L_z}{\Delta\sqrt{R}}\,\mathrm{d}r - \int \frac{L_z\cot^2\theta}{\sqrt{\Theta}}\,\mathrm{d}\theta = 0\,,\end{aligned} \tag{15}$$

$$\varphi = \int^r \frac{r(r-2M)L_z + 2MarE}{\Delta\sqrt{R}}\,\mathrm{d}r + \int^\theta \frac{L_z\cot^2\theta}{\sqrt{\Theta}}\,\mathrm{d}\theta\,, \tag{16}$$

which can be proved to be the same formula as the one given by Chandrasekhar (1983, Equation 181)

$$\varphi = a\int^r \frac{(r^2+a^2)E - aL_z}{\Delta\sqrt{R}}\,\mathrm{d}r + \int^\theta \frac{L_z\sin^{-2}\theta - aE}{\sqrt{\Theta}}\,\mathrm{d}\theta\,. \tag{17}$$

3 SOLUTIONS FOR PHOTON TRAJECTORIES

Null geodesics have $\delta = 0$ and if we define dimensionless quantities for the constant of motions $\lambda = L_z/E = -p_\varphi/p_t$ and $q = Q/E^2$ and replace $\cos\theta$ with μ, the set of equations of motion become

$$\int^r \frac{1}{\sqrt{R(r)}}\,\mathrm{d}r = \int^\mu \frac{1}{\sqrt{\Theta_\mu(\mu)}}\,\mathrm{d}\mu\,, \tag{18}$$

$$\Delta t = \int^r \frac{r^2(r^2+a^2) + 2ar(a-\lambda)}{\Delta\sqrt{R(r)}}\,dr + a^2\int^\mu \frac{\mu^2}{\sqrt{\Theta_\mu(\mu)}}\,\mathrm{d}\mu\,, \tag{19}$$

$$\Delta\phi = \int^r \frac{2ar - \lambda a^2}{\Delta\sqrt{R(r)}}\,\mathrm{d}r + \int^\mu \frac{\lambda}{(1-\mu^2)\sqrt{\Theta_\mu(\mu)}}\,\mathrm{d}\mu\,, \tag{20}$$

$$R(r) = r^4 + (a^2 - \lambda^2 - q)r^2 + 2\left(q + (\lambda - a)^2\right)r - a^2q\,, \tag{21}$$

$$\Theta_\mu(\mu) = q + (a^2 - \lambda^2 - q)\mu^2 - a^2\mu^4 = a^2(\mu_-^2 + \mu^2))(\mu_+^2 - \mu^2))\,. \tag{22}$$

This should be accompanied by equations for photon 4-momentum

$$\Sigma\frac{\mathrm{d}k^t}{\mathrm{d}\tau} = -a\left[a(1-\mu^2) - \lambda\right] + (r^2+a^2)\frac{r^2+a^2-a\lambda}{\Delta}\,, \tag{23a}$$

$$\Sigma\frac{\mathrm{d}k^r}{\mathrm{d}\tau} = \pm\sqrt{R(r)}\,, \tag{23b}$$

$$\Sigma\frac{\mathrm{d}k^\theta}{\mathrm{d}\tau} = \pm\sqrt{\Theta(\theta)} = \pm\sqrt{\Theta_\mu(\mu)/(1-\mu^2)}\,, \tag{23c}$$

$$\Sigma\frac{\mathrm{d}k^\varphi}{\mathrm{d}\tau} = -a + \frac{\lambda}{1-\mu^2} + \frac{a(r^2+a^2-a\lambda)}{\Delta}\,. \tag{23d}$$

The integration over r and μ goes from one endpoint (an emitter) to the other (an observer) of the trajectory and the signs of $R^{1/2}$ and $\Theta_\mu^{1/2}$ must be the same as those of $\mathrm{d}r$ and $\mathrm{d}\theta$, which change each time the integration passes through a radial or a poloidal turning point, where $R(r)=0$ or $\Theta_\mu(\mu)=0$, respectively. There can be at most one radial turning point, but many poloidal turning points along a particular trajectory as it may wind up around the photon orbit.

Starting with Eq. 18, both $R(r)$ and $\Theta_\mu(\mu)$ are quartic polynomials, meaning that both integrals can be evaluated in terms of an elliptic integral of the first kind $F(\phi|m)$, where the modulus is only function of the constants of motion and ϕ is a suitable function of r or μ, respectively. Calculating the change in the azimuthal position and the travel time involves more complex integrands that evaluate to elliptic integral of the second and third kind.

Eventually, all necessary integrals can be expressed in terms of Jacobi elliptic functions $\mathrm{sn}(u|m)$, $\mathrm{cn}(u|m)$, $\mathrm{dn}(u|m)$, $\mathrm{tn}(u|m)$ and their inversions and in terms of elliptic integrals of the first, second and third kind that boil down to evaluation of Carlson elliptic integral functions. The book of elliptic integrals by Byrd and Friedman (1971, hereafter BF) becomes helpful in finding the transformations of various integrals to Jacobi and Carlson functions. Numerical implementation of Carlson's elliptic integrals $\mathrm{R_C}(x,y)$, $\mathrm{R_D}(x,y,z)$, $\mathrm{R_F}(x,y,z)$, $\mathrm{R_J}(x,y,z,p)$, Legendre elliptic integrals $\mathrm{F}(\phi|m)$, $\mathrm{E}(\phi|m)$, $\Pi(\phi|m)$ and Jacobi elliptic functions $\mathrm{sn}(u|m)$, $\mathrm{cn}(u|m)$, $\mathrm{dn}(u|m)$, $\mathrm{tn}(u|m)=\mathrm{sn}(u|m)/\mathrm{cn}(u|m)$ can be found e.g. in Press (1992, Numerical Recipes, Chapter 6). For inverse Jacobi elliptic functions, we can use the relation

$$z=\mathrm{sn}(u|m)\,,\quad u=\mathrm{sn}^{-1}(z|m) \tag{24}$$

and similarly for $\mathrm{cn}(u|m)$, $\mathrm{dn}(u|m)$ and $\mathrm{tn}(u|m)$. Then we get from the definition of the functions (BF, Eq. 131.00)

$$\mathrm{sn}^{-1}(z|m)=z\;\mathrm{R_F}\left(1-z^2,1-mz^2,1\right), \tag{25a}$$
$$\mathrm{cn}^{-1}(z|m)=\mathrm{sn}^{-1}(\sqrt{(1-z^2)}\,|\,m)\,, \tag{25b}$$
$$\mathrm{dn}^{-1}(z|m)=\mathrm{sn}^{-1}(\sqrt{(1-z^2)/m}\,|\,m)\,, \tag{25c}$$
$$\mathrm{tn}^{-1}(z|m)=\mathrm{sn}^{-1}(\sqrt{z^2/(1+z^2)}\,|\,m)\,, \tag{25d}$$

A convention for the modulus in elliptic integrals and elliptic functions is used throughout this paper, which differs by a square from what Byrd and Friedman (1971) use; e.g. what we denote as $\mathrm{sn}(u|m)$ is $\mathrm{sn}(u|\sqrt{m})$ in BF.

3.1 Radial integral

In order to express the R-integral in terms of elliptic functions, we need to factorize function $R(r)$ and find its roots r_1, r_2, r_3, r_4. Since $R(0)=-a^2q$, there are two options. For geodesics that cross the equatorial plane and have $q\geq 0$ or $a=0$, $R(0)\leq 0$ and because $R(\pm\infty)\to+\infty$, the expression has to have two or four real roots. For geodesics that have $q<0$ and do not cross the equatorial plane, $R(0)>0$ and $R(r)$ can have four or zero real roots. We can thus consider three separate cases:

Four real roots. Let us assume roots in the order $r_1 > r_2 > r_3 > r_4$, then $R(0) = r_1\,r_2\,r_3\,r_4 = -a^2 q$ means that $r_4 < 0$ and that photons are allowed to exist in region $r > r_1$ (outer region, both endpoints at infinity) or in region $r_3 < r < r_2$ (inner region, both endpoints under the event horizon). Analytic formulae for evaluating the root values have been given by Čadež et al. (1998). In the outer region, the integral evaluates to (BF, Eq. 258.00)

$$\int_{r_1}^{r} \frac{\mathrm{d}r}{\sqrt{R(r)}} = \int_{r_1}^{r} \frac{\mathrm{d}r}{\sqrt{(r-r_1)(r-r_2)(r-r_3)(r-r_4)}} = \frac{2}{\sqrt{(r_1-r_3)(r_2-r_4)}}\,\mathrm{sn}^{-1}\left[\sqrt{\frac{(r_2-r_4)(r-r_1)}{(r_1-r_4)(r-r_2)}}\middle| m_4\right], \tag{26}$$

where

$$m_4 = \frac{(r_1-r_4)(r_2-r_3)}{(r_1-r_3)(r_2-r_4)}\,. \tag{27}$$

In the inner region, the integral evaluates to (BF, Eq. 255.00)

$$\int_{r}^{r_2} \frac{\mathrm{d}r}{\sqrt{R(r)}} = \int_{r}^{r_2} \frac{\mathrm{d}r}{\sqrt{(r-r_1)(r-r_2)(r-r_3)(r-r_4)}} = \frac{2}{\sqrt{(r_1-r_3)(r_2-r_4)}}\,\mathrm{sn}^{-1}\left[\sqrt{\frac{(r_1-r_3)(r_2-r)}{(r_2-r_3)(r_1-r)}}\middle| m_4\right]. \tag{28}$$

In case of double real root $r_1 = r_2$, the above expressions fail, because the inverse Jacobi elliptic function $\mathrm{sn}^{-1}(1|1) = \infty$ and the evaluation requires a special treatment (Li et al., 2005, Eq. A11 and A13). In practice, however, such a case hardly ever happens with a numerical approach.

Two real and two complex roots. Let us assume roots in the order $r_1 > r_2$ for the two real roots and $r_3 = r_4^\star$ (complex conjugate) for the two complex roots. Since $r_1 r_2 r_3 r_4 = r_1 r_2 |r_3|^2 = -a^2 Q \le 0$, r_1 must be positive and r_2 must be negative. They cannot be equal as in that case they both would have to be zero, for which (21) implies also $r_3 = r_4 = 0$. The R-integral then evaluates to (BF, Eq. 260.00)

$$\int_{r_1}^{r} \frac{\mathrm{d}r}{\sqrt{R(r)}} = \frac{1}{\sqrt{AB}}\,\mathrm{cn}^{-1}\left[\frac{(A-B)r + r_1 B - r_2 A}{(A+B)r - r_1 B - r_2 A}\middle| m_2\right]. \tag{29}$$

where

$$m_2 = \frac{(A+B)^2 - (r_1-r_2)^2}{4AB}\,, \tag{30a}$$

$$A = \left[(r_1-u)^2 + v^2\right]^{1/2}\,, \quad B = \left[(r_2-u)^2 + v^2\right]^{1/2} \tag{30b}$$

with u and v being respectively the real and imaginary part of r_3.

Four complex roots roots. Let us assume roots $r_1 = r_2^\star$ and $r_3 = r_4^\star$ (* stands for a complex conjugate). Then $R(r)$ can be written as $R(r) = [(r-b_1)^2 + a_1^2][(r-b_2)^2 + a_2^2]$ and the radial integral is (BF, Eq. 267.00)

$$\int_{r_0}^{r} \frac{\mathrm{d}r}{\sqrt{R(r)}} = \int_{r_0}^{r} \frac{\mathrm{d}r}{\sqrt{[(r-b_1)^2 + a_1^2][(r-b_2)^2 + a_2^2]}} = \\ = \frac{2}{A+B}\ \mathrm{tn}^{-1}\left(\frac{r-r_0}{a_1 + b_1 g_1 - g_1 r} \middle| m_0 \right), \tag{31}$$

where

$$b_1 = (r_1 + r_2)/2 = \mathrm{Re}(r_1), \qquad a_1^2 = -(r_1 - r_2)^2/4 = \mathrm{Im}(r_1)^2, \tag{32a}$$
$$b_2 = (r_3 + r_4)/2 = \mathrm{Re}(r_3), \qquad a_2^2 = -(r_3 - r_4)^2/4 = \mathrm{Im}(r_3)^2, \tag{32b}$$
$$A^2 = (b_1 - b_2)^2 + (a_1 + a_2)^2, \qquad B^2 = (b_1 - b_2)^2 + (a_1 - a_2)^2, \tag{32c}$$
$$g_1 = \frac{4a_1^2 - (A-B)^2}{(A+B)^2 - 4a_a^2}, \qquad m_0 = \frac{4AB}{(A+B)^2}\,. \tag{32d}$$

Note that now the lower limit of the integral does not go from the largest real root of $R(r)$, but it is

$$r_0 = b_1 - a_1 g_1\,. \tag{33}$$

Let us introduce a quantity

$$P_r(r) \equiv \int_r^\infty \frac{\mathrm{d}r}{\sqrt{R(r)}} = \int_{r_1}^\infty \frac{\mathrm{d}r}{\sqrt{R(r)}} \pm \int_{r_1}^{r} \frac{\mathrm{d}r}{\sqrt{R(r)}} = P_{r_1} \pm \int_{r_1}^{r} \frac{\mathrm{d}r}{\sqrt{R(r)}}\,. \tag{34}$$

We can then describe the whole trajectory by the value of P_r, which is zero for $r = \infty$, then increases up to $P_{r_1} = \int_{r_1}^\infty$ as r reaches the turning point and further increases to $P_r = 2P_{r_1}$ as $r \to \infty$ at the other end of the trajectory (behind the pericenter). Such a parametrization can be used instead of the affine parameter (if we do not need the affine property) as the value of P_r uniquely identifies any point of the trajectory. For the inbound orbit this is similarly

$$P_r(r) \equiv \int_{r_3}^{r} \frac{\mathrm{d}r}{\sqrt{R(r)}} = \int_{r_3}^{r_2} \frac{\mathrm{d}r}{\sqrt{R(r)}} \pm \int_{r}^{r_2} \frac{\mathrm{d}r}{\sqrt{R(r)}} = P_{r_2} \pm \int_{r}^{r_2} \frac{\mathrm{d}r}{\sqrt{R(r)}}\,. \tag{35}$$

Equations (26), (28), (29) and (31) can be inverted based on relations (24) and (25) to obtain radius from the known value of the integral.

For the case of four real roots and the outer region we have

$$r = \frac{r_1(r_2 - r_4) - r_2(r_1 - r_4)\,\mathrm{sn}^2(\xi_{4a}|m_4)}{(r_2 - r_4) - (r_1 - r_4)\,\mathrm{sn}^2(\xi_{4a}|m_4)}\,, \tag{36}$$

where

$$\xi_{4a} = \pm\frac{1}{2}(P_r - P_{r_1})\sqrt{(r_1 - r_3)(r_2 - r_4)} \tag{37}$$

with the sign chosen such that ξ_{4a} is positive.

For the case of four real roots and the inner region we have

$$r = \frac{r_2(r_1 - r_3) - r_1(r_2 - r_3)\,\mathrm{sn}^2(\xi_{4b}|m_4)}{(r_1 - r_3) - (r_2 - r_3)\,\mathrm{sn}^2(\xi_{4b}|m_4)}\,, \tag{38}$$

where

$$\xi_{4b} = \pm\frac{1}{2}(P_r - P_{r_2})\sqrt{(r_1 - r_3)(r_2 - r_4)}\,. \tag{39}$$

For the case of two real and two complex roots we have

$$r = \frac{(r_2 A - r_1 B) - (r_2 A + r_1 B)\,\mathrm{cn}(\xi_2|m_2)}{(A - B) - (A + B)\,\mathrm{cn}(\xi_2|m_2)}\,, \tag{40}$$

where $\xi_2 = (P_{r_1} - P_r)\sqrt{AB}$ and A and B are given by (30).
Finally, for the case of four complex roots we have

$$r = \frac{(b_1 - a_1 g_1) + (a_1 + b_1 g_1)\,\mathrm{tn}(\xi_0|m_0)}{1 + \mathrm{tn}(\xi_0|m_0)}\,, \tag{41}$$

where $\xi_0 = (P_{r_0} - P_r)(A + B)/2$ and r_0, A, B are given by (32).

3.2 Poloidal integral

Evaluation of the poloidal integral also depends on the value of q. From (22) follows that $\mu_+^2\mu_-^2 = q/a^2$. If $q > 0$, both μ_+^2 and μ_-^2 must be positive and the poloidal motion is allowed in the range of $-\mu_+ < \mu < +\mu_+$. If $q < 0$, μ_-^2 must be negative (which causes no problems) and the motion is allowed only in the range of $\sqrt{-\mu_-^2} < \mu < \mu_+$ and $-\mu_+ < \mu < -\sqrt{-\mu_-^2}$, and such orbits do not cross the equatorial plane. Moreover, $q + (a - \lambda)^2$ must be positive. Based on these two cases, the integral on the right-hand side of (18) can be worked out as (BF, Eq. 213.00 and 218.00)

$$\int_\mu^{\mu_+} \frac{\mathrm{d}\mu}{\sqrt{\Theta_\mu(\mu)}} = \int_\mu^{\mu_+} \frac{\mathrm{d}\mu}{\sqrt{a^2(\mu_-^2 + \mu^2)(\mu_+^2 - \mu^2)}} =$$
$$= \begin{cases} \dfrac{1}{\sqrt{a^2(\mu_+^2 + \mu_-^2)}}\ \mathrm{cn}^{-1}\left(\dfrac{\mu}{\mu_+}\middle|\dfrac{\mu_+^2}{\mu_+^2 + \mu_-^2}\right) & \text{for } \mu_-^2 > 0\,, \\ \dfrac{1}{\sqrt{a^2\mu_+^2}}\ \mathrm{sn}^{-1}\left(\sqrt{\dfrac{\mu_+^2 - \mu^2}{\mu_+ + \mu_-}}\middle|\dfrac{\mu_+^2 + \mu_-^2}{\mu_+^2}\right) & \text{for } \mu_-^2 < 0\,. \end{cases} \tag{42}$$

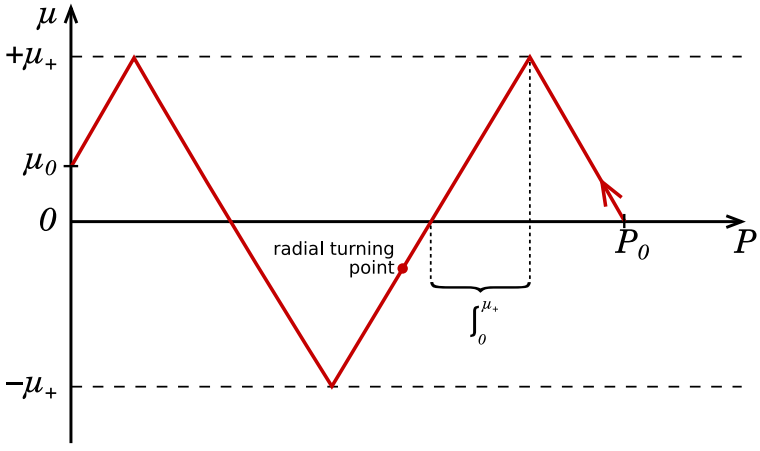

Figure 1. An illustration of a photon trajectory shown in terms of varying poloidal coordinate $\mu = \cos\theta$ (vertical axis) and radial coordinate (horizontal axis). The radial coordinate is, however, expressed indirectly by the value of the R-integral. Note that the radial and poloidal integral change at the same pace ($P_r(r) = P_\mu(\mu)$), so the path has a triangular shape and segments between any two turning poloidal points have identical change in the value of the integral.

It should be noted that trajectories may oscillate between turning points several times depending on the exact aiming. For example (see Fig. 1 and read it from right to left), we may have a trajectory that starts off the equatorial plane, goes up, then crosses the equatorial plane $\mu = 0$, goes bellow it, then back above it and it finally reaches its final value of poloidal angle μ_0 after passing through one more turning point at μ_+. The value of P is zero at the end of trajectory, which means that this end is at infinity, while it starts from the equatorial plane at some radius r_0, which corresponds to the value of the radial integral $P = P_0$. Somewhere along the trajectory, there lies also the radial turning point.

For the trajectory in Fig. 1, the value of the poloidal integral is

$$P_\mu = \left(\int_0^{+\mu_+} + 2\int_{-\mu_+}^{+\mu_+} + \int_{\mu_0}^{+\mu_+} \right) \frac{\mathrm{d}\mu}{\sqrt{\Theta_\mu(\mu)}} \tag{43}$$

and it has to match the value of the radial integral at each point of the trajectory,

$$P_r(r) = P_\mu(\mu)\,, \tag{44}$$

which makes a unique link between radial and poloidal coordinate at any given point along the trajectory and allows, from a known value P of the radial/poloidal integral, to determine coordinates $r(P)$ (Eq. 36, 38, 40, 41) and $\mu(P)$ through inversion

$$\mu = \mu_+ \,\mathrm{cn}\left(\frac{P_\mu}{m_K} \middle| m_\mu \right)\,. \tag{45}$$

The last expression requires some caution, because it only works within a single segment of the trajectory between $-\mu_+$ and $+\mu_+$ meaning that P_μ has to be in the range $0 \leq P_\mu \leq$

$2P_\mu(0)$ and a suitable multiple of $\int_0^{\mu_+}$ has to be subtracted from P_μ together with any bit of $\int_{\mu_0}^{\mu_+}$ remaining at the other end of the trajectory.

3.3 Time integral

The time integral (19) can be solved after the polynomial in the radial part of the integral has been factorized. For the integrand of the radial part we get (dropping factor $1/\sqrt{R(r)}$ for a moment)

$$\frac{r^2(r^2+a^2)+2ar(a-\lambda)}{\Delta} = r^2+2r+4+\frac{2(-a\lambda+4)r-4a^2}{\Delta}\,. \tag{46}$$

The first three terms can be evaluated with suitable integrals and we can still manipulate with the fourth term assuming that $\Delta = r^2-2r+a^2 = (r-r_+)(r-r_-)$. After bit of an algebra, we find that

$$\frac{2(-a\lambda+4)r-4a^2}{\Delta} = \frac{2(-a\lambda+4)r_+-4a^2}{(r_+-r_-)(r-r_+)} + \frac{-2(-a\lambda+4)r_++4a^2}{(r_+-r_-)(r-r_-)}\,. \tag{47}$$

The final expression for coordinate travel time therefore is

$$\begin{aligned}\Delta t = &\int^r \frac{r^2}{\sqrt{R(r)}}\,\mathrm{d}r + 2\int^r \frac{r}{\sqrt{R(r)}}\,\mathrm{d}r + 4\int^r \frac{1}{\sqrt{R(r)}}\,\mathrm{d}r + \\ &+ \frac{(-a\lambda+4)r_+-2a^2}{\sqrt{1-a^2}}\int^r \frac{1}{(r-r_+)\sqrt{R(r)}}\,\mathrm{d}r - \\ &- \frac{(-a\lambda+4)r_--2a^2}{\sqrt{1-a^2}}\int^r \frac{1}{(r-r_-)\sqrt{R(r)}}\,\mathrm{d}r + \\ &+ a^2\int^\mu \frac{\mu^2}{\sqrt{\Theta_\mu(\mu)}}\,\mathrm{d}\mu\,.\end{aligned} \tag{48}$$

The integrals in the above expression can all be evaluated in terms of elliptic functions. The expressions get lengthy, so we only point out the formulae to be used. In case of 4 real roots of $R(r)$ function, we use BF formula 258.11+340.02 for the first integral, 258.11+340.01 for the second, 258.00 for the third and 258.39+340.01 for the last two radial integrals. In case of 2 real and 2 complex roots of $R(r)$, we use formulae 260.03+341.02-04, 260.03+341.02-03, 260.00 and 260.04+341.02-03, respectively. In case of 4 complex roots, we use formulae 267.01+342.02-04, 267.01+341.02-03, 267.00 and 267.02+342.02-03, respectively. The poloidal integral can be evaluated using formula 213.06+312.02 or 218.01. All integrals have to be taken with proper limits as it has been discussed in Sections 3.1 and 3.2.

3.4 Azimuthal integral

Finally, the change of azimuthal coordinate along the trajectory can be calculated from Eq. 20. After a similar factorization of the radial part of the integral that we have used in

the previous section we obtain

$$\Delta\varphi = \int^r \frac{2ar-\lambda a^2}{\Delta\sqrt{R(r)}}\,\mathrm{d}r + \int^\mu \frac{\lambda}{(1-\mu^2)\sqrt{\Theta_\mu(\mu)}}\,\mathrm{d}\mu = \\ = \frac{2ar_+-\lambda a^2}{2\sqrt{1-a^2}}\int^r \frac{\mathrm{d}r}{(r-r_+)\sqrt{R(r)}} - \frac{2ar_--\lambda a^2}{2\sqrt{1-a^2}}\int^r \frac{\mathrm{d}r}{(r-r_-)\sqrt{R(r)}} + \\ + \lambda\int^\mu \frac{\mathrm{d}\mu}{(1-\mu^2)\sqrt{\Theta_\mu(\mu)}}\,. \tag{49}$$

The first two radial integrals are of the same type as the terms in the time integral and the same formulae as listed in the previous subsection are used to evaluate them. The last integral can be evaluated using formula 213.02 or 218.02. Again, all integrals has to be taken with proper limits.

3.5 Integration of geodesic equation

We spend the rest of this section with another way of getting a purely numerical solution of photon trajectories that directly integrates the geodesic equation (1). Such an approach becomes useful when one deals with a non-Kerr metric, either a different analytic metric or a numeric metric. In fact, it is often the only possible approach in such cases.

There are many methods published in the literature that can be used to integrate second-order differential equations with Runge-Kutta method probably being in the lead of the most frequently used ones. Other choices my include Dormand-Prince method or Burlirsch-Stoer algorithm. Those methods however require multiple evaluation of the derivative function, which can be time consuming. This is indeed the case of geodesic equation, where components of the connection tensor have to be evaluated. This is rank 3 tensor that may contain up to 40 independent components. If performance is an issue, one seeks for a method that gives a reasonable precision while minimizing the number of necessary evaluation of the derivatives. Verlet algorithm is one of such methods.

Verlet algorithm is a numerical method frequently used to integrate equations of motion in Newtonian kinematics or particle trajectories in molecular dynamics simulations. Dolence et al. (2009) give a version of the algorithm for integrating the geodesic equation. The integration starts with an initial position x^μ_0 of the photon, its initial 4-momentum k^μ_0

and momentum derivative $\mathrm{d}k_0^\mu/\,\mathrm{d}\lambda$ and follows the scheme

$$x^\mu_{n+1} = x^\mu_n + k^\mu_n \Delta\lambda + \frac{1}{2}\left(\frac{\mathrm{d}k^\mu}{\mathrm{d}\lambda}\right)_n (\Delta\lambda)^2\,, \tag{50a}$$

$$k'^\mu = k^\mu_n + \left(\frac{\mathrm{d}k^\mu}{\mathrm{d}\lambda}\right)_n \Delta\lambda\,, \tag{50b}$$

$$\left(\frac{\mathrm{d}k^\mu}{\mathrm{d}\lambda}\right)_{n+1} = -\Gamma^\mu_{\alpha\beta}(x_{n+1})\, k'^\alpha\, k'^\beta\,, \tag{50c}$$

$$k^\mu_{n+1} = k^\mu_n + \frac{1}{2}\left[\left(\frac{\mathrm{d}k^\mu}{\mathrm{d}\lambda}\right)_n + \left(\frac{\mathrm{d}k^\mu}{\mathrm{d}\lambda}\right)_{n+1}\right]\Delta\lambda\,. \tag{50d}$$

(50e)

Intermediate steps (50b) and (50c) are repeated few times until the required accuracy is reached. The expensive calculation of the connection coefficients Γ is, however, done only once. The accuracy can be controlled at each step by checking the error of $k^\mu k_\mu$ (that is supposed to be zero), k_t or Carter's constant Q (that are supposed to conserve their initial values) and the integration routine can adjust the step size $\Delta\lambda$ accordingly.

4 NUMERICAL IMPLEMENTATION

All the above given formulae are implemented in SIM5[1] library, which is an extensive collection of routines for raytracing and radiative transport in general relativity.

The core of the library contains a C implementation of Carlson elliptic integrals and Jacobi elliptic functions after Press (1992), with various enhancements. Those function have been checked against their implementation in Mathematica, ver. 7 to provide same results including extensions to the supported range of parameters where necessary. This is supplemented by implementation of required formulae for reduction of elliptic integrals from Byrd and Friedman (1971) book.

On top of these low-level functions, the library builds a set of routines that give solutions for integrals of photon motions. Those routines use a uniform way of parametrization of geodesics based on the value of R-integral.

There is also a routine for numerical integration of the geodesic equation, which is an implementation of Eq. 50. The routine controls the accuracy of the integration by checking the values of $k^\mu k_\mu$ and k_t, which can be evaluated faster than Carter's constant, and adjusts the step size $\Delta\lambda$ to keep the accuracy in tolerance. The overall precision of the integration is controlled via a parameter, allowing for faster less accurate or slower and more reliable calculations.

The library is freely available for use at GitHub.

[1] `https://github.com/mbursa/sim5`

5 CONCLUSIONS

The paper outlines ways of solving photon geodesics (mainly) in Kerr spacetime with the aim of giving a complete summary of the equations needed for obtaining all the coordinates along a trajectory. Major focus is put on the analytic solution of the equations of photon motion using elliptic integrals and elliptic functions, because it provides a fast and efficient way of evaluating light ray paths in Kerr spacetime. Sometimes, a step-wise approach of geodesic integration may be better suited for a particular task or a different spacetime than Kerr is of interest. For those cases, a method of direct numerical integration of geodesic equation is discussed, which is one of many ways how such an equation may be integrated, however it is a choice that gives balanced ratio between performance and accuracy.

ACKNOWLEDGEMENTS

The present work has been financialy supported from the EU FP7 grant 312789 and from CZ grant LTAUSA17095.

REFERENCES

Bardeen, J. M., Press, W. H. and Teukolsky, S. A. (1972), Rotating Black Holes: Locally Nonrotating Frames, Energy Extraction, and Scalar Synchrotron Radiation, *ApJ*, **178**, pp. 347–370.

Bini, D., Falanga, M., Geralico, A. and Stella, L. (2012), The signal from an emitting source moving in a Schwarzschild spacetime under the influence of a radiation field, *Classical and Quantum Gravity*, **29**(6), 065014, arXiv: 1408.5256.

Bozza, V. (2008), Optical caustics of Kerr spacetime: The full structure, *Phys.Rev.D*, **78**(6), 063014, arXiv: 0806.4102.

Byrd, P. F. and Friedman, M. D. (1971), *Handbook of elliptic integrals for engineers and scientists*, Grundlehren der mathematischen Wissenschaften, Springer-Verlag, ISBN 9783540053187.

Carter, B. (1968), Global Structure of the Kerr Family of Gravitational Fields, *Physical Review*, **174**, pp. 1559–1571.

Chandrasekhar, S. (1983), *The Mathematical Theory of Black Holes*, International series of monographs on physics, Oxford.

Dolence, J. C., Gammie, C. F., Mościbrodzka, M. and Leung, P. K. (2009), grmonty: A Monte Carlo Code for Relativistic Radiative Transport, *ApJS*, **184**, pp. 387–397, arXiv: 0909.0708.

Li, L.-X., Zimmerman, E. R., Narayan, R. and McClintock, J. E. (2005), Multitemperature Blackbody Spectrum of a Thin Accretion Disk around a Kerr Black Hole: Model Computations and Comparison with Observations, *ApJS*, **157**, pp. 335–370, arXiv: astro-ph/0411583.

Misner, C. W., Thorne, K. S. and Wheeler, J. A. (1973), *Gravitation*, Freeman, San Francisco.

Noether, E. (1918), Invariante variationsprobleme, *Nachr. D. Knig. Gesellsch. D. Wiss. Zu Gttingen, Math-phys. Klasse*, p. 235.

Press, W. (1992), *Numerical Recipes in C: The Art of Scientific Computing*, bk. 4, Cambridge University Press, ISBN 9780521437202.

Rauch, K. P. and Blandford, R. D. (1994), Optical caustics in a kerr spacetime and the origin of rapid X-ray variability in active galactic nuclei, *APJ*, **421**, pp. 46–68.

Čadež, A., Fanton, C. and Calvani, M. (1998), Line emission from accretion discs around black holes: the analytic approach, *New Astronomy*, **3**, pp. 647–654.

Wald, R. M. (1984), *General Relativity*, The University of Chicago Press.

Walker, M. and Penrose, R. (1970), On quadratic first integrals of the geodesic equations for type {22} spacetimes, *Communications in Mathematical Physics*, **18**, pp. 265–274.

Wolfram Research, Inc. (2008), Mathematica, version 7.0, Champaign, IL.

Yang, X. and Wang, J. (2013), YNOGK: A New Public Code for Calculating Null Geodesics in the Kerr Spacetime, *ApJS*, **207**, 6, arXiv: 1305.1250.

Proceedings of *RAGtime 17–19, 17–19/23–26 Oct., 1–5 Nov., 2015/2016/2017, Opava, Czech Republic*
Z. Stuchlík, G. Török and V. Karas, editors, Silesian University in Opava, 2017, pp. 23–32

Innermost stable circular orbits around compact stars: Terms that are quadratic in spin

Kateřina Goluchová[1], Gabriel Török[1,a], Martin Urbanec[1], Gabriela Urbancová[1,2] and Eva Šrámková[1]

[1] Institute of Physics and Research Centre for Computational Physics and Data Processing, Faculty of Philosophy & Science, Silesian University in Opava, Bezručovo nám. 13, CZ-746 01 Opava, Czech Republic
[2] Astronomical Institute, Boční II 1401/2a, CZ-14131 Praha 4 – Spořilov, Czech Republic
[a] gabriel.torok@gmail.com

ABSTRACT
Orbital motion close to a rotating compact star is largely affected by strong gravity. Location of the innermost stable circular orbit (ISCO) is determined trough interplay between the effects of general relativity and the effects of Newtonian physics that are associated to oblateness of the compact star. The Keplerian frequency at this orbit may increase as well as decrease when the compact star angular momentum increases. In this context we explore behaviour of the ISCO frequency for compact star models calculated within the Hartle–Thorne spacetime approximation.

Keywords: X-Rays: Binaries — Accretion, Accretion Disks — Stars: Neutron

1 INTRODUCTION

The Keplerian circular trajectories of test particles orbiting at external radii $r \in (r_{\text{NT}}, \infty)$ around a spherical central body of mass M and radial extension r_{NT} in Newtonian theory poses monotonic behaviour of the angular momentum ℓ,

$$\frac{\partial \ell^2}{\partial r} > 0\,. \tag{1}$$

This inequality implies that the trajectories are stable to small radial perturbations (the Rayleigh and Solberg criterion, Rayleigh, 1917; Solberg, 1936; Abramowicz et al., 1984). When such trajectories are investigated in general relativistic approach the $\ell^2(r)$ curve is no longer found to be monotonic since a minimum of the angular momentum occurs. This minimum is associated with the presence of the well–known marginally stable circular orbit, $r = r_{\text{ms}}$. For $r < r_{\text{ms}}$ only unstable circular orbits may exist (e.g., Bardeen et al. (1972)). When dealing with both test particle and fluid motion, $r = r_{\text{ms}}$ is often considered

978-80-7510-257-7

as the innermost stable circular orbit (ISCO) of an accretion disc that orbits a black hole (BH) or a relativistic compact star (CS),

$$r_{\rm ISCO} = r_{\rm ms} \,. \tag{2}$$

Spacetimes around slowly rotating CSs and the associated frame–dragging effects are frequently approximated using the Lense–Thirring, also called linear–Hartle, metric (Lense and Thirring, 1918; Hartle and Sharp, 1967; Hartle, 1967). Kluzniak and Wagoner (1985) discussed a relativistic formula for the Keplerian orbital frequency at $r_{\rm ISCO}$ expressed in the units of Hertz,

$$\nu_{\rm ISCO} \equiv \nu_K(r_{\rm ISCO}) = \frac{c^3 M_\odot}{2\pi G M M_\odot} \, (1 + 0.75\, j) \,. \tag{3}$$

This formula, which is linear in j, can equivalently be written in the familiar form as

$$\nu_{\rm ISCO} = \frac{2200 M_\odot}{M} \, (1 + 0.75\, j) \, [\rm Hz], \tag{4}$$

with the compact object mass being given in the solar mass units. For its simplicity and robustness it is often used within miscellaneous astrophysical applications.

The ISCO is commonly seen as a unique prediction of Einstein general relativity. It has however been pointed out that it also appears around highly elliptic bodies described within purely Newtonian approach (Gondek-Rosińska et al., 2001; Zdunik and Gourgoulhon, 2001; Amsterdamski et al., 2002; Kluźniak and Rosińska, 2013; Kluźniak, 2014). In that context the ISCO frequency behaviour for rotating CSs can be understood in terms of interplay between the effects of general relativity and the effects of Newtonian physics that are associated to the CS oblateness. Such interplay affects outcomes of precise computations of rotating CS models and related ISCO frequencies.

Within the linear approximation (4) the ISCO frequency increases with growing j. This agrees with the behaviour of ISCO known for BHs that are described by Kerr geometry. The effects of Newtonian physics, on the other hand, influence the ISCO frequency in the opposite way. This leads us to an immediate question: How important are the terms which are quadratic in j ?

2 THE HARTLE-THORNE APPROXIMATION

In order to investigate the main trends in the ISCO frequency behaviour we use the Hartle–Thorne (HT) approximation of the CS spacetime in its usual form, which involves the first– and second–order terms in j and the first–order terms in the CS quadrupole moment q. The ISCO radius can be expressed in the units of the compact object gravitational mass as (e.g. Abramowicz et al., 2003)

$$\begin{aligned} r_{\rm ISCO} &= 6\left[1 - j\,\frac{2}{3}\sqrt{\frac{2}{3}} + j^2\left(\frac{251647}{2592} - 240\ln\frac{3}{2}\right) + q\left(-\frac{9325}{96} + 240\ln\frac{3}{2}\right)\right] \\ &\approx 6\left[1 - 0.54\, j - 0.23\, j^2 + 0.18\, q\right] \,. \end{aligned} \tag{5}$$

The ISCO frequency can then be written in the units of Hertz in the form

$$\begin{aligned}\nu_{\rm ISCO} =& \frac{2200 M_\odot}{M}\left[1+\frac{11\,j}{6^{3/2}}+\frac{1}{864}j^2\left(-160583+397710\ln\frac{3}{2}\right)\right.\\ &\left.+\frac{5}{32}q\left(1193-2946\ln\frac{3}{2}\right)\right]\\ \approx& \frac{2200 M_\odot}{M}\left[1+0.75\,j+0.78\,j^2-0.23q\right]. \end{aligned} \tag{6}$$

In Figure 1 we illustrate the dependence of $\nu_{\rm ISCO}$ on j and q. In this Figure we also include the dependency of $\nu_{\rm ISCO}$ on a scaled quadrupole moment $\tilde{q} \equiv q/j^2$. One may now introduce a quadratic correction to the linear relation (4) given by coefficient

$$\delta \simeq 0.78 - 0.23\tilde{q} \tag{7}$$

and rewrite equation (6) as

$$\nu_{\rm ISCO} \approx \frac{2200 M_\odot}{M}\left(1+0.75\,j+\delta\,j^2\right). \tag{8}$$

2.1 The Maximal ISCO frequency

For fixed values of $\tilde{q}$ in relation (8), one can find a maximal frequency,

$$\nu_{\rm ISCO} = \nu_{\rm ISCO}^{\rm max} \Leftrightarrow \frac{\partial \nu_{\rm ISCO}}{\partial j} = 0, \tag{9}$$

which arises for

$$j_{\rm max} = -\left(\frac{11\sqrt{6}}{72}\right)\frac{1}{\delta} \approx -\frac{0.375}{\delta}. \tag{10}$$

We illustrate the existence and behaviour of $\nu_{\rm ISCO}^{\rm max}$ in Figure 1b. The physical nature of this non–monotonicity follows from the qualitative difference between the influence of the effects of general relativity and Newtonian physics (Kluźniak and Rosińska, 2014) reflected by a decrease of $r_{\rm ISCO}$ with increasing j and its increase with increasing q. As discussed by Török et al. (2014), the $r_{\rm ISCO}(j)$ function has a minimum when j and q are related as follows

$$j_{\rm min} \approx \frac{0.27}{-0.23+0.18\,\tilde{q}_{\rm min}}. \tag{11}$$

The minimal allowed ISCO radius is then given by

$$r_{\rm ISCO}^{\rm min} = 6 - 2\,j_{\rm min}\sqrt{2/3}, \tag{12}$$

and the ISCO frequency corresponding to this radius is

$$\nu_{\rm ISCO}^{\rm min} \approx \frac{2200 M_\odot}{M}\left[1+0.41\,j_{min}+0.49\,j_{min}^2\right]. \tag{13}$$

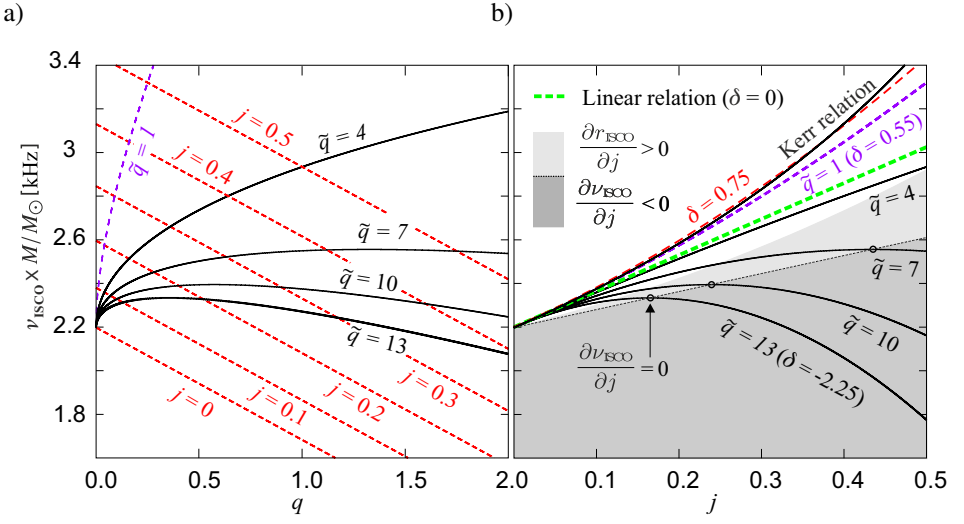

Figure 1. Dependence of the ISCO frequency ν_{ISCO} on the CS angular momentum j and the scaled quadrupole moment, $\tilde{q} = q/j^2$. a) The $\nu_{ISCO}(q)$ curves drawn for constant values of j (the red curves) and $\tilde{q}$ (the black curves) including the Kerr limit, $\tilde{q} = 1$ (the purple line). b) The $\nu_{ISCO}(j)$ curves drawn for constant values of $\tilde{q}$ from panel a), the linear dependency (4), the $\nu_{ISCO}(j)$ function calculated for Kerr spacetime and relation (8) for $\delta = 0.75$. The shaded area indicates the region corresponding to equation (10) where, in a qualitative disagreement with the relativistic relation (4), the value of ν_{ISCO} decreases and value of r_{ISCO} increases with increasing j. The light shadow region indicates the region where both r_{ISCO} and ν_{ISCO} increase with increasing j.

This frequency is however not the highest allowed ISCO frequency for a given $\tilde{q}$. For a fixed orbital radius and q, there is $\partial \nu_K / \partial j > 0$. The maximum of ν_{ISCO} for a given value of $\tilde{q}$ therefore occurs for a somewhat higher value of j given by relation (10),

$$j_{\max} \approx -\frac{0.375}{0.78 - 0.23\tilde{q}_{\min}}. \tag{14}$$

The corresponding ISCO radius is now given by

$$r_{ISCO}^{\max} = 6\left[1 - 0.25 j_{max} + 0.38 j_{max}^2\right], \tag{15}$$

and the maximal ISCO frequency can be expressed as

$$\begin{aligned} \nu_{ISCO}^{\max} &= \frac{2200 M_\odot}{M}\left[1 - \left(\frac{11\sqrt{6}}{72}\right)^2 \frac{1}{\delta}\right] \approx \frac{2200 M_\odot}{M}\left[1 - \frac{0.375^2}{0.78 - 0.23\tilde{q}}\right] \\ &= \frac{2200 M_\odot}{M}\left[1 + 0.375 j_{\max}\right]. \end{aligned} \tag{16}$$

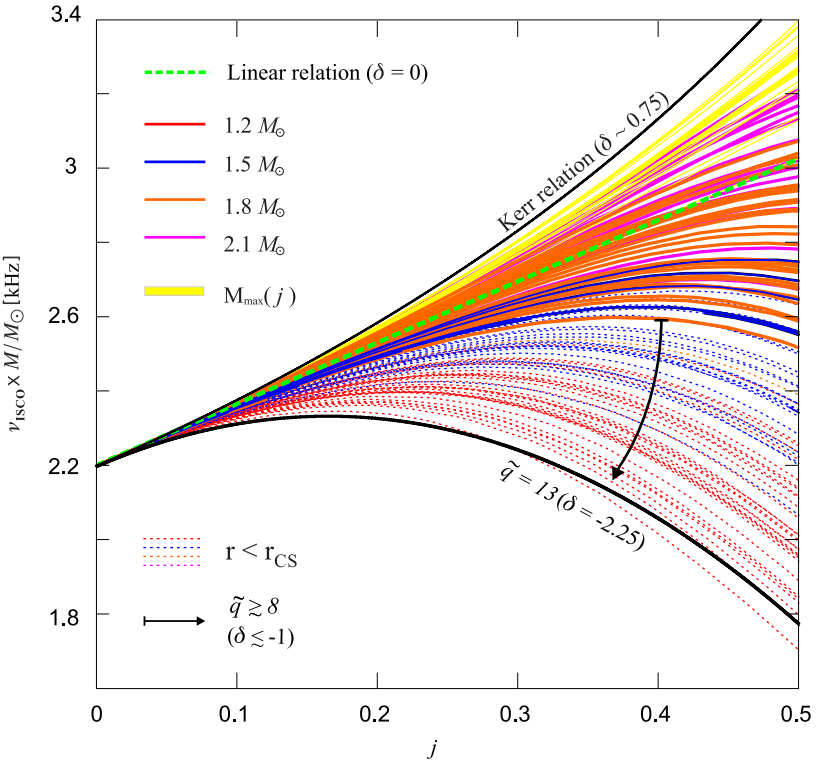

Figure 2. The $\nu_{ISCO}(j)$ dependence calculated assuming the HT approximation for 37 EoS and four different CS masses M that are colour–coded. The set of yellow curves is drawn for the case of maximal mass, $M_{\rm max} = M_{\rm max}(j,\ {\rm EoS}) > 2.1 M_\odot$.

The maximal allowed ISCO frequency is therefore dedined by a linear function of j. We note that this limit exists only for $\tilde{q} \gtrsim 3.4$. In Figure 1b we denote the regions in the j–ν_{ISCO} plane corresponding to $\partial r_{\rm ISCO}/\partial j > 0$ and $\partial \nu_{ISCO}/\partial j < 0$.

3 THE SCENARIO IMPLIED BY MODELS OF A ROTATING CS

The quadrupole moment of a rotating CS occurs due to rotationally induced CS oblateness. In the case of numerical models of rotating CSs associated with a given equation of state (EoS), the effects described in the previous Section therefore manifest themselves through a certain type of ν_{ISCO} behaviour. Figure 2 displays the $\nu_{ISCO}(j)$ behaviour for several values of M and the maximal allowed gravitational masses $M_{\rm max}$ for a large set of EoS, which are listed in table 1. The Figure is based on calculations following the approach of Hartle and Sharp (1967), Hartle (1967), Miller (1977), Urbanec et al. (2013), and Török et al. (2016).

3.1 Compactness vs. oblateness

For $\tilde{q} \doteq 3.4$ we have $\delta = 0$ and the quadratic relation (8) merges with the linear term (4). For $\tilde{q} < 3.4$ the ISCO frequency monotonically increases with growing j (see Figure 1b). The values of $\tilde{q} \in (1, 3)$ correspond to very compact CSs with the highest possible ρ and M that can be achieved by assuming modern EoS (see, e.g., Urbanec et al., 2013). Typical values of M are around $\sim 2M_\odot$ but they strongly depend on the specific form of EoS and j. The behaviour of ν_{ISCO} in this situation is illustrated in the yellow region of Figure 2. In the limit of $\tilde{q} = 1$, the CS (HT) spacetime approaches (up to the second–order in j) the Kerr spacetime. One may therefore write $\delta \doteq 0.55$ and

$$\nu_{\mathrm{ISCO}} = \frac{2200 M_\odot}{M}\left(1 + 0.75\, j + 0.55\, j^2\right). \tag{17}$$

Considering $\delta = 0.75$ one can write

$$\nu_{\mathrm{ISCO}} = \frac{2200 M_\odot}{M}\left[1 + 0.75\left(j + j^2\right)\right]. \tag{18}$$

This simple relation almost exactly matches the ISCO frequency in Kerr spacetimes for j up to ~ 0.5 (see Figure 1b). It has been suggested as a rough upper limit for the ISCO frequencies for CSs (Török et al., 2010).

A qualitatively different situation occurs for $\tilde{q} \gtrsim 3.4$. In such case, when the less compact CSs posses a large influence of the CS oblateness, we have

$$\delta < 0 \tag{19}$$

and ν_{ISCO} is not a monotonic function of j. Inspecting the curves drawn in Figure 2 for different EoS, we in many cases find a non–monotonic ν_{ISCO} behaviour analogic to that shown in panel b) of Figure 1.

4 DISCUSSION AND CONCLUSIONS

Our results regarding the ISCO frequency behaviour obtained for the HT spacetimes demonstrate the importance of the second–order terms in j. The non–monotonicities of r_{ISCO} and ν_{ISCO} determined by relations (11) and (14) can be of clear astrophysical relevance (e.g. Török et al., 2014). It is therefore important that, as demonstrated in Section 3, these non–monotonicities arise for given CS models calculated within the HT approximation.

The outcomes based on the HT approximation should be compared to outputs of exact calculations assuming numerical spacetimes. In Figures 3 and 4 we present several results that were obtained using the LORENE code (Gourgoulhon et al., 2016). These are drawn for a particular ApR EoS. Figure 3 illustrates the behaviour of ν_{ISCO} for two sequences of rotating CSs calculated for a fixed central CS density ρ. Remarkably, the exact results are in good agreement with those obtained within the HT approximation. We note that the non–monotonicity of ν_{ISCO} in this case arises mainly due to the increase of M implied by the CS rotation. Figure 4 includes a similar consideration, but for a fixed M. Although there is no obvious maximum here we can see that $\partial \nu_{\mathrm{ISCO}}/\partial \nu_{\mathrm{s}}$ vanishes when r_{ISCO} approaches r_{CS} (see panel d of Figure 4).

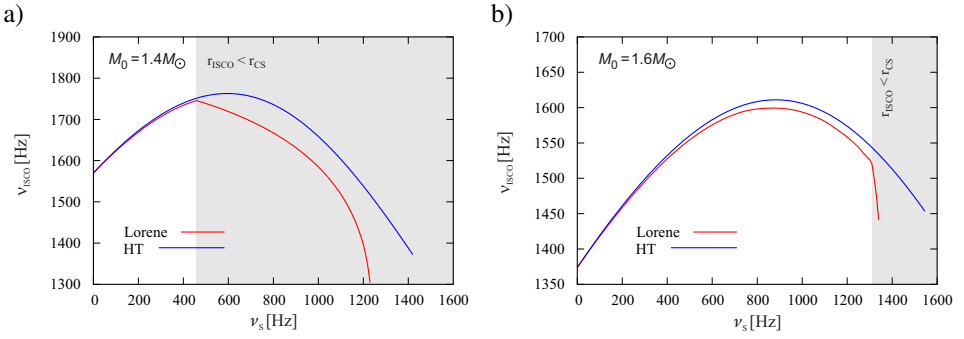

Figure 3. Behaviour of ν_{ISCO} (and the frequency of the CS surface rotation). The exact curves (the red colour) obtained using the LORENE numerical code are compared to those based on the HT approximation (the blue colour). The APR EoS and a fixed central density ρ_c are considered here. a) Plotted for a non–rotating CS mass $M_0 = 1.4M_\odot$. b) For a non–rotating CS mass $M_0 = 1.6M_\odot$. The maximum of ν_{ISCO} occurs close to $\nu_S = 800$Hz.

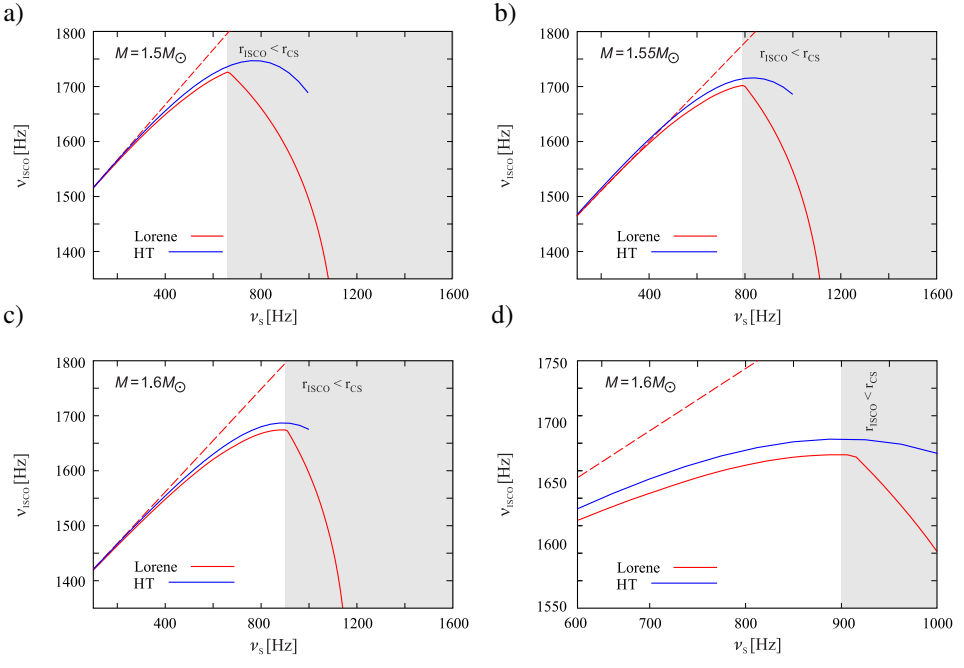

Figure 4. Behaviour of ν_{ISCO} (and the frequency of the CS surface rotation). The exact curves (the red colour) obtained using the LORENE numerical code are compared to those based on the HT approximation (the blue colour). The APR EoS and a fixed gravitational mass M are considered here. a) Plotted for a gravitational mass $M = 1.5M_\odot$. b) For a gravitational mass $M = 1.55M_\odot$. c) For a gravitational mass $M = 1.6M_\odot$. d) An enlarged view of panel c.

Table 1. The EoS assumed in this study. Along with relevant references the individual columns indicate for each EoS the maximal mass and the corresponding radius, and the central baryon number density.

EoS	$M_{\max}^{j=0}$ $[M_\odot]$	R [km]	n_c $[fm]^{-3}$	$\mathcal{R}_{1.4}$	$M_{\max}^{\nu_S=600}$ $[M_\odot]$	Ref.
L	2.66	13.63	0.65	5.18	2.72	Arnett and Bowers (1977)
GLENDNH3	1.96	11.38	1.05	4.90	2.00	Glendenning (1985)
SkI5	2.18	11.29	0.97	4.88	2.21	Rikovska Stone et al. (2003)
SV	2.38	11.95	0.80	4.78	2.42	Rikovska Stone et al. (2003)
N	2.63	12.77	0.72	4.77	2.68	Arnett and Bowers (1977)
SkI2	2.11	11.00	1.03	4.70	2.14	Rikovska Stone et al. (2003)
Gs	2.08	10.77	1.08	4.58	2.11	Arnett and Bowers (1977)
l	1.92	11.33	1.04	4.48	1.96	Urbanec et al. (2010)
SGI	2.22	10.93	1.01	4.46	2.25	Rikovska Stone et al. (2003)
QMC700	1.95	12.57	0.61	4.45	2.02	Rikovska Stone et al. (2007)
O	2.38	11.51	0.89	4.43	2.41	Arnett and Bowers (1977)
nocross	2.39	12.48	0.67	4.42	2.44	Urbanec et al. (2010)
J35L80	2.05	10.50	1.13	4.38	2.08	Newton et al. (2013)
UBS	2.20	12.08	0.67	4.36	2.24	Urbanec et al. (2010)
PNML80	2.02	10.41	1.16	4.35	2.04	Newton et al. (2013)
SkO	1.97	10.27	1.19	4.31	2.00	Rikovska Stone et al. (2003)
SkT5	1.82	9.95	1.31	4.23	1.84	Rikovska Stone et al. (2003)
SkO’	1.95	10.06	1.24	4.19	1.97	Rikovska Stone et al. (2003)
C	1.85	9.92	1.31	4.11	1.87	Arnett and Bowers (1977)
APR	2.21	10.16	1.12	4.10	2.23	Akmal et al. (1998)
Gandolfi	2.20	9.82	1.16	4.06	2.22	Gandolfi et al. (2010)
NRAPR	1.93	9.85	1.29	4.06	1.95	Steiner et al. (2005)
SLy4	2.04	9.95	1.21	4.03	2.06	Rikovska Stone et al. (2003)
KDE0v1	1.96	9.72	1.29	3.98	1.98	Agrawal et al. (2005)
BBB2	1.92	9.49	1.35	3.84	1.94	Baldo et al. (1997)
UU	2.19	9.81	1.16	3.84	2.21	Wiringa et al. (1988)
WS	1.84	9.52	1.38	3.77	1.86	Wiringa et al. (1988)
FPS	1.80	9.27	1.46	3.75	1.82	Lorenz et al. (1993)
AU	2.13	9.38	1.25	3.59	2.14	Wiringa et al. (1988)

Our overall conclusion is that the second–order terms in j are clearly important, but further systematic studies will be necessary before making key statements on the HT approximation applicability.

ACKNOWLEDGEMENTS

We would like to acknowledge the Czech Science Foundation grant No. 17-16287S, the INTER-TRANSFER project No. LTT17003, and the internal grant No. SGS /15/2016. GU acknowledges the Albert Einstein Center for Gravitation and Astrophysics supported by the Czech Science Foundation grant No. 14-37086G. We are grateful to Marek Abramowicz and Omer Blaes for useful discussions. Last but not least, we would like to acknowledge the hospitality of University of California in Santa Barbara, and to express our thanks to concierges of Mlýnská hotel in Uherské Hradiště, Czech Republic for their participation in organizing frequent workshops of Silesian University and Astronomical Institute of the Czech Academy of Sciences.

REFERENCES

Abramowicz, M. A., Almergren, G. J. E., Kluzniak, W. and Thampan, A. V. (2003), The Hartle-Thorne circular geodesics, *ArXiv e-prints: gr-qc/0312070*, arXiv: gr-qc/0312070.

Abramowicz, M. A., Livio, M., Piran, T. and Wiita, P. J. (1984), Local stability of thick accretion disks. I - Basic equations and parallel perturbations in the negligible viscosity case, *ApJ*, **279**, pp. 367–383.

Agrawal, B. K., Shlomo, S. and Au, V. K. (2005), Determination of the parameters of a Skyrme type effective interaction using the simulated annealing approach, *Pys. Rev. C*, **72**(1), 014310, arXiv: nucl-th/0505071.

Akmal, A., Pandharipande, V. R. and Ravenhall, D. G. (1998), Equation of state of nucleon matter and neutron star structure, *Phys. Rev. C*, **58**, pp. 1804–1828, arXiv: nucl-th/9804027.

Amsterdamski, P., Bulik, T., Gondek-Rosińska, D. and Kluźniak, W. (2002), Marginally stable orbits around Maclaurin spheroids and low-mass quark stars, *A&A*, **381**, pp. L21–L24, arXiv: astro-ph/0012547.

Arnett, W. D. and Bowers, R. L. (1977), A Microscopic Interpretation of Neutron Star Structure, *ApJ Supp.*, **33**, p. 415.

Baldo, M., Bombaci, I. and Burgio, G. F. (1997), Microscopic nuclear equation of state with three-body forces and neutron star structure, *A&A*, **328**, pp. 274–282, arXiv: astro-ph/9707277.

Bardeen, J. M., Press, W. H. and Teukolsky, S. A. (1972), Rotating Black Holes: Locally Nonrotating Frames, Energy Extraction, and Scalar Synchrotron Radiation, *ApJ*, **178**, pp. 347–370.

Gandolfi, S., Illarionov, A. Y., Fantoni, S., Miller, J. C., Pederiva, F. and Schmidt, K. E. (2010), Microscopic calculation of the equation of state of nuclear matter and neutron star structure, *MNRAS*, **404**, pp. L35–L39, arXiv: 0909.3487.

Glendenning, N. K. (1985), Neutron stars are giant hypernuclei?, *ApJ*, **293**, pp. 470–493.

Gondek-Rosińska, D., Bulik, T., Kluzniak, W., Zdunik, J. L. and Gourgoulhon, E. (2001), Innermost stable circular orbits around rotating compact quark stars and QPOs, in A. Gimenez, V. Reglero and C. Winkler, editors, *Exploring the Gamma-Ray Universe*, volume 459 of *ESA Special Publication*, pp. 223–225, arXiv: astro-ph/0012540.

Gourgoulhon, E., Grandclément, P., Marck, J.-A., Novak, J. and Taniguchi, K. (2016), LORENE: Spectral methods differential equations solver, Astrophysics Source Code Library, arXiv: 1608.018.

Hartle, J. B. (1967), Slowly Rotating Relativistic Stars. I. Equations of Structure, *ApJ*, **150**, p. 1005.

Hartle, J. B. and Sharp, D. H. (1967), Variational Principle for the Equilibrium of a Relativistic, Rotating Star, *Apj*, **147**, p. 317.

Kluźniak, W. (2014), Exploring GR effects in Newtonian physics, in *XXXVI Polish Astronomical Society Meeting*, pp. 21–26.

Kluźniak, W. and Rosińska, D. (2013), Orbital and epicyclic frequencies of Maclaurin spheroids, *MNRAS*, **434**, pp. 2825–2829.

Kluźniak, W. and Rosińska, D. (2014), Kerr-like behavior of orbits around rotating Newtonian stars, in *Jour. of Phys. Conf. Ser.*, volume 496 of *Journal of Physics Conference Series*, p. 012016.

Kluzniak, W. and Wagoner, R. V. (1985), Evolution of the innermost stable orbits around accreting neutron stars, *ApJ*, **297**, pp. 548–554.

Lense, J. and Thirring, H. (1918), Über den Einfluß der Eigenrotation der Zentralkörper auf die Bewegung der Planeten und Monde nach der Einsteinschen Gravitationstheorie, *PZ*, **19**.

Lorenz, C. P., Ravenhall, D. G. and Pethick, C. J. (1993), Neutron star crusts, *PRL*, **70**, pp. 379–382.

Miller, J. C. (1977), Quasi-stationary gravitational collapse of slowly rotating bodies in general relativity, *MNRAS*, **179**, pp. 483–498.

Newton, W. G., Gearheart, M. and Li, B.-A. (2013), A Survey of the Parameter Space of the Compressible Liquid Drop Model as Applied to the Neutron Star Inner Crust, *Apj Supp.*, **204**, 9, arXiv: 1110.4043.

Rayleigh, L. (1917), On the Dynamics of Revolving Fluids, *Proceedings of the Royal Society of London Series A*, **93**, pp. 148–154.

Rikovska Stone, J., Guichon, P. A. M., Matevosyan, H. H. and Thomas, A. W. (2007), Cold uniform matter and neutron stars in the quark meson-coupling model, *Nuclear Physics A*, **792**, pp. 341–369, arXiv: nucl-th/0611030.

Rikovska Stone, J., Miller, J. C., Koncewicz, R., Stevenson, P. D. and Strayer, M. R. (2003), Nuclear matter and neutron-star properties calculated with the Skyrme interaction, *PRC*, **68**(3), 034324.

Solberg, H. (1936), Le mouvement d'inertie de l'atmosphere stable et son role dans le theorie des cyclones, in *Proces-Verbaux Tss. Meteor U.G.G.I 6 e Assemblee Generale (Edinburgh)*.

Steiner, A. W., Prakash, M., Lattimer, J. M. and Ellis, P. J. (2005), Isospin asymmetry in nuclei and neutron stars [review article], *Phys. Rep.*, **411**, pp. 325–375, arXiv: nucl-th/0410066.

Török, G., Bakala, P., Šrámková, E., Stuchlík, Z. and Urbanec, M. (2010), On Mass Constraints Implied by the Relativistic Precession Model of Twin-peak Quasi-periodic Oscillations in Circinus X-1, *AJ*, **714**, pp. 748–757, arXiv: 1008.0088.

Török, G., Goluchová, K., Urbanec, M., Šrámková, E., Adámek, K., Urbancová, G., Pecháček, T., Bakala, P., Stuchlík, Z., Horák, J. and Juryšek, J. (2016), Constraining Models of Twin-Peak Quasi-periodic Oscillations with Realistic Neutron Star Equations of State, *The Astrophysical Journal*, **833**, 273, arXiv: 1611.06087.

Török, G., Urbanec, M., Adámek, K. and Urbancová, G. (2014), Appearance of innermost stable circular orbits of accretion discs around rotating neutron stars, *A&A*, **564**, L5, arXiv: 1403.3728.

Urbanec, M., Běták, E. and Stuchlík, Z. (2010), Observational Tests of Neutron Star Relativistic Mean Field Equations of State, *Acta Astron.*, **60**, pp. 149–163, arXiv: 1007.3446.

Urbanec, M., Miller, J. C. and Stuchlík, Z. (2013), Quadrupole moments of rotating neutron stars and strange stars, *MNRAS*, **433**, pp. 1903–1909, arXiv: 1301.5925.

Wiringa, R. B., Fiks, V. and Fabrocini, A. (1988), Equation of state for dense nucleon matter, *Phys. Rev. C*, **38**, pp. 1010–1037.

Zdunik, J. L. and Gourgoulhon, E. (2001), Small strange stars and marginally stable orbit in Newtonian theory, *PRD*, **63**(8), 087501, arXiv: astro-ph/0011028.

Proceedings of *RAGtime 17–19, 17–19/23–26 Oct., 1–5 Nov., 2015/2016/2017, Opava, Czech Republic*
Z. Stuchlík, G. Török and V. Karas, editors, Silesian University in Opava, 2017, pp. 33–46

Wave excitation at Lindblad resonances using the method of multiple scales

Jiří Horák

Astronomical Institute, Academy of Sciences, Boční II 141 31 Prague, Czech Republic

ABSTRACT
In this note, the method of multiple scales is adopted to the problem of excitation of non–axisymmetric acoustic waves in vertically integrated disk by tidal gravitational fields. We derive a formula describing a waveform of exited wave that is uniformly valid in a whole disk as long as only a single Lindblad resonance is present. Our formalism is subsequently applied to two classical problems: trapped p–mode oscillations in relativistic accretion disks and the excitation of waves in infinite disks.

Keywords: perturbation methods – disk dynamics

1 INTRODUCTION

A linear wave dynamics and wave excitation in fluid disks due to time–varying non–axisymmetric tidal fields have been extensively studied since publishing the seminal work on this subject by Goldreich and Tremaine (1979). In addition to small–amplitude long–scale non–resonant deformations of the disk, tides (originating in e.g. due to a companion star) may excite short–wavelength non–axisymmetric density waves at Lindblad resonances, where the frequency of a disturbing potential measured in a fluid frame matches the local epicyclic frequency.

Dynamics of a thin disk under the influence of the disturbing tidal field is described by following dimensionless equations

$$\frac{\partial u}{\partial t} + \Omega\frac{\partial u}{\partial \phi} - 2\Omega v + \epsilon_{\mathrm{d}}^2\frac{\partial h}{\partial r} = -\epsilon_\varphi \varphi'(r)\exp\left[\mathrm{i}(m\phi - \omega t)\right], \tag{1}$$

$$\frac{\partial v}{\partial t} + \Omega\frac{\partial v}{\partial \phi} + \frac{\kappa^2}{2\Omega}u + \frac{\epsilon_{\mathrm{d}}^2}{r}\frac{\partial h}{\partial \phi} = -\frac{\mathrm{i}m}{r}\epsilon_\varphi \varphi(r)\exp\left[\mathrm{i}(m\phi - \omega t)\right], \tag{2}$$

$$\frac{\partial h}{\partial t} + \Omega\frac{\partial h}{\partial \phi} + c_{\mathrm{s}}^2\left[\frac{1}{r\Sigma}\frac{\partial(r\Sigma u)}{\partial r} + \frac{1}{r}\frac{\partial v}{\partial \phi}\right] = 0. \tag{3}$$

Here, u and v are perturbations of the radial and tangential velocity, h is a perturbation of the enthalpy related to the wave, $\varphi(r)$ is a component of a disturbing gravitational potential, with azimuthal wavenumber m and the angular frequency ω, Ω and κ is the equilibrium orbital velocity and epicyclic frequency $\Omega = \kappa \propto r^{-3/2}$ for a Keplerian disk) and c_{s} is

the constant sound speed (assuming the isothermal equation of state). All quantities are dimensionless, expressing ratios of corresponding dimensional physical quantities to their typical (characteristic) values. Radial distances are scaled by r_*, a characteristic radius that plays a role of a natural length unit. The angular frequency at this radius defines a scaling of all frequencies and introduces a natural time unit $t_* = 1/\Omega_*$. The velocity perturbations u and v are expressed in units $r_*\Omega_*$. On the other hand, the enthalpy perturbations h are of the order of a local sound speed and it is natural to express them in units of $c_{s*} = c_s(r_*)$. Finally, Σ expresses the density in units of $\Sigma_* = \Sigma(r_*)$ and a disturbing gravitational potential φ is rescaled by its typical value, say φ_*. Because we introduced c_{s*} and φ_* independently to r_* and Ω_*, two dimensionless parameters pops up in equations (1)–(3),

$$\epsilon_d \equiv \frac{c_{s*}}{r_*\Omega_*}, \quad \epsilon_\varphi \equiv \frac{\varphi_*}{r_*^2\Omega_*^2}. \tag{4}$$

The first one is proportional to the disk aspect ratio, $\epsilon_d \ll 1$ for thin disks. The second one expresses a relative importance of gravities of the central and perturbing object. The perturbation approach introduced in this note is appropriate in situations when both ϵ_d and ϵ_φ are much smaller then unity.

As shown by Goldreich and Tremaine (1979), a wave of the form of $\propto \exp[\mathrm{i}(m\phi - \omega t)]$ is excited at radii, where

$$D \equiv \kappa^2 - (\omega - m\Omega)^2 = -[\omega - (m\Omega - \kappa)]\,[\omega - (m\Omega + \kappa)] = 0, \tag{5}$$

from which we find $\omega = m\Omega \pm \kappa$. The upper/lower sign corresponds to the outer/inner Lindblad resonance. We assume that a single Lindblad resonance exists inside the disk and denote the corresponding radius $r = r_L$. Our task is to find a waveform corresponding to the excited wave.

2 SCALING THE VARIABLES, FAST RADIUS

We approach this problem using the method of multiple scales. In addition to the slow radial variable r, we introduce a fast radial coordinate x as

$$x \equiv \chi(r)/\delta, \tag{6}$$

where $\delta \ll 1$ is a free small parameter and $\chi(r)$ is a "normally" varying function of r (i.e. $\chi'(r) = O(1)$). Both δ and $\chi(r)$ will be determined later. We allow the solutions u, v and h to depend on both r and x. We just assume that derivatives of the solutions with respect to r and x does not change the order in δ, that is we assume that $\partial/\partial x$ and $\partial/\partial r$ applied to the solutions remains of the order of unity. Hence, variations with respect to x correspond to fast (oscillatory) changes, while those with respect r describe slow (secular) changes of the solutions (for example in the local wavelength).

The radial derivative $\partial/\partial r$ is substituted by

$$\frac{\partial}{\partial r} \to \frac{\partial}{\partial r} + \frac{\chi'}{\delta}\frac{\partial}{\partial x}. \tag{7}$$

In addition, we assume the dependence $\propto \exp[\mathrm{i}(m\phi - \omega t)]$ of the solution variables u, v and h on time and azimuth and rescale them as

$$u(r,\phi,t) = \epsilon_u \hat{u}(r,x)\mathrm{e}^{\mathrm{i}(m\phi-\omega t)}, \tag{8}$$
$$v(r,\phi,t) = \epsilon_u \hat{v}(r,x)\mathrm{e}^{\mathrm{i}(m\phi-\omega t)}, \tag{9}$$
$$h(r,\phi,t) = \epsilon_h \hat{h}(r,x)\mathrm{e}^{\mathrm{i}(m\phi-\omega t)}. \tag{10}$$

A relation of the additional scaling parameters δ, ϵ_u and ϵ_h to ϵ_φ and ϵ_d will be found using a dominant–balance argument. Introducing the Doppler–shifted frequency $\tilde{\omega}(r) = \omega - m\Omega(r)$, substituting (8)–(10) into (1)–(3) and factorizing out the time and azimuthal dependence, we obtain

$$\epsilon_u\left(-\mathrm{i}\tilde{\omega}\hat{u} - 2\Omega\hat{v}\right) + \frac{\epsilon_u\epsilon_h}{\delta}\chi'\frac{\partial\hat{h}}{\partial x} + \epsilon_\mathrm{d}^2\epsilon_h\frac{\partial\hat{h}}{\partial r} = -\epsilon_\varphi\varphi', \tag{11}$$
$$\epsilon_u\left(\frac{\kappa^2}{2\Omega}\hat{u} - \mathrm{i}\tilde{\omega}\hat{v}\right) + \epsilon_\mathrm{d}^2\epsilon_h\frac{\mathrm{i}m}{r}\hat{h} = -\epsilon_\varphi\frac{\mathrm{i}m}{r}\varphi, \tag{12}$$
$$-\mathrm{i}\epsilon_h\tilde{\omega}\hat{h} + \frac{\epsilon_u}{\delta}c_\mathrm{s}^2\chi'\frac{\partial\hat{u}}{\partial x} + \epsilon_u c_\mathrm{s}^2\left[\frac{1}{r\Sigma}\frac{\partial(r\Sigma\hat{u})}{\partial r} + \frac{\mathrm{i}m}{r}\hat{v}\right] = 0. \tag{13}$$

The first two equations are algebraic in $\hat{u}$ and $\hat{v}$. Eliminating $\hat{u}$ from them, we find

$$\mathrm{i}\epsilon_u D\hat{u} + \frac{\epsilon_\mathrm{d}^2\epsilon_h}{\delta}\tilde{\omega}\chi'\frac{\partial\hat{h}}{\partial x} + \epsilon_\mathrm{d}^2\epsilon_h\left(\tilde{\omega}\frac{\partial\hat{h}}{\partial r} - \frac{2m\Omega}{r}\hat{h}\right) = -\epsilon_\varphi\left(\tilde{\omega}\varphi' - \frac{2m\Omega}{r}\varphi\right). \tag{14}$$

The variable $D \equiv \kappa^2 - \tilde{\omega}^2$ vanishes at $r = r_\mathrm{L}$, a position of Lindblad resonance. We want our solution to be valid also at this radius. Therefore it is reasonable to set

$$D = \chi(r)\mathcal{D}(r) = \delta\mathcal{D}(r)x \tag{15}$$

with

$$\chi(r_\mathrm{L}) = 0. \tag{16}$$

Here $\mathcal{D}(r)$ is a positive function of the slow radius r of the order of unity. Therefore, in the vicinity of r_L, $\chi(r)$ is either increasing or decreasing function depending on the type of the Lindblad resonance. The inner Lindblad resonance corresponds to $\chi'(r_\mathrm{L}) > 0$, while $\chi'(r_\mathrm{L}) < 0$ for the the outer one. In the latter case, x increases with decreasing r as can be seen from equation (6). Hence, we adopt a convention of x being negative in the wave propagation region and positive in the wave evanescent region.

We next proceed with the dominant balance argument. We identify the essential terms in the governing equations and adjust the small parameters ϵ_u, ϵ_h and δ accordingly, so that they appear in the leading order of the expansion. In the case of equation (13), it is clear that the first term must balance the second one, because the third one is always less important than the second. Keeping just one of the first two terms in the leading order would result in trivial solution (either $\hat{h}$ or $\partial\hat{u}/\partial x$ would be zero in the leading order).

Hence, we require $\epsilon_u = O(\epsilon_h/\delta)$. The same argument applies to the equation (14), where we again has to balance the first and the second term in the leading approximation in order to keep a nontrivial dependence of the leading–order solution on the fast variable x. This leads to a requirement $\epsilon_u = O(\epsilon_\mathrm{d}^2\epsilon_h/\delta^2)$. Finally, we want the forcing terms in equation (14) that involves the gravitational–field perturbation to which the disk reacts to appear in the leading order as well, this imply $\epsilon_\mathrm{u} = O(\epsilon_\varphi/\delta)$. To sum up, we introduce the scaling

$$\delta = \epsilon_\mathrm{d}^{2/3}, \quad \epsilon_u = \frac{\epsilon_\varphi}{\delta}, \quad \epsilon_h = \frac{\epsilon_\varphi}{\delta^2}. \tag{17}$$

The magnitude of all terms in equations (14), (12) and (13) is then proportional to ϵ_φ, that can be factorized out. Upon dividing equation (14) by $\mathcal{D}(r)$, we obtain

$$\mathrm{i}x\hat{u} + \frac{\tilde{\omega}\chi'}{\mathcal{D}}\frac{\partial\hat{h}}{\partial x} + \frac{\delta}{\mathcal{D}}\left(\tilde{\omega}\frac{\partial\hat{h}}{\partial r} - \frac{2m\Omega}{r}\hat{h}\right) = \Phi(r) \tag{18}$$

$$\frac{\kappa^2}{2\Omega}\hat{u} - \mathrm{i}\tilde{\omega}\hat{v} + \delta\frac{\mathrm{i}m}{r}\hat{h} = -\delta\frac{\mathrm{i}m}{r}\varphi, \tag{19}$$

$$-\mathrm{i}\tilde{\omega}\hat{h} + c_\mathrm{s}^2\chi'\frac{\partial\hat{u}}{\partial x} + \delta c_\mathrm{s}^2\left[\frac{1}{r\Sigma}\frac{\partial(r\Sigma\hat{u})}{\partial r} + \frac{\mathrm{i}m}{r}\hat{v}\right] = 0, \tag{20}$$

where

$$\Phi(r) \equiv \frac{1}{\mathcal{D}}\left(\tilde{\omega}\varphi' - \frac{2m\Omega}{r}\varphi\right). \tag{21}$$

Finally, for the reasons that will be obvious later, it is necessary to involve the fast scale x also in the slowly varying function $\Phi(r)$ on the right–hand side of equation (18). Whe therefore rewrite it as

$$\Phi(r) = \Phi_0(r) + \chi(r)\Phi_1(r) \equiv \Phi_0(r) + \delta\Phi_1(r)x. \tag{22}$$

The exact form of function $\Phi_0(r)$ will be determined later, once determined the function $\Phi_1(r)$ is given by

$$\Phi_1(r) = \frac{1}{\chi(r)}\left[\Phi(r) - \Phi_0(r)\right]. \tag{23}$$

Equations (18)–(20) are now suitable for the perturbative solution.

3 PERTURBATIVE SOLUTION

We assume the solutions $\hat{u}$, $\hat{v}$ and $\hat{h}$ of the form of power series in terms of δ,

$$\hat{u} = u_0 + \delta u_1 + \ldots, \quad \hat{v} = v_0 + \delta v_1 + \ldots, \quad \hat{h} = h_0 + \delta h_1 + \ldots. \tag{24}$$

Substituting these expansions into equations (18)–(20) and comparing the terms of the same order of δ, we obtain equations leading the approximations of various orders. For our purposes it is sufficient to consider only zeroth order (leading) and first order equations.

3.1 Zeroth order

The zeroth–order equations are

$$\mathrm{i}xu_0 + \frac{\tilde{\omega}\chi'}{\mathcal{D}}\frac{\partial h_0}{\partial x} = \Phi_0, \quad \frac{\kappa^2}{2\Omega}u_0 - \mathrm{i}\tilde{\omega}v_0 = 0, \quad -\mathrm{i}\tilde{\omega}h_0 + c_\mathrm{s}^2\chi'\frac{\partial u_0}{\partial x} = 0. \tag{25}$$

Hence,

$$\frac{(c_\mathrm{s}\chi')^2}{\mathcal{D}}\frac{\partial^2 u_0}{\partial x^2} - xu_0 = \mathrm{i}\Phi_0. \tag{26}$$

We still have a freedom to chose $\chi(r)$. A natural choice is to put

$$\frac{(c_\mathrm{s}\chi')^2}{\mathcal{D}} = \frac{\chi\,(c_\mathrm{s}\chi')^2}{D} = 1, \tag{27}$$

what together with the condition (16) leads to

$$\chi(r) = \left[\frac{3}{2}\int_{r_0}^{r} q(r')\mathrm{d}r'\right]^{2/3}, \quad q(r) = \frac{\sqrt{D}}{c_\mathrm{s}}. \tag{28}$$

This brings the equation (26) to the form

$$\frac{\partial^2 u_0}{\partial x^2} - xu_0 = \mathrm{i}\Phi_0, \tag{29}$$

which is just the inhomogeneous Airy equation. Its general solution reads

$$u_0(r,x) = A(r)\mathrm{Ai}(x) + B(r)\mathrm{Bi}(x) - \mathrm{i}\pi\Phi_0(r)\mathrm{Gi}(x), \tag{30}$$

where $\mathrm{Ai}(x)$, $\mathrm{Bi}(x)$ and $\mathrm{Gi}(x)$ are Airy functions and $A(r)$ and $B(r)$ are integration constants whose dependence on the slow variable will be determined in the next order of approximation. The other variables follow easily,

$$v_0 = \frac{\mathrm{i}\kappa^2}{2\Omega\tilde{\omega}}u_0, \quad h_0 = -\frac{\mathrm{i}c_\mathrm{s}^2\chi'}{\tilde{\omega}}\frac{\partial u_0}{\partial x}. \tag{31}$$

3.2 First order

In the first order, we have to solve following equations

$$\mathrm{i}xu_1 + \frac{\tilde{\omega}\chi'}{\mathcal{D}}\frac{\partial h_1}{\partial x} = \frac{\tilde{\omega}}{\mathcal{D}}\frac{\partial h_0}{\partial r} + \frac{2m\Omega}{r}h_0 + x\Phi_1(r), \tag{32}$$

$$\frac{\kappa^2}{2\Omega}u_1 - \mathrm{i}\tilde{\omega}v_1 = -\frac{\mathrm{i}m}{r}\varphi, \tag{33}$$

$$-\mathrm{i}\tilde{\omega}h_1 + c_\mathrm{s}^2\chi'\frac{\partial u_1}{\partial x} = -c_\mathrm{s}^2\left[\frac{1}{r\Sigma}\frac{\partial(r\Sigma u_0)}{\partial r} + \frac{\mathrm{i}m}{r}v_0\right]. \tag{34}$$

After some algebra and using the equation (28), one finds

$$\frac{\partial^2 u_1}{\partial x^2} - x u_1 = -\frac{1}{\chi'}\left(\frac{\mathrm{d}}{\mathrm{d}r}\ln\frac{r\Sigma\chi'}{\tilde{\omega}^2}\right)\frac{\partial u_0}{\partial x} - \frac{2}{\chi'}\frac{\partial^2 u_0}{\partial r \partial x} + \mathrm{i}x\Phi_1(r). \tag{35}$$

When the zeroth–order solutions are substituted into this equation, one finally obtains

$$\frac{\partial^2 u_1}{\partial x^2} - x u_1 = -\frac{2}{\chi'\psi}\left[\frac{\mathrm{d}(\psi A)}{\mathrm{d}r}\mathrm{Ai}'(x) + \frac{\mathrm{d}(\psi B)}{\mathrm{d}r}\mathrm{Bi}'(x) - \mathrm{i}\pi\frac{\mathrm{d}(\psi\Phi_0)}{\mathrm{d}r}\mathrm{Gi}'(x)\right] + \mathrm{i}x\Phi_1(r) \tag{36}$$

with

$$\psi(r) \equiv \frac{\sqrt{r\Sigma\chi'}}{\tilde{\omega}} = \frac{\sqrt{r\Sigma q}}{\tilde{\omega}}\chi^{-1/4}. \tag{37}$$

We are interested in a particular solution of this equation as the solutions of the homogeneous equation can be absorbed into zeroth order approximation u_0. Due to linearity, a particular solution will be sum of particular solutions to all individual terms on the right–hand side. The first three terms consist of slowly varying functions of r multiplied by derivatives of Airy functions. The corresponding particular solutions will be thus given by the Airy functions multiplied by $x/2$. This will cause non–uniformity in our expansion at $x = O(1/\delta)$, when the first order approximation u_1 becomes equally important as the zeroth order one u_0. Our strategy is therefore to introduce suitably varying functions $A(r)$, $B(r)$ and $\Phi_0(r)$ in order to kill these terms and avoid the non–uniformity of the final expansion. This leads us to require $A(r)$, $B(r)$ and $\Phi_0(r)$ to vary as $\propto \psi(r)^{-1}$,

$$A(r) = \frac{a}{\psi(r)}, \quad B(r) = \frac{b}{\psi(r)}, \quad \Phi_0(r) = \frac{\psi_\mathrm{L}\Phi_\mathrm{L}}{\psi(r)}, \tag{38}$$

where a and b are constants that must be determined from boundary conditions and the index 'L' denotes evaluation of the corresponding quantity at r_L. Note that

$$\psi_\mathrm{L}\Phi_\mathrm{L} = \left(\frac{\sqrt{r\Sigma}}{\kappa}\right)_\mathrm{L}\left(\tilde{\omega}\varphi' - \frac{2m\Omega}{r}\varphi\right)_\mathrm{L}. \tag{39}$$

Equation (38) describes slow (secular) evolution of the amplitudes of individual Airy functions with changing radius. At this point, it is also obvious why we imposed the decomposition (22) on the potential function $\Phi(r)$. Keeping it in its original form in the zeroth–order equations would lead to appearance of the unavoidable secular term $\propto x\Phi(r)\mathrm{Gi}(x)$ in the first–order approximation and would result in the non–uniform expansion.

The particular solution of equation (36) after elimination of the secular terms using (38) reads

$$u_1(r,x) = -\mathrm{i}\Phi_1(r) = -\frac{\mathrm{i}}{\chi(r)}\left[\Phi(r) - \frac{\psi_\mathrm{L}\Phi_\mathrm{L}}{\psi(r)}\right]. \tag{40}$$

3.3 Uniform approximation

Putting equations (30), (38), (28) and (40) together, we find the final solution valid up to the first order in the perturbation parameter δ,

$$\begin{aligned}\hat{u}(r,x) =& \frac{\tilde{\omega}}{\sqrt{r\Sigma q}}\chi^{1/4}\left[a\mathrm{Ai}(x) + b\mathrm{Bi}(x) - \mathrm{i}\pi\psi_{\mathrm{L}}\Phi_{\mathrm{L}}\mathrm{Gi}(x)\right] \\ & - \frac{\mathrm{i}\delta}{\chi(r)}\left[\Phi(r) - \frac{\psi_{\mathrm{L}}\Phi_{\mathrm{L}}}{\psi(r)}\right].\end{aligned} \tag{41}$$

The expression (41) represents an uniform approximation of the waveform of perturbation that is valid in the whole disk as far as a single Lindblad resonance is present. The case of several Lindblad resonances will be treated in the section 4.3. The constants a and b can be chosen freely according to the boundary conditions imposed on the perturbation at disk boundaries. In the following sections 4.1 and 4.2 we give two specific examples.

4 APPLICATIONS

4.1 Frequencies of trapped p–modes in relativistic disks

In thin relativistic disks, the acoustic waves can be trapped between the inner edge of the disk and the inner Lindblad resonance establishing the standing wave patterns, so called p–modes. The frequencies of these modes take discrete values ω_n that are given by physical conditions of the flow at the disk inner edge located at the marginally stable orbit r_{ms} (Kato and Fukue, 1980; Nowak and Wagoner, 1991; Wagoner, 1999). Thus measuring their values may serve as another important probe into physical properties of the accreted matter in the very vicinity of relativistic objects. The frequencies of the lowest order p–modes (i.e. those with low number of nodes in the radial direction) are always close to $m\Omega(r_{\mathrm{ms}})$ and their propagation regions are rather narrow. On the other hand they occupy portions of a disk from which most of the radiation emerges and thus they may still be observed. Moreover, if the underlying compact object is a neutron star, these modes may likely strongly modulate accretion rate of a falling matter and therefore contribute significantly to the variability of the emission from its surface (Paczynski, 1987; Horák, 2005; Abramowicz et al., 2007).

Here we derive an approximate formula for the discrete frequency spectra of both, axisymmetric and nonaxisymmetric p–modes. For simplicity, we assume that the disk is terminated at r_{ms} and fix the inner boundary condition to be $u(r_{\mathrm{ms}}) = 0$. As we consider free oscillations, we put $\Phi(r) = 0$ and $\Phi_{\mathrm{L}} = 0$ in equation (41). Because the solution has to be bounded, we also cut off its divergent part proportional to $\mathrm{Bi}(x)$ by putting $b = 0$. The waveform (eigenfunction) of the p–mode is thus roughly described by

$$\hat{u}(r,x) = \frac{a\tilde{\omega}}{\sqrt{r\Sigma q}}\chi^{1/4}\mathrm{Ai}(x), \tag{42}$$

where a is now an arbitrary normalization constant and x is given by equations (6) and (28).

The inner Lindblad resonance corresponds to $x = 0$, while $x = x_{\mathrm{ms}}$ corresponds to the disk inner boundary. The value of x_{ms} depends on the frequency ω of the oscillations, hence

$x_{\rm ms} = x_{\rm ms}(\omega)$. Because we demand vanishing velocity perturbation at the inner edge, the discrete modes have to correspond to the points x_n, where the Airy function vanishes. Thus

$$x_{\rm ms}(\omega_n) = x_n, \quad {\rm Ai}(x_n) = 0. \tag{43}$$

From the theory of Airy functions, it follows that

$$x_n \approx -\left[\frac{3\pi}{8}\,(4n+3)\right]^{2/3}, \quad n = 0, 1, 2, \ldots. \tag{44}$$

Therefore, our task is to evaluate the function $x_{\rm ms}(\omega)$. As we expect ω close to $m\Omega_{\rm ms}$, we put

$$\omega = m\Omega_{\rm ms} + \delta^{\alpha}\omega_1, \tag{45}$$

where $\alpha > 0$ will be specified later on. Close to $r_{\rm ms}$ the orbital and epicyclic frequencies can be approximated as

$$\Omega(r) \approx \Omega_{\rm ms} + \Omega_1\,(r - r_{\rm ms}), \quad \kappa^2(r) \approx \kappa_1^2\,(r - r_{\rm ms}), \tag{46}$$

where

$$\Omega_1 \equiv \left(\frac{{\rm d}\Omega}{{\rm d}r}\right)_{\rm ms}, \quad \kappa_1^2 \equiv \left(\frac{{\rm d}\kappa^2}{{\rm d}r}\right)_{\rm ms}. \tag{47}$$

Introducing a scaled variable ρ using $r = r_{\rm ms} + \delta^{\beta}\rho$, we obtain

$$D = \kappa^2 - \tilde{\omega}^2 = \delta^{\beta}\kappa_1^2\rho - \delta^{2\alpha}\omega_1^2 - 2\delta^{\alpha+\beta}m\Omega_1\omega_1\rho - \delta^{2\beta}m\Omega_1^2\rho^2. \tag{48}$$

The last two terms are obviously sub–dominant with respect to the first one and will be neglected further on. At the Lindblad resonance $D = 0$. This can be achieved only by balancing the first two terms giving $\beta = 2\alpha$. In terms of ρ the position of the resonance corresponds to

$$\rho_{\rm L} = \frac{\omega_1^2}{\kappa_1^2}. \tag{49}$$

The integral in equation (28) may be therefore evaluated as

$$\int_{r_0}^{r_{\rm ms}} \frac{\sqrt{D}}{c_{\rm s}}{\rm d}r' = -\frac{\delta^{3\beta/2}}{c_{\rm s}}\int_0^{\rho_{\rm L}} \sqrt{\kappa_1^2\rho' - \omega_1^2}\,{\rm d}\rho' = -\delta^{3\beta/2}\frac{2{\rm i}\omega_1^3}{3c_{\rm s}\kappa_1^2}. \tag{50}$$

Therefore,

$$x_{\rm ms}(\omega) = -\frac{\omega_1^2}{\left(c_{\rm s}\kappa_1^2\right)^{2/3}}, \tag{51}$$

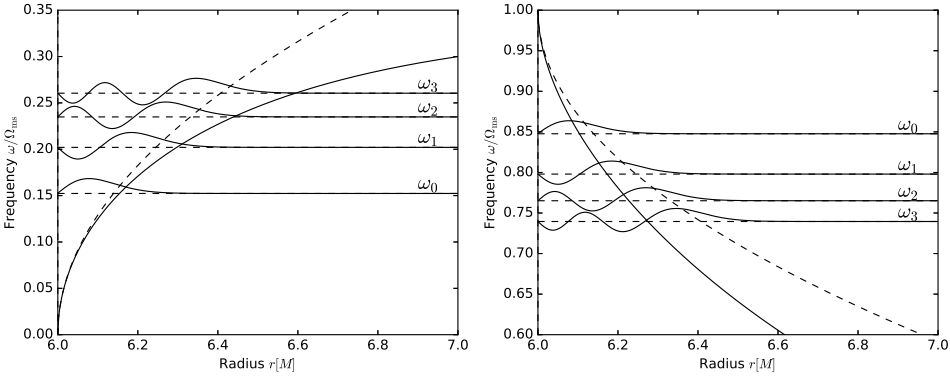

Figure 1. The spectrum of the lowest–order trapped axisymmetric p–modes in a relativistic thin disk surrounding the Schwarzschild black hole according to formula (52). The left and right panel shows the case of the axisymmetric and non–axisymmetric ($m = 1$) modes, respectively. The oscillations are trapped between the disk inner edge at $r = r_{\rm ms} = 6M$ and the inner Lindblad resonance located at positions, where the Doppler–shifted oscillation frequency $|\tilde{\omega}|$ matches the local epicyclic frequency $\kappa(r)$ (shown by solid lines). The approximate positions of the inner Lindblad resonance used in the calculations are shown by the dashed lines. The frequencies of the four discrete modes are calculated for the sound speed $c_{\rm s} = 10^{-3}(r\Omega)_{\rm ms}$.

where we have set $\beta = 1$, in order to obtain $x_{\rm ms}$ of the order of unity. Finally, from the conditions (43) and (44) and using (45) we get,

$$\omega = m\Omega_{\rm ms} \pm \epsilon_{\rm d}^{1/3}\left[\frac{3\pi}{8}(4n+3)\left(c_{\rm s}\kappa_1^2\right)\right]^{1/3}. \tag{52}$$

The eigenfrequencies and eigenfunctions calculated using (52) and (42) for the lowest–order axisymmetric modes ($n \leq 4$) are shown in Fig. 1. For the epicylic frequency, we have used $\kappa(r) = (1 - r_{\rm ms}/r)^{1/2}\Omega(r)$ with $r_{\rm ms} = 6M$ suitable for the Schwarzschild black hole. The dashed line shows positions of the inner Lindblad resonance based on our approximation of $\kappa(r)$ using the square–root function (see eq. (46)). The formula describes the eigenfrequencies well the lowest–order modes with small propagation regions, as the trapping cavity opens up, our simple approximation of the epicyclic frequency ceases to describe its real profile and the formula (52) fails. However, a higher precision could be achieved by considering additional terms in the expansions of $\kappa(r)$ and $\Omega(r)$.

4.2 Excitation of waves in infinite disks

Another application concerns excitation of waves in the infinite disk by a time and azimuthally dependent tidal field (for example due to orbital motion of a secondary star). The solution is described by equation (41) with $\varphi(r)$ corresponding to a Fourier component of the tidal potential that changes as $\exp(m\phi - \omega t)$. In the case of a secondary orbiting on the strictly circular orbit $\omega = m\Omega_*$ with Ω_* being the orbital period. The constants a and b in

the equation (41) has to be fixed by boundary condition. For this, it is useful to explore asymptotic behavior of the solution far from the resonance. Suppose for the moment that wave is excited at the inner Lindblad resonance. The waves may propagate only at smaller radii where D is negative. Far from the resonance, at $r \ll r_{\rm L}$, the solution behaves as

$$\begin{aligned}\hat{u}(r,x) \sim \delta^{1/4}\frac{\tilde{\omega}}{\sqrt{4\pi r\Sigma k}}&\left\{[a-\pi\psi_{\rm L}\Phi_{\rm L}-{\rm i}b]\exp\left[-\frac{\rm i}{\epsilon_{\rm d}}\left(\int_r^{r_{\rm L}}k\,{\rm d}r'+\frac{\pi}{4}\right)\right]\right.\\&\left.+\,[a+\pi\psi_{\rm L}\Phi_{\rm L}+{\rm i}b]\exp\left[\frac{\rm i}{\epsilon_{\rm d}}\left(\int_r^{r_{\rm L}}k\,{\rm d}r'-\frac{\pi}{4}\right)\right]\right\}\\&+\frac{\delta}{D}\left(\tilde{\omega}\varphi'-\frac{2m\Omega}{r}\varphi\right),\end{aligned}\tag{53}$$

where $k = -{\rm i}q = \sqrt{-D}/c_{\rm s}$. The solution has three components. The first two terms in the brace bracket describe ingoing and outgoing waves with respect to the Lindblad resonance. The energy tcarried by the waves is transported with group velocity $c_{\rm g} = {\rm d}\omega/{\rm d}k = (k/\tilde{\omega})c_{\rm s}^2$. The sign of $c_{\rm g}$ determines whether the wave is ingoing or outgoing with respect to the resonance. In our case of the inner Lindblad resonance and $\omega > 0$, the first term corresponds to the ougoing wave and the second one to the ingoing wave (compare to Zhang and Lai, 2006). The last third term represents a non–resonant non–wave response of the disk ('deformation') due to the tidal field. On the other side of the resonance, we have for $r \gg r_{\rm L}$,

$$\begin{aligned}\hat{u}(r,x) \sim \delta^{1/4}\frac{\tilde{\omega}}{\sqrt{\pi r\Sigma q}}&\left[\frac{a}{2}\exp\left(-\frac{1}{\epsilon_{\rm d}}\int_{r_{\rm L}}^{r}q\,{\rm d}r'\right)+b\exp\left(\frac{1}{\epsilon_{\rm d}}\int_{r_{\rm L}}^{r}q\,{\rm d}r'\right)\right]\\&+\frac{\delta}{D}\left(\tilde{\omega}\varphi'-\frac{2m\Omega}{r}\varphi\right),\end{aligned}\tag{54}$$

The solution comprises of two exponentials and the non–wave response that has the same form as in the other region.

A natural step is to put $b = 0$, what kills the divergent part of the solution (54) in the wave–evanescent region. Other constraint that fixes the constant a is imposed in wave–propagation region on (53). A traditional approach is to assume that the excited wave can propagate freely toward smaller radii, where it is either absorbed or damped by other physical processes like viscosity or turbulence. Then one requires the ingoing–wave part of the solution (53) to vanish what gives $a = \pi\psi_{\rm L}\Phi_{\rm L}$. The uniform approximation of the wave part of the solution then becomes

$$\hat{u}_{\rm wave}(r,x) = \frac{\pi\tilde{\omega}}{\sqrt{r\Sigma q}}\psi_{\rm L}\Phi_{\rm L}\chi^{1/4}\left[{\rm Ai}(x)-{\rm i}{\rm Gi}(x)\right].\tag{55}$$

In a more general case when the waves can be partially reflected back towards the resonance, let us introduce the complex reflectivity as a ratio of the ingoing and outgoing (i.e. outgoing and ingoing with respect to a reflector) wave amplitudes,

$$R \equiv \frac{a-\pi\psi_{\rm L}\Phi_{\rm L}}{a+\pi\psi_{\rm L}\Phi_{\rm L}}.\tag{56}$$

Then

$$a = \frac{1+R}{1-R}\pi\psi_{\rm L}\Phi_{\rm L} \tag{57}$$

and

$$\hat{u}_{\rm wave}(r,x) = \frac{\pi\tilde{\omega}}{\sqrt{r\Sigma q}}\psi_{\rm L}\Phi_{\rm L}\chi^{1/4}\left[\frac{1+R}{1-R}{\rm Ai}(x) - {\rm iGi}(x)\right]. \tag{58}$$

We observe that in absence of the forcing ($\Phi_{\rm L} = 0$), the solution (58) is trivial, $\hat{u}_{\rm wave}(r,x) = 0$, unless $R = 1$. The case $R = 1$ corresponds to the situation when there exists a free oscillation mode whose eigenfrequency equals the frequency of the forcing and has to be treated in a different way.

4.3 Asymptotic matching

Finally, few words on the possibility of using our approach in the cases when there are more than one Lindblad resonance in the disk. This is typically the case of relativistic disks, where the axisymmetric p–mode oscillations with frequencies close to the maximum of the epicylic frequency can penetrate the potential barrier and carry some energy out from the trapping region. Clearly, the solution (41) cannot be applied to these situations, because the variable x does not know about the presence of the other resonances. Several attempts of the author to use non–monotonic functions instead of the always increasing or decreasing function $\chi(r)$ have not provided a reasonably simple way of calculations yet. Hence, so far the only way how to treat these situations is asymptotic matching of individual expressions (41) far from the resonances.

In order to demonstrate this procedure, let us consider a particular case of two Lindblad resonaces (inner and outer) located at radii r_1 and r_2 ($r_1 < r_2$). The wave–evanescent region corresponds to the interval (r_1, r_2), the regions corresponding to $r < r_1$ and $r > r_2$ allows waves to propagate freely. The solution (41) describing a single Lindblad resonance can be applied on both the inner and outer resonance. Denote $\hat{u}_1$ the solution corresponding to the inner resonance and $\hat{u}_2$ the solution corresponding to the outer one. The inner solution $\hat{u}_1$ is valid for $r < r_2$; close to r_2, $\hat{u}_1$ breaks down because of presence of the outer resonance. Similarly the solution $\hat{u}_2$ is valid for $r > r_1$. The evanescent region is the overlap, where both solutions are valid. Let us consider a radius r from the evanescent region, not too close to its boundaries. At this radius, the wave part of the solution $\hat{u}_1$ behaves as

$$\hat{u}_{1,\rm wave}(r,x) \sim \frac{\delta^{1/4}\tilde{\omega}}{\sqrt{\pi r\Sigma q}}\left[\frac{a_1}{2}\exp\left(-\frac{1}{\epsilon_{\rm d}}\int_{r_1}^{r} q\,{\rm d}r'\right) + b_1\exp\left(\frac{1}{\epsilon_{\rm d}}\int_{r_1}^{r} q\,{\rm d}r'\right)\right] \tag{59}$$

and similarly

$$\hat{u}_{2,\rm wave}(r,x) \sim \frac{\delta^{1/4}\tilde{\omega}}{\sqrt{\pi r\Sigma q}}\left[\frac{a_2}{2}\exp\left(-\frac{1}{\epsilon_{\rm d}}\int_{r}^{r_2} q\,{\rm d}r'\right) + b_2\exp\left(\frac{1}{\epsilon_{\rm d}}\int_{r}^{r_2} q\,{\rm d}r'\right)\right]. \tag{60}$$

By putting $\hat{u}_{1,\rm wave} = \hat{u}_{2,\rm wave}$, we obtain a relation between the constants a_1, b_1 and a_2, b_2,

$$a_2 = 2\Psi_{12}b_1, \quad b_2 = \frac{1}{2}\Psi_{12}^{-1}a_1, \quad \Psi_{12} \equiv \exp\left(\frac{1}{\epsilon_{\rm d}}\int_{r_1}^{r_2} q\,{\rm d}r'\right). \tag{61}$$

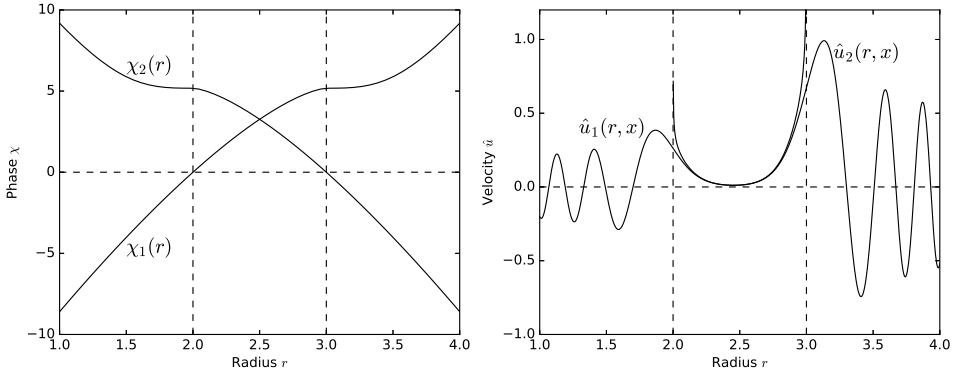

Figure 2. Example of matching the single–resonance solutions (41) in the case when two Lindblad resonances are present. The inner and outer Linblad resonance are located at $r_1 = 2$ and $r_2 = 3$, respectivelly (the radii are in arbitrary units r_*). For simplicity, we have assumed that $D = -(r - r_1)(r - r_2)$, $r\Sigma = \text{const}$ and c_s to be 5% of the orbital velocity at r_1. Left panel shows the individual phase functions $\chi_1(r)$ and $\chi_2(r)$ calculated according to equation (28). The right panel shows the solutions $\hat{u}_1(r,x)$ and $\hat{u}_2(r,x)$ for $a_1 = 2$, $b_1 = 0.001$ and a_2 and b_2 calculated using equation (61). Well inside the evanscent region between the resonances, these two solutions coincide and one may switch from the one to another.

The relation between the functions $\chi_1(r)$ and $\chi_2(r)$ is

$$\chi_2 = \left(\frac{3}{2}\ln\Psi_{12} - \chi_1^{3/2}\right)^{2/3}. \tag{62}$$

An example of the matching procedure is shown in Fig. 2. In practice, one builds up the solution $\hat{u}_1(r,x)$ and $\hat{u}_2(r,x)$ independently using (41) and (28). Then constants a and b are fixed so that they satisfy relations (61). And finally the solutions $\hat{u}_1(r,x)$ and $\hat{u}_2(r,x)$ are connected at an arbitrary radius r_m, well inside the evanescent region. The response of the disk is thus given by a piecewise function,

$$\hat{u}(r,x;a,b) = \begin{cases} \hat{u}_1(r,x;a,b), & r < r_m, \\ \hat{u}_2\left(r,x;2\Psi_{12}b,\tfrac{1}{2}\Psi_{12}^{-1}a\right), & r \geq r_m. \end{cases} \tag{63}$$

The relation (62) is satisfied authomatically.

5 CONCLUSION

In this note, we have introduced an alternative approach to calculations of wave excitation in thin disks. Our approach is based on the method of multiple scales and should be understood as an alternative to traditional and rather tedious calculations based on the method of matched asymptotic expansions. The main advantage of this method is in obtaining *global* solutions, what is especially useful in cases when one is interested in global

properties of the excited waves rather than in the process of excitation itself. The main applications of this method therefore include properties of trapped or partially trapped oscillations (modes). Another interesting feature of our global solution is that it clearly separates short–scale changes characteristic for waves behavior and the long–scale changes of wave overall properties such as their amplitudes and phases, as each of them occurs on a different variable. Finally, it has also immediately revealed a non–resonant response of the disk.

We have also presented two particular examples of using the method. In section 4.1, we have studied a discrete spectra of p–mode oscillations trapped close to inner edge in relativistic disks and derived an approximative general formula for their frequencies. Although this formula describes well only fundamental modes and first few overtones due to rather crude approximations we have made, extending its applicability by including higher order therms in description of profiles of orbital and epicyclic frequency is rather straightforward.

In section 4.2, we have revisited a textbook example of a disk response to the time and azimuthally dependent tidal field. Also in this case our method may be useful, especially in the cases when the excited waves maybe trapped or it may interact with other perturbations of the disk. Among possible applications are tidally driven eccentric instabilities during superhump events in dwarf novae (Lubow, 1991) or non–linear excitation of trapped g–modes in warped disks (Kato, 2004; Ferreira and Ogilvie, 2008). In the latter case however, it is necessary to extend our calculations to g–mode oscillations. We plan to revisit these problems in near future.

ACKNOWLEDGEMENTS

This work was supported by the GAČR grant no. 17–16287S.

REFERENCES

Abramowicz, M. A., Horak, J. and Kluzniak, W. (2007), Modulation of the Neutron Star Boundary Layer Luminosity by Disk Oscillations, *Acta Astronomica*, **57**, pp. 1–10.

Ferreira, B. T. and Ogilvie, G. I. (2008), On an excitation mechanism for trapped inertial waves in discs around black holes, *Mounthly Notices Roy.Astronom.Soc.*, **386**, pp. 2297–2310, arXiv: 0803.1671.

Goldreich, P. and Tremaine, S. (1979), The excitation of density waves at the Lindblad and corotation resonances by an external potential, *Astrophys.J.*, **233**, pp. 857–871.

Horák, J. (2005), A possible mechanism for QPOs modulation in neutron star sources, *Astronomische Nachrichten*, **326**, pp. 845–848, arXiv: astro-ph/0511569.

Kato, S. (2004), Resonant Excitation of Disk Oscillations by Warps: A Model of kHz QPOs, *PASJ*, **56**, pp. 905–922, arXiv: astro-ph/0409051.

Kato, S. and Fukue, J. (1980), Trapped Radial Oscillations of Gaseous Disks around a Black Hole, *PASJ*, **32**, p. 377.

Lubow, S. H. (1991), A model for tidally driven eccentric instabilities in fluid disks, *Astrophys.J.*, **381**, pp. 259–267.

Nowak, M. A. and Wagoner, R. V. (1991), Diskoseismology: Probing accretion disks. I - Trapped adiabatic oscillations, *Astrophys.J.*, **378**, pp. 656–664.

Paczynski, B. (1987), Possible relation between the X-ray QPO phenomenon and general relativity, *Nature*, **327**, p. 303.

Wagoner, R. V. (1999), Relativistic diskoseismology., *Physics Reports*, **311**, pp. 259–269, arXiv: astro-ph/9805028.

Zhang, H. and Lai, D. (2006), Wave excitation in three-dimensional discs by external potential, *Mounthly Notices Roy.Astronom.Soc.*, **368**, pp. 917–934, arXiv: astro-ph/0510069.

Proceedings of *RAGtime 17–19, 17–19/23–26 Oct., 1–5 Nov., 2015/2016/2017, Opava, Czech Republic*
Z. Stuchlík, G. Török and V. Karas, editors, Silesian University in Opava, 2017, pp. 47–59

Epicyclic oscillations of thick relativistic disks

Jiří Horák [1], Odelle Straub [2], Eva Šrámková [3], Kateřina Goluchová [3] and Gabriel Török [3]

[1]Astronomical Institute, Academy of Sciences,
Boční II 141 31 Prague, Czech Republic
[2]LUTH, Observatoire de Paris, CNRS UMR 8102,
Universite Paris-Diderot, 5 place Jules Janssen, F-92195 Meudon, France
[3]Institute of Physics, Silesian University in Opava,
Bezručovo nám. 13, CZ-746 01 Opava, Czech Republic

ABSTRACT
We study epicyclic oscillations of thick relativistic tori with constant specific angular momentum distribution using the finite element numerical method. We have compared frequencies of the axisymmetric and non-axisymmetric modes with the analytic formulae obtained by Straub and Šrámková (2009) and Fragile et al. (2016). We have found excellent agreement in the case of axisymmetric radial epicyclic modes. In the case of the axisymmetric vertical epicyclic modes and non-axisymmetric modes in general, the analytic approximation agrees with numerical results only for tori of moderate thicknesses. Our analysis also revealed an instability of the thick constant angular momentum tori with respect to the radial epicyclic oscillations.

Keywords: black hole physics – accretion disks – oscillations – FEM method

1 INTRODUCTION

A short-period variability of accreting neutron stars and black holes has motivated many studies of oscillation properties of relativistic flows. Because a detailed geometry of accretion is not yet well understood, the most works concentrate either on oscillations of Keplerian razor-thin disk-like flows or on geometrically thick toroidal flows of toroidal shape, whose angular momentum profiles differ significantly from the Keplerian distribution. Although simple models of thick tori are known to be dynamically unstable to global non-axisymmetric perturbation (Papaloizou and Pringle, 1984) and perhaps also locally unstable, due to the magneto-rotational instability (Wielgus et al., 2015), they are often used as first approximations of hot thick parts of accretion flows. In the truncated disk scenario (Done et al., 2007), the outer thin disk is truncated at larger radii and the inner part of the accretion flow has a form of geometrically thick flow. Numerical simulations of the radiatively inefficient flow also often produce flow of substantial geometrical thickness and significantly sub-Keplerian specific angular momentum distributions. These features point to a significant pressure support, just as in the case of simple thick disk models and

978-80-7510-257-7

perhaps also oscillations of these flows share many properties. In this context, the oscillations of thick disks still remains an active field of research. For example, Rezzolla et al. (2003) and Montero et al. (2004) studied radial axisymmetric oscillations in vertically integrated thick disks. Abramowicz et al. (2006) pointed out the existence of global epicyclic modes in relativistic slender tori. Their work was followed by Blaes et al. (2006), who presented a complete analysis of slender tori modes. Straub and Šrámková (2009) studied properties of the epicyclic modes in thicker tori using the perturbation expansion in the torus thickness around the slender torus limit. Recently, minor errors in their analysis were corrected subsequently by Fragile et al. (2016), who used their results to understand both a high-frequency and low-frequency variability of accreting black-hole GRO J1655-40.

In this note, we show that these considerations should be taken with some care. Our main finding is that tori of sufficient thickness are unstable with respect to the non-axisymmetric radial epicyclic oscillations. We also compare the analytical results of Fragile et al. (2016) with direct numerical solutions of the torus-oscillation problem. The plan of the paper is as follows. In section 2, we summarize the most relevant aspects of the theory of relativistic stationary thick disks relevant to our work. Section 3 contain a brief introduction the problem of thick disk oscillations, including some relevant mathematical results. Our numerical method is introduced in section 4. The results for axisymmetric and non-axisymmetric epicyclic modes are presented in sections 5 and 6, respectively. The section 7 discuss the mechanism of the instability and finally, section 8 is devoted to our conclusions.

2 EQUILIBRIUM

The equilibrium disk model corresponds to a relativistic torus orbiting a compact object in a stationary axially-symmetric spacetime. The complete analytic description of these solutions has been given by Abramowicz et al. (1978), (see also Kozlowski et al., 1978). The symmetries of the spacetime are described by two Killing vectors, t^μ (corresponding to stationarity) and ϕ^ν (corresponding to axial symmetry).

The matter forming the torus is described by the stress-energy tensor of ideal fluid,

$$T^\alpha_\beta = (e + p)u^\alpha u_\beta + p\delta^\alpha_\beta, \tag{1}$$

where e and p are the total energy density (including both, the rest-mass density and the internal energy) and pressure measured in the rest frame of the fluid. In the equilibrium, the four-velocity of the flow u^μ corresponds to a pure rotation,

$$u^\mu = A\left(t^\mu + \Omega\phi^\mu\right), \tag{2}$$

where $\Omega = \mathrm{d}\phi/\mathrm{d}t$ is the angular velocity of the flow measured at infinity and A is the redshift factor, a normalization constant following from the condition $u^\nu u_\nu = -1$. As already mentioned, we consider only tori with constant specific angular momentum ℓ. Therefore, we have

$$\Omega = \frac{g^{\phi t} - \ell g^{\phi\phi}}{g^{tt} - \ell g^{t\phi}}, \quad \ell \equiv -\frac{(u_\nu \phi^\nu)}{(u_\nu t^\nu)} = \text{const}, \tag{3}$$

where $g^{\mu\nu}$ denote contravariant components of the metric tensor.

The dynamics of the flow follows from the relativistic conservation laws; the Euler equation and the continuity equation,

$$\nabla_\alpha (\rho u^\alpha) = 0, \quad \nabla_\alpha T^\alpha_\beta = 0 \tag{4}$$

with ρ being the rest-mass density (e.g. particle number density multiplied by mass of a single particle). In our case, the continuity equation is satisfied trivially by the assumed symmetries of the flow and the nontrivial component of the Euler euqation gives

$$(e + p)\boldsymbol{a} + \boldsymbol{\nabla} p = 0, \quad \boldsymbol{a} = \boldsymbol{\nabla} \ln E \tag{5}$$

with $\boldsymbol{a}$ being a poloidal part of the four-acceleration and

$$E \equiv -u_\nu t^\nu = (-g^{tt} + 2\ell g^{t\phi} - \ell^2 g^{\phi\phi})^{-1/2} \tag{6}$$

being a sum of the kinetic and gravitational energies. In the case of adiabatic flows, $p = p(e)$ and $\Omega = \Omega(\ell)$, the equation (5) can be integrated to

$$Eh = \text{const}, \quad h \equiv \frac{e + p}{\rho}, \tag{7}$$

where h is the enthalpy. We restrict ourselves to the polytropic equation of state,

$$e = \rho + np, \quad p = K\rho^{1+1/n}, \tag{8}$$

where K and n are the polytropic constant and index. Surfaces of constant density and pressure coincide with surfaces of constant E ('equipotential' surfaces). As can be seen from equation (5), the equatorial circle $r = \text{const} \equiv r_0$ of the maximal pressure ('main circle' or the 'center' of the torus, r being the circumferential radius) corresponds to the geodesic. The flow rotates with Keplerian angular momentum at this radius. Inside/outside this radius, the motion is accelerated by the pressure gradient leading to super-/sub-Keplerian rotation. The location of the torus boundary (the equipotential with $p = 0$) depends on the parameter β, first introduced by Abramowicz et al. (2006),

$$\beta \equiv \frac{\sqrt{2n}c_{s0}}{A_0 r_0 \Omega_0}, \quad 0 < \beta < \beta_{\max}, \tag{9}$$

where c_{s0} is the local sound speed and the subscript '0' denotes an evaluation of the corresponding quantity at the torus center. This parameter roughly describes a ratio of the radial extend of the torus to the main-circle radius r_0 and will be further referred to as the thickness parameter. The lower limit $\beta \to 0$ corresponds to slender tori with small extend whose equipotential have elliptical cross-sections (Abramowicz et al., 2006). The upper bound $\beta_{\max}$ is determined by the maximal closed equipotential surrounding the main circle. This euipotential corresponds either to the self-crossing surface (in that case, the torus has a finite extend and terminates by the cusp at its inner edge) or to an open surface of the quasi-parabolic shape (in that case the torus outer edge is at infinity). The first case occurs in tori with centers located close to the compact object, the latter limits the torus sizes farther away. Fig. 1 shows few examples of these maximal configurations in Kerr spacetimes.

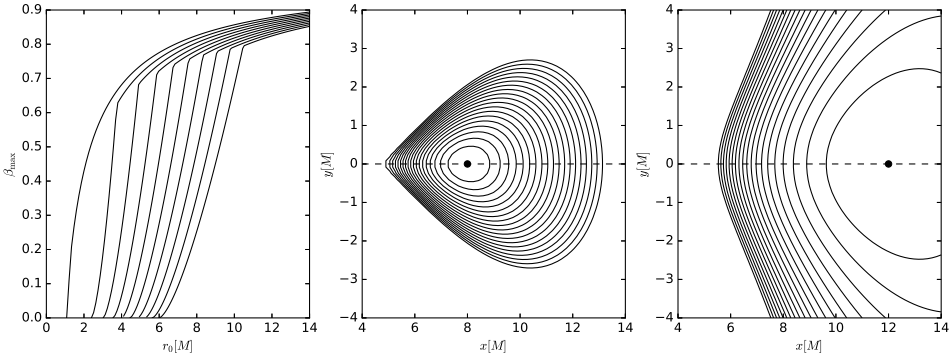

Figure 1. .Left: The upper bound on the torus thickness parameter $\beta_{\max}$ as a function of its main-circle radius r_0 for different black-hole spins (the curves from the right to left correspond to $a = 0, 0.1, 0.2, .., 0.9$ and 1). The polytropic index of the fluid is $n = 3$. The size of the torus is limited either by self-crossing equipotential surface or by first quasi-parabolical surface that opens to infinity. The first case corresponds to the initial steeper part of the $\beta_{\max}(r_0)$-curves closer to the black hole, the second case corresponds to the subsequent moderate growth farther away. Middle and right panels show examples of the two maximal configurations: torus terminated by the cusp for $a = 0$, $r_0 = 8M$ (middle) and an infinite torus for $a = 0$, $r_0 = 12M$ (right).

3 PERTURBATIONS

Due to the symmetries of the stationary configuration, a general linear perturbation of the torus can be decomposed into normal modes, whose dependence on time and azimuth is of the form of $\exp[\mathrm{i}(m\phi - \omega t)]$ with m being an integer azimuthal wavenumber and ω is the oscillation frequency (eigenfrequency) of the mode as measured by a distant observer. Papaloizou and Pringle (1984) introduced a perturbation variable W to describe the spatial shape of the perturbations. Later on, its relativistic version has been introduced by Abramowicz et al. (2006) (see also Blaes et al., 2006)

$$W \equiv -\frac{\delta h}{\tilde{\omega}}, \tag{10}$$

where $\tilde{\omega} = A(\omega - m\Omega)$ is the frequency of oscillations measured in the comoving frame of the fluid. Perturbations of other quantities follow from W using

$$\delta \boldsymbol{u} = \frac{\mathrm{i}}{h}\boldsymbol{\nabla} W, \quad \delta u_t = \frac{\tilde{m}A}{\Omega h} W, \quad \delta u_\phi = -\frac{\tilde{m}A}{h} W, \quad \delta p = -\rho\tilde{\omega} W, \tag{11}$$

where $\tilde{m} = E(m - \ell\omega)$ and, again, boldface letters denote components of four-vectors in the poloidal plane $t = \text{const}$, $\phi = \text{const}$. The variable W is governed by the relativistic Papaloizou-Pringle equation

$$\frac{h}{\rho R}\boldsymbol{\nabla}\cdot\left(\frac{\rho R}{h}\boldsymbol{\nabla} W\right) + \left[\frac{\tilde{\omega}^2}{c_{\mathrm{s}}^2} - \frac{\tilde{m}^2}{R^2}\right] W = 0, \tag{12}$$

where $R \equiv [(t_\nu \phi^\nu)^2 - (t_\nu t^\nu)(\phi_\nu \phi^\nu)]^{1/2} = (g_{t\phi}^2 - g_{tt} g_{\phi\phi})^{1/2}$. The equation (12), apart of some errors, has been first derived by Abramowicz et al. (2006). The boundary condition is that

of the free surface (i.e. vanishing Lagrangian pressure variation at the torus boundary). In terms of W, it is enough to demand W to be finite at the torus boundary.

Mathematically, the equation (12) represents a quadratic eigenvalue problem. To see it more explicitly, we can rewrite it as

$$\hat{L}W + (\omega - m\Omega_1)(\omega - m\Omega_2)W = 0, \tag{13}$$

where

$$\hat{L} \equiv \frac{h}{\rho R \mathcal{B}} \nabla \cdot \left(\frac{\rho R}{h} \nabla \right), \quad \mathcal{B} \equiv \frac{A^2}{c_s^2} - \frac{E^2 \ell^2}{R^2}, \quad \Omega_{1,2} \equiv \frac{AR\Omega \pm c_s E}{AR \pm c_s E \ell}. \tag{14}$$

Both, Ω_1 and Ω_2 tend to the rotational frequency Ω in the limit of vanishing sound speed. For a given value of the azimuthal wavenumber m, there is a set of discrete frequencies and eigenfunctions $\{\omega_n, W_n(\boldsymbol{x})\}$ that satisfy equation (13) with the boundary condition describing various modes of torus oscillations.

Consider now two functions U and V defined on the torus poloidal cross-section S and finite at its boundary ∂S. One may show that the operator $\hat{L}$ is self-adjoint with respect to the scalar product

$$\langle U|V\rangle \equiv \int_S U(\boldsymbol{x})V(\boldsymbol{x})w(\boldsymbol{x})\mathrm{d}S, \quad w(\boldsymbol{x}) = \frac{\rho R \mathcal{B}}{h}. \tag{15}$$

In the limit of slender tori, $\beta \to 0$, $\Omega_1 \approx \Omega_2 \approx \Omega_0$, the equation (13) becomes a linear self-adjoint eigenvalue problem with $\sigma^2 = (\omega - m\Omega_0)^2$ being the eigenvalue. Because the operator $\hat{L}$ is self-adjoint, it follows that its eigenvalues σ^2 are real and the corresponding eigenfunctions $W_n(\boldsymbol{x})$ form a complete orthogonal set.

Blaes et al. (2006) obtained analytic formulae describing lowest-order oscillation modes of relativistic slender tori. They also realized that due to a convenient structure of the operator $\hat{L}$ in this limit, the eigenfunctions are given by polynomials of finite order in the poloidal coordinates. In particular, the linear eigenfunctions correspond to the epicyclic modes. Later on, Straub and Šrámková (2009) studied the epicyclic modes in thicker tori (described by small but finite β) using perturbation expansion in the thickness parameter β. They expanded the eigenfunctions of a thicker torus in the basis of eigenfunctions of slender torus and found corrections due to a finite torus thickness to be

$$\omega_\mathrm{r} = \omega_\mathrm{r}^{(0)} + \beta^2 \omega_\mathrm{r}^{(2)} + O(\beta^3), \quad W_\mathrm{r} = W_\mathrm{r}^{(0)} + \beta W_\mathrm{r}^{(1)} + O(\beta^2) \tag{16}$$

and

$$\omega_\mathrm{v} = \omega_\mathrm{v}^{(0)} + \beta^2 \omega_\mathrm{v}^{(2)} + O(\beta^3), \quad W_\mathrm{v} = W_\mathrm{v}^{(0)} + \beta W_\mathrm{v}^{(1)} + O(\beta^2). \tag{17}$$

The leading-order correction $\omega_i^{(2)}$ and $W_i^{(1)}(\boldsymbol{x})$ are of the second order in the eigenfrequencies and of the first order in the eigenfunctions. They are given by the location of the pressure maximum r_0 and polytropic index n. The zeroth-order eigenfrequencies read $\omega_\mathrm{r}^{(0)} = \omega_r + m\Omega_0$ and $\omega_\mathrm{v}^{(0)} = \omega_\theta + m\Omega_0$, where ω_r and ω_θ are just radial and vertical geodesic epicyclic frequency, respectively. The Straub and Šrámková (2009) solution describes well a qualitative behavior of the epicyclic modes, nevertheless it was based on the Abramowicz et al. (2006) form of the Papaloizou-Pringle equation that contained few errors. The problem has been recently revisited by Fragile et al. (2016), who used a correct form of the Papaloizou-Pringle equation, and whose analytical results are used here.

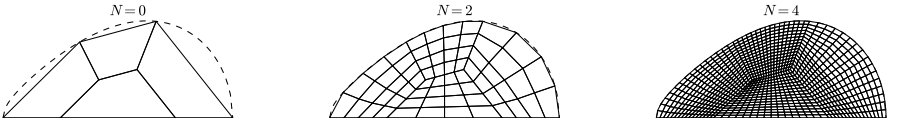

Figure 2. Quadrilateral triangulations covering the upper half of the torus cross-section used in the calculations. The initial ($N = 0$) triangulation is shown on the left, triangulations after $N = 2$ and $N = 4$ global refinements are shown in the middle and on the right, respectively. The number of the quadrilaterals after N global refinements is 4^{N+1}. The dashed line denotes the surface of the torus.

4 NUMERICAL CALCULATIONS

In this note, we use the finite elements method (FEM) to solve equation (13). By introducing an additional solution variable $\tilde{W} \equiv (\omega - m\Omega_1)W$, the quadratic eigenvalue problem is reduced to the linear one for a two-component solution vector $[W(\boldsymbol{x}), \tilde{W}(\boldsymbol{x})]$. We then find a weak form of the problem that is further discretized by expanding the solution in a finite set of suitable chosen shape functions (finite elements). This way the problem is finally reduced to an eigenvalue problem of a large sparse matrix.

Our implementation of FEM is based on the C++ library deal.II (Arndt et al., 2017). It uses a quadrilateral solution mesh ('quadrilateral triangulation'). We take advance of the equatorial plane symmetry of the stationary flow and solve the Papaloizou-Pringle equation in the upper half of the torus only. In the equatorial plane we impose additional boundary condition $W = 0$ or $\boldsymbol{n}\cdot\nabla W = 0$ ($\boldsymbol{n}$ is a normal vector to the equatorial plane) according to the parity of the modes. Initially, we start with the triangulation consisting of 4 quadrilateral cells roughly resembling overall shape of the torus cross-section. The initial mesh is then N-times refined globally. In each refinement step, every cell is divided into four smaller cells, so the total number of quadrilaterals after N refinements is 4^{N+1} (see Fig. 2). We use standard scalar Lagrange finite elements Qp for both W and $\tilde{W}$ components. This yields a solution in terms of piecewise polynomials of the order of p. In this note we the simplest elements corresponding to $p = 1$. Indeed, using higher values of p would reduce a total number of cells needed to obtain the same accuracy of approximations, however at the same time it would increase the number of degree of freedoms per cell. The matrix eigenvalue problem is solved with the aid of the numerical library ARPACK. When the solution is obtained, its error is estimated by taking one more refinement step and comparing the new eigenfrequency with the previous one. We have tested this procedure on the case of very slender torus, where the eigenfunctions and eigenfrequencies are given by analytic expressions Blaes et al. (2006). Generally, we have found that the mashes of the order of $N = 2$ or 3 are sufficient for determination of eigenfrequencies of the epicylic modes with precision better then 1%.

When examining the oscillation modes in thick tori, we assume that their eigenfrequencies and eigenfunctions are continuous functions of torus thickness. We trace the eigenfunctions of epicyclic modes in thick tori by starting at given radius with a slender torus and searching for a modes whose eigenfrequency is closest to the local epicyclic frequencies. We also check whether the corresponding eigenfunctions agree with Blaes et al. (2006) an-

alytic formula. We then gradually increase the thickness parameter β of the torus by steps $\Delta\beta$. In the $(i+1)$-th step we first select few (10) closest eigenfrequencies to the one obtained in the previous step (ω_i). For these modes, we map the corresponding eigenfunctions to the cross-section of the torus dealt with in the previous (i-th) step and calculate its correlation with the eigenfunction found in the i-th step. Finally, we chose the mode with the highest correlation. If no candidate mode gives acceptable correlation, we reduce the step size $\Delta\beta$ and repeat the procedure. Practically, we set the lower limit of acceptable correlation to 0.99. A typical step-size corresponding to this limit is $\Delta\beta = 0.01$. We trace the epicyclic modes over full range of $0 < \beta < \beta_{\rm max}$ at various radii. This way we build up a grid covering all possible radii and thicknesses. The eigenfrequencies corresponding to a torus of a given r_0 and β are then found by an interpolation over this grid.

Although our numerical calculation is suitable for a general axisymmetric spacetime, in this note, we further restrict ourselves to relativistic tori around Kerr black holes. We also set the polytropic index to $n = 3$, what corresponds to radiation-pressure dominated flows.

5 AXISYMMETRIC EPICYCLIC MODES

Figure 3 shows behavior of the eigenfrequencies of the radial and vertical axisymmetric ($m = 0$) epicyclic modes with changing thickness parameter β. Each line corresponds to a given spin of the black hole and position of the torus center r_0 and traces the eigenfrequency over a full range of the thickness parameter. Therefore their endpoints thus correspond either to infinite tori or to finite tori with cusps at their inner edges. In the latter case, the eigenfrequencies vanishes as $\beta \to \beta_{\rm max}$, because a torus center of the mass gradually moves to large radii. The analytic approximation based on Fragile et al. (2016) calculations are shown by dashed lines for comparison. In the case of the radial axisymmetric epicyclic mode, the second-order analytic predictions and the numerical calculations are in excellent agreement. On the other hand, use the analytic approximation for the vertical mode is rather limited to $\beta \lesssim 0.1$.

Figure 4 shows poloidal velocity fields corresponding to the two epicyclic modes in the cusp tori around Schwarzschild black hole, whose center is located at $r_0 = 9M$. We plot the contravariant components of the four-velocity in the Boyer-Lindquist coordinates calculated using equation (11). As can be seen from these relations, the four-velocity has also very small azimuthal component of purely relativistic origin, because $\tilde{m}$ does not vanish even for axisymmetric modes. The velocity patterns corresponding to epicyclic oscillations of thick tori differ substantially from uniform velocity fields found in slender tori. The oscillations take place mostly in outermost parts of the torus, while close to the cusp, the matter is practically unaffected.

6 NON-AXISYMMETRIC MODES

To explore properties of non-axisymmetric epicyclic modes, we concentrate on the $m = 1$ case. Since the equation (13) remains unchanged under the transformation $\omega \to -\omega$, $m \to -m$, all the results presented in this section can be applied to the case $m = -1$ as well. In slender tori, the eigenfrequencies of the non-axisymmetric oscillation modes are given by

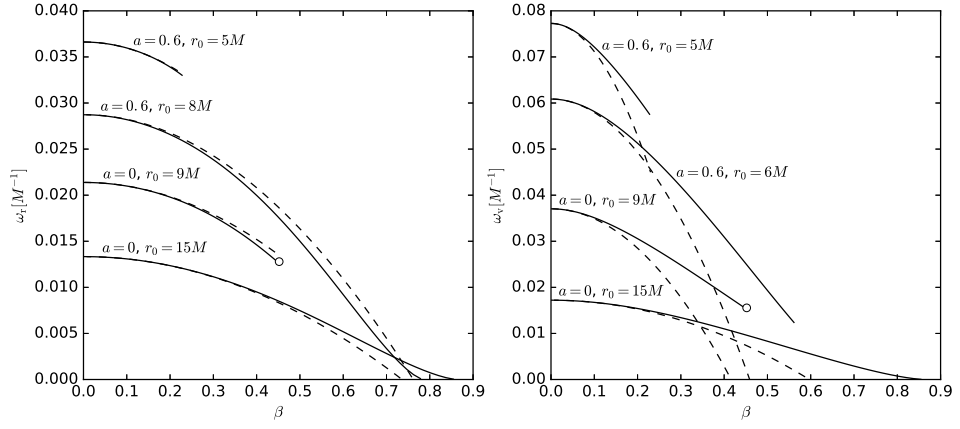

Figure 3. Eigenfrequencies of the radial (left) and vertical (right) epicyclic modes in relativistic tori surrounding Kerr black hole. The dashed lines show the analytical approximation of Fragile et al. (2016). The solid lines denote the numerical solutions of the equation (13). Each line corresponds to a sequence of tori with constant main-circle radius r_0 and changing thickness parameter β in a full range, $0 < \beta < \beta_{\max}$. The polytropic index is set to $n = 3$. The lines terminating at nonzero frequencies correspond to sequences terminating with a cusp torus. The circle indicates the solutions shown in Fig. 4.

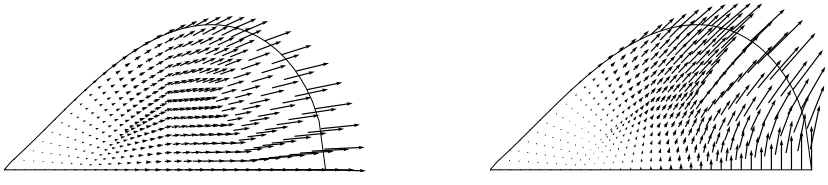

Figure 4. Eigenfunctions of the radial (left) and vertical (right) epicyclic modes of relativistic tori with cusp surrounding Schwarzschild black hole. The arrows show contravariant Boyer-Lindquist components of the local velocity δv^i calculated using equation (11). The parameters of the torus are $r_0 = 9M, \beta = 0.452$ and $n = 3$ in both cases and correposond to the solutions indicated in Fig. 3 by the circle.

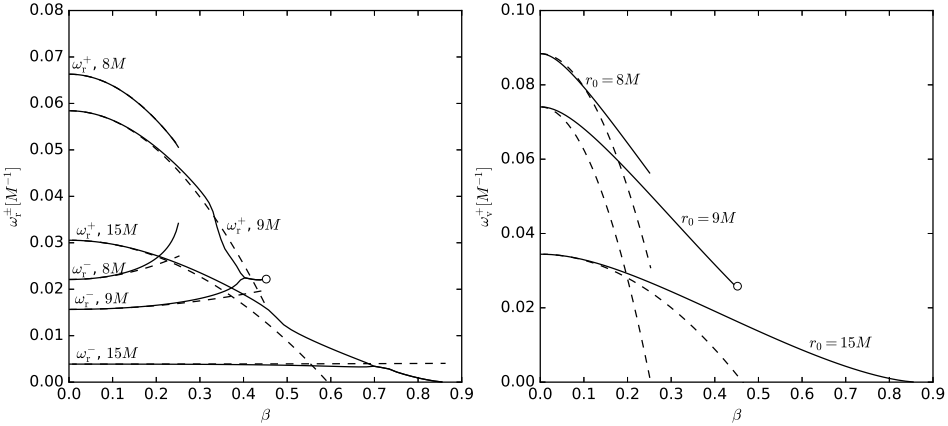

Figure 5. Eigenfrequencies of the non-axisymmetric ($m = 1$) radial and vertical epicyclic modes in relativistic tori surrounding Schwarzschild black hole at $r_0 = 8M, 9M$ and $15M$. Meaning of the lines is the same as in Fig. 3. In the case of radial modes (left), we show both, the r^+ and r^- modes. If the torus is located sufficiently far away from the black hole (here the case of $r_0 = 9M$ and $15M$), the two radial epicyclic modes merge and create a couple of an overstable and damped mode. In the case of vertical modes (right), we show only the ω_v^+-mode, as ω_v^- vanishes identically due to spherical symmetry. The circles denote the solutions, whose eigenfunctions are shown in Fig. 6.

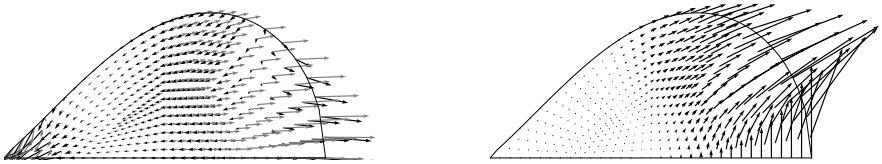

Figure 6. Eigenfunctions of the radial (left) and vertical (right) non-axisymmetric epicyclic oscillations of relativistic tori with cusp surrounding Schwarzschild black hole. In the case of the radial epicyclic mode, we show the eigenfunction of the unstable mode corresponding to merged $\omega_r^{\pm}$ branches. The eigenfunction is complex, the real and imaginary part of the velocity perturbation is shown by black and gray arrows, respectively. In the case of the vertical oscillations, we show the eigenfunction corresponding to v^+-mode. The parameters of the torus are $r_0 = 9M, \beta = \beta_{\max} = 0.452$ and $n = 3$ in both cases and correspond to the circles in Fig. 5.

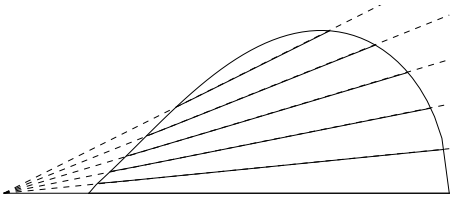

Figure 7. Eigenfunction of the nonaxisymmetric ($m = 1$) v^--mode of tori surrounding Schwarzschild black hole may serve as an independent check of the accuracy of the numerical procedure. From the symmetry reasons, the eigenfunctions of this mode has to be $W^-_{\mathrm{v}} = C\cot\theta$, independently of the torus thickness. The solid lines are contours of constant W^-_{v} in the numerical eigenfunction. The dashed lines corresponds to $\theta = \mathrm{const}$. The parameters of the torus are $r_0 = 9M$, $\beta = \beta_{\mathrm{max}} = 0.452$ and $n = 3$.

$\omega = m\Omega_0 \pm \sigma$, where σ is an eigenfrequency of the axisymmetric problem. In particular, for a given m, there are two radial (denoted as $\mathrm{r}^\pm$) and two vertical ($\mathrm{v}^\pm$) epicyclic modes with frequencies $\omega^\pm_{\mathrm{r}} = m\Omega_0 \pm \omega_r$ and $\omega^\pm_{\mathrm{v}} = m\Omega_0 \pm \omega_\theta$. We examine a behavior of all four modes with increasing torus thickness. We restrict ourselves to tori surrounding Schwarzschild black hole.

Figure 5 shows behavior of the $\mathrm{r}^\pm$-radial modes and v^+-vertical mode with changing thickness parameter β for three representative radii, $r_0 = 8M$, $9M$ and $15M$. As in the axisymmetric case, the solid lines represent numerical solution of the equation (13) and dashed lines correspond to analytical approximations of Fragile et al. (2016). Examples of the corresponding eigenfunctions are shown in Fig. 6.

In the case of the radial oscillations, the numeric and analytic curves agrees well for tori of moderate thicknesses, $\beta \lesssim 0.3$. However, at higher thicknesses we observe qualitatively different type of behavior: the two branches corresponding to $\omega^\pm_{\mathrm{r}}$ merge and develop a couple of overstable and damped modes. The two new modes oscillate with the same frequency (given by real parts of their eigenfrequencies), and opposite growth rates (imaginary parts). Consequently, their eigenfunctions are complex conjugated. An example of the overstable mode eigenfunction is shown in left panel of Fig. 6. The mechanism behind is related to the Papaloizou-Pringle instability and is discussed in more details in section 7.

In the case of the vertical oscillations, the behaivor of the oscillation frequencies and accuracy of the analytic approximations is similar to the axisymmetric case. We show only v^+ oscillations in Fig. 5 as the eigenfrequencies ω^-_{v} vanish identically for the case of Schwarzschild black hole. This is a consequence of spherical symmetry of the spacetime. The v^- oscillations in the $m = 1$ case (and by symmetry v^+ oscillations in the $m = -1$ case as well) can be separated out by introducing a suitably chosen tilt of the equatorial plane. These oscillations therefore correspond to neutral modes. Nevertheless, these mode may serve us as a very useful check of the accuracy of the numerical calculations. Being just a rigid infinitesimal tilt, it is possible to show that their eigenfunctions are simply given by $W^-_{\mathrm{v}} = C\cot\theta$, where C is a normalization constant and θ is the meridional angle of the Schwarzschild coordinates (Blaes, 2017, unpublished). In other words, the lines of

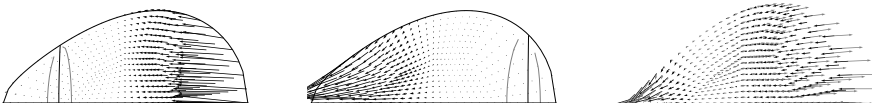

Figure 8. The eigenfunctions of the non-axisymmetric ($m = 1$) radial epicyclic modes and the mechanism of the instability. The left and middle panel show eigenfunctions of the $\mathrm{r}^{\pm}$ modes in the torus of moderate thickness ($\beta = 0.6\beta_{\max} = 0.27$). The right panel shows the eigenfunction of the unstable modes developed after $\omega_{\mathrm{r}}^{\pm}$ merges and corresponds to $\beta = 0.9\beta_{\max} = 0.407$. The center of the torus is located at $r_0 = 9M$. The black and gray arrows show real and imaginary parts of the velocity fields. The black solid line denote corotation radius. The inner and outer sonic radii are shown by gray curves.

constant W_{v}^{-} on the torus cross-section coincide with those of constant θ. Fig. 7 shows that the eigenfunctions W_{v}^{-} calculated using our numerical method have this property.

7 PAPALOIZOU-PRINGLE INSTABILITY

Dynamics of the $\mathrm{r}^{\pm}$ non-axisymmetric modes share many common features with those of a simplified shearing sheet model of Narayan et al. (1987). In this section we apply their essential results to our problem in order to qualitative understand behavior of the non-axisymmetric radial epicyclic modes.

The left and middle panels of Fig. 8 show eigenfunctions of the r^{+} and r^{-} modes for $r_0 = 9M$ and $\beta = 0.6\beta_{\max} = 0.27$. They correspond to two distinct real eigenfrequencies on separate $\omega_{\mathrm{r}}^{\pm}$ branches before the two modes merge (see Fig. 5, left). In each panel we also plot the lines where the local frequency of the oscillations matches the orbital velocity of the fluid Ω ('corotation radius') and the frequencies $\Omega_{1,2}$ (outer and inner 'sonic radii'). An observer moving with the fluid at these radii would measure either zero or sonic pattern speed of the oscillations. The two eigenfunctions show very different velocity patterns; while the most of the oscillations is concentrated to the outer parts of the torus in the case of the r^{+}, in the case of the r^{-} the most variable is the inner part. This behavior can be understand by exploring conditions for a wave propagation in the torus.A WKBJ analysis of equation (13) shows that the wave-like disturbances can freely propagate only outside the region limited by the sonic radii, while there is an wave-evanescent region in between. In the case of isolated $\mathrm{r}^{\pm}$ modes, the oscillations are trapped in a larger region, either between the outer sonic radius and the outer boundary of the torus (the case of r^{+} mode), or between the inner sonic radius and inner edge of the torus (the case of r^{-} mode).

According to Narayan et al. (1987), waves propagating outside or inside the corotation radius carry positive or negative conserved wave action, respectively. Therefore, the total action of the r^{+} mode is positive and that of r^{-} mode is negative. As the torus thickness further increase, the corotation and sonic radii gradually move towards the center of the torus allowing another trapping cavity to appear on the other side of the corotation. As a consequence, a wave trapped in this cavity reduce the absolute value of the total action of

the modes. At the moment when the $\omega_r^{\pm}$ branches merge, a standing wave pattern on both sides of the corotation is established and the total action of the mode vanishes, because the waves trapped in the two cavities carry exactly opposite actions. As time passes, these actions are further increased by tunneling effect through the evanescent region from one side of the corotation to another. As a result, an overstable neutral mode develops (see the right panel of Fig. 8).

8 CONCLUSIONS

This note summarizes some aspects of our ongoing study of oscillation modes of thick relativistic disks. We concentrated here only on the case of constant specific angular momentum flows. We reviewed a basic theory of stationary thick disks solutions and briefly discussed occurrence of the two possible maximal configuration – radially infinite tori and finite tori terminating by the cusps at their inner edges. We have noted that the cusp tori can be constructed only in a close vicinity of black holes; with increasing black-hole spin, a possible region reduces significantly. We also mentioned several mathematical aspects of the theory of torus oscillations and introduced the finite-element numerical method to solve the corresponding eigenvalue problem.

The main motivation for our study was to explore range of applicability of the second-order analytic approximations of Fragile et al. (2016) in terms of a torus thickness parameter β. Although Fragile et al. (2016) considered also higher-order modes (X, plus, and breathing), we have restricted ourselves to the epicyclic modes only. We have found that analytic approximation can be safely applied to the axisymmetric radial epicyclic mode almost in a whole range of possible β. Its agreement with the numerical solutions in this case is astonishing. On the other hand, a comparison of the results in the case of vertical axisymmetric oscillations is not so impressive. The analytic formula give a reasonable approximation only for $\beta \lesssim 0.1$. Behind this limit, the dependence of the eigenfrequencies on the torus thickness seems to be rather linear, in contrast to the quadratic one proposed by Fragile et al. (2016).

The situation is more complicated in the case of the non-axisymmetric modes where the numerical solution revealed an instability of the radial epicyclic modes. We have provided a qualitative description of the instability mechanism based on the general analysis of Narayan et al. (1987). As the instability occurs in a limited range of *finite* torus thicknesses, it is very unlikely that this behavior could be captured by analytic perturbation calculations based on an expansion around a slender-torus limit.

ACKNOWLEDGEMENTS

The authors thank Omer Blaes for valuable comments and the University of California at Santa Barbara for hospitality during our stay. This work was supported by GAČR grant no. 17-16287S.

REFERENCES

Abramowicz, M., Jaroszynski, M. and Sikora, M. (1978), Relativistic, accreting disks, *Astronomy and Astrophysics*, **63**, pp. 221–224.

Abramowicz, M. A., Blaes, O. M., Horák, J., Kluzniak, W. and Rebusco, P. (2006), Epicyclic oscillations of fluid bodies: II. Strong gravity, *Classical and Quantum Gravity*, **23**, pp. 1689–1696, arXiv: astro-ph/0511375.

Arndt, A., Bangerth, W., Davydov, D., Heister, T., Heltari, L., Kronbichler, M., Maier, M., Pelteret, J. P., Turcksin, B. and Wells, D. (2017), The deal.II Library, Version 8.5, *Journal of Numerical Mathematics*, **25**(3), pp. 137–146.

Blaes, O. M., Arras, P. and Fragile, P. C. (2006), Oscillation modes of relativistic slender tori, *Mounthly Notices Roy.Astronom.Soc.*, **369**, pp. 1235–1252, arXiv: astro-ph/0601379.

Done, C., Gierliński, M. and Kubota, A. (2007), Modelling the behaviour of accretion flows in X-ray binaries. Everything you always wanted to know about accretion but were afraid to ask, *The Astronomy and Astrophysics Review*, **15**, pp. 1–66, arXiv: 0708.0148.

Fragile, P. C., Straub, O. and Blaes, O. (2016), High-frequency and type-C QPOs from oscillating, precessing hot, thick flow, *Mounthly Notices Roy.Astronom.Soc.*, **461**, pp. 1356–1362, arXiv: 1602.08082.

Kozlowski, M., Jaroszynski, M. and Abramowicz, M. A. (1978), The analytic theory of fluid disks orbiting the Kerr black hole, *Astronomy and Astrophysics*, **63**, pp. 209–220.

Montero, P. J., Rezzolla, L. and Yoshida, S. (2004), Oscillations of vertically integrated relativistic tori - II. Axisymmetric modes in a Kerr space-time, *Mounthly Notices Roy.Astronom.Soc.*, **354**, pp. 1040–1052, arXiv: astro-ph/0407642.

Narayan, R., Goldreich, P. and Goodman, J. (1987), Physics of modes in a differentially rotating system - Analysis of the shearing sheet, *Mounthly Notices Roy.Astronom.Soc.*, **228**, pp. 1–41.

Papaloizou, J. C. B. and Pringle, J. E. (1984), The dynamical stability of differentially rotating discs with constant specific angular momentum, *Mounthly Notices Roy.Astronom.Soc.*, **208**, pp. 721–750.

Rezzolla, L., Yoshida, S. and Zanotti, O. (2003), Oscillations of vertically integrated relativistic tori - I. Axisymmetric modes in a Schwarzschild space-time, *Mounthly Notices Roy.Astronom.Soc.*, **344**, pp. 978–992, arXiv: astro-ph/0307488.

Straub, O. and Šrámková, E. (2009), Epicyclic oscillations of non-slender fluid tori around Kerr black holes, *Classical and Quantum Gravity*, **26**(5), 055011, arXiv: 0901.1635.

Wielgus, M., Fragile, P. C., Wang, Z. and Wilson, J. (2015), Local stability of strongly magnetized black hole tori, *Mounthly Notices Roy.Astronom.Soc.*, **447**, pp. 3593–3601, arXiv: 1412.4561.

Proceedings of *RAGtime 17–19, 17–19/23–26 Oct., 1–5 Nov., 2015/2016/2017, Opava, Czech Republic*
Z. Stuchlík, G. Török and V. Karas, editors, Silesian University in Opava, 2017, pp. 61–84

Quantum entanglement and quantum information in biological systems (DNA)

Ivan Hubač,[1,a] Miloslav Švec[2,b] and Stephen Wilson[3,c]

[1] Institute of Physics, Faculty of Philosophy & Science, Silesian University, 74601 Opava, Czechia
[2] Physics Department, Dawson College, Montreal, Quebec H3Z 1A4, Canada
[3] Physical and Theoretical Chemistry Laboratory, South Parks Road, Oxford OX13QZ, England
[a] belaxx@gmail.com
[b] svec@hep.physics.mcgill.ca
[c] quantumsystems@gmail.com, ORCID 0000-0001-5651-5669

ABSTRACT
Recent studies of DNA show that the hydrogen bonds between given base pairs can be treated as diabatic systems with spin-orbit coupling. For solid state systems strong diabaticity and spin-orbit coupling the possibility of forming Majorana fermions has been discussed. We analyze the hydrogen bonds in the base pairs in DNA from this perspective. Our analysis is based on a quasiparticle supersymmetric transformation which couples electronic and vibrational motion and includes normal coordinates and the corresponding momenta. We define qubits formed by Majorana fermions in the hydrogen bonds and also discuss the entangled states in base pairs. Quantum information and quantum entropy are introduced. In addition to the well-known classical information connected with the DNA base pairs, we also consider quantum information and show that the classical and quantum information are closely connected.

Keywords: Quantum entanglement – quantum entropy – biological systems

1 INTRODUCTION

There is growing evidence that living systems harness some of the unique features of quantum mechanics (Lambert et al., 2012). Examples include quantum coherent energy transport in photosynthesis (Blankenship, 2014; Cogdell et al., 2008) and avian magnetoreception (Wiltschko et al., 2010).

In this paper, we find theoretical support, using the Majorana quasiparticle formalism, for the conjecture that quantum mechanics and quantum information may also have a role in the DNA molecule. In particular, we propose that Majorana fermions can be connected with the delocalized electron associated with each of the hydrogen bonds between the base pairs. These Majorana fermions can define Majorana qubits which give rise to entanglement and

form the foundation of quantum information processes. As Lambert et al. (2012) have asked in their review of quantum biology:

> "...has nature already beaten us in leveraging quantum effects to achieve something an equivalent classical system cannot? Certainly nature can harvest energy extremely efficiently, sense weak magnetic fields and *create human minds complex enough to even be asking these questions*."

where the italics have been added by the present authors. In this work, we demonstrate a mechanism for quantum information processes in the DNA molecule. This quantum mechanism may be exploited alongside the well-known classical information processes in DNA.

In the following section, we present some of the background to this work.

2 BACKGROUND

Recent years have witnessed a growing interest in Majorana fermions (Wilczek, 2009; Franz, 2013; Leijnse and Flensberg, 2012; Elliott and Franz, 2015; Alicea, 2012) which were first proposed eight decades ago by Ettore Majorana (1937). (A review of the work of Majorana is given in the recent volume by Esposito (2014).) Majorana developed a specific representation of Dirac equation (Dirac, 1928) with solutions describing a neutral spin $\frac{1}{2}$ particle which is its own antiparticle. This particle is termed a Majorana fermion. The Majorana fermion has been extensively investigated in nuclear and particle physics as a potential fundamental particle with the neutrino being the favoured candidate. In condensed matter systems, the electrons are, of course, Dirac fermions, but Majorana fermions can arise as *emergent quasiparticles* (Wilczek, 2009; Franz, 2013; Leijnse and Flensberg, 2012; Elliott and Franz, 2015). Majorana quasiparticles were found (Mourik et al., 2012; Williams et al., 2012; Rokhinson et al., 2012; Deng et al., 2012; Das et al., 2012; Finck et al., 2013; Nadj-Perge et al., 2014; Bunkov and Gazizulin, 2015) recently although their existence was predicted theoretically by Kitaev (2001) using a one-dimensional model of a topological superconductor. Here electronic and vibrational motions are coupled together. The Majorana formalism has the potential importance in a number of areas of science, e.g. solid state physics, cosmology and quantum computation.

In this paper, we apply the Majorana quasiparticle formalism to a biological system, in particular, to the hydrogen bonds in DNA. A number of authors have considered biological systems as a source of quantum biological information, e.g. Lambert et al. (2012); Koruga (2012); dos Santos et al. (2015); Guerra et al. (1999); Abbott et al. (2008); Loewenstein (2013); Asano et al. (2015); Arndt et al. (2009); Sergi (2009); Craddock et al. (2014); Vedral (2014). Although Dirac fermions play the central role in solid state physics and practically the whole of chemistry (e.g. in the determination of the structure and properties of condensed matter and molecular systems), we suggest that Majorana fermions can play an important role in quantum biology because of their role in quantum information theory (Hassler, 2014).

Influenced by Schrödinger's book *What is Life?* (Schrödinger, 1944) and his idea of the *aperiodic crystal* as the basis of life, Watson and Crick (1953) established the double helix structure of DNA, deoxyribonucleic acid, consisting of two polynucleotide strands held

together by hydrogen bonds between pairs of complementary purines (adenine (A) and guanine (G)) and pyrimidines (thymine (T) and cytosine (C)). Adenine is always hydrogen bonded to thymine and guanine to cytosine. The two strands have a backbone consisting of a repeating unit of a sugar (deoxyribose) connected to a phosphate which form hydrogen bonds to external water molecules, whereas the purine-pyrimidine base pairs are located in

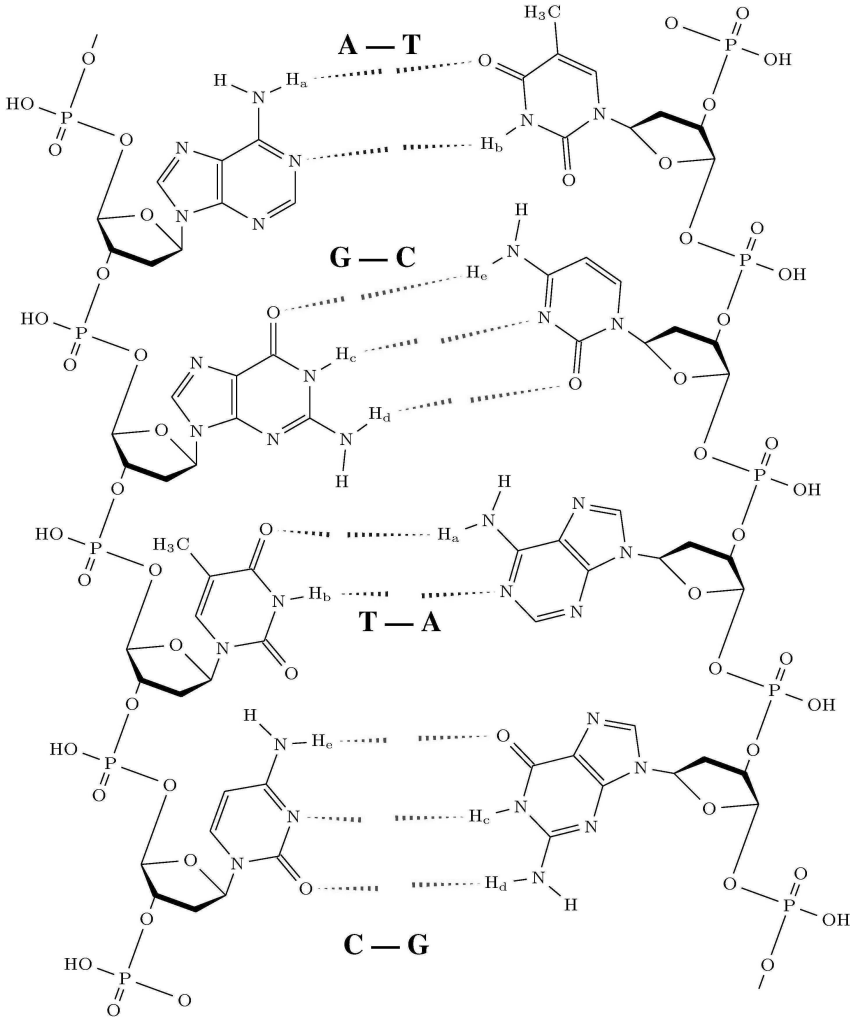

Figure 1. Structure of the DNA macromolecule with the sugar-phosphate backbone of the two helices on the left- and right-hand side and the Adenine (A)-Thymine (T) and Guanine (G)-Cytosine (C) base pairs between them. There are two hydrogen bonds (a one qubit systems) between A and T and three hydrogen bonds (a two qubit system) between G and C. The base pairs are located in the centre of the DNA molecule where they are protected from the aqueous environment.

the centre of the DNA molecule where they are protected from the aqueous environment. The structure of the DNA molecule is shown schematically in Fig. 1. DNA provides the genetic code for protein synthesis. Each triplet of nucleic acids forms a *codon*. These codons translate into amino acids. The one or more polypeptide chains, from which proteins are made, are synthesized by condensing together amino acids with the elimination of water (Crick, 1963, 1967; Watson et al., 2014). This model provides a classical approach to the DNA-protein scheme. In this model DNA is a classical information system using a ternary coding system with $4^3 = 64$ coding words (Crick, 1963). The vast majority of the ~3000 million base pairs of the human genome do not code for proteins. The ENCODE project (ENCODE Project Consortium, 2004, 2012; Djebali et al., 2012; Thurman et al., 2012; Neph et al., 2012; Gerstein et al., 2012; Sanyal et al., 2012; Birney et al., 2007) has shown that these stretches of what had been called 'junk' DNA contain regions that bind proteins and RNA molecules, bringing them into positions from which they regulate the function and level of expression of protein-coding genes. Furthermore, it appears that transcription from non-coding DNA has the potential to provide a reservoir for the creation of new functional molecules, such as regulatory RNAs. Parrington's recent book *The deeper genome* (Parrington, 2017) provides an account of developments in our understanding of the genome over recent years.

The hydrogen bond involves the attraction of a hydrogen atom bound to an electronegative atom, such as N, O or F, to another electronegative atom (Jeffrey, 1997; Gilli and Gilli, 2009; Desiraju and Steiner, 2001; Scheiner, 1997). Normal hydrogen bonds are primarily electrostatic in nature and generally linear. Other types of hydrogen bond are described as 'proton-shared' and 'blue-shifting' (Joseph and Jemmis, 2007; Buckingham et al., 2008; McDowell and Buckingham, 2010; Arunan et al., 2011a,b). Experimentally, hydrogen bonding can be identified by crystal structure analysis, by vibrational spectroscopy and by gas-phase rotational spectroscopy (Desiraju and Steiner, 2001). Infrared spectrum analysis, for example, can be used to identify changes in vibrational spectra attributable to hydrogen bonding. The hydrogen bond in DNA is a diabatic system (Buckingham et al., 2008) and therefore it should be treated with diabatic Hamiltonian. Computational quantum chemistry allows the displacements of nuclei, which comprise the normal modes of vibration, to be studied with an accuracy beyond that afforded by experimental data (Scheiner, 1997). The importance of hydrogen bonding in the structure and function of biological macromolecules was recognized at an early stage (Pauling et al., 1951). In DNA and RNA hydrogen bonds between complementary pairs of bases stabilize the double helix structure with guanine-cytosine and adenine-thymine pairs in DNA and thymine replaced by uracil in RNA (Watson et al., 2014). In the 1960s, Löwdin (1962, 1966) published pioneering studies of the quantum tunnelling of hydrogen in the DNA and RNA molecules which helped to established the field of 'quantum biology.' (For a recent overview of quantum tunnelling of hydrogen in DNA see (Al-Khalili, 2013).) Santos et al. have recently studied quantum confinement in the hydrogen bonding for proteins in the NH and OH groups (dos Santos et al., 2015). In very recent work (dos Santos et al., 2015), these authors consider the quantum confinement of the hydrogen in the NH group of the nucleic acids. Figure 2 shows the quantum confinement of hydrogen in the X-baseH$\cdots$Y system. Quantum entanglement between the electron clouds of nucleic acids in DNA was studied by Rieper et al.

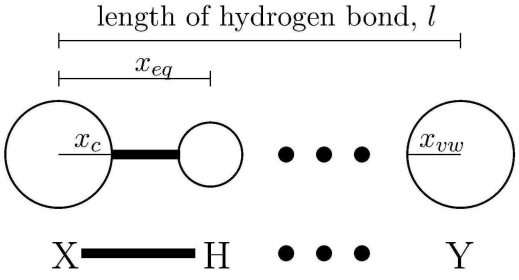

Figure 2. Schematic representation of a hydrogen bond showing the interaction between the proton donor X-H and a proton acceptor Y. x_c is the covalent radius of the donor atom, x_{vw} is the van der Waals radius of the acceptor atom, and x_{eq} is the equilibrium distance of covalent bond X-H.

(2010) using a model in which the electron clouds of the nucleic acids were viewed as a chain of coupled quantum harmonic oscillators.

In solid state theory, Majorana fermions can arise as emergent quasiparticles which can be regarded as collective excitations of the quantum many-body state describing a system of interacting electrons (Leijnse and Flensberg, 2012; Elliott and Franz, 2015). Any fermion can be written as a combination of two Majorana fermions. Essentially, a fermion can be divided into a real part and an imaginary part, each of these components being a Majorana fermion. This purely formal mathematical operation becomes interesting when the Majorana fermions are spatially well separated. In this situation, they are protected from decoherence since local perturbations cannot affect only one of the Majorana fermions. However, the state can be manipulated by physical exchange of Majorana fermions because of their non-abelian statistics. This leads to the idea of low-decoherence topological quantum computation (Nayak et al., 2008).

Here we try to identify the Majorana fermions in the hydrogen bond in DNA and to introduce qubits in connection with this hydrogen bond. Since the Majorana fermions were discussed in connection with superconductivity, where electronic and vibrational motions are coupled together, we start with a short discussion about coupling electronic and vibrational motions in molecules.

The structure of the remainder of this paper is as follows: In Section 3, we present a canonical transformation which couples the electronic and vibrational motions in molecular Hamiltonian by building on our previous work (Hubač and Wilson, 2008). Majorana transformations are then applied to this diabatic transformation in Section 4 leading to Majorana fermions in the molecule. In section 5, we introduce Majorana qubits and quantum information entropy. Quantum information in the DNA molecule is considered in section 6. Section 7 contains our conclusions and our perspective on the outlook for future work.

3 DERIVATION OF THE ADIABATIC VIBRATIONAL-ELECTRONIC HAMILTONIAN OPERATOR USING CANONICAL TRANSFORMATIONS

We have presented a detailed derivation of the adiabatic and the diabatic Hamiltonian by canonical transformations previously (Hubač and Wilson, 2008; Hubač and Svrček, 1988, 1992b,a). Here we summarize the details required for the application to the hydrogen bonds in the DNA molecule considered in this paper.

We can allow the electrons to experience the R-dependence of the nuclear terms by coupling the electronic and vibrational motions by means of a series of canonical transformations. The transformation from a basis set defined with respect to a fixed geometry R_0, $\{|p\rangle, |q\rangle, \ldots\}$, to an R-dependent basis set, $\{|p(R)\rangle, |q(R)\rangle, \ldots\}$, can be written:

$$|p\rangle \rightarrow |p(R)\rangle = \sum_q C_{qp}(R)\,|q\rangle \ .$$

This transformation employs a mixed set of second quantized operators and leads to a new representation in terms of *fermions* and *bosons* rather than *electrons* and *phonons*. The new fermion creation and annihilation operators are defined as $\{\bar{a}_p, \bar{a}_q, \ldots\}$ and $\{\bar{a}_p^\dagger, \bar{a}_q^\dagger, \ldots\}$, and new boson operators as $\{\bar{b}_r, \ldots\}$ and $\{\bar{b}_r^\dagger, \ldots\}$. The new fermion operators can be required to commute with the new boson operators. The quasi-particle transformation relating the 'crude adiabatic representation' with our new representation may then be written as follows:

$$\bar{a}_p = a_p + \sum_q \sum_{k=1}^{\infty} \frac{1}{k!} \sum_{r_1 \ldots r_k} C_{pq}^{r_1 \ldots r_k} B_{r_1} \ldots B_{r_k} a_q \,, \tag{1a}$$

$$\bar{a}_p^\dagger = a_p^\dagger + \sum_q \sum_{k=1}^{\infty} \frac{1}{k!} \sum_{r_1 \ldots r_k} C_{pq}^{r_1 \ldots r_k} B_{r_1} \ldots B_{r_k} a_q^\dagger \,, \tag{1b}$$

$$\bar{b}_r = b_r + \sum_{pq} \sum_{k=0}^{\infty} \frac{1}{k!} \sum_{s_1 \ldots s_k} D_{rPQ}^{s_1 \ldots s_k} B_{s_1} \ldots B_{s_k} a_p^\dagger a_q \,, \tag{1c}$$

$$\bar{b}_r^\dagger = b_r^\dagger + \sum_{pq} \sum_{k=0}^{\infty} \frac{1}{k!} \sum_{s_1 \ldots s_k} D_{rpq}^{s_1 \ldots s_k *} B_{s_1} \ldots B_{s_k} a_q^\dagger a_p \,. \tag{1d}$$

where B_{r_i} are the normal coordinates and C_{pq} and D_{rpq} are expansion coefficients.

Equations (1b) can be cast in the more compact forms:

$$\bar{a}_p = \sum_q \sum_{k=0}^{\infty} C_{pq}^{(k)} a_q = \sum_q C_{pq} a_q \quad \text{and} \quad \bar{a}_p^\dagger = \sum_q \sum_{k=0}^{\infty} C_{pq}^{(k)} a_q^\dagger = \sum_q C_{pq} a_q^\dagger$$

and similar formulae can be written for equations (1d) in terms of the D_{rpq} coefficients.

Operators for the fermions satisfy anticommutation relations whilst those for the bosons satisfy commutation relations. We require that operators for the fermions and bosons commute and therefore the total vibrational-electronic wave function can be written

$$\Psi(r, R) = \psi_k(r, R)\chi_k(R) \,,$$

where $\psi_k(r,R)$ is the fermion wave function and $\chi_k(R)$ is the boson wave function. It is found that there are two invariants of the transformation – the number of fermions is conserved, i.e. $\bar{N} = N$ so that we are free to redefine the Fermi vacuum, and the normal coordinate is unchanged, i.e. $\bar{B} = B$.

The canonical transformations (1) leads to an expression for the total vibrational-electronic Hamiltonian operator which can be written a sum of two parts: $\mathrm{H} = \mathrm{H}_A + \mathrm{H}_B$. Here the operator H_A can be written:

$$\mathrm{H}_A = E_{NN}(B) - E^{(2)}_{NN}(B) - V^{(2)}_N(B) + E_{\mathrm{SCF}} + \sum_{pq} f_{pq} N\left[a^\dagger_p a_q\right] + \frac{1}{2}\sum_{pqrs} v_{pqrs} N\left[a^\dagger_p a^\dagger_q a_s a_r\right],$$

where the terms $E_{NN}(B)$ and $E^{(2)}_{NN}$ arise from a Taylor expansion in normal coordinates (Hubač and Svrček, 1988) and $V^{(2)}_N(B)$ is the new effective potential. The new quasi-particle Fermi vacuum allows a new quasi-particle Hartree–Fock energy to be defined as:

$$E_{\mathrm{SCF}} = \sum_{rsi} h_{rs} C_{ri} C_{si} + \frac{1}{2}\sum_{rstkij}\left(v^0_{rtsu} - v^0_{rstu}\right) C_{ri} C_{si} C_{tj} C_{uj},$$

together with a corresponding Hartree–Fock operator f with matrix elements

$$f_{pq} = \sum_{rs} h_{rs} C_{rp} C_{sq} + \sum_{rtsui}\left(v^0_{rtsu} - v^0_{rstu}\right) C_{rp} C_{sq} C_{ti} C_{ui},$$

and the new two-particle integral

$$v_{pqrs} = \sum_{tuvw} v^0_{tuvw} C_{tp} C_{uq} C_{vr} C_{ws}.$$

The coefficients C_{pq} can be determined by solving the *coupled perturbed Hartree–Fock (CPHF)* equations (Stevens et al., 1963; Gerratt and Mills, 1968a,b; Pople et al., 1979; Takada et al., 1983; Pulay, 1977; Simons et al., 1984). Carrying out the inverse transformation of the transformations (1) and then applying Wick's theorem, we obtain the result (Hubač and Svrček, 1988):

$$\mathrm{H}_A = E^0_{NN} + E^0_{\mathrm{SCF}} + \sum_p N\left[a^\dagger_p a_p\right] + \sum_{n=1}^{\infty}\sum_{k=0}^{[n/2]} E^{(k,n-2k)} B^{(n-2k)} + \sum_{n=1}^{\infty}\sum_{k=0}^{[n/2]}\sum_{pq} f^{(k,n-2k)}_{pq} B^{(n-2k)} N\left[a^\dagger_p a_p\right] + \frac{1}{2}\sum_{n=0}^{\infty}\sum_{k=0}^{[n/2]}\sum_{pqrs} v^{(k,n-2k)}_{pqsr} B^{(n-2k)} N\left[a^\dagger_p a^\dagger_q a_s a_R\right].$$

The second part of the vibrational-electronic Hamiltonian, H_B, can be handled in a similar fashion to give:

$$\begin{aligned}\mathrm{H}_B = \sum_r \hbar\omega_r \left(b_r^\dagger b_r + \tfrac{1}{2}\right) &+ \sum_{air} \hbar\omega_r (D_{rai})^2 \\ &+ \sum_{pqr} \hbar\omega_r \left(b_r^\dagger D_{rpq} + D_{rpq} b_r\right) N\left[a_p^\dagger a_q\right] \\ &+ \sum_{pqair} \hbar\omega_r \left(D_{rpa} D_{rqa} - D_{rpi} D_{rqi}\right) N\left[a_p^\dagger a_q\right] \\ &+ \sum_{pqrsr} \hbar\omega_r D_{rps} D_{rqr} N\left[a_p^\dagger a_q^\dagger a_s a_r\right] .\end{aligned}$$

3.1 Generalization of the canonical transformations

Up to this point in our discussion, we have based the quasi-particle transformation on the normal coordinates using the follow expressions:

$$\begin{aligned}\bar{a}_p &= \sum_Q C_{PQ}(B) a_Q , & \bar{a}_p^+ &= \sum_Q C_{PQ}(B)^+ a_Q^+ , \\ \bar{b}_r &= b_r \sum_{PQ} D_{rPQ}(B) a_P^+ a_Q , & \bar{b}_r^+ &= b_r^+ \sum_{PQ} D_{rPQ}(B)^+ a_Q^+ a_Q ,\end{aligned} \tag{2}$$

where we have used the normal coordinate: $B = b + b^+$.

For the non-adiabatic representation, we can generalize the transformations (2). By analogy with the normal coordinate operator B_r, we can introduce the momentum operator: $\tilde{B} = b - b^+$ and then generalize the transformations (2) so as to define new fermion operators which represent the dependence of the motion of electrons on both the coordinates and the momenta of the nuclei. Because of their finite mass, the electrons do not follow to the motion of the nuclei adiabatically. The motion of the electrons is phase-shifted with respect to the motion of the nuclei.

The case of strong coupling has been consider in the recent work by Dahnovsky (2007) on *Ab Initio electron propagators in molecules with strong electron-phonon interaction*. Dahnovsky uses the exponential transformation:

$$T = \mathrm{e}^S ,$$

where

$$S = \sum_{i,g} c_i^+ c_i \frac{N_g^i}{W_g} (b^+ - b) \quad \text{and} \quad \bar{C}_i = \mathrm{e}^S c_i e^{-S} .$$

In the present approach, the general canonical transformation from the old set of second quantized operators $\{a_p\}$, $\{a_p^+\}$, $\{b_r\}$ and $\{b_r^+\}$ to the new set of operators $\{\bar{a}_p\}$, $\{\bar{a}_p^+\}$, $\{\bar{b}_r\}$ and

$\{\bar{b}_r^+\}$ should be (Svrček, 1986):

$$\bar{a}_P = \sum_Q C_{PQ}(B,\tilde{B})a_Q\,, \qquad \bar{a}_P^+ = \sum_Q C_{PQ}(B,\tilde{B})^+ a_Q^+\,,$$
$$\bar{b}_r = b_r + \sum_{PQ} D_{rPQ}(B,\tilde{B})a_P^+ a_Q\,, \quad \bar{b}_r^+ = b_r^+ + \sum_{PQ} D_{rPQ}(B,\tilde{B})^+ a_P^+ a_Q\,.$$

These general transformations are rather complicated. The general coefficients, $C_{PQ}(B,\tilde{B})$ and $D_{rPQ}(B,\tilde{B})$, satisfy complicated conditions. To make progress, we introduce a simple approximation in which the coefficients are written as products, i.e.

$$C_{PQ}(B,\tilde{B}) = C_{PQ}(B)\cdot\tilde{C}_{PQ}(\tilde{B})\,.$$

This is expected to be a good approximation since coordinates and momenta are independent variables. The coefficients $C_{PQ}(B)$ correspond to the adiabatic transformation describe above whilst coefficients $\tilde{C}_{PQ}(\tilde{B})$ correspond to the new transformation which we term the non-adiabatic transformation. The non-adiabatic representation results from the combination of both transformations. The canonical transformation from the old set of second quantized operators $\{a_P\}$, $\{a_P^+\}$, $\{b_r\}$ and $\{b_r^+\}$ to the new set of operators $\{\tilde{a}_P\}$, $\{\tilde{a}_P^+\}$, $\{\tilde{b}_r\}$ and $\{\tilde{b}_r^+\}$ is (Svrček, 1986):

$$\begin{aligned}
&\tilde{a}_P = \sum_Q \tilde{C}_{PQ}(\tilde{B})a_Q\,, && \tilde{a}_P^+ = \sum_Q \tilde{C}_{PQ}(\tilde{B})^+ a_Q^+\,,\\
&\tilde{b}_r = b_r + \sum_{PQ} \tilde{D}_{rPQ}(\tilde{B})a_P^+ a_Q\,, && \tilde{b}_r^+ = b_r^+ + \sum_{PQ} \tilde{D}_{rPQ}(\tilde{B})^+ a_P^+ a_Q\,.
\end{aligned} \tag{3}$$

The coefficients $\tilde{C}_{PQ}(\tilde{B})$ and $\tilde{d}_{rPQ}(\tilde{B})$ are given by the Taylor expansions

$$\tilde{C}_{PQ}(\tilde{B}) = \sum_{k=0}^{\infty}\frac{1}{k!}\sum_{r_1\ldots r_k}\tilde{C}_{PQ}^{r_1\ldots r_k}\tilde{B}_{r_1}\ldots\tilde{B}_{r_k}, \qquad \tilde{D}_{rPQ}(\tilde{B}) = \sum_{k=0}^{\infty}\frac{1}{k!}\sum_{s_1\ldots s_k}\tilde{D}_{rPQ}^{s_1\ldots s_k}\tilde{B}_{s_1}\ldots\tilde{B}_{s_k}.$$

This transformation has the form of a supersymmetric transformation. We make the approximation that terms beyond first order can be neglected.

3.2 Fermionic part of the vibrational-electronic Hamiltonian

By performing the generalized canonical transformation defined in equations (3), we can obtain an expression for the fermionic part of the non-adiabatic Hamiltonian in the non-adiabatic representation. To simplify the notation, we shall omit the tilde from the operators $\{\tilde{a}_P\}$, $\{\tilde{a}_P^+\}$, $\{\tilde{b}_r\}$ and $\{\tilde{b}_r^+\}$ in the following. Our expression for the fermionic part of the non-

adiabatic Hamiltonian can then be written in the form

$$
\begin{aligned}
H_F = {} & \overbrace{E^0_{NN} + E^0_{SCF}}^{1.} + \sum_{AI} \hbar\omega_2 \left(\left| C^r_{AI} \right|^2 - \left| \tilde{C}^r_{AI} \right|^2 \right) + \overbrace{\sum_P \varepsilon^0_P N \left[a^+_P a_P \right]}^{2.} \\
& + \sum_{PQr} \hbar\omega_2 \left[\sum_A \left(C^r_{PA} C^{r*}_{QA} - \tilde{C}^r_{PA} \tilde{C}^{r*}_{QA} \right) - \sum_I \left(C^r_{PI} C^{r*}_{QI} - \tilde{C}^r_{PI} \tilde{C}^{r*}_{QI} \right) \right] N \left[a^+_P a_Q \right] \\
& - 2 \sum_{PQr} E^{r*} \tilde{C}^r_{PQ} N \left[a^+_P a_Q \right] \\
& + \sum_{PQr} \left[(h(P) - p(P)) \, \varepsilon^{r*}_P + (h(Q) - p(Q)) \, \varepsilon^r_Q \right] \tilde{C}^r_{PQ} N \left[a^+_P a_Q \right] \\
& - \sum_{PQAIr} \left[\left(v^r_{PIQA} - v^r_{PIAQ} \right) \tilde{C}^r_{IA} + \left(v^r_{PAQI} - v^r_{PAIQ} \right) \tilde{C}^{r*}_{AI} \right] N \left[a^+_P a_Q \right] \\
& + \overbrace{\frac{1}{2} \sum_{PQRS} v^0_{PQRS} N \left[a^+_P a^+_Q a_S a_R \right]}^{3.} + \sum_{PQRSr} \hbar\omega_2 \left(C^r_{PR} C^{r*}_{SQ} - \tilde{C}^r_{PR} \tilde{C}^{r*}_{SQ} \right) N \left[a^+_P a^+_Q a_S a_R \right] \\
& - 2 \sum_{PQSr} \varepsilon^r_P \tilde{C}^{r*}_{SQ} N \left[a^+_P a^+_Q a_S a_R \right] \\
& + \sum_{PQRSTr} \Bigg\{ \sum_I \left[v^0_{PQTS} C^r_{TI} - v^0_{PQTI} C^r_{TS} + \left(v^0_{TQSI} - v^0_{TQIS} \right) C^r_{PT} \right] \tilde{C}^{r*}_{RI} \\
& + \sum_I \left[v^0_{TIRS} C^r_{QT} - v^0_{TQRS} C^r_{IT} + \left(v^0_{IQTS} - v^0_{IQST} \right) C^r_{TR} \right] \tilde{C}^{r*}_{IP} \\
& - \sum_A \left[v^0_{PQTS} C^r_{TA} - v^0_{PQTA} C^r_{TS} + \left(v^0_{TQSA} - v^0_{TQAS} \right) C^r_{PT} \right] \tilde{C}^{r*}_{RA} \\
& - \sum_A \left[v^0_{TARS} C^r_{QT} - v^0_{TQRS} C^r_{AT} + \left(v^0_{AQTS} - v^0_{AQST} \right) C^r_{TR} \right] \tilde{C}^{r*}_{AP} \Bigg\} N \left[a^+_P a^+_Q a_S a_R \right] ,
\end{aligned}
\tag{4}
$$

where we have overbraced the terms which arise in the usual electronic Hamiltonian operator. We can see immediately that if we set the $\tilde{C}_{PQ}$ coefficients to zero then we obtain the adiabatic Hamiltonian. If we put both the $\tilde{C}_{PQ}$ coefficients and the C_{PQ} coefficients equal to zero, we get the electronic Hamiltonian.

Let us now summarize, what we have achieved so far. We have derived a new kinetic energy term, as well as a new potential energy term, depending on the coefficients C_{PQ} and $\tilde{C}_{PQ}$.

$$
\begin{aligned}
& H = H_A + H_B \,, && H_B = E_{\text{kinetic}}(\tilde{B}) + E_{\text{potential}}(B) \,, \\
& E_{\text{potential}}(B) = E^{(2)}_{NN}(B) + V^{(2)}_N(B) \,, && E_{\text{kinetic}}(\tilde{B}) = T_N(\tilde{B}) + W^{(2)}_N(\tilde{B}) \,.
\end{aligned}
$$

We have to specify the C_{PQ} and $\tilde{C}_{PQ}$ coefficients from our transformation. We shall require that our new fermions, which we call *renormalized fermions*, are such that when partitioning the Hamiltonian H_A into an unperturbed part and a perturbation, the first order corrections vanish.

The equations for the C_{PQ} and $\tilde{C}_{PQ}$ coefficients are

$$u^r_{PQ} + \left(\varepsilon^0_P - \varepsilon^0_Q\right) C^r_{PQ} + \sum_{AI} \left[\left(v^0_{PIQA} - v^0_{PIAQ}\right) C^r_{AI} - \left(v^0_{PAQI} - v^0_{PAIQ}\right)\right] - \hbar\omega_r \tilde{C}^r_{PQ} = \varepsilon^r_P \delta_{PQ} \tag{5}$$

and

$$\left(\varepsilon^0_P - \varepsilon^0_Q\right) \tilde{C}^r_{PQ} + \sum_{AI} \left[\left(v^0_{PIQA} - v^0_{PIAQ}\right) \tilde{C}^r_{AI} - \left(v^0_{PAQI} - v^0_{PAIQ}\right) \tilde{C}^r_{IA}\right] - \hbar\omega_r C^r_{PQ} = \varepsilon^r_P \delta_{PQ} \,. \tag{6}$$

The new vibrational potential energy V^{rs}_N, which originate from the interaction between the nuclei and electrons, is:

$$V^{rs}_N = \sum_I u^{rs}_{II} + \sum_{AI} \left[\left(u^r_{IA} + \hbar\omega_r \tilde{C}^r_{IA}\right) C^s_{AI} + \left(u^s_{IA} + \hbar\omega_s \tilde{C}^s_{IA}\right) C^r_{AI}\right].$$

Let us compare this expression for the potential energy with that obtained in the representations considered previously in this paper. In the 'crude adiabatic approximation' we have

$$V^{rs}_N = \sum_I u^{rs}_{II} \,.$$

In the 'adiabatic' approximation, we have

$$V^{rs}_N = \sum_I u^{rs}_{II} + \sum_{AI} \left(u^r_{IA} C^s_{AI} + u^s_{IA} C^r_{AI}\right).$$

The kinetic energy term in the 'renormalized fermion' representation has the form

$$W^{rs}_N = 2\hbar\omega_r \sum_{AI} C^r_{AI} \tilde{C}^s_{IA} \,.$$

In a previous paper (Hubač and Wilson, 2008) (see also (Hubač and Svrček, 1992b,a)), we demonstrated that this Hamiltonian is equivalent to the diabatic Hamiltonian used in solid state physics theory. To demonstrate this equivalence we show its transformation to solid state notation.

3.3 Simplifications and connections with solid state theory

In this section, we shall introduce some simplifying approximations to the formalism developed above. In this way we shall establish connections with solid state theory.

In solid state theory, as in quantum chemistry, it is common to work with models or effective Hamiltonians. In general terms, a model is a conceptual representation of some physical phenomenon. Such models usually underpin computer programs which allow simulation and visualization of phenomena and/or processes. Examples of such approximations or

models in solid state theory and quantum chemistry include the Hubbard model (Hubbard, 1963), the Hückel Hamiltonian (Hückel, 1931b,a, 1932, 1933; Streitwieser, 1961; Coulson et al., 1978), the Pariser–Parr–Pople (PPP) approximation (Pariser and Parr, 1953; Pople, 1953; Pariser, 1990b,a; Pople, 1990) and the Anderson Hamiltonian (Anderson, 1961).

In this section, we shall gain some understanding of the new terms which arise in the fermionic Hamiltonian given above in equation (4) by introducing some simplifying approximations, by considering model systems.

We have seen above that the C^r_{PQ} and $\tilde{C}^r_{PQ}$ coefficients are solutions of the equations (5) and (6).

Let us explore the simplifications obtained by putting

$$v^0_{PQRS} \to 0\,,$$

that is, by assuming that two-electron Coulomb interactions vanish. We then obtain from equations (5) and (6) the following pair of equations:

$$\begin{aligned} &u^r_{PQ} + \left(\varepsilon^0_P - \varepsilon^0_Q\right) C^r_{PQ} - \hbar\omega_r \tilde{C}^r_{PQ} = \varepsilon^r_P \delta_{PQ}\,,\\ &\left(\varepsilon^0_P - \varepsilon^0_Q\right) \tilde{C}^r_{PQ} - \hbar\omega_r C^r_{PQ} = \varepsilon^r_P \delta_{PQ}\,. \end{aligned}$$

By solving these equations for C^r_{PQ} and $\tilde{C}^r_{PQ}$ we get:

$$C^r_{PQ} = u^r_{PQ} \frac{\varepsilon^0_P - \varepsilon^0_Q}{(\hbar\omega_r)^2 - \left(\varepsilon^0_P - \varepsilon^0_Q\right)^2} \tag{7}$$

and

$$\tilde{C}^r_{PQ} = \begin{cases} u^r_{PQ} \dfrac{\hbar\omega_r}{(\hbar\omega_r)^2 - \left(\varepsilon^0_P - \varepsilon^0_Q\right)^2} & \text{for } P \neq Q\,,\\ 0 & \text{for } P = Q\,. \end{cases} \tag{8}$$

Let us focus our attention on the term which corrects the ground state energy,

$$\Delta E_0 = \sum_{AIr} \hbar\omega_r \left(\left|C^r_{AI}\right|^2 - \left|\tilde{C}^r_{AI}\right|^2\right).$$

Substitute the expressions for C^r_{PQ} and $\tilde{C}^r_{PQ}$ given in equations (7) and (8), respectively, we get:

$$\Delta E_0 = \sum_{AIr} \left|u^r_{AI}\right|^2 \frac{\hbar\omega_r}{\left(\varepsilon^0_A - \varepsilon^0_I\right)^2 - (\hbar\omega_r)^2}\,. \tag{9}$$

Now let us re-write equation (9) in a notation more familiar in solid state theory[1]. The boson vibrational modes will be denoted by the index of quasimomentum $\mathbf{q}$, and spin orbitals (fermion) by $(\mathbf{k}, \sigma)$, where $\mathbf{k}$ is the quasimomentum of the fermion and σ is the spin

[1] See, for example, (Gross et al., 1991).

function. Then we can write:

$r \to \mathbf{q}$,
$\tilde{r} \to -\mathbf{q}$,
$I \to (\mathbf{k}, \sigma)$, occupation factor: $f_{\mathbf{k}}$,
$A \to (\mathbf{k}', \sigma')$, occupation factor: $1 - f_{\mathbf{k}'}$

together with

$$\epsilon_I^0 \to \epsilon_{\mathbf{k}}, \quad \epsilon_A^0 \to \epsilon_{\mathbf{k}'} \quad \text{and} \quad u_{AI}^r \to u_{\mathbf{k}'\mathbf{k}}^{\mathbf{q}} = u^{\mathbf{q}} = u^{\mathbf{k}'-\mathbf{k}}.$$

In the notation of solid state theory defined above, expression (9) for the energy correction becomes:

$$\Delta E_0 = 2 \sum_{\mathbf{k},\mathbf{k}'} \left| u^{\mathbf{k}'-\mathbf{k}} \right|^2 f_{\mathbf{k}} \left(1 - f_{\mathbf{k}'}\right) \frac{\hbar\omega_{\mathbf{k}'-\mathbf{k}}}{\left(\epsilon_{\mathbf{k}'} - \epsilon_{\mathbf{k}}\right)^2 - \left(\hbar\omega_{\mathbf{k}'-\mathbf{k}}\right)^2}.$$

This can be recognized as exactly the expression first given by Fröhlich (1950).

4 MAJORANA TRANSFORMATION OF THE DIABATIC HAMILTONIAN

In the previous section we demonstrated that our diabatic molecular Hamiltonian based on quasiparticle transformations through normal coordinates and corresponding momenta is fully equivalent to diabatic Hamiltonian used in solid state theory. This Hamiltonian plays a central role in theory of superconductivity and, more generally, in situations where electron-phonon interactions are important. Recently, this Hamiltonian was studied in connection of diabaticity and Majorana fermions (McKenzie, 2014).

In section 2, we recalled that the hydrogen bonds in the DNA molecule are known to be strongly diabatic systems (Scheurer and Shnirman, 2013). In the present study, we examine the diabaticity of the hydrogen bonds in the DNA molecule by using our diabatic molecular Hamiltonian with a Majorana transformation similarly to that studied in solid state theory (McKenzie, 2014).

In next section, we shall show that the hydrogen bonds in the DNA molecule carry quantum information through Majorana fermions. We show that the A-T and/or T-A segments (i.e. two hydrogen bonds, as can be seen in Fig. 2) segments represent one qubit. (Four Majorana fermions are necessary to form one qubit.) The segments C-G and/or G-C (i.e. three hydrogen bonds, as seen in Fig. 2) are entangled states and, therefore, carry quantum information (Tichy et al., 2011).

Majorana fermions for the molecular diabatic Hamiltonian can be introduced in the following way. The diabatic quasiparticle fermions are given by

$$\bar{a}_P = \sum_Q C_{PQ}(B, \tilde{B}) a_Q$$

and

$$\bar{a}_P^+ = \sum_Q C_{PQ}(B, \tilde{B})^+ a_Q^+.$$

We can put

$$\bar{a}_P = \gamma_1 + i\gamma_2$$

and

$$\bar{a}_P^+ = \gamma_1 - i\gamma_2\,,$$

where γ_1 and γ_2 are Majorana fermions. They are emergent quasiparticles. They play a central role in the quantum information theory associated with in the hydrogen bonds in the DNA molecule to which we turn in the following section.

5 MAJORANA QUBITS AND QUANTUM INFORMATION ENTROPY

Let us consider any fermion f with spatially well separated Majorana fermions γ_1 and γ_2. The Majorana fermions satisfy anti-commutation relations

$$\left\{\gamma_i, \gamma_j\right\} = 2\delta_{ij}\,. \tag{10}$$

It follows from (10) that $\gamma_i^2 = 1$. As a result there is no Pauli principle for the Majorana fermions. If we define a Majorana number operator $n_i^{MF} = \gamma_i^+\gamma_i$ we find $n_i^{MF} \equiv 1$. Similarly $\gamma_i\gamma_i^+ \equiv 1$. Experimentally measurable are the well-defined occupation numbers $n^f = 0, 1$ of the fermion f which are the eigenvalues of the fermion number operator $n^f = f^+f$ corresponding to the eigenvectors $|0, f\rangle$,$|1, f\rangle$.

To define Majorana qubits we need at least two fermions (Leijnse and Flensberg, 2012; Bravyi, 2006) with well separated Majorana fermions. Let us consider a system of three fermions f_1, f_2, f_3 each of them with spatially well separated Majorana fermions $\gamma_{1,k}$ and $\gamma_{2,k}$, $k = 1, 2, 3$. We define two subsystems of two fermions $X = (f_1, f_2)$ and $Y = (f_2, f_3)$. Let $|0, f_k\rangle, |1, f_k\rangle$ be the eigenvectors of the number operator $f_k^+ f_k$, $k = 1, 2, 3$.

For the subsystem X we define Majorana qubits as follows (Leijnse and Flensberg, 2012)

$$|0, X\rangle = |0, f_1\rangle\,|0, f_2\rangle\ ,$$
$$|1, X\rangle = |1, f_1\rangle\,|1, f_2\rangle\ .$$

These states may exist in a qubit superposition state

$$|q, X\rangle = a_0(X)\,|0, X\rangle + a_1(X)\,|1, X\rangle$$

with a density matrix

$$\rho(X) = |q, X\rangle\,\langle q, X| = \sum_{i,j=0}^{1} a_i(X)a_j^*(X)\,|i, X\rangle\,\langle j, X|\ . \tag{11}$$

Similarly, we define Majorana qubits for the subsystem Y

$$|0, Y\rangle = |0, f_2\rangle\,|0, f_3\rangle\ ,$$
$$|1, Y\rangle = |1, f_2\rangle\,|1, f_3\rangle$$

and their qubit superposition state

$$|q, Y\rangle = a_0(Y)\,|0, Y\rangle + a_1(Y)\,|1, Y\rangle$$

with a density matrix

$$\rho(Y) = |q, Y\rangle\langle q, Y| = \sum_{i,j=0}^{1} a_i(Y)a_j^*(Y)\,|i, X\rangle\langle j, X| \ .$$

The system S of subsystems X and Y may be entangled

$$|X, Y\rangle = a_{00}\,|0, X\rangle\,|0, Y\rangle + a_{01}\,|0, X\rangle\,|1, Y\rangle + a_{10}\,|1, X\rangle\,|0, Y\rangle + a_{11}\,|1, X\rangle\,|1, Y\rangle$$

with a density matrix

$$\rho(X, Y) = |X, Y\rangle\langle X, Y| = \sum_{i,j=0}^{1}\sum_{i',j'=0}^{1} a_{ij}a_{i'j'}^*\,|i, X\rangle\,|j, Y\rangle\langle i', X|\langle j', Y| \ . \tag{12}$$

A quantum state described by a density matrix ρ carries a quantum information $S(\rho)$ quantified by von Neumann entropy

$$S(\rho) = -\mathrm{Tr}(\rho\log\rho)\,,$$

where log is a logarithm with a base 2. The von Neumann entropy is zero $S(\rho) = 0$ for pure states ρ and is non-zero $S(\rho) \neq 0$ for mixed states. The values of the entropy are limited to the range

$$S_{\min} = 0 \leq S(\rho) \leq S_{\max} = \log N\,,$$

where N is the dimension of the Hilbert space.

6 QUANTUM INFORMATION IN DNA

We now apply the formalism developed in the Section 5 to the hydrogen bonds between complimentary base pairs in the DNA molecule. The hydrogen bonds in the DNA molecule can be viewed as a one-dimensional chain (or 'wire') of quasiparticles. In solid state physics, Majorana fermions have been found in systems containing a one-dimensional wire as well as superconductivity. Hirsch (2010) points out that in 1937 'London suggested that the diamagnetic currents in aromatic rings are analogous to supercurrents superconductors' (London, 1937). Aromatic rings are present in the pairs of complementary purines and pyrimidines in DNA. Figure 1 shows the structural formulae of the DNA molecule with the sugar-phosphate backbone of the two helices on the left- and right-hand side and the Adenine (A)-Thymine (T) and Guanine (G) -Cytosine (C) base pairs between them. There are two hydrogen bonds in A-T/T-A base pairing and three hydrogen bonds in G-C/C-G base pairing. Figure 2 shows the asymmetry of the hydrogen bond with a strong

covalent bond X-H and weak hydrogen bonding to Y. In DNA complimentary base pairing. the strong bond always involves nitrogen and the weak bond involves either oxygen or nitrogen.

Recall that hydrogen bond can be viewed as a chain of fermion quasiparticles. This chain is delocalized. This means that there is a high probability p of finding $-i\gamma_2$ at the site X and a high probability p of finding γ_1 at the site Y. At the same time there is a low probability $1-p$ of finding $-i\gamma_2$ at the site Y and the same low probability $1-p$ of finding γ_1 at the site X.

This interpretation implies that in the hydrogen bond the Majorana fermions γ_1 and γ_2 are always spatially well separated and we can define Majorana qubits. Four Majorana fermions and therefore two hydrogen bonds are required to form a qubit. In the G-C or C-G base pairing the three electrons f_1, f_2, f_3 define the entangled two-qubit density matrix $\rho(X,Y)$ in (12) which we assume to be a mixed state with a non-zero entropy. In the isolated A-T or T-A base pairing we have single qubit pure state $\rho(X)$ in (11) with zero entropy. However two adjacent A-T and T-A base pairings can combine to form two-qubit states $\rho(X,Y)$ of systems $X = (f_1, f_2)$ and $Y = (f_3, f_4)$ formed by their two pairs of Majorana fermions. This state will also be assumed to be a mixed state with non-zero entropy. Since the probability of finding the Majorana fermion γ_2 at the site X is a high p and a low $1-p$ at the site Y, the combined density matrix is a mixed state

$$p\rho(X,Y) + (1-p)\rho(X,Y) = \rho(X,Y)\,.$$

A similar identity holds for the state $\rho(X)$.

The DNA molecule consists of protein coding and protein non-coding sequences of complimentary base pairs. In each sequence we assign to each base pair C-G or G-C, each adjacent pair of base pairs A-T/T-A and each isolated base pair A-T or T-A the value of the quantum information entropy of their Majorana density matrices. The corresponding sequence of the quantum information entropy we term Quantum Entropy Sequence (QES). The ensemble of all such quantum entropy sequences of the DNA molecule constitutes quantum information in DNA.

The question arises what is the role of the quantum information in the operation and evolution of the living organisms and their systems. Entropy is an important measure of the complexity of a system (Mitchell, 2009). It is well known that the fraction of protein non-coding sequences in DNA rises dramatically with the complexity of the organism and is largest in humans at $\sim 98\,\%$ (Koruga, 2012). This suggests that the total quantum information content of the DNA increases with the complexity of the organism. The complex activity of the genome involves junk DNA in many complex ways (Carey, 2017). The expression of this complex activity may involve also the quantum states of the hydrogen bonds of the DNA bases and thus the quantum information sequences of both coding and non-coding sequences, relating the quantum information directly to the complexity of the living organisms. We suggest that the quantum information in DNA is related to the complexity and diversity of living organisms.

7 CONCLUSIONS AND OUTLOOK

We have shown that quasiparticle transformations leading to coupling of electronic and vibrational motion in the vibrational-electronic molecular Hamiltonian can be subjected to Majorana transformations to give relations that describe a chain of Majorana fermions akin to Kitaev chain. Majorana fermions that are localized at the two ends of this chain define a delocalized fermion state. Such delocalized fermions within a complex molecule define Majorana qubits.

We then make the suggestion that these Majorana qubits give rise to entanglement and form the foundation of molecular quantum information processes. We focus on systems with two and three fermions with well separated Majorana fermions and define their Majorana single-qubit and Majorana two-qubit density matrices, respectively.

We show that in hydrogen bonds of the A-T and C-G base pairs of the DNA molecule the Majorana fermions of the hydrogen electrons are spatially well separated. While the two-hydrogen bonds of isolated A-T or T-A base pairs are pure single-qubit states, the three-hydrogen bonds of the C-G or G-C base pairs are mixed two-qubit states. Two adjacent A-T/T-A base pairs are also mixed two-qubit states. In each protein coding or non-coding sequence we assign to each complimentary base pair A-T, C-G and the coupled base pairs A-T/T-A a value of von Neumann quantum information entropy thus forming a quantum information sequence. The ensemble of all such quantum information sequences in the DNA molecule constitutes its quantum information. We suggest that the quantum information in DNA is related to the complexity of living organisms and may play a role in the evolution of Life.

In this work, we have demonstrated a mechanism for quantum information processes in the DNA molecule but we have not considered how these processes might be exploited by nature. It is emphasize that this mechanism is distinct from the classical information processes currently used in explaining the function of the DNA molecule. It would be interesting, for example, to study the role of quantum information on the telomeres which form the end of chromosomes.

Quantum information in DNA could be exploited technologically in data storage systems. The recent paper by Mayer et al. (2016), for example, demonstrates that classical information in DNA can be exploited in practical data storage systems.

ACKNOWLEDGEMENTS

I. H. thanks P. Babinec, F. Blaschke, M. Blaschke and A. Jančeková for their help and for useful discussions. M. S. acknowledges with thanks helpful discussions with Etela Milanova.

REFERENCES

Abbott, D., Davies, P. C. W. and Pati, A. K. (2008), *Quantum Aspects of Life*, Imperial College Press, London, ISBN 978-1-84816-253-2, foreword by Sir Roger Penrose, URL http://trove.nla.gov.au/work/25126106?q&versionId=44708369.

Al-Khalili, J. (2013), Nature's quantum subways, *Physics World*, **26**(03), p. 42, URL http://stacks.iop.org/2058-7058/26/i=03/a=35.

Alicea, J. (2012), New directions in the pursuit of Majorana fermions in solid state systems, *Reports on Progress in Physics*, **75**(7), p. 076501, URL http://stacks.iop.org/0034-4885/75/i=7/a=076501.

Anderson, P. W. (1961), Localized magnetic states in metals, *Phys. Rev.*, **124**(1), pp. 41–53, URL https://link.aps.org/doi/10.1103/PhysRev.124.41.

Arndt, M., Juffmann, T. and Vedral, V. (2009), Quantum physics meets biology, *ArXiv e-prints*, arXiv: 0911.0155.

Arunan, E., Desiraju, G. R., Klein, R. A. et al. (2011a), Defining the hydrogen bond: An account (IUPAC Technical Report), *Pure and Applied Chemistry*, **83**(8), pp. 1619–1636, ISSN 1365-3075, URL https://www.degruyter.com/view/j/pac.2011.83.issue-8/pac-rep-10-01-01/pac-rep-10-01-01.xml.

Arunan, E., Desiraju, G. R., Klein, R. A. et al. (2011b), Definition of the hydrogen bond (IUPAC Recommendations 2011), *Pure and Applied Chemistry*, **83**(8), pp. 1637–1641, ISSN 1365-3075, URL https://www.iupac.org/publications/pac/83/8/1637/references/index.html.

Asano, M., Basieva, I., Khrennikov, A., Ohya, M., Tanaka, Y. and Yamato, I. (2015), Quantum Information Biology: From Information Interpretation of Quantum Mechanics to Applications in Molecular Biology and Cognitive Psychology, *Found. Phys.*, **45**(10), pp. 1362–1378, ISSN 1572-9516, URL http://dx.doi.org/10.1007/s10701-015-9929-y.

Birney, E. et al. (2007), Identification and analysis of functional elements in 1 % of the human genome by the ENCODE pilot project, *Nature*, **447**, pp. 799–816, URL http://dx.doi.org/10.1038/nature05874.

Blankenship, R. E. (2014), *Molecular Mechanisms of Photosynthesis*, Wiley-Blackwell, Oxford, 2nd edition, ISBN 978-1-4051-8976-7, URL http://eu.wiley.com/WileyCDA/WileyTitle/productCd-1405189762.html.

Bravyi, S. (2006), Universal quantum computation with the $\nu = 5/2$ fractional quantum Hall state, *Phys. Rev. A*, **73**, p. 042313, URL https://link.aps.org/doi/10.1103/PhysRevA.73.042313.

Buckingham, A. D., Del Bene, J. E. and McDowell, S. A. C. (2008), The hydrogen bond, *Chem. Phys. Lett.*, **463**(1), pp. 1–10, ISSN 0009-2614, URL http://www.sciencedirect.com/science/article/pii/S0009261408008361.

Bunkov, Y. M. and Gazizulin, R. R. (2015), Majorana Fermions: Direct Observation in ^{3}He, *ArXiv e-prints*, arXiv: 1504.01711.

Carey, N. (2017), *Junk DNA: A Journey Through the Dark Matter of the Genome*, Columbia University Press, New York, ISBN 9780231170857, URL https://cup.columbia.edu/book/junk-dna/9780231170840.

Cogdell, R. J., Gardiner, A. T., Hashimoto, H. and Brotosudarmo, T. H. P. (2008), A comparative look at the first few milliseconds of the light reactions of photosynthesis, *Photochem. Photobiol. Sci.*, **7**, pp. 1150–1158, ISSN 1474-905X, URL http://dx.doi.org/10.1039/B807201A.

Coulson, C. A., O'Leary, B. and Mallion, R. B. (1978), *Hückel theory for organic chemists*, Academic Press, London, New York, ISBN 0121932508, URL http://trove.nla.gov.au/work/8650568.

Craddock, T. J. A., Friesen, D., Mane, J., Hameroff, S. and Tuszynski, J. A. (2014), The feasibility of coherent energy transfer in microtubules, *Journal of The Royal Society Interface*, **11**(100), ISSN 1742-5689, arXiv: http://rsif.royalsocietypublishing.org/content/11/100/20140677.full.pdf, URL http://rsif.royalsocietypublishing.org/content/11/

100/20140677.

Crick, F. H. C. (1963), The Recent Excitement in the Coding Problem, in J. N. Davidson and W. E. Cohn, editors, *Progress in Nucleic Acid Research and Molecular Biology*, volume 1, pp. 163–217, Academic Press, New York, supplement C, URL http://www.sciencedirect.com/science/article/pii/S007966030860642X.

Crick, F. H. C. (1967), The Croonian Lecture, 1966: The Genetic Code, *Proc. Roy. Soc. London Ser. B: Biological Sciences*, **167**(1009), pp. 331–347, ISSN 0080-4649, arXiv: http://rspb.royalsocietypublishing.org/content/167/1009/331.full.pdf, URL http://rspb.royalsocietypublishing.org/content/167/1009/331.

Dahnovsky, Y. (2007), Ab initio electron propagators in molecules with strong electron-phonon interaction. I. Phonon averages, *TheJ. Chem. Phys.*, **126**(23), p. 234111, URL https://doi.org/10.1063/1.2741528.

Das, A., Ronen, Y., Most, Y., Oreg, Y., Heiblum, M. and Shtrikman, H. (2012), Zero-bias peaks and splitting in an Al-InAs nanowire topological superconductor as a signature of Majorana fermions, *Nature Physics*, **8**, p. 887, URL http://dx.doi.org/10.1038/nphys2479.

Deng, M. T., Yu, C. L., Huang, G. Y., Larsson, M., Caroff, P. and Xu, H. Q. (2012), Anomalous Zero-Bias Conductance Peak in a Nb-InSb Nanowire-Nb Hybrid Device, *Nano Letters*, **12**(12), pp. 6414–6419, pMID: 23181691, URL http://dx.doi.org/10.1021/nl303758w.

Desiraju, G. R. and Steiner, T. (2001), *The Weak Hydrogen Bond in Structural Chemistry and Biology*, Oxford University Press, Oxford, ISBN 9780198509707, URL http://dx.doi.org/10.1093/acprof:oso/9780198509707.001.0001.

Dirac, P. A. M. (1928), The quantum theory of the electron, *Proc. Roy. Soc. London Ser. A*, **117**(778), pp. 610–624, ISSN 0950-1207, arXiv: http://rspa.royalsocietypublishing.org/content/117/778/610.full.pdf, URL http://dx.doi.org/10.1098/rspa.1928.0023.

Djebali, S. et al. (2012), Landscape of transcription in human cells, *Nature*, **489**, pp. 101–108, URL http://dx.doi.org/10.1038/nature11233.

dos Santos, C. S., Drigo Filho, E. and Ricotta, R. M. (2015), Quantum confinement in hydrogen bond of DNA and RNA, *Journal of Physics: Conference Series*, **597**(1), p. 012033, ISSN 1742-6596, URL http://stacks.iop.org/1742-6596/597/i=1/a=012033.

dos Santos, C. S., Drigo Filho, E. and Ricotta, R. M. (2015), Quantum confinement in hydrogen bond of DNA and RNA, *Journal of Physics: Conference Series*, **597**(1), p. 012033, URL http://stacks.iop.org/1742-6596/597/i=1/a=012033.

Elliott, S. R. and Franz, M. (2015), Colloquium: Majorana Fermions in nuclear, particle and solid-state physics, *Rev. Modern Phys.*, **87**(1), pp. 137–163, URL http://dx.doi.org/10.1103/RevModPhys.87.137.

ENCODE Project Consortium (2004), The ENCODE (ENCyclopedia Of DNA Elements) Project, *Science*, **306**(5696), pp. 636–640, ISSN 0036-8075, arXiv: http://science.sciencemag.org/content/306/5696/636.full.pdf, URL http://science.sciencemag.org/content/306/5696/636.

ENCODE Project Consortium (2012), An integrated encyclopedia of DNA elements in the human genome, *Nature*, **489**, p. 57, URL http://dx.doi.org/10.1038/nature11247.

Esposito, S. (2014), *The Physics of Ettore Majorana: Theoretical, Mathematical, and Phenomenological*, Cambridge University Press, Cambridge, ISBN 9781107044029, URL https://goo.gl/7jYniZ.

Finck, A. D. K., Van Harlingen, D. J., Mohseni, P. K., Jung, K. and Li, X. (2013), Anomalous Modulation of a Zero-Bias Peak in a Hybrid Nanowire-Superconductor Device, *Phys. Rev.*

Lett., **110**(12), p. 126406, URL https://link.aps.org/doi/10.1103/PhysRevLett.110.126406.

Franz, M. (2013), Majorana's wires, *Nature Nanotechnology*, **8**, p. 149, URL http://dx.doi.org/10.1038/nnano.2013.33.

Fröhlich, H. (1950), Theory of the Superconducting State. I. The Ground State at the Absolute Zero of Temperature, *Phys. Rev.*, **79**, pp. 845–856, URL https://link.aps.org/doi/10.1103/PhysRev.79.845.

Gerratt, J. and Mills, I. M. (1968a), Force Constants and Dipole-Moment Derivatives of Molecules from Perturbed Hartree-Fock Calculations. I, *TheJ. Chem. Phys.*, **49**(4), pp. 1719–1729, URL https://doi.org/10.1063/1.1670299.

Gerratt, J. and Mills, I. M. (1968b), Force Constants and Dipole-Moment Derivatives of Molecules from Perturbed Hartree-Fock Calculations. II. Applications to Limited Basis-Set SCF-MO Wavefunctions, *TheJ. Chem. Phys.*, **49**(4), pp. 1730–1739, URL https://doi.org/10.1063/1.1670300.

Gerstein, M. B. et al. (2012), Architecture of the human regulatory network derived from ENCODE data, *Nature*, **489**, pp. 91–100, URL http://dx.doi.org/10.1038/nature11245.

Gilli, G. and Gilli, P. (2009), *The Nature of the Hydrogen Bond: Outline of a Comprehensive Hydrogen Bond Theory*, Oxford University Press, Oxford, ISBN 9780199558964, URL http://www.oxfordscholarship.com/view/10.1093/acprof:oso/9780199558964.001.0001/acprof-9780199558964.

Gross, E. K. U., Runge, E. and Heinonen, O. (1991), *Many-Particle Theory*, Adam Hilger, ISBN 978-0750300728.

Guerra, C. F., Bickelhaupt, F. M., Snijders, J. G. and Baerends, E. J. (1999), The nature of the hydrogen bond in DNA base pairs: the role of charge transfer and resonance assistance, *Chemistry: A European Journal*, **5**(12), pp. 3581–3594, ISSN 1521-3765, URL https://scholar.google.com/citations?user=0uok-okAAAAJ.

Hassler, F. (2014), Majorana Qubits, *ArXiv e-prints*, also appears in "Quantum Information Processing. Lecture Notes of the 44th IFF Spring School 2013," edited by D. P. DiVincenzo (Verlag des Forschungszentrums Jülich, 2013), arXiv: 1404.0897, URL http://adsabs.harvard.edu/abs/2014arXiv1404.0897H.

Hirsch, J. E. (2010), Spin-split states in aromatic molecules and superconductors, *Phys. Lett. A*, **374**(36), pp. 3777–3783, ISSN 0375-9601, arXiv: 1007.2813, URL http://www.sciencedirect.com/science/article/pii/S0375960110008480.

Hubač, I. and Svrček, M. (1988), The quasiparticle concept in vibrational-electronic problems in molecules. I. Partitioning of the vibrational-electronic Hamiltonian, *Internat. J. Quantum Chem.*, **33**(5), pp. 403–443, ISSN 1097-461X, URL http://dx.doi.org/10.1002/qua.560330504.

Hubač, I. and Svrček, M. (1992a), Many-Body Perturbation Theory for Vibrational Electronic Molecular Hamiltonian, in S. Wilson and G. H. F. Diercksen, editors, *Methods in Computational Molecular Physics*, volume 293 of *NATO ASI Series (Series B: Physics)*, pp. 471–512, Springer, Boston, MA, ISBN 978-1-4615-7419-4, URL https://doi.org/10.1007/978-1-4615-7419-4.

Hubač, I. and Svrček, M. (1992b), The Many-Body Perturbation Theory of the Vibrational-Electronic Problem in Molecules, in S. Wilson, editor, *Methods in Computational Chemistry*, volume 4: Molecular Vibrations, p. 145, Springer US, ISBN 9780306441684, URL https://books.google.cz/books?id=Qt7vAAAAMAAJ.

Hubač, I. and Wilson, S. (2008), The Non-Adiabatic Molecular Hamiltonian: A Derivation Using Quasiparticle Canonical Transformations, in S. Wilson, P. J. Grout, J. Maruani, G. Delgado-Barrio and P. Piecuch, editors, *Frontiers in Quantum Systems in Chemistry and Physics. Progress in*

Theoretical Chemistry and Physics, volume 18, p. 403, Springer, Dordrecht, ISBN 978-1-4020-8707-3, URL https://doi.org/10.1007/978-1-4020-8707-3_19.

Hubbard, J. (1963), Electron correlations in narrow energy bands, *Proc. Roy. Soc. London Ser. A: Mathematical, Physical and Engineering Sciences*, **276**(1365), pp. 238–257, ISSN 0080-4630, URL http://rspa.royalsocietypublishing.org/content/276/1365/238.

Hückel, E. (1931a), Quanstentheoretische Beiträge zum Benzolproblem. II. Quantentheorie der induzierten Polaritäten, *Zeischrifft für Physik*, **72**(5), pp. 310–337, ISSN 0044-3328, URL https://doi.org/10.1007/BF01341953.

Hückel, E. (1931b), Quantentheoretische Beiträge zum Benzolproblem. I. Die Elektronenkonfiguration des Benzols und verwandter Verbindungen, *Zeischrifft für Physik*, **70**(3), pp. 204–286, ISSN 0044-3328, URL https://doi.org/10.1007/BF01339530.

Hückel, E. (1932), Quantentheoretische Beiträge zum Problem der aromatischen und ungesättigten Verbindungen. III, *Zeischrifft für Physik*, **76**(9), pp. 628–648, ISSN 0044-3328, URL https://doi.org/10.1007/BF01341936.

Hückel, E. (1933), Die freien Radikale der organischen Chemie, *Zeischrifft für Physik*, **83**(9), pp. 632–668, ISSN 0044-3328, URL https://doi.org/10.1007/BF01330865.

Jeffrey, G. A. (1997), *An Introduction to Hydrogen Bonding*, Topics in Physical Chemistry – Oxford University Press, Oxford University Press, Oxford, ISBN 9780195095494, URL https://books.google.cz/books?id=ZRAFifo37QsC.

Joseph, J. and Jemmis, E. D. (2007), Red-, Blue-, or No-Shift in Hydrogen Bonds: A Unified Explanation, *J. Amer. Chem. Soc.*, **129**(15), pp. 4620–4632, pMID: 17375920, URL http://dx.doi.org/10.1021/ja067545z.

Kitaev, A. Y. (2001), Unpaired Majorana fermions in quantum wires, *Physics-Uspekhi*, **44**(10S), p. 131, ISSN 1468-4780, URL http://stacks.iop.org/1063-7869/44/i=10S/a=S29.

Koruga, D. (2012), Classical and quantum processing in DNA-protein coding, in B. Obradović, editor, *Cell and Tissue Engineering*, pp. 9–26, Springer-Verlag, Berlin, ISBN 978-86-7466-408-7, URL https://goo.gl/aqX43c.

Lambert, N., Chen, Y.-N., Cheng, Y.-C., Li, C.-M., Chen, G.-Y. and Nori, F. (2012), Quantum Biology, *Nature Physics*, **9**, pp. 10–18, ISSN 1745-2481 (online), URL http://dx.doi.org/10.1038/nphys2474.

Leijnse, M. and Flensberg, K. (2012), Introduction to topological superconductivity and Majorana fermions, *Semiconductor Science and Technology*, **27**(12), p. 124003, URL http://stacks.iop.org/0268-1242/27/i=12/a=124003.

Loewenstein, W. R. (2013), *Physics in Mind: A Quantum View of the Brain*, Basic Books, New York, 1st edition, ISBN 978-0465029846, URL https://www.amazon.com/Physics-Mind-Quantum-View-Brain/dp/0465029841.

London, F. (1937), Théorie quantique des courants interatomiques dans les combinaisons aromatiques (Quantum theory of interatomic currents in aromatic compounds), *J. Phys. Radium*, **8**(10), pp. 397–409, URL https://doi.org/10.1051/jphysrad:01937008010039700.

Löwdin, P.-O. (1962), The Normal Constants of Motion in Quantum Mechanics Treated by Projection Technique, *Rev. Modern Phys.*, **34**, pp. 520–530, URL https://link.aps.org/doi/10.1103/RevModPhys.34.520.

Löwdin, P.-O. (1966), *Advances in Quantum Chemistry*, volume 2, Academic Press, 1st edition, ISBN 9780080582276, URL https://www.elsevier.com/books/advances-in-quantum-chemistry/lowdin/978-0-12-034802-2.

Majorana, E. (1937), Teoria simmetrica dell'elettrone e del positrone, *Il Nuovo Cimento (1924-1942)*, **14**(4), p. 171, ISSN 1827-6121, english translation: Sobryushiron Kenkyu **63**, 149 (1981).,

URL http://dx.doi.org/10.1007/BF02961314.

Mayer, C., McInroy, G. R., Murat, P., Van Delft, P. and Balasubramanian, S. (2016), An Epigenetics-Inspired DNA-Based Data Storage System, *Angewandte Chemie International Edition*, **55**(37), pp. 11144–11148, ISSN 1521-3773, URL http://dx.doi.org/10.1002/anie.201605531.

McDowell, S. A. C. and Buckingham, A. D. (2010), Cooperative and diminutive hydrogen bonding in $Y \cdots HCN \cdots HCN$ and $NCH \cdots Y \cdots HCN$ trimers ($Y = BF, CO, N_2$), *TheJ. Chem. Phys.*, **132**(6), p. 064303, URL https://doi.org/10.1063/1.3297894.

McKenzie, R. H. (2014), A diabatic state model for double proton transfer in hydrogen bonded complexes, *TheJ. Chem. Phys.*, **141**(10), p. 104314, arXiv: 1504.01711, URL https://doi.org/10.1063/1.4895007.

Mitchell, M. (2009), *Complexity: A Guided Tour*, Oxford University Press, Oxford, New York, ISBN 978-0-19-512441-5, URL https://global.oup.com/academic/product/complexity-9780195124415.

Mourik, V., Zuo, K., Frolov, S. M., Plissard, S. R., Bakkers, E. P. A. M. and Kouwenhoven, L. P. (2012), Signatures of Majorana Fermions in Hybrid Superconductor-Semiconductor Nanowire Devices, *Science*, **336**(6084), pp. 1003–1007, ISSN 0036-8075, arXiv: http://science.sciencemag.org/content/336/6084/1003.full.pdf, URL http://science.sciencemag.org/content/336/6084/1003.

Nadj-Perge, S., Drozdov, I. K., Li, J., Chen, H., Jeon, S., Seo, J., MacDonald, A. H., Bernevig, B. A. and Yazdani, A. (2014), Observation of Majorana fermions in ferromagnetic atomic chains on a superconductor, *Science*, **346**(6209), pp. 602–607, ISSN 0036-8075, arXiv: http://science.sciencemag.org/content/346/6209/602.full.pdf, URL http://science.sciencemag.org/content/346/6209/602.

Nayak, C., Simon, S. H., Stern, A., Freedman, M. and Das Sarma, S. (2008), Non-Abelian anyons and topological quantum computation, *Rev. Modern Phys.*, **80**(3), pp. 1083–1159, URL https://link.aps.org/doi/10.1103/RevModPhys.80.1083.

Neph, S. et al. (2012), An expansive human regulatory lexicon encoded in transcription factor footprints, *Nature*, **489**, pp. 83–90, URL http://dx.doi.org/10.1038/nature11212.

Pariser, R. (1990a), On the genesis of a theory, *Internat. J. Quantum Chem.*, **37**(4), pp. 327–347, ISSN 1097-461X, URL http://dx.doi.org/10.1002/qua.560370407.

Pariser, R. (1990b), On the origins of the PPP method, *Internat. J. Quantum Chem.*, **37**(4), pp. 319–325, ISSN 1097-461X, URL http://dx.doi.org/10.1002/qua.560370406.

Pariser, R. and Parr, R. G. (1953), A Semi-Empirical Theory of the Electronic Spectra and Electronic Structure of Complex Unsaturated Molecules. II, *TheJ. Chem. Phys.*, **21**(5), pp. 767–776, URL https://doi.org/10.1063/1.1699030.

Parrington, J. (2017), *The Deeper Genome. Why there is more to the human genome than meets the eye*, Oxford University Press, Oxford, ISBN 9780198813095, URL https://global.oup.com/academic/product/the-deeper-genome-9780198813095.

Pauling, L., Corey, R. B. and Branson, H. R. (1951), The structure of proteins; two hydrogen-bonded helical configurations of the polypeptide chain, *Proc. Nat. Acad. Sci. U.S.A.*, **37**(4), pp. 205–211, ISSN 1091-6490, pMID: 14816373, PMCID: PMC1063337, URL https://www.ncbi.nlm.nih.gov/pubmed/14816373.

Pople, J. A. (1953), Electron interaction in unsaturated hydrocarbons, *Trans. Faraday Soc.*, **49**, pp. 1375–1385, URL http://dx.doi.org/10.1039/TF9534901375.

Pople, J. A. (1990), The origin of PPP theory, *Internat. J. Quantum Chem.*, **37**(4), pp. 349–371, ISSN 1097-461X, URL http://dx.doi.org/10.1002/qua.560370408.

Pople, J. A., Krishnan, R., Schlegel, H. B. and Binkley, J. S. (1979), Derivative studies in Hartree–Fock and Møller–Plesset theories, *Internat. J. Quantum Chem.*, **16**(S13), pp. 225–241, ISSN 1097-461X, URL http://dx.doi.org/10.1002/qua.560160825.

Pulay, P. (1977), Direct Use of the Gradient for Investigating Molecular Energy Surfaces, in H. Schaefer, editor, *Applications of Electronic Structure Theory*, volume 4 of *Modern Theoretical Chemistry*, pp. 153–185, Springer US, Boston, MA, ISBN 978-1-4684-8541-7, URL http://dx.doi.org/10.1007/978-1-4684-8541-7.

Rieper, E., Anders, J. and Vedral, V. (2010), Quantum entanglement between the electron clouds of nucleic acids in DNA, *ArXiv e-prints*, arXiv: 1006.4053, URL http://adsabs.harvard.edu/abs/2010arXiv1006.4053R.

Rokhinson, L. P., Liu, X. and Furdyna, J. K. (2012), The fractional a.c. Josephson effect in a semiconductor-superconductor nanowire as a signature of Majorana particles, *Nature Physics*, **8**, p. 795, URL http://dx.doi.org/10.1038/nphys2429.

Sanyal, A., Lajoie, B. R., Jain, G. and Dekker, J. (2012), The long-range interaction landscape of gene promoters, *Nature*, **489**, pp. 109–113, URL http://dx.doi.org/10.1038/nature11279.

Scheiner, S. (1997), *Hydrogen Bonding: A Theoretical Perspective*, Oxford University Press, Oxford, ISBN 9780195090116, URL https://global.oup.com/academic/product/hydrogen-bonding-9780195090116.

Scheurer, M. S. and Shnirman, A. (2013), Nonadiabatic processes in Majorana qubit systems, *Phys. Rev. B*, **88**, p. 064515, arXiv: 1305.4923, URL https://link.aps.org/doi/10.1103/PhysRevB.88.064515.

Schrödinger, E. (1944), *What is life*, Cambridge University Press, Cambridge, ISBN 0-521-42708-8, URL http://dx.doi.org/10.1017/CBO9781139644129.

Sergi, A. (2009), Quantum Biology, *ArXiv e-prints*, arXiv: 0907.1968.

Simons, J., Jørgensen, P. and Helgaker, T. U. (1984), Higher molecular-deformation derivatives of the configuration-interaction energy, *Chem. Phys.*, **86**(3), pp. 413–432, ISSN 0301-0104, URL http://www.sciencedirect.com/science/article/pii/0301010484800294.

Stevens, R. M., Pitzer, R. M. and Lipscomb, W. N. (1963), Perturbed Hartree-Fock Calculations. I. Magnetic Susceptibility and Shielding in the LiH Molecule, *TheJ. Chem. Phys.*, **38**(2), pp. 550–560, URL https://doi.org/10.1063/1.1733693.

Streitwieser, A. (1961), *Molecular orbital theory for organic chemists*, Wiley, New York, ISBN 9780471833581, URL http://science.sciencemag.org/content/136/3511/143.1.

Svrček, M. (1986), Ph.D. thesis, Faculty of Mathematics and Physics, Comenius University, Bratislava.

Takada, T., Dupuis, M. and King, H. F. (1983), Molecular symmetry. IV. The coupled perturbed Hartree–Fock method, *J. Comput. Chem.*, **4**(2), pp. 234–240, ISSN 1096-987X, URL http://dx.doi.org/10.1002/jcc.540040214.

Thurman, R. E. et al. (2012), The accessible chromatin landscape of the human genome, *Nature*, **489**, pp. 75–82, URL http://dx.doi.org/10.1038/nature11232.

Tichy, M. C., Mintert, F. and Buchleitner, A. (2011), Essential entanglement for atomic and molecular physics, *J. Phys. B: Atomic, Molecular and Optical Physics*, **44**(19), p. 192001, arXiv: 1012.3940, URL http://stacks.iop.org/0953-4075/44/i=19/a=192001.

Vedral, V. (2014), Quantum entanglement, *Nature Physics*, **10**, p. 256, ISSN 1745-2481, URL http://dx.doi.org/10.1038/nphys2904.

Watson, J. D., Baker, T. A., Bell, S. P., Gann, A., Michael, L. and Richard, L. (2014), *Molecular Biology of the Gene*, Pearson Education, 7th edition, ISBN 9780321762436, URL https://www.pearson.com/us/higher-education/product/

Watson-Molecular-Biology-of-the-Gene-7th-Edition/9780321762436.html.

Watson, J. D. and Crick, F. H. C. (1953), A Structure for Deoxyribose Nucleic Acid, *Nature*, **171**(4356), pp. 737–738, URL https://www.nature.com/nature/dna50/archive.html.

Wilczek, F. (2009), Majorana returns, *Nature Physics*, **5**, p. 614, URL http://dx.doi.org/10.1038/nphys1380.

Williams, J. R., Bestwick, A. J., Gallagher, P., Hong, S. S., Cui, Y., Bleich, A. S., Analytis, J. G., Fisher, I. R. and Goldhaber-Gordon, D. (2012), Unconventional Josephson Effect in Hybrid Superconductor-Topological Insulator Devices, *Phys. Rev. Lett.*, **109**(5), p. 056803, URL http://dx.doi.org/10.1103/PhysRevLett.109.056803.

Wiltschko, R., Stapput, K., Thalau, P. and Wiltschko, W. (2010), Directional orientation of birds by the magnetic field under different light conditions, *Journal of The Royal Society Interface*, **7**(Suppl 2), pp. S163–S177, ISSN 1742-5689, arXiv: http://rsif.royalsocietypublishing.org/content/7/Suppl_2/S163.full.pdf, URL http://rsif.royalsocietypublishing.org/content/7/Suppl_2/S163.

Proceedings of *RAGtime 17–19, 17–19/23–26 Oct., 1–5 Nov., 2015/2016/2017, Opava, Czech Republic*
Z. Stuchlík, G. Török and V. Karas, editors, Silesian University in Opava, 2017, pp. 85–90

The motion of the test particle near the black hole embedded into dust: The flat space case

Pavlína Jalůvková,[1,2] Elena Kopteva[1] and Zdeněk Stuchlík[1]

[1]Institute of Physics, Faculty of Philosophy & Science, Silesian University in Opava, Bezručovo nám. 13, CZ-746 01 Opava, Czech Republic
[2]Joint Institute for Nuclear Research, Dubna, Russia

ABSTRACT
In this work we investigate the motion of free particle in the field of strongly gravitating object which is embedded into dust cosmological background. We use newly obtained exact solution of Einstein equations in comoving coordinates for the system under consideration in case of zero spatial curvature. Observable velocity of the particle moving relatively to the observer comoving with cosmological expansion is found from geodesic equations.

Keywords: black hole – cosmological background – LTB solution – test particle – exact solutions of Einstein equations

1 INTRODUCTION

The problem of building a model of the black hole that embedded into space which is not empty but filled with some matter is of great interest in wide set of research directions, including the thermodynamics of black holes (Giddings, 2012), (Firouzjaee and Mansouri, 2012), (Firouzjaee and Ellis, 2015a), (Firouzjaee and Ellis, 2015b), the black hole horizon dynamics (Firouzjaee and Mansouri, 2010), studying the influence of cosmological expansion on the evolution of local objects (Moradi et al., 2010), (Faraoni and Jacques, 2009) etc.

In this work we focus on investigation of the motion of the test particle near the black hole in a cosmological background. This will help in explaining how the effect of cosmological expansion could be relevant for local dynamics near the astrophysical black holes today. Many papers devoted to this problem were appearing over the years (see (Senovilla et al., 1999), (Krasinski, 1997) for brief reviews) but the problem is steel staying a point for active discussions. New exact solutions can help to better understand this problem.

Recently a new exact solution describing the black hole embedded into dust matter was found by means of the mass function method (Korkina and Kopteva, 2012b), (Korkina and Kopteva, 2012a). Using this solution in particular case of flat space we study the motion of the test particle in resulting space–time solving the geodesic equations.

978-80-7510-257-7

The paper is organized as follows. In section 2 briefly present the idea of the mass function method and our exact solution. In section 3 we write the geodesic equations and solve them for pure radial and orbital motion. In conclusions section we summarize the results.

2 THE SOLUTION

The mass function method is the method for solving the Einstein equations by means of introducing the mass function (Misner and Sharp, 1964) – (Zannias, 1990)

$$m(R,t) = r(R,t)(1 + e^{-\nu(R,t)}\dot{r}^2 - e^{-\lambda(R,t)}r'^2) \tag{1}$$

which is one of four algebraic invariants for the spherically symmetric metric

$$ds^2 = e^{\nu(R,t)}dt^2 - e^{\lambda(R,t)}dR^2 - r^2(R,t)d\sigma^2. \tag{2}$$

Using (1) it is possible to rewrite the Einstein equations in much more simple way

$$m' = \varepsilon r^2 r'; \tag{3}$$

$$\dot{m} = -p_{\parallel} r^2 \dot{r}; \tag{4}$$

$$2\dot{r}' = \nu' \dot{r} + \dot{\lambda} r'; \tag{5}$$

$$2\dot{m}' = m' \frac{\dot{r}}{r'} \nu' + \dot{m} \frac{r'}{\dot{r}} \dot{\lambda} - 4r\dot{r}r' p_{\perp}; \tag{6}$$

Here and further we use the units were $c = 1$ and $8\pi G = 1$; dot means derivative with respect to t and prime means derivative with respect to R; ε is energy density, $p_{\perp}$ is tangential pressure, and $p_{\parallel}$ is radial pressure.

In our consideration we use the comoving coordinates, which are known to become synchronous for the dust.

Let us take the metric describing dust distribution in Tolman–Bondi form (Tolman, 1969)

$$ds^2 = dt^2 - \frac{r'^2(R,t)}{f^2(R)}dR^2 - r^2(R,t)d\sigma^2, \tag{7}$$

were $f(R)$ is arbitrary function having sense of total energy in mc^2 units in the shell R.

The Schwarzschild solution as well as Friedman solution are the particular cases of the Tolman–Bondi solution under certain choice of functions $m(R)$, $f(R)$ and $t_0(R)$. Namely $m(R) = r_g$ for the Schwarzschild solution and $m(R) = a_0 R^3$, $f(R) = 1$, $t_0(R) = 0$ for the flat Friedman one.

The mass function has a meaning of total mass in the shell R, so it is additive function. And hence the solution for the Schwarzschild–like black hole in the Tolman–Bondi space–time will be the Tolman–Bondi solution with the mass function

$$m(R) \to r_g + m(R). \tag{8}$$

Thus the solution for the flat Friedman world together with the Schwarzschild–like black hole for the case of expansion takes the form

$$r(R,t) = \left[\pm\frac{3}{2}\sqrt{r_g + a_0R^3}(t - t_0(R))\right]^{\frac{2}{3}}. \tag{9}$$

One should notice that this solution does not describe the pure Friedman world but describes the world of Tolman–Bondi with mass function chosen the same as Friedman one.

The metric (7) has two true singularities under $r(R,t) = 0$ and $r'(R,t) = 0$. The energy density in the resulting space–time can be found from the equation (3) regarding the mass function

$$m(R) = (r_g + a_0R^3). \tag{10}$$

It reads

$$\varepsilon(R,t) = \frac{4a_0R^2}{(a_0R^2(3t - 5R) - 2r_g)(t - R)} \tag{11}$$

The expansion starts for each shell R at the moment $t = R$ with infinite energy density and then for each shell the energy density tends to zero with time. The black hole horizon is absent in comoving coordinates, but there is one more singularity which gives divergence of the energy density along $r'(R,t) = 0$. Thus the observer with constant R and φ will always see the overdense region near small R what might be treated as the manifestation of the black hole.

3 THE EQUATION OF MOTION

In this section we consider the motion of the test particle in obtained model with respect to observer comoving with the cosmological expansion. We fix θ coordinate $\theta = \pi/2$, and chose the arbitrary function $t_0(R)$ to be just R to get analogy with Lemaitre solution.

For the solution (9) with mass function (10) and metric

$$ds^2 = dt^2 - r'^2(R,t)dR^2 - r^2(R,t)d\varphi^2 \tag{12}$$

the geodesic equations gives

$$\frac{d^2t}{ds^2} + \dot{r}'r'\Big(\frac{dR}{ds}\Big)^2 + \dot{r}r\Big(\frac{d\varphi}{ds}\Big)^2 = 0 \tag{13}$$

$$\frac{d^2R}{ds^2} + \frac{r''}{r'}\Big(\frac{dR}{ds}\Big)^2 - \frac{r}{r'}\Big(\frac{d\varphi}{ds}\Big)^2 + 2\frac{\dot{r}'}{r'}\frac{dt}{ds}\frac{dR}{ds} = 0 \tag{14}$$

$$\frac{d^2\varphi}{ds^2} + 2\frac{r'}{r}\frac{dR}{ds}\frac{d\varphi}{ds} + 2\frac{\dot{r}}{r}\frac{d\varphi}{ds}\frac{dt}{ds} = 0 \tag{15}$$

For the case when the particle starts from rest with respect to comoving coordinates R, φ one has

$$\frac{dR}{ds} = 0, \quad \frac{d\varphi}{ds} = 0, \quad \frac{dt}{ds} = 1, \tag{16}$$

and hence from the system (13)-(15) it follows that

$$\frac{d^2t}{ds^2} = 0, \quad \frac{d^2R}{ds^2} = 0, \quad \frac{d^2\varphi}{ds^2} = 0. \tag{17}$$

This means that starting from rest the particle is staying in rest respectively to comoving observer and follows the cosmological expansion as all matter averagely do.

If the particle has arbitrary initial velocity in $\theta = \pi/2$ plane then integrating (14) and (15) and using the interval (12) one can obtain the following expressions

$$\frac{ds}{dt} = Bu_1 r'^2 e^{-\frac{u_3}{u_1}\varphi} \tag{18}$$

$$\frac{ds}{dt} = Aru_3 \tag{19}$$

where A and B are arbitrary constants of integration.

$$\left(\frac{ds}{dt}\right)^2 = 1 - (u_1^2 + u_3^2) = 1 - u^2 \tag{20}$$

where $u_1 = r'dR/dt$ is observable velocity of the particle in radial direction, and $u_3 = rd\varphi/dt$ is observable orbital velocity.

Let us consider first the pure radial motion. Then putting $u_3 = 0$ in (18) and (20) we obtain

$$u_1 = \frac{1}{\sqrt{r'^4 + 1}}. \tag{21}$$

For the pure orbital motion one has $u_1 = 0$ and hence

$$u_3 = \frac{1}{\sqrt{r^2 + 1}}. \tag{22}$$

And finally the total velocity reads

$$u^2 = u_1^2 + u_3^2 = \frac{1}{r'^4 + 1} + \frac{1}{r^2 + 1} \tag{23}$$

Thus we have obtained the observable velocity of the test particle which would be measured by the observer being in rest in comoving coordinate frame with his usual instruments. From the expressions for the velocity it follows that even if the test particle has a nonzero initial orbital velocity it will lose its angular momentum with time and moreover will lose its total velocity and will be involved to the cosmological expansion. Yet another situation is possible when the particle falls into the black hole with total velocity tending to the speed of light. The profile of the total velocity in dependence on R and t is represented at fig.1.

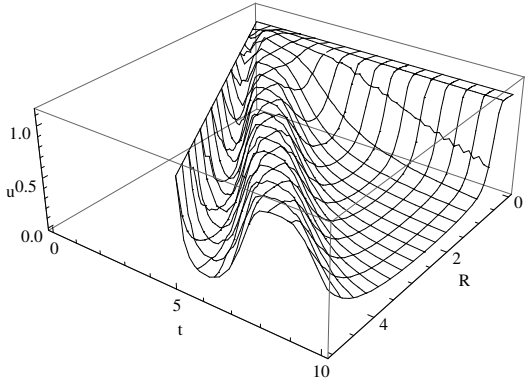

Figure 1. Total velocity profile of the test particle

4 CONCLUSIONS

To conclude one should say that the model under consideration answers the part of questions concerning the behaviour of the test particle moving in the space–time generated by the Schwarzschild–like black hole embedded into the dust matter cosmological background. On the basis of exact solution of the Einstein equations we have obtained the exact analytical expressions for the velocity of the particle, and it turned out that the total velocity of the particle tends to zero with time, that means that the particle will be involved to the cosmological expansion in case it was not traveling towards the center $R = 0$, in this case it would fall into the singularity. The specific character of the coordinate frame makes it impossible to analyze the questions concerning the black hole horizon. And some other interesting problems in this issue were also left for our future consideration.

ACKNOWLEDGEMENTS

The present work was supported by the Czech Grant MSM 4781305903.

REFERENCES

Faraoni, V. and Jacques, A. (2009), Cosmological expansion and local physics, *Phys. Rev. D*, **76**(6), p. 063510, arXiv: 0707.1350.

Firouzjaee, J. T. and Ellis, G. F. R. (2015a), Cosmic Matter Flux May Turn Hawking Radiation Off, *Gen. Rel. Grav.*, **47**(2), p. 6, arXiv: 1408.0778.

Firouzjaee, J. T. and Ellis, G. F. R. (2015b), Particle creation from the quantum stress tensor, *Phys. Rev. D*, **91**(10), p. 103002, arXiv: 1503.05020.

Firouzjaee, J. T. and Mansouri, R. (2010), Asymptotically FRW black holes, Gen. Relativity Gravitation, *Gen. Rel. Grav.*, **42**(10), pp. 2431–2452, arXiv: 0812.5108.

Firouzjaee, J. T. and Mansouri, R. (2012), Radiation from the LTB black hole, *Europhys. Lett.*, **97**, p. 29002, arXiv: 1104.0530.

Giddings, S. B. (2012), Black holes, quantum information, and unitary evolution, *Phys. Rev. D*, **85**(12), p. 124063, arXiv: 1201.1037.

Korkina, M. and Kopteva, E. (2012a), *The Mass Function Method*, Dnepropetrovsk National University Press, Dnepropetrovsk.

Korkina, M. and Kopteva, E. (2012b), The mass function method for obtaining exact solutions in General Relativity, *Space, Time and Fundamental Interactions*, **1**, pp. 38–47, arXiv: 1604.08247.

Krasinski, A. (1997), *Inhomogeneous Cosmological Models*, Cambridge University Press, Cambridge.

Misner, C. W. and Sharp, D. H. (1964), Relativistic equations for adiabatic, spherically symmetric gravitational collapse, *Phys. Rev.*, **136**(2B), p. B571.

Moradi, R., Firouzjaee, J. T. and Mansouri, R. (2010), Cosmological black holes: the spherical perfect fluid collapse with pressure in a FRW background, arXiv: 1504.04746v2.

Senovilla, J., Mars, M. and Vera, R. (1999), *Phys. World*, **20**, p. 1005.

Tolman, R. (1969), *Relativity Thermodynamics and Cosmology*, Oxford: Clarendon Press, Oxford.

Zannias, T. (1990), Spacetimes admitting a three-parameter group of isometries and quasilocal gravitational mass, *Phys. Rev. D.*, **41**, pp. 3252–3254.

Proceedings of *RAGtime 17–19, 17–19/23–26 Oct., 1–5 Nov., 2015/2016/2017, Opava, Czech Republic*
Z. Stuchlík, G. Török and V. Karas, editors, Silesian University in Opava, 2017, pp. 91–98

Magnetic field generated by current loop in flat spacetime

Martin Kološ

Institute of Physics, Faculty of Philosophy & Science, Silesian University in Opava,
Bezručovo nám. 13, CZ-746 01 Opava, Czech Republic
Martin.Kolos@fpf.slu.cz

ABSTRACT
Magnetic field generated by circular current loop located in flat spacetime is studied. Ampere's law has been solved using two different methods of expansions into infinite series: multipole expansion and power series expansion. Both infinite series solutions are compared with full analytic solution and their pros and cons are discusses.

Keywords: current loop – magnetic field – flat spacetime

1 INTRODUCTION

Gravitation and electromagnetisms are the only two long range forces important in astrophysics. Gravitational collapsed object - black hole can be well described by Kerr metric if we will assume electromagnetic field to be weak, i.e. stress-energy tensor for electromagnetic field does not contribute to the geometry of background spacetime. Any electric charge will be discharged quite quick for astrophysical compact object surrounded by plasma, so only magnetic field will remain in play. The exact shape and intensity of magnetic field surrounding the black hole (black hole magnetosphere) is still not yet properly resolved, but strong connection to the accretion processes is assumed (Meier, 2012). In this article we will focus on magnetic field generated by circular current loop, located in equatorial plane, as a model of toroidal current floating inside the accretion disks. We will focus on flat spacetime in this preliminary study only, but full relativistic approach will be used.

Our search for proper shape of black hole magnetosphere is motivated by our study of charged particle motion in vicinity of magnetized black hole (Kološ et al., 2015; Stuchlík and Kološ, 2016) where we have been using simple model of uniform magnetic field only, and now we are looking for more realistic magnetic field solution. It is known, that even weak magnetic field can have significant influence on the charged particles motion - all depend on test particle specific charge (particle charge to mass ratio). The "charged particle" can represent matter ranging from electron to some charged inhomogeneity orbiting in the innermost region of the accretion disk surrounding the black hole. To have a smooth

978-80-7510-257-7

charged particle trajectory, the spacetime metric and tensor of electromagnetic field must be sufficiently smooth in the region where the motion of particle occur. As we will see further, some magnetic field solutions are composed of two branches matched at some radii and hence does not meet smoothness criteria.

2 MAXWELL'S EQUATIONS

Gravity will not be included at this stage and the spacetime is flat with line element

$$\mathrm{d}s^2 = -\mathrm{d}t^2 + \mathrm{d}r^2 + r^2\,\mathrm{d}\theta^2 + r^2\sin^2\theta\,\mathrm{d}\phi^2. \tag{1}$$

Cartesian coordinates x, y, z can be obtained by the coordinate transformations

$$x = r\,\cos\phi\,\sin\theta, \quad y = r\,\sin\phi\,\sin\theta, \quad z = r\,\cos\theta. \tag{2}$$

Vectors and tensors can be expressed in local frame of reference using relations

$$A^{\widehat{\mu}} = \frac{\partial x^{\widehat{\mu}}}{\partial x^{\mu}} A^{\mu}, \qquad F^{\widehat{\mu}\widehat{\nu}} = \frac{\partial x^{\widehat{\mu}}}{\partial x^{\mu}}\frac{\partial x^{\widehat{\nu}}}{\partial x^{\nu}} F^{\mu\nu}, \tag{3}$$

where the local observer coordinates are

$$\mathrm{d}\widehat{t} = \mathrm{d}t, \quad \mathrm{d}\widehat{r} = \mathrm{d}r, \quad \mathrm{d}\widehat{\theta} = r\,\mathrm{d}\theta, \quad \mathrm{d}\widehat{\phi} = r\sin\theta\,\mathrm{d}\phi. \tag{4}$$

The metric $g_{\widehat{\mu}\widehat{\nu}}$ constructed by local observer coordinates has very simple form $g_{\widehat{\mu}\widehat{\nu}} = \mathrm{diag}(-1, 1, 1, 1)$ and vectors has $A^{\widehat{\mu}} = A_{\widehat{\mu}}$ for all $\mu \in \{r, \theta, \phi\}$.

Ampere's law from classical Maxwell's equations can be written as (Jackson, 1998)

$$\nabla \times \mathbf{B} = \mu_0 \mathbf{J}, \qquad (\mathbf{B} = \nabla \times \mathbf{A}), \tag{5}$$

where $\mathbf{B}$ is vector of magnetic field, $\mathbf{J}$ is vector of the current density and $\mathbf{A}$ is vector potential. Using Coulomb gauge $\nabla \cdot \mathbf{A} = 0$, the Ampere's law can be rewritten

$$\nabla^2 \mathbf{A} = \mu_0 \mathbf{J}, \qquad (\nabla \times (\nabla \times \mathbf{A}) = \nabla \cdot (\nabla \cdot \mathbf{A}) - \nabla^2 \mathbf{A} = \mu_0 \mathbf{J}). \tag{6}$$

In SI units we are using vacuum permeability μ_0, in Gaussian units one must substitute μ_0 with $4\pi/c$.

Relativistic formulation of Maxwell's equations in flat spacetime is

$$\partial_\alpha F_{\mu\nu} + \partial_\nu F_{\alpha\mu} + \partial_\mu F_{\nu\alpha} = 0, \qquad \partial_\alpha F^{\alpha\beta} = \mu_0 J^{\beta}. \tag{7}$$

where J^β is electric current four-vector. Electromagnetic tensor $F_{\mu\nu}$ is given by

$$F_{\mu\nu} = \partial_\mu A_\nu - \partial_\nu A_\mu, \tag{8}$$

where A^μ is electromagnetic four-vector. Assuming axial symmetry and absence of electric field, the only non-zero component of A^μ will be A^ϕ

$$A^\mu = (0, 0, 0, A^\phi), \quad A^\phi = A^\phi(r, \theta), \quad A_\phi = A^\phi\, r^2 \sin^2\theta = A^{\widehat{\phi}}\, r \sin\theta. \tag{9}$$

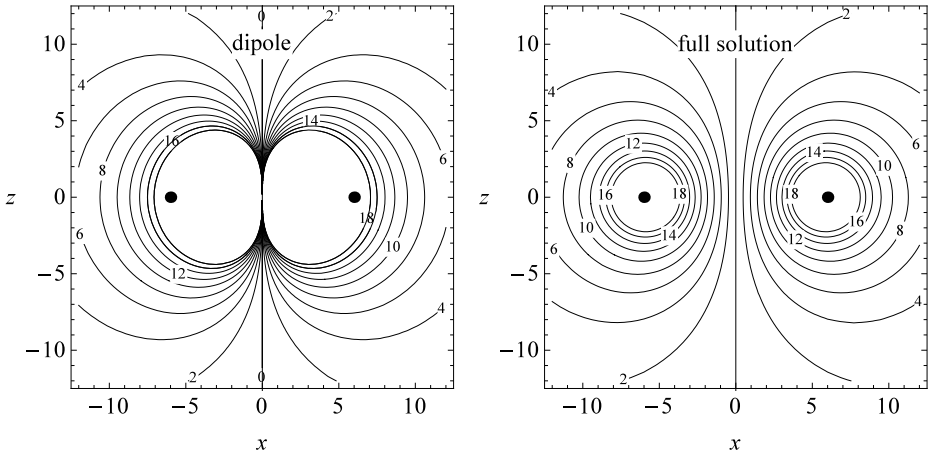

Figure 1. Shape of magnetic field lines around current loop with radius $a = 6$ in flat spacetime. Dipole approximation (left) and full analytic solution (right) are plotted.

The first of Maxwell's equations (7) is satisfied identically, while the second is giving the equation which we will be solving in this proceeding

$$r^2 \frac{\partial}{\partial r}\left(\frac{\partial}{\partial r} A_\phi\right) + \sin\theta \frac{\partial}{\partial \theta}\left(\frac{1}{\sin\theta}\frac{\partial}{\partial \theta} A_\phi\right) = -\mu_0 J^\phi r^4 \sin^2\theta. \tag{10}$$

We will call this equation Ampere's law, but it can be also wield as special case of Grad—Shafranov equation well known from MHD (Meier, 2012).

Magnetic field three-vector $\mathbf{B} = (B^{\widehat{r}}, B^{\widehat{\theta}}, B^{\widehat{\phi}})$ can be related to four-vector A_ϕ

$$B^{\widehat{r}} = \frac{A_{\phi,\theta}}{r^2 \sin\theta}, \quad B^{\widehat{\theta}} = -\frac{A_{\phi,r}}{r\sin\theta}, \quad B^{\widehat{\theta}} = 0. \tag{11}$$

Circular current loop with radius a is located in x-y plane (equatorial plane $\theta = \pi/2$). Although the current is created by moving charge, the loop itself is considered to be neutral. The current loop is given by current density J^μ, but due to symmetry, only J^ϕ component will be non-zero

$$J^\phi(r,\theta) = \frac{I}{r^2}\,\delta(r-a)\,\delta(\theta-\pi/2), \qquad \int J^{\hat{\phi}}\,\mathrm{d}\hat{r}\,\mathrm{d}\hat{\theta} = \int J^\phi r^2 \sin\theta\,\mathrm{d}r\,\mathrm{d}\theta = I. \tag{12}$$

where δ is Dirac delta function and the total current through r-θ plane (x-z plane) is normalized to I. Since the current density is given by delta functions $\delta(r-a)$ and $\delta(\theta-\pi)$, it is zero except for one point $r = a$ in equatorial plane. We will be looking for the solution of eq. (10) with the right side equal to zero, and the current existence will be important as boundary condition only.

3 SOLUTIONS OF MAXWELL'S EQUATIONS

In classical electromagnetism we could express the Ampere's law in integral form. The analytic solution for vector potential **A** can be found using

$$\mathbf{A}(\mathbf{x}) = \frac{\mu_0}{4\pi} \int \frac{\mathbf{J}(\tilde{\mathbf{x}})}{|\mathbf{x} - \tilde{\mathbf{x}}|} \, \mathrm{d}^3 \tilde{x}. \tag{13}$$

The exact solution for circular current loop can be found using complete elliptic integral of the first $K(m)$ and second $E(m)$ kind (Jackson, 1998)

$$A^{\widehat{\phi}}(r, \theta) = \mu_0 I a \, \frac{(2 - k^2)K(k^2) - 2E(k^2)}{\pi k^2 \sqrt{a^2 + 2ar \sin\theta + r^2}}, \quad k^2 = \frac{4ar \sin\theta}{a^2 + r^2 + 2ar \sin\theta}. \tag{14}$$

Far away from the current loop $r >> a$ ($\mathbf{x} \approx \tilde{\mathbf{x}}$) simpler expression can be found

$$A^{\widehat{\phi}}(r, \theta) = \frac{\mu_0 I a^2 r \sin\theta}{4r^3}, \qquad \mathbf{A} = \frac{\mu_0}{4\pi r^2} \frac{\mathbf{m} \times \mathbf{r}}{r}, \tag{15}$$

where **m** current loop magnetic dipole moment $\mathbf{m} = \pi I a^2 \mathbf{z}$, **z** is unit base vector in z direction and $4\pi r^2$ is the surface of a sphere with radius r.

Assuming the current J^{ϕ} to be completely zero (no current loop), there exist another very simple solution to the Ampere's law (10)

$$A^{\widehat{\phi}}(r, \theta) = \frac{B}{2} r \sin\theta = \frac{B}{2} x, \qquad B^{\widehat{r}} = B \cos\theta, \quad B^{\widehat{\theta}} = -B \sin\theta. \tag{16}$$

This form of vector potential $A^{\widehat{\phi}}$ represent uniform magnetic field with strength B oriented perpendicularly to the equatorial plane (Wald, 1974)

Magnetic field **B** is fully specified by electromagnetic four-potential A^{μ}, see eq (11). We can provide the exact form of magnetic field **B**, but it is more elegant to work with electromagnetic potential A^{μ} instead. Shape of magnetic field **B** can be easily plotted using contour lines of electromagnetic potential

$$A^{\widehat{\phi}}(r, \theta) = \text{const.} \tag{17}$$

For example for uniform magnetic field (16), equally spaced straight lines parallel to z axis can be obtained. For compassion the full analytic solution of vector potential (14) and its dipole approximation (15) are plotted in Fig. 1.

3.1 Multipole expansion

Using substitution $A_{\phi} = R(r) \cdot \Theta(\theta)$ for the electromagnetic four-potential A_{ϕ}, the Ampere's law (10) can be separated in two second order linear ordinary differential equations. The solution can be written as multipole expansion into spherical harmonics (Jackson, 1998)

$$A_{\phi} = \mu_0 J \sum_{n=0,2}^{\infty} \frac{\sqrt{\pi} \sin\theta \, P^1_{n+1}(0) \, Y^1_{n+1}(\theta, 0)}{\sqrt{(n+1)(n+2)(2n+3)}} \cdot \begin{cases} r^{n+2} \, a^{-n-1} & \text{for} \quad r \in (0, a) \\ a^{n+2} \, r^{-n-1} & \text{for} \quad r \in (a, \infty) \end{cases} \tag{18}$$

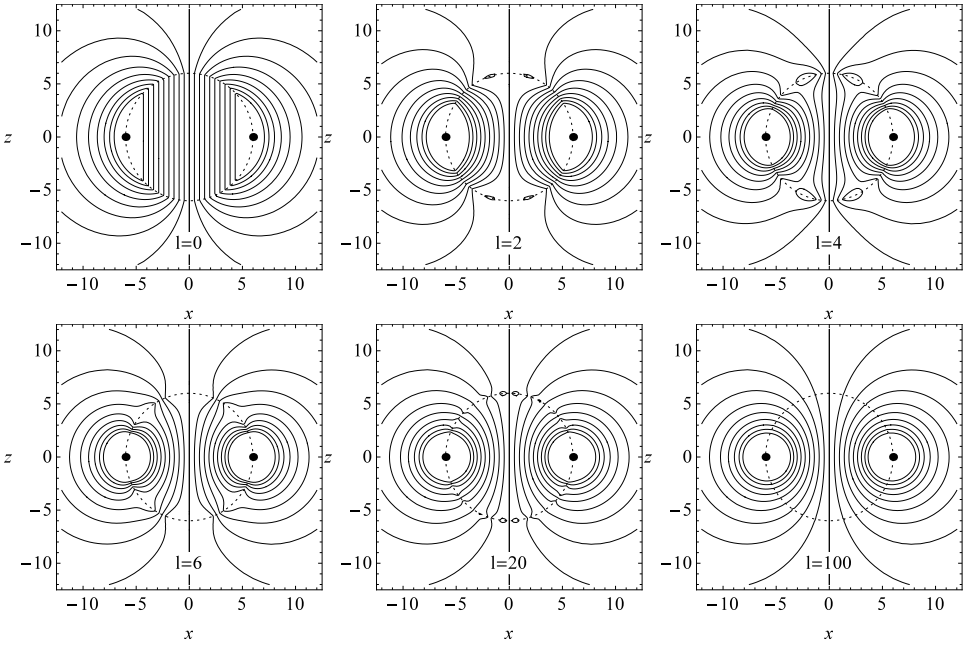

Figure 2. Current loop magnetic field shape for different orders of multipole expansion.

where $Y_n^1(\theta, 0)$ are Laplace's spherical harmonics (contains trigonometric functions) and $P_n^1(0)$ are associated Legendre polynomial (number coefficients). The same solution can be also expressed in different infinite series form (Petterson, 1974)

$$A_\phi = \frac{-\mu_0 J}{\sqrt{\pi}} \sum_{l=0,2}^{\infty} \mathrm{M}(l) \cdot \sin^2\theta \cdot \mathrm{C}_1^{\frac{3}{2}}(\cos\theta) \cdot \begin{cases} a^{-2l-3} r^{l+2} & \text{for} \quad r \in (0, a) \\ r^{-l-1} & \text{for} \quad r \in (a, \infty) \end{cases} \tag{19}$$

where $\mathrm{C}_1^{3/2}(\cos\theta)$ are Gegenbauer polynomials (special case of the Jacobi polynomials), $\Gamma(n)$ is Euler gamma function and the coefficients $\mathrm{M}(l)$ are given by

$$\mathrm{M}(l) = (-1)^{\frac{l+2}{2}} \frac{\left(l + \frac{3}{2}\right) \Gamma\left(\frac{1}{2} l + \frac{1}{2}\right)}{(l+2) \left(\frac{l}{2}\right)! \, (2l+3)} a^{l+2}. \tag{20}$$

Multipole expansion of A_ϕ consist of two parts: inner $r < a$ and outer $r > a$; only even terms will contribute to the sum while all odd terms are zero. While every each term of the infinite sum (18) is solution of (10) equation, the matching of inner and outer solution is not smooth for individual terms. Only if the total sum is taken into account, the discontinuity at sphere with radii $r = a$ will disappear. Magnetic fields for different terms of multipole expansions (18) are plotted in Fig. 2, where we clearly see how the discontinuity at $r = a$ radii disappear with increasing order of expansion and finally reaching the full analytic shape from Fig. 1.

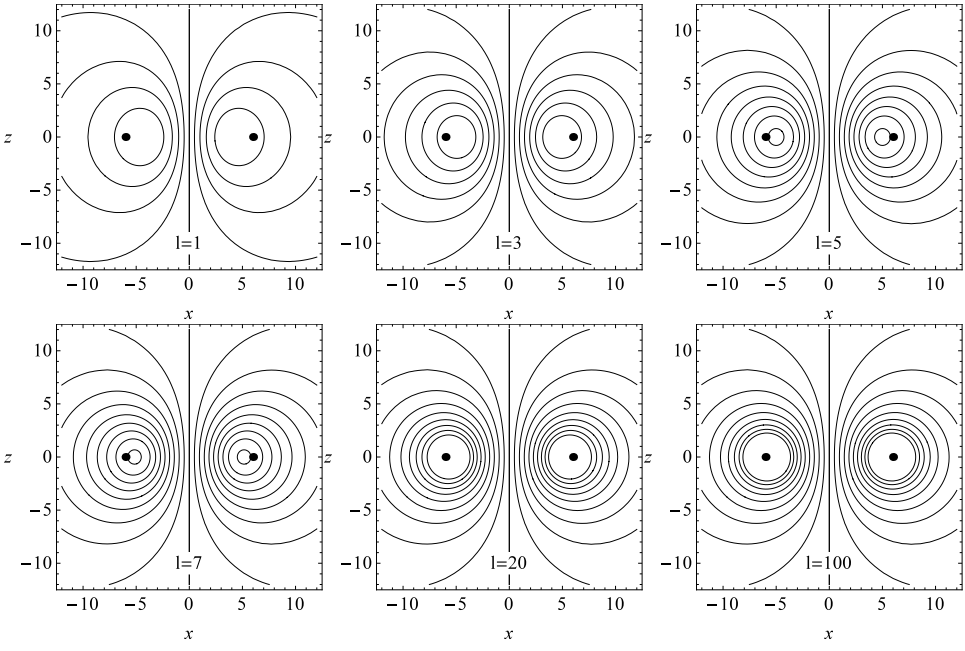

Figure 3. Current loop magnetic field shape for different orders of power series expansion.

Fist terms of the (18) and (19) series are

$$r \in (0,a) \quad A^{\widehat{\phi}} = \frac{\mu_0 J r \sin\theta}{4a} + \ldots \qquad r \in (a,\infty) \quad A^{\widehat{\phi}} = \frac{\mu_0 J a^2 \sin\theta}{4r^2} + \ldots \tag{21}$$

As we can see, the first term stands for uniform magnetic field ($B = \mu_0 J/2a$) in the case of inner solution $r < a$, while dipole field in the case of outer solution $r > a$.

3.2 Power series expansion

An alternative expansion was mentioned in (Jackson, 1998). Using powers series expansion, the solution to the (10) equation can be written as

$$A_{\phi(n)}(r,\theta) = \frac{\mu_0 J}{2} \sum_{l=1,2}^{n} \frac{\pi\left[(-1)^{n+1}+1\right](2n)!}{(n!)^2\,\Gamma\left(-\frac{n}{2}\right)^2\Gamma(n+2)} \cdot \frac{(ar\sin\theta)^{n+1}}{\left(a^2+r^2\right)^{n+\frac{1}{2}}} \tag{22}$$

where $\Gamma(n)$ is Euler gamma function and $n \to \infty$. All even terms are zero and only odd terms will contribute to the sum. Fist terms of the (22) expansions are

$$A^{\widehat{\phi}}(r,\theta) = \frac{\mu_0 J a^2 r \sin\theta}{4\left(a^2+r^2\right)^{3/2}} + \frac{15\mu_0 J a^4 r^3 \sin^3\theta}{32\left(a^2+r^2\right)^{7/2}} + \frac{315\mu_0 J a^6 r^5 \sin^5\theta}{256\left(a^2+r^2\right)^{11/2}} + \ldots \tag{23}$$

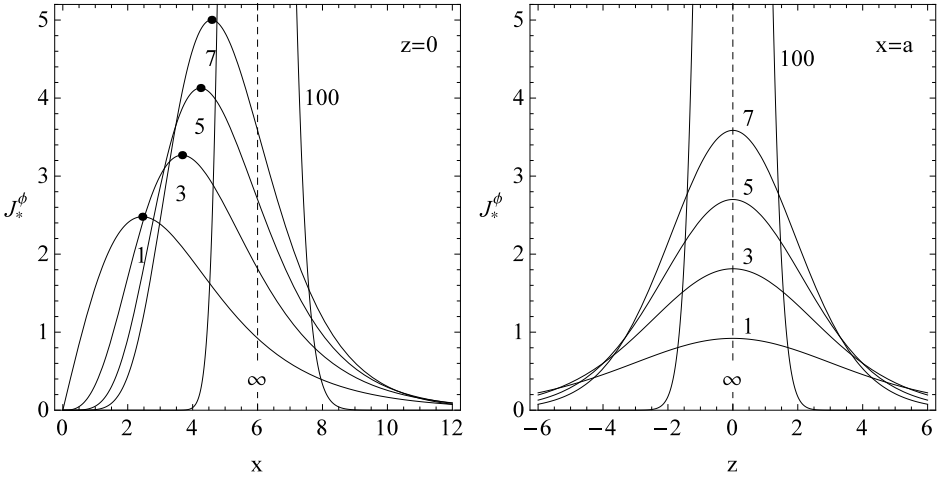

Figure 4. Different modes of current density $J^{\phi}_{*(n)}(r,\theta)$ for power series expansion (22).

While any individual term of (22) expansion are smooth function of r and θ coordinates, only the total sum A_ϕ is solution of (10) equation with current (12). Individual terms of (22) expansion are solutions of (12) equation with current J^ϕ not in thin steep delta function shape, but given by

$$J^{\widehat{\phi}}_{(n)}(r,\theta) = \frac{2a^3 I}{\sqrt{\pi}} \frac{\Gamma\left(n+\frac{5}{2}\right)}{\Gamma\left(\frac{n+1}{2}\right)\Gamma\left(\frac{n+3}{2}\right)} \frac{(ar\sin\theta)^n}{(a^2+r^2)^{n+\frac{5}{2}}}. \tag{24}$$

The current distribution $J^{\phi}_{*(n)}$ has been already summed up. The maximum of the current distribution function $J^{\phi}_{*(n)}(r,\theta)$, for individual term n of power expansion (22), is located in equatorial plane and below the actual current loop position a

$$r_{\max(n)} = a\sqrt{n}/\sqrt{n+5}, \quad \theta_{\max(n)} = \pi/2. \tag{25}$$

Also maximum of the electromagnetic four-potential $A^\phi(r,\theta)$ is shifted below the actual position of the current loop and its peak value is level down.

Magnetic field shape for different terms in power series expansion (22) is plotted in Fig. 3. As we can see, even the first term of power series expansion (22) is in very good agreement with the full analytic solution (14), if you are not close to position of the current loop. Contrary to the multipole expansion (18), the terms of power expansion are smooth and suitable for charged particle trajectory calculation.

4 CONCLUSIONS

The physics is the art of neglecting and hence in many physical models only the most relevant first terms of expansion are taken into account. Let assume, that the black hole magnetosphere has been generated by toroidal currents inside the accretion disk. With multipole expansion (18) we could use uniform magnetic field when we study charged particle motion below (inside) the current loop, while dipole magnetic field when studying particle moving above (outside) the loop.

Simple model of relativistic jet as a stream of charged particles escaping the inner parts of accretion disk along uniform magnetic filed lines has been studied in (Stuchlík and Kološ, 2016). More realistic black hole magnetosphere then simple uniform one should be considered, for example magnetosphere generated by toroidal current at radius a. But in multipole expansion the charged particle escaping from inner region of accretion disk (below the current loop) to infinity (above the current loop) will feel the discontinuity at sphere $r = a$. On the contrary, the power series expansion (22) is smooth everywhere and hence much more suitable for this charged particle jet model.

Multiple expansion of magnetic filed generated by current loop in black hole background has been already studied in literature, see summary in (Pejcha, 2014). This contribution has been done for flat spacetime only, focusing on power series expansion (22) and descriptive figures. In flat spacetime the full analytic solution si known and hence we can easily draw a comparisons of both multipole and power expansions with full analytic solution. We are now working on the magnetic field power series expansion, but in the Schwarzschild black hole spacetime.

ACKNOWLEDGEMENTS

The present work was supported by the GAČR grant No. 16-03564Y.

REFERENCES

Jackson, J. D. (1998), *Classical electrodynamics*, ISBN 047130932X.

Kološ, M., Stuchlík, Z. and Tursunov, A. (2015), Quasi-harmonic oscillatory motion of charged particles around a Schwarzschild black hole immersed in a uniform magnetic field, *Classical and Quantum Gravity*, **32**(16), 165009, arXiv: 1506.06799.

Meier, D. L. (2012), *Black Hole Astrophysics: The Engine Paradigm*.

Pejcha, J. (2014), *Magnetická pole proudových smyček kolem černých děr*, B.S. Thesis, MFF Charles University, Prague, Czech Republic.

Petterson, J. A. (1974), Magnetic field of a current loop around a Schwarzschild black hole, *Phys. Rev. D*, **10**, pp. 3166–3170.

Stuchlík, Z. and Kološ, M. (2016), Acceleration of the charged particles due to chaotic scattering in the combined black hole gravitational field and asymptotically uniform magnetic field, *European Physical Journal C*, **76**, 32, arXiv: 1511.02936.

Wald, R. M. (1974), Black hole in a uniform magnetic field, *Phys. Rev. D*, **10**, pp. 1680–1685.

Proceedings of *RAGtime 17–19, 17–19/23–26 Oct., 1–5 Nov., 2015/2016/2017, Opava, Czech Republic*
Z. Stuchlík, G. Török and V. Karas, editors, Silesian University in Opava, 2017, pp. 99–110

Comparison of charged particle dynamics around compact object immersed into uniform or dipole magnetic field

Martin Kološ[1,a] and Arman Tursunov[1,b]

[1]Institute of Physics, Faculty of Philosophy & Science, Silesian University in Opava, Bezručovo nám. 13, CZ-746 01 Opava, Czech Republic
[a]Martin.Kolos@fpf.slu.cz [b]Arman.Tursunov@fpf.slu.cz

ABSTRACT
We compare charge particle dynamics around magnetized compact object for two different configurations of magnetic field, uniform magnetic field and dipole magnetic field. Comparing charged particle trajectories, position of circular orbits and frequencies of small harmonic oscillations in both magnetic fields, we will try to answer the question if the dipole magnetic field can be approximated by uniform magnetic field at last at small scales.

Keywords: charged particle – black holes – uniform magnetic field – dipole magnetic field

1 INTRODUCTION

Magnetic fields plays very important role in astrophysics as they have been detected and measured in nearly all celestial objects. We consider weak magnetic fields that will satisfy test field approximation - have negligible effect on background spacetime or on the motion of neutral particles. However, for the motion of charged test particles the influence of the magnetic field can be really large. For a charged test particle with charge q and mass m moving in vicinity of a black hole with mass M surrounded by an external asymptotically uniform magnetic field of the strength B, one can introduce a dimensionless quantity b that can be identified as relative Lorenz force (Frolov and Shoom, 2010)

$$b = \frac{|q|BGM}{mc^4}. \tag{1}$$

This quantity can be quite large even for weak magnetic fields due to the large value of the specific charge q/m, and the influence of the magnetic field on the motion of charged particles cannot be neglected even for weak magnetic fields. In our approach the "charged particle" can represent matter ranging from electron to some charged inhomogeneity orbiting in the innermost region of the accretion disk. The charged particle specific charges q/m for any such structure will then range from the electron maximum to zero.

978-80-7510-257-7

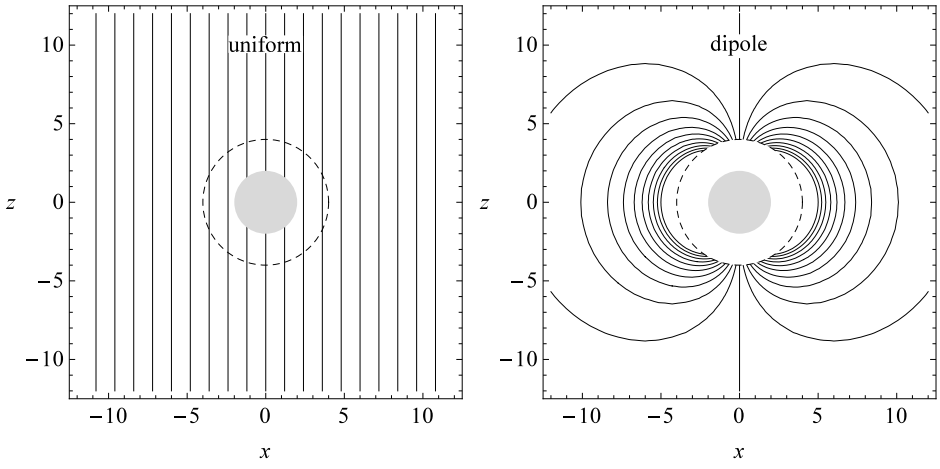

Figure 1. Magnetic field lines for magnetic uniform and dipole fields around Schwarzschild black hole. Uniform magnetic field structure is quite simple - the magnetic field lines are parallel and equally spaced. Dipole magnetic field structure is more complicated and the magnetic field intensity is increasing close to the compact object. Dipole magnetic field is generated by circular current loop with radius $a = 4$, hence magnetic field lines for $2 < r < 4$ are not plotted. The gray disc with radius $r = 2$ represent Schwarzschild black hole horizon, we also plotted dashed circle with radius $r = 4$ representing neutron star surface.

In this paper we will concentrate our attention on two particular cases of magnetized compact object: asymptotically uniform external magnetic field known as Wald solution (Wald, 1974) and relativistic version of dipole magnetic field generated by current loop (Petterson, 1974). Charged particle dynamics in both magnetic filed scenarios has been already widely studied in literature; for example for the uniform magnetic field in (Kopáček et al., 2010; Kološ et al., 2015; Tursunov et al., 2016), while for the dipole magnetic field in (Kovář et al., 2008; Bakala et al., 2010, 2012). The dipole magnetic field configuration is assumed to be much more relevant for neutron stars, while for black holes we can use the uniform field configuration.

Throughout the present paper we use the spacelike signature $(-,+,+,+)$, and the system of geometric units in which $G = 1 = c$.

2 CHARGED PARTICLE DYNAMICS

We describe dynamics of a charged particle with charge $q \neq 0$ in the vicinity of the Schwarzschild black hole embedded in magnetic field, using Lorentz equation and Hamiltonian formalism, and we compare both approachers.

The gravity will enter to the equations of motion through Schwarzschild black hole (with mass M) spacetime line element

$$\mathrm{d}s^2 = -\left(1-\frac{2M}{r}\right)\mathrm{d}t^2 + \left(1-\frac{2M}{r}\right)^{-1}\mathrm{d}r^2 + r^2(\mathrm{d}\theta^2 + \sin^2\theta\mathrm{d}\phi^2). \tag{2}$$

We consider first case of magnetic field which is uniform at the spatial infinity, having strength B there. The field is oriented perpendicularly to the equatorial plane of the black hole spacetime. The only nonzero covariant component of the electromagnetic four-vector potential A^μ takes the form (Wald, 1974)

$$A^{\mathrm{U}}_\phi = \frac{B}{2}\, g_{\phi\phi}. \tag{3}$$

Dipole magnetic field will be generated by circular current loop with radius $a \geq 2$, located on the surface of compact object in equatorial plane. Outer $r > a$ solution for four-vector potential A^μ in Schwarzschild metric is given by only one nonzero covariant component of the electromagnetic four-vector potential (Petterson, 1974)

$$A^{\mathrm{D}}_\phi = -k\left[\ln\left(1-\frac{2M}{r}\right) + \frac{2M}{r}\left(1+\frac{M}{r}\right)\right] g_{\phi\phi}, \tag{4}$$

where the term in square brackets is negative for $r > 2$.

Both uniform and dipole magnetic fields are static, have axial symmetry, and the only nonzero covariant component of four-vector potential A^μ can be written as

$$A^{(U,D)}_\phi = \text{const.}\, f(r)\, g_{\phi\phi}. \tag{5}$$

For uniform magnetic field the $f(r)$ function is quite simple $f^{\mathrm{U}}(r) = 1$, while for dipole magnetic fields the $f(r)$ function is little bit complicated

$$f^{\mathrm{D}}(r) = -\ln\left(1-\frac{2M}{r}\right) - \frac{2M}{r}\left(1+\frac{M}{r}\right). \tag{6}$$

The function $f(r)$ is positive for any $r > 2$.

Hereafter, we put $M = 1$, i.e., we use dimensionless radial coordinate r (and time coordinate t). Cartesian coordinates can be found by the coordinate transformations

$$x = r\cos(\phi)\sin(\theta), \quad y = r\sin(\phi)\sin(\theta), \quad z = r\cos(\theta). \tag{7}$$

The equations of motion for charged particle with charge q and mass m in magnetized Schwarzschild black hole spacetime are given by the Lorentz equation and velocity norming condition

$$\frac{\mathrm{d}u^\mu}{\mathrm{d}\tau} + \Gamma^\mu_{\alpha\beta}u^\alpha u^\beta = \frac{q}{m}g^{\mu\rho}F_{\rho\sigma}u^\sigma, \qquad g_{\mu\nu}u^\mu u^\nu = -1, \tag{8}$$

where $u^\mu = dx^\mu/d\tau$ is the four-velocity of the particle, $\Gamma^\mu_{\alpha\beta}$ are Christoffel symbols for Schwarzschild metric 2 and $F_{\mu\nu}$ is tensor of electromagnetic field, given by

$$\Gamma^\mu_{\alpha\beta} = \frac{1}{2}g^{\mu\gamma}\left(g_{\gamma\alpha,\beta} + g_{\gamma\beta,\alpha} - g_{\alpha\beta,\gamma}\right), \quad F^{\mu\nu} = \partial^\mu A^\nu - \partial^\nu A^\mu. \tag{9}$$

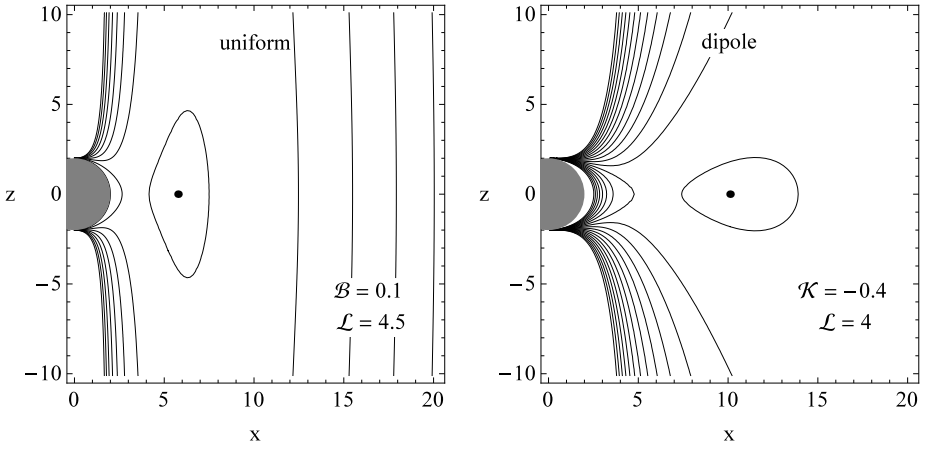

Figure 2. Effective potential for charged particle motion around black hole immersed into uniform (left) or dipole (right) magnetic fields.

The Lorentz equation (8) is set of four second order ordinary differential equations. The main advantage of Lorentz equation is that we can clearly see the Lorentz force $f^{\mu}_{L} = (q/m)F^{\mu\nu}u_{\nu}$ acting on the charged particle.

The equations of motion for charged particle can be also obtained using Hamiltonian formalism

$$\frac{\mathrm{d}x^{\mu}}{\mathrm{d}\zeta} = \frac{\partial H}{\partial \pi_{\mu}}, \quad \frac{\mathrm{d}\pi_{\mu}}{\mathrm{d}\zeta} = -\frac{\partial H}{\partial x^{\mu}}, \qquad H = \frac{1}{2}g^{\alpha\beta}(\pi_{\alpha} - qA_{\alpha})(\pi_{\beta} - qA_{\beta}) + \frac{m^2}{2} = 0, \tag{10}$$

where the kinematical four-momentum $p^{\mu} = mu^{\mu} = \mathrm{d}x^{\mu}/\mathrm{d}\zeta$ is related to the generalized (canonical) four-momentum π^{μ} by the relation $\pi^{\mu} = p^{\mu} + qA^{\mu}$. The affine parameter ζ of the particle is related to its proper time τ by the relation $\zeta = \tau/m$. The Hamiltonian equations (10) is set of eight first order ordinary differential equations. The main advantage of Hamiltonian formalism is the possibility to use very precise numerical integration scheme (symplectic integrator) (Kopáček et al., 2014).

Due to the symmetries of the Schwarzschild spacetime (2) and both uniform and dipole magnetic field (3-4), one can easily find the conserved quantities that are particle energy and axial angular momentum

$$\mathcal{E} = \frac{E}{m} = -\frac{\pi_t}{m} = -g_{tt}u^t, \quad \mathcal{L} = \frac{L}{m} = \frac{\pi_{\phi}}{m} = g_{\phi\phi}u^{\phi} + \frac{q}{m}A_{\phi}. \tag{11}$$

Using such symmetries one can rewrite the Hamiltonian (10) in the form

$$H = \frac{1}{2}g^{rr}p_r^2 + \frac{1}{2}g^{\theta\theta}p_{\theta}^2 + \frac{1}{2}g^{tt}E^2 + \frac{1}{2}g^{\phi\phi}(L - qA_{\phi})^2 + \frac{1}{2}m^2 = H_{\mathrm{D}} + H_{\mathrm{P}}, \tag{12}$$

where we separated total Hamiltonian H into dynamical H_{D} (first two terms) and potential H_{P} (last two terms) parts.

We will define new particle and magnetic field parameters: particle specific charge $\tilde{q}$, and magnetic parameters for uniform $\mathcal{B}$ and dipole $\mathcal{K}$ magnetic fileds

$$\tilde{q} = \frac{q}{m} \qquad \mathcal{B} = \frac{qB}{2m}, \qquad \mathcal{K} = -\frac{qk}{m}. \tag{13}$$

Energetic boundary for particle motion can be expressed from the equation (12)

$$\mathcal{E}^2 = V_{\rm eff}(r,\theta) \quad (\text{for } p_r = p_\theta = 0), \tag{14}$$

We introduced effective potential for charged particle $V_{\rm eff}(r,\theta)$ by the relation

$$\begin{aligned} V_{\rm eff}(r,\theta) &\equiv -g_{tt}\left[g^{\phi\phi}\left(\mathcal{L} - \tilde{q}A_\phi\right)^2 + 1\right] \\ &= \left(1 - \frac{2}{r}\right)\left[\left(\frac{\mathcal{L}}{r\sin(\theta)} - K\,f(r)\,r\sin(\theta)\right)^2 + 1\right], \end{aligned} \tag{15}$$

where magnetic field constants $K \in \{\mathcal{B}, \mathcal{K}\}$ stands $\mathcal{B}$ for uniform and $\mathcal{K}$ for dipole magnetic field, the function $f(r)$ specify the exact magnetic field radial behaviour (5). The effective potential $V_{\rm eff}(r,\theta)$ combine the influence of gravity potential (first term) with the influence of central force potential given by the specific angular momentum $\mathcal{L}$ and electromagnetic potential energy (terms in square brackets). The effective potential (15) shows clear symmetry $(\mathcal{L}, K) \leftrightarrow (-\mathcal{L}, -K)$, hence from now on we will focus on $\mathcal{L} > 0$ case only. The positive angular momentum of a particle $\mathcal{L} > 0$ means that the particle is revolved in the counter-clockwise motion around the black hole in x-y plane. Example of effective potential $V_{\rm eff}(r,\theta)$ behaviour can be found in Fig. 2.

For charged particle we distinguish two following situations

- *Lorentz attractive* (minus configuration), here $K < 0$ - magnetic field and angular momentum parameters have opposite signs and the Lorentz force is attracting the charged particle to the z-axis, towards the black hole.
+ *Lorentz repulsive* (plus configuration), here $K > 0$ - magnetic field and angular momentum parameters have the same signs and the Lorentz force is repulsive, acting outward the black hole.

For uniform magnetic field, if charge of the particle is taken to be positive $q > 0$, the minus configuration $K < 0$ corresponds to the vector of the magnetic field $\boldsymbol{B}$ pointing downwards, while plus configuration $K > 0$ corresponds to the vector of the magnetic field $\boldsymbol{B}$ pointing upwards the z-axis.

3 CIRCULAR ORBITS AND ISCO

Particles on circular orbits around compact object can form Keplerian accretion disk, with its inner edge given by innermost circular orbit (ISCO). The circular orbit parameters and ISCO position can be determined by examination of effective potential $V_{\rm eff}(r,\theta)$ function.

The stationary points of the effective potential $V_{\rm eff}(r,\theta)$ function are given by

$$\partial_r V_{\rm eff}(r,\theta) = 0, \quad \partial_\theta V_{\rm eff}(r,\theta) = 0. \tag{16}$$

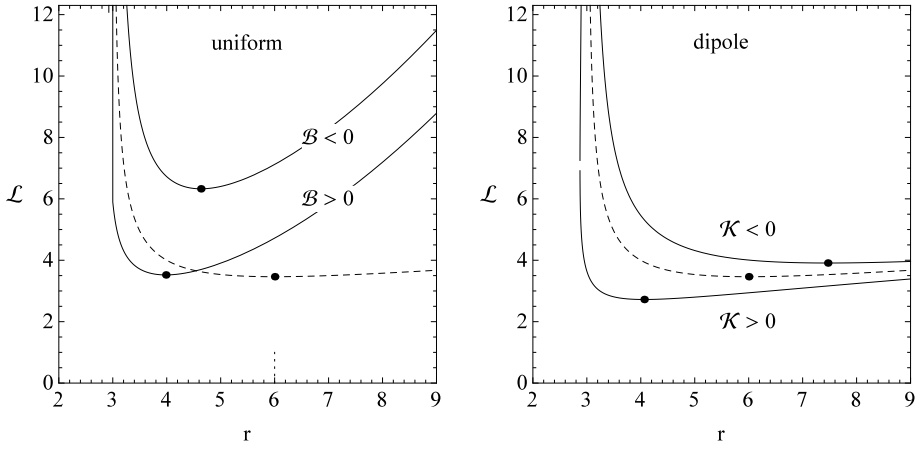

Figure 3. Specific axial angular momentum $\mathcal{L}_{\rm E}(r)$ for charged particle on circular orbit in magnetic field, as function of radial coordinate r. The non-magnetic case is given as dashed curve, the black point are located at minima of $\mathcal{L}_{\rm E}(r)$ function and represents radial position of ISCO.

The second equation in the extrema condition (16) has one root at $\theta = \pi/2$. In another words, there is extrema of the $V_{\rm eff}(r,\theta)$ function located in the equatorial plane. The first equation in the extrema condition (16) leads to a quadratic equation with respect to the specific angular momentum $\mathcal{L}$

$$(r-3)\mathcal{L}^2 + X\mathcal{L} - Y = 0, \tag{17}$$

where functions X, Y are given by

$$X = Kr^2\left[(r-2)rf' + 2f\right], \quad Y = K^2r^4 f\left[(r-2)rf' + (r-1)f\right] + r^2. \tag{18}$$

Real roots of radial coordinate $r > 2$ from eq. (17) determine maxima, minima and inflex points of the $V_{\rm eff}(r, \theta = \pi/2)$ function. Such extrema give stable (minima) and unstable (maxima) equilibrium positions for the circular particle motion, i.e. stable or unstable circular orbits. The inflex points give the marginally stable circular orbits. The solutions of quadratic equation (17) determine the specific angular momentum $\mathcal{L}_{\rm E\pm}(r)$ for any circular orbit with radial coordinate r

$$\mathcal{L}_{\rm E\pm}(r) = \frac{-X \pm \sqrt{X^2 + 4Y(r-3)}}{2(r-3)} \tag{19}$$

The angular momentum $\mathcal{L}_{\rm E\pm}(r)$ function is plotted for uniform and dipole magnetic fields in Fig. 3. One can clearly see the biggest difference between uniform and magnetic field in equatorial plane. The effect of uniform magnetic became more visible with large radii r, because the magnetic field is constant for any r and does not disappear at infinity. The dipole magnetic field gets weaker as one is departing from the generating current loop

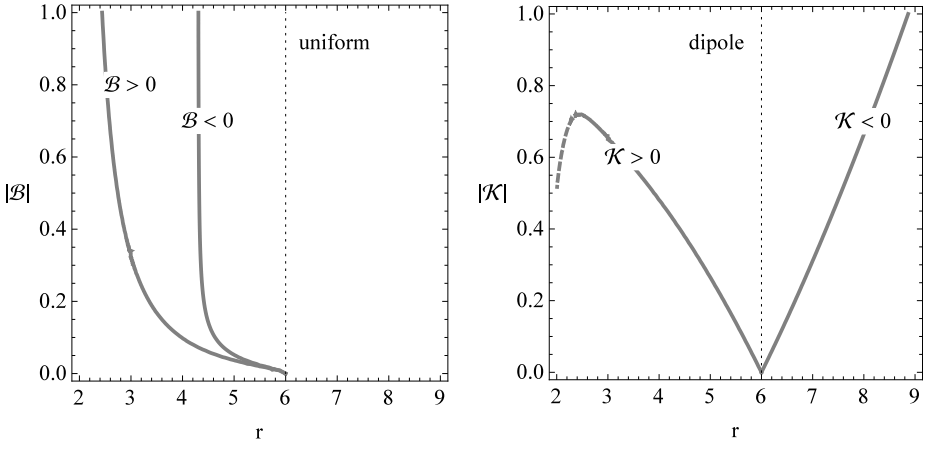

Figure 4. Charged particle ISCO for different values of magnetic field parameters $\mathcal{B}, \mathcal{K}$.

which should be located close to the origin of coordinates but above Schwarzschild horizon, the dipole magnetic field disappear at infinity $r \to \infty$.

The local extrema of the $\mathcal{L}_{\mathrm{E}\pm}(r)$ function (19) determine the innermost stable circular orbits (ISCO). The ISCO radial position for charged particle moving around black hole strongly depends on the magnetic field, see Fig. 4. For uniform magnetic field the charged particle ISCO position is decreasing for both attracting ($\mathcal{B} < 0$) or repulsing ($\mathcal{B} > 0$) Lorentz force configurations. Even for relatively small magnetic field parameter $\mathcal{B} = \pm 0.05$ the ISCO radii is shifted from from $6M$ to $5M$ in the geometrized units. For dipole magnetic field, the charged particle ISCO position is sifted towards to the black hole for attracting Lorentz force ($\mathcal{K} < 0$), while for repulsive Lorentz force ($\mathcal{K} > 0$) the ISCO position is shifted away from black hole.

4 ANY MAGNETIC FIELD IS UNIFORM AT SMALL SCALES

As numerical simulations shows, realistic magnetic field around compact object with accretion disk will be probably quite complicated. The question arise, if one can substitute this realistic magnetic field by some simple analytic solution, at last for large scales. In this article we will focus on much simpler situation. We will try to substitute dipole magnetic field, as model of complicated magnetic field, with the uniform magnetic field.

Any smooth function can be approximated in neighborhood of some point by linear function using Taylor expansion. We can expand complicated dipole magnetic field into uniform magnetic field at given point, just by assuming to have the the same value of Lorentz force there. We give an example of charged particle moving in dipole and uniform magnetic field where the initial conditions and strength of Lorentz force was set to be the same in both dipole and uniform field cases. In Fig. 5. the particle trajectory will stay close

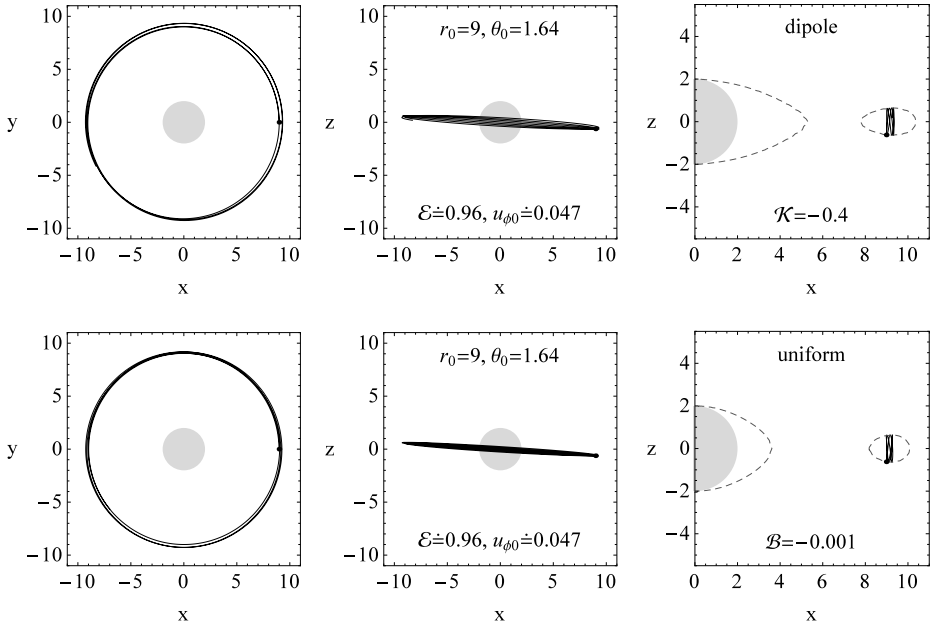

Figure 5. Charged particle trajectory around Schwarzschild black hole with dipole or uniform magnetic filed. Particle initial conditions and strength of Lorentz force are set to be the same in both cases.

to its initial point, because we are close to the effective potential minima. In this case the charged particle trajectory in dipole magnetic field can be well approximated by particle moving in uniform magnetic filed. In Fig. 6. the situation is completely different, since the charged particle in dipole field is exploring large areas below and above equatorial plane, where it will feel the dipole field inhomogeneities. In this situation the approximation by uniform field will valid only for very short time.

Dipole/uniform magnetic field substitution is then possible only for charged particle oscillating around its circular orbit.

5 HARMONIC OSCILLATIONS IN MAGNETIC FIELD

If a charged test particle is slightly displaced from the equilibrium position located in a minimum of the effective potential $V_{\rm eff}(r,\theta)$ at r_0 and $\theta_0 = \pi/2$, corresponding to a stable circular orbit, the particle will start to oscillate around the minimum realizing thus epicyclic motion governed by linear harmonic oscillations. For harmonic oscillations around the minima of the effective potential $V_{\rm eff}$, the evolution of the displacement coordinates $r = r_0 + \delta r, \theta = \theta_0 + \delta\theta$ is governed by the equations

$$\ddot{\delta r} + \omega_{\rm r}^2\,\delta r = 0, \quad \ddot{\delta\theta} + \omega_\theta^2\,\delta\theta = 0, \tag{20}$$

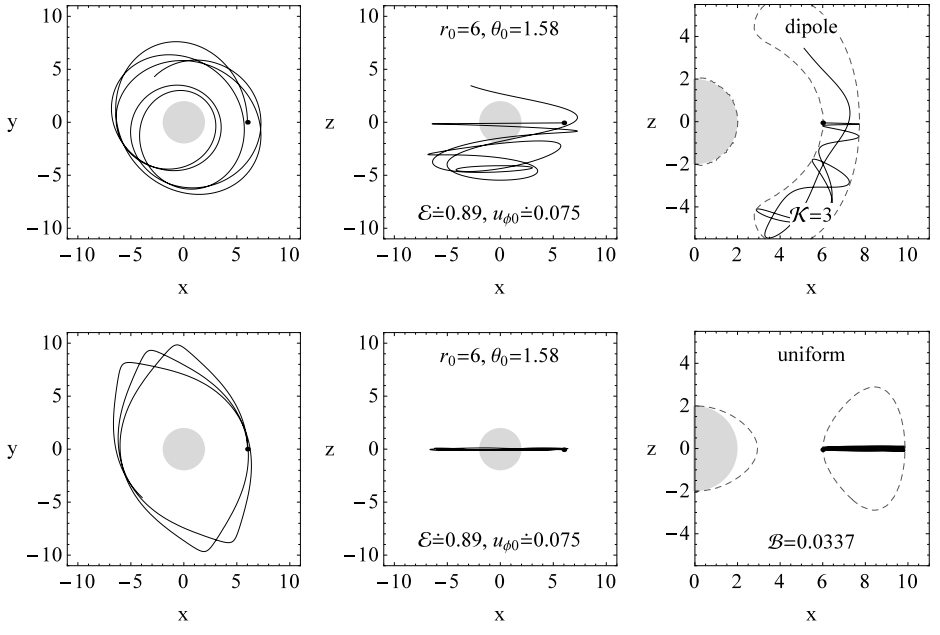

Figure 6. Charged particle trajectory around Schwarzschild black hole with dipole or uniform magnetic filed. Particle initial conditions and strength of Lorentz force are set to be the same in both cases.

where dot denotes derivative with respect to the proper time τ of the particle ($\dot{x} = \mathrm{d}x/\mathrm{d}\tau$), and locally measured angular frequencies of the harmonic oscillatory motion are given by

$$\omega_{\mathrm{r}}^2 = \frac{1}{g_{rr}}\frac{\partial^2 H_{\mathrm{P}}}{\partial r^2}, \quad \omega_\theta^2 = \frac{1}{g_{\theta\theta}}\frac{\partial^2 H_{\mathrm{P}}}{\partial \theta^2}, \quad \omega_\phi = \frac{\mathrm{d}\phi}{\mathrm{d}\tau} = \mathcal{L}g^{\phi\phi} - Kf(r), \tag{21}$$

where we added also the Keplerian (axial) frequency ω_ϕ. We will not put explicit

The locally measured angular frequencies $\omega_{\mathrm{r}}, \omega_\theta$, and ω_ϕ, given by $\omega_\beta = \mathrm{d}\diamond_\beta/\mathrm{d}\tau$ where $\beta \in \{\mathrm{r}, \theta, \phi\}$, are connected to the angular frequencies measured by the static distant observers (in the physical units) by the gravitational redshift transformation

$$\nu_\beta = \frac{1}{2\pi}\frac{c^3}{GM}\frac{\mathrm{d}\diamond_\beta}{\mathrm{d}t} = \frac{1}{2\pi}\frac{c^3}{GM}\frac{\omega_\beta}{-g^{tt}\mathcal{E}(r)}. \tag{22}$$

Behaviour of the frequencies $\nu_{\mathrm{r}}(r), \nu_\theta(r)$ and $\nu_\phi(r)$, as functions of the radial coordinate r, is demonstrated in Fig. 7 for both dipole and uniform magnetic field. For small radii, $r \geq r_{\mathrm{ISCO}}$, we see strong gravitational influence on the angular frequencies in both dipole and uniform cases. For large radii $r \gg r_{\mathrm{ISCO}}$ the influence of the uniform magnetic field is prevailing, while the influence of the dipole magnetic field is fading away and the frequencies are coinciding with non-magnetic case.

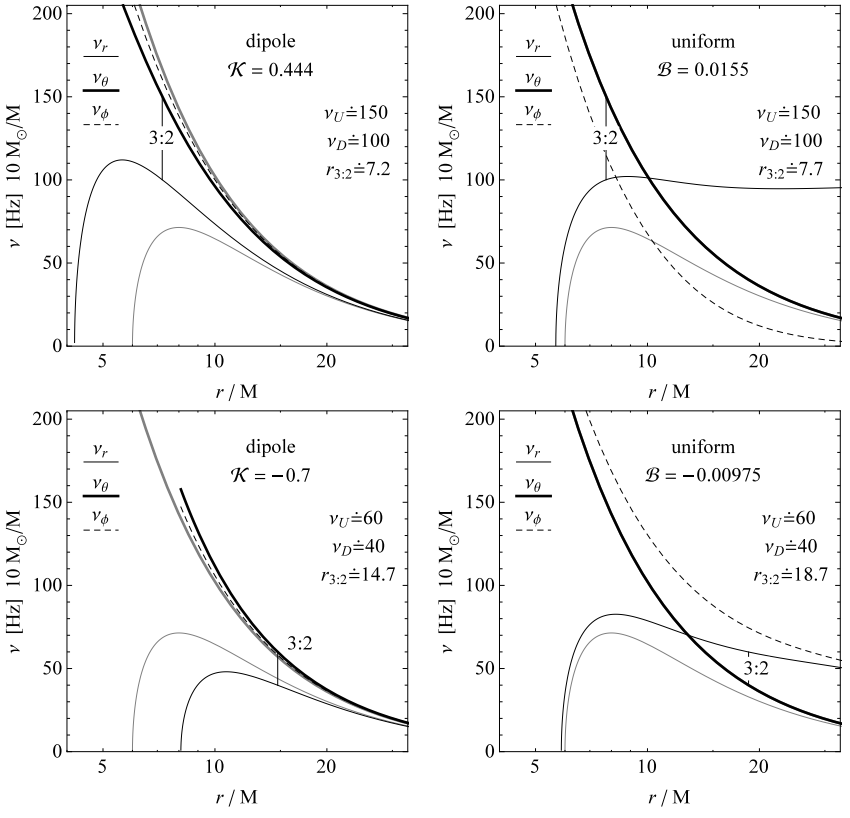

Figure 7. Frequencies $\nu_\theta, \nu_r, \nu_\phi$ of small harmonic charge particle oscillations around magnetized Schwarzschild black hole as measured by static distant observers. One can easily substitute the effect of dipole magnetic field (left figures) with uniform magnetic field (right figures). The black curves are for magnetic case, while the non-magnetic (neutral) case is given by grey curves.

The charged particle oscillations with frequencies $\nu_r(r), \nu_\theta(r)$ and $\nu_\phi(r)$, suggest interesting astrophysical application, related to quasi-periodic oscillations (QPOs) observed in many Galactic Low Mass X-Ray Binaries (LMXB) containing neutron stars or black holes (Bakala et al., 2010; Kološ et al., 2015). According to the observed frequencies of QPOs, which cover the range from few mHz up to 0.5 kHz, different types of QPOs were distinguished. These are the high frequency (HF) and low frequency (LF) QPOs in the timing spectra with frequencies up to 500 Hz and up to 30 Hz, respectively. The HF QPOs are sometimes detected with the twin peaks (upper $f_{\rm up}$ and lower $f_{\rm low}$) which have frequency ratio close to 3 : 2. The simplest geodesic QPOs model is epicyclic resonance (ER) model (Török et al., 2005), where the two resonant modes are identified to be the radial ν_r and vertical ν_θ epicyclic frequencies

$$f_{\rm up} = \nu_{\rm up} \equiv \nu_\theta, \quad f_{\rm low} = \nu_{\rm low} \equiv \nu_r, \quad \nu_{\rm up} : \nu_{\rm low} = 3 : 2, \tag{23}$$

The frequency commensurability is crucial ingredient of the resonant model, and a particular case of this commensurability occurs for the parametric (internal) resonant phenomena that become strongest in the case of the 3 : 2 frequency ratio

The open question is, if we can once again substitute the influence of complicated magnetic field (dipole), with the simple uniform magnetic field. To fit the observed QPOs frequencies $f_{\rm up}$ and $f_{\rm low}$, for compact object with mass M, one must change the dipole magnetic field parameter $\mathcal{K}$ in functions $\nu^{\rm D}_{\rm up}(r_{\rm D}, \mathcal{K}, M), \nu^{\rm D}_{\rm low}(r_{\rm D}, \mathcal{K}, M)$ and hence obtain required frequencies for 3:2 resonant radii $r_{\rm D}$. Frequencies at resonant radii $r_{\rm D}$ for dipole magnetic field with parameter $\mathcal{K}$ can be substituted by frequencies at resonant radii $r_{\rm U}$ for uniform magnetic field $\nu^{\rm U}_{\rm up}(r_{\rm U}, \mathcal{B}, M), \nu^{\rm U}_{\rm low}(r_{\rm U}, \mathcal{B}, M)$ with parameter $\mathcal{B}$ using equations

$$\nu^{\rm D}_{\rm up}(r_{\rm D}, \mathcal{K}, M) = \nu^{\rm U}_{\rm up}(r_{\rm U}, \mathcal{B}, M), \quad \nu^{\rm D}_{\rm low}(r_{\rm D}, \mathcal{K}, M) = \nu^{\rm U}_{\rm low}(r_{\rm U}, \mathcal{B}, M). \tag{24}$$

Examples of frequencies substitution for dipole/uniform magnetic field is show in Fig. 7 for both Lorentz attractive and repulsive cases.

6 CONCLUSIONS

Magnetic field can strongly influence astrophysical processes around compact object. If the specific particle charge q/m is large enough, even weak magnetic field can significantly influence position of Keplerian accretion disc inner edge, the charged particle trajectory and charge particle oscillatory frequencies.

Real magnetic field around compact object will be far away from to be completely uniform, but any magnetic field can be approximated by uniform at last at small scales. Such magnetic field simplification for charged particle motion will work only if the particle trajectory will remain in small region of space. When the particle trajectory will move away from vicinity of its initial position, it will start to feel magnetic field inhomogeneity.

We tested charged particle motion in two magnetic filed configurations: in dipole magnetic field, as representation of complicated filed, and in uniform magnetic field. The charged particle ISCO behave differently for dipole or uniform field: for dipole field the ISCO is increasing or decreasing with the field strength, depending on direction of Lorentz force; for uniform filed is the ISCO always decreasing. Charged particle QPOs frequencies for dipole magnetic field can be substituted by frequencies calculated for uniform magnetic field.

ACKNOWLEDGEMENTS

The present work was supported the Czech Science Foundation Grant No. 16-03564Y.

REFERENCES

Bakala, P., Urbanec, M., Šrámková, E., Stuchlík, Z. and Török, G. (2012), On magnetic-field-induced corrections to the orbital and epicyclic frequencies: paper II. Slowly rotating magnetized neutron stars, *Classical and Quantum Gravity*, **29**(6), 065012.

Bakala, P., Šrámková, E., Stuchlík, Z. and Török, G. (2010), On magnetic-field-induced non-geodesic corrections to relativistic orbital and epicyclic frequencies, *Classical and Quantum Gravity*, **27**(4), 045001.

Frolov, V. P. and Shoom, A. A. (2010), Motion of charged particles near a weakly magnetized Schwarzschild black hole, *Phys. Rev. D* , **82**(8), 084034, arXiv: 1008.2985.

Kološ, M., Stuchlík, Z. and Tursunov, A. (2015), Quasi-harmonic oscillatory motion of charged particles around a Schwarzschild black hole immersed in a uniform magnetic field, *Classical and Quantum Gravity*, **32**(16), 165009, arXiv: 1506.06799.

Kopáček, O., Karas, V., Kovář, J. and Stuchlík, Z. (2010), Transition from Regular to Chaotic Circulation in Magnetized Coronae near Compact Objects, *The Astrophysical Journal* , **722**, pp. 1240–1259, arXiv: 1008.4650.

Kopáček, O., Karas, V., Kovář, J. and Stuchlík, Z. (2014), Application of a symplectic integrator in a non-integrable relativistic system, in Z. Stuchlík, G. Török and T. Pecháček, editors, *RAGtime 10-13: Workshops on black holes and neutron stars*, pp. 123–132.

Kovář, J., Stuchlík, Z. and Karas, V. (2008), Off-equatorial orbits in strong gravitational fields near compact objects, *Classical and Quantum Gravity*, **25**(9), 095011, arXiv: 0803.3155.

Petterson, J. A. (1974), Magnetic field of a current loop around a Schwarzschild black hole, *Phys. Rev. D* , **10**, pp. 3166–3170.

Török, G., Abramowicz, M. A., Kluźniak, W. and Stuchlík, Z. (2005), The orbital resonance model for twin peak kHz quasi periodic oscillations in microquasars, *Astronomy and Astrophysics* , **436**, pp. 1–8.

Tursunov, A., Stuchlík, Z. and Kološ, M. (2016), Circular orbits and related quasi-harmonic oscillatory motion of charged particles around weakly magnetized rotating black holes, *Phys. Rev. D* , **93**(8), 084012, arXiv: 1603.07264.

Wald, R. M. (1974), Black hole in a uniform magnetic field, *Phys. Rev. D* , **10**, pp. 1680–1685.

Proceedings of *RAGtime 17–19, 17–19/23–26 Oct., 1–5 Nov., 2015/2016/2017, Opava, Czech Republic*
Z. Stuchlík, G. Török and V. Karas, editors, Silesian University in Opava, 2017, pp. 111–118

New exact solutions for Schwarzschild-like black holes

Elena Kopteva[1,a] Irina Bormotova[1,2] and Maria Korkina[3]

[1]Institute of Physics, Faculty of Philosophy & Science, Silesian University in Opava, Bezručovo nám. 13, CZ-746 01 Opava, Czech Republic
[2]Bogoliubov Laboratory of Theoretical Physics, Joint Institute for Nuclear Research, 141980 Dubna, Moscow region, Russia
[3]Oles Honchar Dnepropetrovsk National University, Gagarina ave. 72, 49010 Dnepropetrovsk, Ukraine
[a]ekopterix@gmail.com

ABSTRACT
We use the so called mass function method for obtaining new exact solutions for Schwarzschild-like black holes. The mass function is algebraic invariant for general spherically symmetric metric. Rewriting Einstein equations in terms of mass function we consider Schwarzschild-like black holes. We show that Schwarzschild black holes should necessarily contain non-baryonic matter. We furthermore obtain new exact solutions for the black hole embedded into the dust matter universe.

Keywords: Scwarzschild-like lack hole – exact solutions of Einstein equations – black hole immersed in dust medium

1 INTRODUCTION

The mass function (MF) is algebraic invariant for spherically symmetric metric (Narlikar and Karmarkar, 1949). For the interval of general form

$$\mathrm{d}s^2 = e^{\nu(R,t)}\mathrm{d}t^2 - e^{\lambda(R,t)}\mathrm{d}R^2 - r^2(R,t)\mathrm{d}\sigma^2 \tag{1}$$

the MF is defined as follows

$$m(R,t) = r(R,t)\left(1 + e^{-\nu(R,t)}\dot{r}^2 - e^{-\lambda(R,t)}r'^2\right), \tag{2}$$

where prime means $\partial/\partial R$, and dot means $\partial/\partial t$; here and further $c = 1$, $\mathrm{d}\sigma^2$ is a standard metric on 2-sphere.

978-80-7510-257-7

Using MF it is possible to rewrite the Einstein equations in simpler way:

$$m' = \varepsilon r^2 r', \tag{3}$$

$$\dot{m} = -p_{\parallel} r^2 \dot{r}, \tag{4}$$

$$2\dot{r}' = \nu' \dot{r} + \dot{\lambda} r', \tag{5}$$

$$2\dot{m}' = m' \frac{\dot{r}}{r'} \nu' + \dot{m} \frac{r'}{\dot{r}} \dot{\lambda} - 4 r \dot{r} r' p_{\perp}. \tag{6}$$

where ε is energy density, including $8\pi\gamma/c^4$(so that it has a dimension of cm^{-2}), $p_{\parallel}$ is radial pressure, $p_{\perp}$ is tangent pressure ($T_2^2 = -p_{\perp}$) also in cm^{-2}. In the system (3)–(6) the equation (3) corresponds to the equation for T_0^0: $R_0^0 - R/2 = \varepsilon$, the equation (4) corresponds to the one for T_1^1, the equation (5), is in fact a condition of comoving frame $T_0^1 = 0$, the equation (6) follows from the equation for T_2^2.

2 SOLUTIONS FOR THE SCHWARZSCHILD-LIKE BLACK HOLES

Here we consider the class of static spherically-symmetric solutions in curvature coordinates (Gautreau, 1984):

$$\mathrm{d}s^2 = e^{\nu(r)} \mathrm{d}t^2 - e^{\lambda(r)} \mathrm{d}r^2 - r^2 \mathrm{d}\sigma^2. \tag{7}$$

For this metric MF reads

$$m(r) = r\left(1 - e^{-\lambda(r)}\right). \tag{8}$$

And the energy density in this case according to (3) will be

$$\varepsilon(r) = \frac{m'(r)}{r^2}. \tag{9}$$

Let us take anisotropic fluid as a source. Thus we have the stress-energy tensor with following nonzero components: $T_0^0 = \varepsilon$, $T_1^1 = -p_{\parallel}$, $T_2^2 = T_3^3 = -p_{\perp}$.

In order to obtain an exact solution for the case under consideration we will fix the coordinate conditions as follows:

$$e^{\nu(r)} = e^{-\lambda(r)}. \tag{10}$$

Taking into account (10) and (8) one can rewrite the metric (7)

(11)

Einstein equations for the components T_0^0 and T_1^1 under condition (10) will lead to the equality

$$T_0^0 = T_1^1, \tag{12}$$

that means that the radial pressure is always negative $p_{\parallel} = -T_1^1$. Thus one can conclude that under condition (10) the space-time (11) always contains non-baryonic matter.

Let us now consider the stress-energy conservation law $T^{\mu}_{\nu;\mu} = 0$ which is more suitable here than the rest equation for T^2_2. For the case under consideration one has

$$\frac{\partial}{\partial r}T^1_1 + \frac{2}{r}T^1_1 + \frac{2}{r}T^2_2 = 0, \tag{13}$$

here we take into account that $T^2_2 = T^3_3$ for the spherical symmetry. Substituting radial pressure expressed from (9) and (12) into (13) one has for the tangent pressure:

$$T^2_2 = \frac{m''(r)}{2r} = -p_{\perp}. \tag{14}$$

So all the metric coefficients and nonzero components of the stress-energy tensor are expressed in terms of the MF and its derivatives. The state equation in this case (under condition (12)) will be the relation between radial and tangent parts of pressure, and it will completely define the solution.

The metric (8) allows different types of solutions concerning their physical properties.

(1) Under $m(r) < r$ for all r $(0 < r < \infty)$ these solutions describe the only R-region. As far as radial pressure is negative these solutions can possibly describe the spherical configurations with "dark energy".

(2) Under $m(r) > r$ for all r the solutions describe the T-region only. For example the state equation $T^2_2 = \frac{r}{2}T^1_1$ leads to the following T-solution:

$$\mathrm{d}s^2 = \left(\frac{r_0}{t}e^{\frac{t}{r_0}} - 1\right)^{-1}\mathrm{d}t^2 - \left(\frac{r_0}{t}e^{\frac{t}{r_0}} - 1\right)\mathrm{d}r^2 - t^2\mathrm{d}\sigma^2, \tag{15}$$

where r_0 is an arbitrary constant.

(1) If the metric coefficients $e^{\nu(r)}$ and $e^{\lambda(r)}$ are alternating functions the solutions will describe the Schwarzschild-like black holes. Let us suppose that the following equality is valid

$$T^2_2 = \beta T^1_1, \tag{16}$$

where β is an arbitrary constant. From (9) and (14) under condition (16) one obtains the following equation for the MF

$$m''(r) - 2\beta m'(r)\frac{1}{r} = 0, \tag{17}$$

which has the solution

$$m(r) = C_1\frac{r^{2\beta+1}}{2\beta+1} + C_2. \tag{18}$$

Let us choose the constants to be $C_2 = r_g$ ($r_g = \frac{2\gamma M}{c^2}$ is Schwarzschild radius), $\frac{C_1}{2\beta+1} = A$ $(2\beta + 1 \neq 0)$, and rewrite the MF

$$m(r) = r_g + Ar^{2\beta+1}. \tag{19}$$

$\beta = 1$ in (19) gives either de Sitter solution under $r_g = 0$ or the Kottler solution under nonzero r_g. If $\beta = -1$ there will be Reissner-Nordstrem solution. If $\beta = \frac{1}{2}$ one will have the solution obtained in (Mannheim, 2006; Grumiller, 2010) which describe the Rindler space-time which is actively discussed last time concerning the interior of black holes (Culetu, 2012a,b). The case of $\beta = -\frac{1}{2}$ is a special, it gives $e^{-\lambda} = 1 - \frac{r_g}{r} - \frac{r_0}{r} \ln \frac{r}{r_0}$.

For all $\beta \neq -\frac{1}{2}$ it is possible to write the solution in general form

$$ds^2 = \left(1 - \frac{r_g}{r} - \sum_i A_i r^{2\beta_i}\right) dt^2 - \left(1 - \frac{r_g}{r} - \sum_i A_i r^{2\beta_i}\right)^{-1} dr^2 - r^2 d\sigma^2. \tag{20}$$

Here we take into account the additivity of MF. If one has several sources, their contributions to the metric coefficients in (20) will be summarised (under supposition of weak interaction between the sources $\varepsilon = \sum_i \varepsilon_i$, $p = \sum_i p_i$)

The physical sense of different β is not obvious. But in (Fernando, 2012) the black hole was considered surrounded by quintessence that corresponds to $\beta = -\frac{1}{3}$. The problem of investigation of the general properties of such black holes is a question of our further great interest.

3 THE SOLUTIONS FOR THE BLACK HOLES ON THE DUST MATTER BACKGROUND

The problem of building a model of the black hole that embedded into space which is not empty but filled with some matter is of great interest in wide set of research directions.

One of the pioneer works in this direction is the paper by McVittie (McVittie, 1933) were the solution was obtained in the following form

$$ds^2 = \left[\frac{1 - r_g\mu(t)/4R}{1 + r_g\mu(t)/4R}\right]^2 dt^2 - \frac{1}{\mu^2(t)}\left[1 + \frac{r_g\mu(t)}{4R}\right]^4 \left(dR^2 + R^2 d\sigma^2\right). \tag{21}$$

If $\mu(t) = \text{const} = 1$ the expression (21) will give the Schwarzschild metric in isotropic coordinates. Under $r_g = 0$ the metric (21) takes the form

$$ds^2 = dt^2 - \frac{1}{\mu^2(t)}\left(dR^2 + R^2 d\sigma^2\right), \tag{22}$$

that can be treated as a Friedman model for the flat space case. Depending on the choice of $\mu(t)$ it can be either dust model or the model with nonzero pressure. McVittie proposed his solution pretending to be a model of the massive particle in the expanding universe. But in papers (Nolan, 1998; McClure and Dyer, 2006) it was shown that this solution is unsuitable for the point mass in the universe, although it may possibly be used to describe the black hole.

To study the physical point of the solution (21) we will find the expression for the MF for it:

$$m(R,t) = r_g + R^3 \frac{\dot{\mu}^2(t)}{\mu^5(t)}\left(1 + \frac{r_g}{4R}\mu(t)\right)^6. \tag{23}$$

From here one has $m = r_g$ under $\dot{\mu}(t) = 0$, i.e. the MF for the Schwarzschild solution. And under condition $r_g = 0$ and $\frac{\dot{\mu}^2(t)}{\mu^5(t)} = \text{const} \equiv \frac{1}{a_0^2}$ one has the MF for the Friedman solution for the dust. Let us find using 3 and 4 the energy density and pressure for the metric (21):

$$\varepsilon(t) = 3\frac{\dot{\mu}^2(t)}{\mu^2(t)},$$
$$p(R,t) = 6\mu^3(t)\frac{r_g/4R}{\left(r_g/4R\right) - 1}. \tag{24}$$

From the expressions (23) and (24) it is clear that the solution (21) can describe neither point mass nor the black hole in the Friedman space-time (as far as pressure depends on R and t).

The solutions that were obtained in papers (Faraoni and Jacques, 2009; Thakurta, 1981; Sultana and Dyer, 2005), are in fact the modifications of the solution (21). So the solution from (Faraoni and Jacques, 2009) is (21) with metric coefficients near dR^2 and $d\sigma^2$ multiplied by some function of time. The solution from (Thakurta, 1981; Sultana and Dyer, 2005) is (21) with $\mu(t) = \text{const}$ and metric coefficients near dR^2 and $d\sigma^2$ also multiplied by function of time. Analogous consideration of these solutions using the MF method shows that they also describe neither point mass nor the black hole in the Friedman or even Tolman-Bondi space-time because the pressure in them depends both on R and t.

Using the MF method we will now build the model for the black hole embedded into Tolman-Bondi universe.

Tolman-Bondi metric for the spherically-symmetric dust distribution in comoving frame (which is synchronous for the dust) has the form:

$$\mathrm{d}s^2 = \mathrm{d}t^2 - \frac{r'^2(R,t)}{f^2(R)}\mathrm{d}R^2 - r^2(R,t)\mathrm{d}\sigma^2, \tag{25}$$

Three types of the Tolman solution are well known:

Hyperbolic ($f^2(R) > 1$):

$$r(R,t) = \frac{m(R)}{f^2(R) - 1}\sinh^2\frac{\alpha}{2},$$
$$t - t_0(R) = \pm\frac{m(R)}{2(f^2(R) - 1)^{3/2}}(\sinh\alpha - \alpha). \tag{26}$$

Elliptic ($f^2(R) < 1$):

$$r(R,t) = \frac{m(R)}{1 - f^2(R)}\sin^2\frac{\alpha}{2},$$
$$t - t_0(R) = \frac{m(R)}{2(1 - f^2(R))^{3/2}}(\alpha - \sin\alpha). \tag{27}$$

Parabolic($f^2(R) = 1$):

$$r(R,t) = \left[\pm\frac{3}{2}\sqrt{m(R)}(t - t_0(R))\right]^{\frac{2}{3}}. \tag{28}$$

$m(R)$, $f(R)$ and $t_0(R)$ are three arbitrary functions of the solutions. $f(R)$ has the meaning of total energy in mc^2 units in the shell $R = \text{const}$; $m(R)$ is a total mass in the shell $R = \text{const}$:

$$m = \int_0^R \frac{8\pi\gamma}{A^4}\varepsilon(R,t)r^2(R,t)\frac{\partial r}{\partial R}\mathrm{d}R. \tag{29}$$

The Schwarzschild solution is a particular case of the Tolman-Bondi solution under $m(R) = r_g$. The Friedman solution comes from the Tolman-Bondi solution under certain choice of arbitrary functions, for example for the flat case one has $m(R) = a_0R^3$, $f(R) = 1$, $t_0(R) = 0$.

Thus the solution for the Schwarzschild-like black hole in the Tolman-Bondi space-time will be the Tolman-Bondi solution with combined MF:

$$m(R) = r_g + m_F(R). \tag{30}$$

Thus the solution for the flat Friedman world with embedded Schwarzschild black hole will have the form

$$r(R,t) = \left[\pm\frac{3}{2}\sqrt{r_g + a_0R^3}(t - t_0(R))\right]^{\frac{2}{3}}. \tag{31}$$

One should notice that (31) does not describe the pure Friedman world. This is the Tolman-Bondi world with the same MF as in the Friedman solution because $t_0(R)$ can not be zero for the flat Schwarzschild solution (unlike $t_0(R) = 0$ for Friedman).

The solution obtained in (Changjun, 2011)

$$r(R,t) = \left[\frac{3}{2}\left(\sqrt{a_0R^3} + \sqrt{r_g}\right)t + R^{\frac{3}{2}}\right]^{\frac{2}{3}}. \tag{32}$$

has in round brackets the sum of two correspondent expressions for the Friedman and Schwarzschild space-time with chosen $t_0(R) = -R^{3/2}a_0$. The MF for this solution reads

$$m(R) = a_0R^3 + r_g + 2\sqrt{a_0r_g}R^{3/2}. \tag{33}$$

And thus this is black hole in some specific space-time with MF (33) but not in universe filled with dust.

Supposing in (27) $f(R) = \cos R$ as for the closed Friedman solution and taking MF as $m(R) = r_g + a_0\sin^3 R$ one has

$$\begin{aligned} r(R,t) &= \frac{r_g + a_0\sin^3 R}{\sin^2 R}\sin^2\frac{\alpha}{2}, \\ t - t_0(R) &= \frac{r_g + a_0\sin^3 R}{2\sin^3 R}(\alpha - \sin\alpha). \end{aligned} \tag{34}$$

Similarly for (26) choosing $f(R) = \cosh R$ and $m(R) = r_g + a_0 \sinh^3 R$ one obtains

$$r(R,t) = \frac{r_g + a_0 \sinh^3 R}{\sinh^2 R} \sinh^2 \frac{\alpha}{2},$$
$$t - t_0(R) = \frac{r_g + a_0 \sinh^3 R}{2 \sinh^3 R}(\sinh \alpha - \alpha). \tag{35}$$

So by means of the MF method we have obtained new exact solutions (32), (34), (35) for the black hole on the dust background for the flat, closed and open cases respectively.

4 CONCLUSIONS

In this paper exact solutions for the empty space were considered from the point of view of the mass function method. The generalized solutions for the Schwarzschild-like black holes were obtained. It was shown that such black holes necessarily contain non-baryonic matter.

The problem of constructing the model of the black hole in non-empty space was investigated. It was shown why the known solutions pretending to describe such model are not consistent with the model itself. New exact solutions for the black hole embedded into the dust universe were obtained.

ACKNOWLEDGEMENTS

This work is supported by the Grant of the Plenipotentiary Representative of the Czech Republic in JINR under Contract No. 189 from 29/03/2016.

REFERENCES

Changjun, G. (2011), Black Holes in the Universe: Generalized Lemaitre-Tolman-Bondi Solutions, *Phys. Rev. D*, **84**, p. 104047, arXiv: 1110.6708.

Culetu, H. (2012a), Rindler-type geometry inside a black hole, *Phys. Lett.*, **A376**, pp. 2817–2821, arXiv: 1103.2645.

Culetu, H. (2012b), Time dependent embedding of spherically symmetric Rindler-like spacetime, *Class. Quant. Grav.*, **29**, p. 235021, arXiv: 1202.4296.

Faraoni, V. and Jacques, A. (2009), Cosmological expansion and local physics, *Phys. Rev. D*, **76**(6), p. 063510, arXiv: 0707.1350.

Fernando, S. (2012), Schwarzschild black hole surrounded by quintessence: Null geodesics, *Gen. Rel. Grav.*, **44**, pp. 1857–1879, arXiv: 1202.1502.

Gautreau, R. (1984), Curvature coordinates in cosmology, *Phys. Rev. D*, **29**(2), pp. 186–197, URL http://link.aps.org/doi/10.1103/PhysRevD.29.186.

Grumiller, D. (2010), Model for gravity at large distances, *Phys. Rev. Lett.*, **105**, pp. 211–303, arXiv: 1011.3625.

Mannheim, P. D. (2006), Alternatives to dark matter and dark energy, *Prog. Part. Nucl. Phys.*, **56**, pp. 340–445, arXiv: astro-ph/0505266.

McClure, M. L. and Dyer, C. C. (2006), Asymptotically Einstein-de Sitter cosmological black holes and the problem of energy conditions, *Class. Quant. Grav.*, **23**, pp. 1971–1987.

McVittie, G. C. (1933), The mass-particle in an expanding universe, *Mon. Not. Roy. Astron. Soc.*, **93**, pp. 325–339.

Narlikar, J. V. and Karmarkar, K. R. (1949), The scalar invariants of a general gravitational metric, *Proceedings of the Indian Academy of Sciences*, **29**(2), pp. 91–97.

Nolan, B. C. (1998), A Point mass in an isotropic universe: Existence, uniqueness and basic properties, *Phys. Rev. D*, **58**, p. 064006, arXiv: gr-qc/9805041.

Sultana, J. and Dyer, C. C. (2005), Cosmological black holes: A black hole in the Einstein-de Sitter universe, *Gen. Rel. Grav.*, **37**, pp. 1347–1370.

Thakurta, S. N. G. (1981), Kerr metric in an expanding universe, *Indian J. Phys.*, **55B**, pp. 304–310.

Proceedings of *RAGtime 17–19, 17–19/23–26 Oct., 1–5 Nov., 2015/2016/2017, Opava, Czech Republic*
Z. Stuchlík, G. Török and V. Karas, editors, Silesian University in Opava, 2017, pp. 119–125

Analytical solution for charged fluid pressure profiles - circulation in combined electromagnetic field

Jiří Kovář[1,a], Petr Slaný[1], Zdeněk Stuchlík[1],
Vladimír Karas[2] and Audrey Trova[3]

[1]Institute of Physics, Faculty of Philosophy and Science, Silesian University in Opava,
Bezručovo nám. 13, 746 01 Opava, Czech Republic
[2]Astronomical Institute, Academy of Sciences, Boční II, 141 31 Prague, Czech Republic
[3]Center of Applied Space Technology and Microgravity (ZARM),
University of Bremen, 28359 Bremen, Germany
[a]jiri.kovar@fpf.slu.cz

ABSTRACT
We introduce a general transformation leading to an integral form of pressure equations characterizing equilibrium configurations of charged perfect fluid circling in strong gravitational and combined electromagnetic fields. The transformation generalizes our recent analytical treatment applicable to electric or magnetic fields treated separately along with the gravitational one. As an example, we present a particular solution for a fluid circling close to a charged rotating black hole immersed in an asymptotically uniform magnetic field.

Keywords: Charged perfect fluid – toroidal structures – compact objects – spacetime – electromagnetic field – pressure equations – unified integral form – Wald configuration – polar clouds – covering shells

1 INTRODUCTION

Investigation of fluids under astrophysical conditions represents one of the most challenging tasks in physics. Encircling sources of strong gravity, such as black holes and neutron stars (compact objects), astrophysical fluids manifest as compressible (gaseous) fluids, typically. We can find them in a form of pure neutral or quasi–neutral ionized gas (plasma), as a neutral or charged microscopic dust, or dust grains (pressure–less fluid), and very often as a dispersed medium, such as dusty gas, dusty plasma, etc. The gaseous fluids can range from extremely diluted ones (represented by separated particles, and described within the test–particles approach), through diluted ones (described within the kinetic approach), up to dense fluids (conveniently studied within the magneto–hydrodynamic approach).

From another point of view, astrophysical fluids can whirl in extremely complex dynamical situations, for instance, falling down and accreting onto compact objects, or being

978-80-7510-257-7

launched in the form of winds or jets; on the other hand, fluids can settle down in equilibrium configurations and circle around compact objects.

In recent years, we have been focusing on the latter scenario, i.e on the magneto–hydrodynamic study of electrically charged fluids forming equilibrium toroidal–like structures around compact objects. For this purpose, in a serie of papers, we developed a relevant basic general relativistic (Kovář et al., 2011, 2014, 2016) and Newtonian (Slaný et al., 2013; Trova et al., 2016) models, and introduced them in several gravito–electromagnetic backgrounds, revealing interesting configurations of the charged fluid. For instance, in contrast to the neutral perfect fluid being capable to form toroidal structures only in the equatorial plane (Kozłowski et al., 1978; Abramowicz et al., 1978), the charged fluid circling in a proper electromagnetic background can soar up the equatorial plane and form a 'levitating' torus, or it can 'hover' above the compact object as a 'polar cloud'.

The toroidal structures are well determined by their pressure profiles as solutions of the coupled pressure differential equations – the fundamental equations characterizing the considered model. These pressure equations, being accompanied by an integrability condition and equations of state, can be satisfactorily solved in a numerical way. The analytical treatment, however, is more traditional, enabling easier subsequent processing and bringing a deeper insight into the studied problem.

Here, we focus on the general relativistic approach, and introduce a transformation leading to an unified integral form of the pressure equations characterizing the charged fluid motion in more general background than considered up to now. The transformation enables us to analytically treat the fluid circulation in gravitational field being accompanied by a combined electromagnetic field, i.e. by the field characterized by two non–zero components of its vector potential.

2 MODEL IN DIFFERENTIAL DESCRIPTION

The considered model of charged fluid circling in strong gravitational and electromagnetic fields can be characterized by the following assumptions: 1) pure azimuthal circulation of the fluid with elementary charges adherent to the moving fluid components, 2) gravito–electromagnetic test fluid, and axial symmetry and stationarity of the gravito–electromagnetic background, 3) fluid properties to be of the perfect fluid one and satisfying the polytropic pressure–density relation; utilization of these assumptions within the general relativistic magneto–hydrodynamic equations (conservation laws, Maxwell equations and Ohm law) provides us with the basic coupled pressure equations.

2.1 Pressure equations

The rotating fluid with profiles of charge density q_ρ and total energy density ϵ forms a structure being determined by the iso–surfaces of the pressure p (equi–pressure surfaces), which can be determined from the coupled pressure equations

$$\begin{aligned} \partial_r p &= -(p+\epsilon)\mathbb{R}_1 + q_\rho \mathbb{R}_2 \equiv \mathbb{R}, \\ \partial_\theta p &= -(p+\epsilon)\mathbb{T}_1 + q_\rho \mathbb{T}_2 \equiv \mathbb{T}, \end{aligned} \tag{1}$$

where $\mathbb{R} = \mathbb{R}(r,\theta)$ and $\mathbb{T} = \mathbb{T}(r,\theta)$ denote the right hand sides of these equations, and

$$\mathbb{R}_1 = \partial_r \ln|U_t| - \frac{\omega\partial_r\ell}{1-\omega\ell}, \quad \mathbb{R}_2 = U^t\partial_r A_t + U^\phi\partial_r A_\phi, \tag{2}$$
$$\mathbb{T}_1 = \partial_\theta \ln|U_t| - \frac{\omega\partial_\theta\ell}{1-\omega\ell}, \quad \mathbb{T}_2 = U^t\partial_\theta A_t + U^\phi\partial_\theta A_\phi.$$

Here, the electromagnetic vector potential has the t and ϕ independent form $A_\alpha = (A_t, 0, A_\phi, 0)$ in the coordinate system (t, r, ϕ, θ), $U^\alpha = (U^t, 0, U^\phi, 0)$ is the fluid 4-velocity, $\ell = -U_\phi/U_t$ the specific angular momentum and $\omega = U^\phi/U^t$ the the angular velocity, all related by the formulae

$$\omega = -\frac{\ell g_{tt} + g_{t\phi}}{\ell g_{t\phi} + g_{\phi\phi}}, \quad (U_t)^2 = \frac{g_{t\phi}^2 - g_{tt}g_{\phi\phi}}{\ell^2 g_{tt} + 2\ell g_{t\phi} + g_{\phi\phi}}, \tag{3}$$

in a prescribed gravitational field $g_{\alpha\beta}$. Note that a derivation of the pressure equations (1) can be found in (Kovář et al., 2011, 2014, 2016); their uncharged limit $q_\rho = 0$ corresponds to the Euler equations describing a rotating electrically neutral perfect fluid (Kozłowski et al., 1978; Abramowicz et al., 1978).

2.2 Rotation regime, charge distribution and thermodynamic setup

The pressure equations (1) are not generally integrable and must be accompanied by the integrability condition

$$\partial_\theta\mathbb{R} + \mathbb{T}\partial_p\mathbb{R} = \partial_r\mathbb{T} + \mathbb{R}\partial_p\mathbb{T}. \tag{4}$$

From the physical point of view, this condition relates the charge density distribution $q_\rho = q_\rho(r,\theta)$ throughout the torus and its rotation regime $\ell = \ell(r,\theta)$ (or $\omega(r,\theta)$), which must be properly adjusted to each other according to this condition.

Formally, to close the system of equations, it is necessary to specify relations for the pressure and total energy density. For the purpose of basic theoretical investigation, we can consider a compressible perfect fluid satisfying the general polytropic equation of state for the pressure

$$p = \kappa\rho^\Gamma, \tag{5}$$

together with the total energy density relation

$$\epsilon = \rho + \frac{1}{\Gamma - 1}p, \tag{6}$$

with κ and Γ being the polytropic coefficient and exponent, and ρ the rest–mass density.

3 UNIQUE SOLUTION

In order to avoid numerical integrations of the pressure equations (1) and the related integrability condition (4), we can introduce a transformation of the charge density together with a transformation of the pressure. Then under certain conditions specified below, the system of differential pressure equations can be uniquely rewritten, unified and integrated.

3.1 Transformation of pressure equations and correction function

Defining the charge density transformation by the relation

$$K = \frac{q_\rho}{\epsilon + p}, \tag{7}$$

where we address the function K as the 'correction function' (on the basis of integrability condition (4) mathematically ensuring the integrability of the pressure equations (1) after the profiles $\ell(r,\theta)$ or $\omega(r,\theta)$ are set), and the pressure transformation by the coupled equations

$$\partial_r h = \frac{\partial_r p}{(p+\epsilon)}, \quad \partial_\theta h = \frac{\partial_\theta p}{(p+\epsilon)}, \tag{8}$$

where we address the function h as the 'auxiliary function', we get the system of transformed pressure equations in the form

$$\begin{aligned} \partial_r h &= -(\mathbb{R}_1 - K\mathbb{R}_2), \\ \partial_\theta h &= -(\mathbb{T}_1 - K\mathbb{T}_2), \end{aligned} \tag{9}$$

accompanied by the integrability condition

$$\partial_\theta(\mathbb{R}_1 - K\mathbb{R}_2) = \partial_r(\mathbb{T}_1 - K\mathbb{T}_2). \tag{10}$$

Providing that $\epsilon = \epsilon(p)$, which is guaranteed by the chosen thermodynamic alignment (5)-(6), the auxiliary function can be explicitly expressed as

$$h = \int_0^h \mathrm{d}h = \int_0^p \frac{\mathrm{d}p}{p+\epsilon} = \ln\left(1 + \frac{\Gamma \kappa^{\frac{1}{\Gamma}} p^{\frac{\Gamma-1}{\Gamma}}}{\Gamma - 1}\right). \tag{11}$$

In the considered combined electromagnetic field, it is, moreover, very convenient to rescale the correction functions as

$$\mathcal{K} = KU^\phi. \tag{12}$$

Then, our system of the transformed pressure equations (9) can be written in the form

$$\begin{aligned} \partial_r h &= -\partial_r \ln|U_t| + \frac{\omega \partial_r \ell}{1-\omega\ell} + \mathcal{K}(\omega^{-1}\partial_r A_t + \partial_r A_\phi), \\ \partial_\theta h &= -\partial_\theta \ln|U_t| + \frac{\omega \partial_\theta \ell}{1-\omega\ell} + \mathcal{K}(\omega^{-1}\partial_\theta A_t + \partial_\theta A_\phi), \end{aligned} \tag{13}$$

indicating a possible unification. After an introduction of the electromagnetic vector time–component transformation according to the relations

$$\partial_r a_t = \omega^{-1}\partial_r A_t, \quad \partial_\theta a_t = \omega^{-1}\partial_\theta A_t, \tag{14}$$

and the 'magnetic function' $A = a_t + A_\phi$, we get the final system of the transformed pressure equations

$$\partial_r h = -\partial_r \ln|U_t| + \frac{\omega\partial_r \ell}{1-\omega\ell} + \mathcal{K}\partial_r A, \tag{15}$$
$$\partial_\theta h = -\partial_\theta \ln|U_t| + \frac{\omega\partial_\theta \ell}{1-\omega\ell} + \mathcal{K}\partial_\theta A.$$

3.2 Solution for the h-function

Providing that $\omega = \omega(\ell)$ and $\mathcal{K} = \mathcal{K}(A)$, on one hand restricting degrees of freedom in the model, but still providing realistic physical scenarios, we can join equations of the system (15) into the unified integral form

$$\int_0^h \mathrm{d}h = -\ln\left|\frac{U_t}{U_{t_{\rm in}}}\right| + \int_{\ell_{\rm in}}^{\ell} \frac{\omega \mathrm{d}\ell}{1-\omega\ell} + \int_{A_{\rm in}}^{A} \mathcal{K}\mathrm{d}A, \tag{16}$$

with the solution written in the closed form

$$h = -H + H_{\rm in}. \tag{17}$$

Here, the function $H(r,\theta)$ represents the variable part (potential) in the right–hand side of equation (16) after the integration, and the subscript 'in' refers to the inner edge of the structure at $r = r_{\rm in}$ and $\theta = \theta_{\rm in}$, determining the constants of integration being coupled in $H_{\rm in}$. Then, thanks to the transformation (11), equi–pressure surfaces $p = \text{const}$ determining the topology of the fluid structure take the same shapes as equi–potential surfaces $H = \text{const}$.

3.3 Solution in Wald configuration

As an example, we can present our charged fluid structures circling close to a rotating charged black hole immersed in an asymptotically uniform magnetic field. Such a background can be advantageously described by the Wald test–field solution of Maxwell equations (Wald, 1974) in the Kerr spacetime. In the standard general relativistic dimensionless units, it reads

$$A_t = \tfrac{1}{2} B\Big(g_{t\phi} + 2a\, g_{tt}\Big) - \tfrac{1}{2} Q\, g_{tt} - \tfrac{1}{2} Q, \tag{18}$$
$$A_\phi = \tfrac{1}{2} B\Big(g_{\phi\phi} + 2a\, g_{t\phi}\Big) - \tfrac{1}{2} Q\, g_{t\phi}, \tag{19}$$

where the charge Q and magnetic field strength B parameters are only test-field parameters, thus not influencing the background spacetime geometry $g_{\alpha\beta}$.

By setting the rigid rotation regime of the fluid, i.e. $\omega = \text{const}$, the electromagnetic vector time–component transformation can be chosen in the form $a_t = \omega^{-1} A_t$, and the corresponding magnetic function will take the form $A = \omega^{-1} A_t + A_\phi$. Next, for the purpose of a basic illustration, even if we choose the rescaled correction function with a very simple profile, such as

$$\mathcal{K} = \mathcal{K}(A) = kA, \tag{20}$$

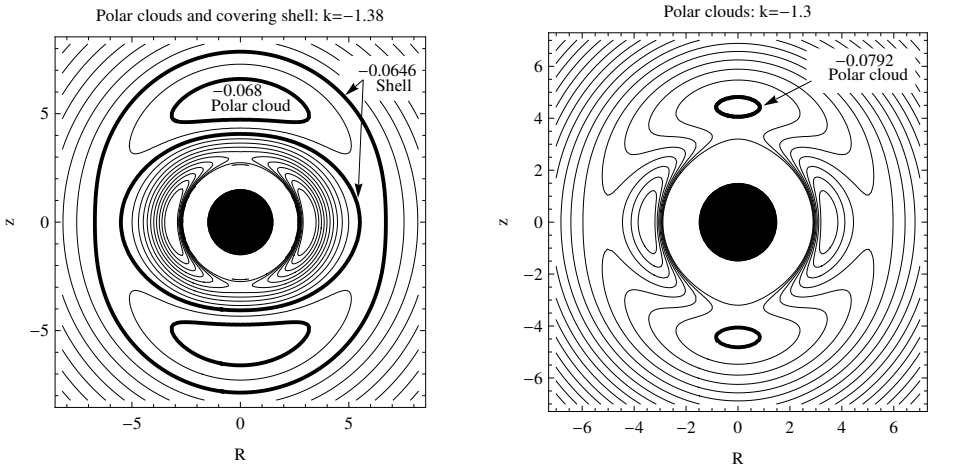

Figure 1. Two examples of typical behavior of the potential $H(r,\theta)$ shown in terms of the poloidal equi–potential contours plotted in the cylindrical coordinates $R = r\sin\theta$, $z = r\cos\theta$. Particularly, we present topologies embodying two polar potential minima surrounded by closed equi–potential surfaces (polar clouds) and two equatorial maxima, corresponding to the background and fluid parameters $a = 0.9$, $Q = 3.99 \times 10^{-3}$, $B = 6.5 \times 10^{-5}$, $\omega = -1.6 \times 10^{-3}$, and $k = -1.38$ and $k = -1.3$. The topology corresponding to the case $k = -1.38$ (left) embodies also coupled closed equi–potential surfaces (covering shell) all around the central black hole.

where the coefficient k scales the charge profile of the fluid, we reveal very interesting behavior of the related H–potential. The behavior of the potential H shows that along with the typical tori centered and circling in the equatorial plane, the topology of the charged fluid structures can also exhibit structures such as 'polar clouds' or 'covering shells' (see Fig. 1).

4 CONCLUSIONS

The introduced integral form of the pressure equations (16) represents an extremely convenient formula, allowing us to avoid a standard general treatment of coupled partial differential equations; its uncharged limit is referred to as Boyer's condition and useful for investigation of the neutral fluid toroidal structures – the so–called 'Polish doughnuts' (Abramowicz et al., 1978). On the other hand, the restricting conditions for the unification $p = p(\epsilon)$, $\omega = \omega(\ell)$ and $\mathcal{K} = \mathcal{K}(A)$ can prevent us from treating some more general interesting regimes in this way; a numerical integration of the pressure equations is then necessary.

The presented example of the pressure equations unification in the case of the Wald configuration could provide an illustration how efficient the procedure can be, despite of the physical complexity of the studied scenario – the interplay of strong gravity and electro-

magnetism forming a rotating charged fluid. No doubt, the introduced rigidly rotating polar clouds and covering shells represent sufficient reasoning for a detailed survey of different possible classes of the toroidal topology not only in the Wald configuration. Note that the existence of the polar clouds was already mentioned in (Kovář et al., 2014). There, however, the situation was considered simpler (the background spacetime did not rotate, $a = 0$), and the unification of the pressure equations was not introduced; an analytical solution was obtained by a direct solution of the coupled pressure equations.

ACKNOWLEDGEMENTS

The authors JK, PS, ZS and VK acknowledge the project 'Albert Einstein Center for Gravitation and Astrophysics' - Czech Science Foundation GAČR No. 14-37086G. JK, PS and ZS would also like to express their acknowledgment for the Institutional support of the Faculty of Philosophy and Science, Silesian University in Opava, VK acknowledges the project COST Action CA16214 'The multi-messenger Physics and Astrophysics of neutron Stars' (PHAROS) and AT the research training group 1620 'Models of Gravity' funded by the German Research Foundation (DFG).

REFERENCES

Abramowicz, M. A., Jaroszyński, M. and Sikora, M. (1978), Relativistic, accreting disks, *Astronomy and Astrophysics*, **63**, p. 221.

Kovář, J., Slaný, P., Cremaschini, C., Stuchlík, Z., Karas, V. and Trova, A. (2014), Electrically charged matter in rigid rotation around magnetized black hole, *Physical Review D*, **90**, p. 044029.

Kovář, J., Slaný, P., Cremaschini, C., Stuchlík, Z., Karas, V. and Trova, A. (2016), Charged perfect fluid tori in strong central gravitational and dipolar magnetic fields, *Physical Review D*, **93**, p. 124055.

Kovář, J., Slaný, P., Stuchlík, Z., Karas, V., Cremaschini, C. and Miller, J. C. (2011), Role of electric charge in shaping equilibrium configurations of fluid tori encircling black holes, *Physical Review D*, **84**, p. 084002.

Kozłowski, M., Jaroszyński, M. and Abramowicz, M. A. (1978), The analytic theory of fluid disks orbiting the kerr black hole, *Astronomy and Astrophysics*, **63**, p. 209.

Slaný, P., Kovář, J., Stuchlík, Z. and Karas, V. (2013), Charged tori in spherical gravitational and dipolar magnetic fields, *The Astrophysical Journal Supplement*, **205**, p. 3.

Trova, A., Karas, V., Slaný, P. and Kovář, J. (2016), Electrically charged matter in permanent rotation around magnetized black holes: A toy model for self-gravitating fluid tori, *The Astrophysical Journal Supplement Series*, **226**, p. 12.

Wald, R. M. (1974), Black hole in a uniform magnetic field, *Physical Review D*, **10**, p. 1680.

Proceedings of *RAGtime 17–19, 17–19/23–26 Oct., 1–5 Nov., 2015/2016/2017, Opava, Czech Republic*
Z. Stuchlík, G. Török and V. Karas, editors, Silesian University in Opava, 2017, pp. 127–136

The study on behaviour of thin accretion disc affected by Poynting–Robertson effect

Debora Lančová[1,a] Pavel Bakala [1,4] Kateřina Goluchová [1], Maurizio Falanga [2], Vittorio De Falco [2] and Luigi Stella [3]

[1]Institute of Physics and Research Centre for Computational Physics and Data Processing, Faculty of Philosophy & Science in Opava, Silesian University in Opava, Bezručovo nám. 13, CZ-746 01 Opava, Czech Republic
[2]International Space Science Institute, Hallerstrasse 6, 3012 Bern, Switzerland
[3]INAF – Osservatorio Astronomico di Roma, Via Frascati, 33, Monteporzio Catone, Rome, I-00040, Italy
[4]M. R. Štefánik Observatory and Planetarium, Sládkovičova 41, 920 01 Hlohovec, Slovak Republic
[a]debora.lancova@fpf.slu.cz

ABSTRACT
This study deals with the structure of a thin accretion disc under the influence of radiation pressure and Poynting–Roberson effect. The disc is approximated by inhomogeneous dust consisting of point–like particles in vicinity of a point–like source of radiation. We have developed code *PR Trajectories* which computes trajectories of millions of particles forming an accretion disc and provides a lot of informations about the accretion disc.

Keywords: Dust accretion disc –Radiation –Neutron stars –Black holes

1 INTRODUCTION

In the Low–Mass X–ray binaries (LMXBs) with neutron star or black hole, the luminosity of the central object can have a significant influence on the structure of the accretion disc surrounding the compact object. Despite the radiation pressure we also take into consideration the Poynting–Robertson effect which causes changes of angular momentum of a small particle on an orbit of radiating compact body. The accretion disc approximated by inhomogeneous dust consist of point–like particles is exposed to radiation and we can study the changes of its structure, density and time development. The central body is approximated as a point–like source of radiation and we take into account only the photons emitted in equatorial plane. The influence of the radiation to the motion of particles around a compact object is a well-known problem. Abramowicz et al. (1990) found the stress-energy tensor for a three-dimensional sphere in spherically-symmetric spacetime, the Poynting-Robertson effect has been studied in Stahl et al. (2012). Cases with non-stable luminosity were studied in Stahl et al. (2013) and there are many works on accretion on a luminous

978-80-7510-257-7

star (Miller and Lamb, 2016; Miller et al., 1996). Our work is based on a work of Bini et al. (2011). In the first section we introduce the geometry of studied settings, the equations of motion and problem of the critical radius. In the next section the motion of single particles under influence of the PR effect is presented. Then we are describing used numerical approach for the dust accretion disc. Finally the results are presented as a set of images of stable solution.

2 POYNTING–ROBERTSON EFFECT IN STRONG GRAVITY

The general relativistic description of Poynting–Robertson effect was published in (Bini et al., 2011) involving non–zero photon momentum. The equations of motion are constructed on the background of Kerr metric defined by space–time element parametrized by the specific angular momentum (spin) a in Boyer–Lindquist coordinates

$$\begin{aligned} \mathrm{d}s^2 = &-\left(1-\frac{2r}{\Sigma}\right)\mathrm{d}t^2 - \frac{4ra}{\Sigma}\sin^2\theta\,\mathrm{d}t\,\mathrm{d}\varphi + \frac{\Sigma}{\Delta}\mathrm{d}r^2 + \\ &+\Sigma\,\mathrm{d}\theta^2 + \left(r^2+a^2+\frac{2ra^2\sin^2\theta}{\Sigma}\right)\sin^2\theta\,\mathrm{d}\varphi^2, \end{aligned} \tag{1}$$

using geometrized units ($c = G = M = 1$), where $\Sigma \equiv r^2 + a^2\cos^2\theta$ and $\Delta \equiv r^2 - 2r + a^2$. We consider the motion of particles only in equatorial plane where $\theta = \frac{\pi}{2}$.

The Kerr metric describing the final state of the gravitational collapse of a massive rotating star into a black hole can also be applied to describe the spacetime in the vicinity of a massive, fast rotating neutron star (Török et al., 2012).

2.1 Radiation field

The central body is approximated by a point-like source of photons. We consider only photons emitted in equatorial plane, the photons angular momentum b is one of the free parameters. (Bini et al., 2011).

The strength of the radiation is represented by constant A which corresponds to the luminosity of central object measured by observer in infinity to the Eddington limit

$$A = \frac{L_{inf}}{L_{Edd}}. \tag{2}$$

The parameters are connected by relation

$$\cos\beta = \frac{bE}{\sqrt{g_{\phi\phi}}E(n)}, \tag{3}$$

where E is a energy of photons and β is azimuthal angle of the photon 4–momentum measured in the local frame related to ZAMO (Zero Angular Momentum Observer) on given radius.

2.2 Equations of motion

We have rewritten the equations of motion published in (Bini et al., 2011) explicitly for the case of the Kerr spacetime as the set of four first–order differential equations. The first pair of equations describes test particle motion in the ZAMO frame by the local spatial velocity v and its azimuthal angle α. The second pair transforms these ZAMO quantities into the radial velocity v_r and the angular velocity ω measured by the static observer at infinity.

$$
\begin{aligned}
\frac{\mathrm{d}v}{\mathrm{d}t} =& -\sqrt{\frac{\Delta}{g_{\phi\phi}}}\gamma^{-2}\,\sin\alpha\left(a^{\hat{r}}+2v\cos\alpha\theta^{\hat{r}}{}_{\hat{\phi}}\right)\\
&+\Psi\,\left[\cos(\alpha-\beta)-v\right]\left[1-v\cos(\alpha-\beta)\right],\\
\frac{\mathrm{d}\alpha}{\mathrm{d}t} =& -\sqrt{\frac{\Delta}{g_{\phi\phi}}}v^{-1}\,\cos\alpha\left(a^{\hat{r}}+2v\cos\alpha\theta^{\hat{r}}{}_{\hat{\phi}}+v^2k^{\hat{r}}_{(lie)}\right)\\
&+\Psi\,\left[v^{-1}-\cos(\alpha-\beta)\right]\sin(\alpha-\beta),\\
\frac{\mathrm{d}r}{\mathrm{d}t} =& v^r=\sqrt{\frac{\Sigma}{g_{\phi\phi}}}\,v\sin\alpha,\\
\frac{\mathrm{d}\phi}{\mathrm{d}t} =& \omega=\frac{\sqrt{\Delta}}{g_{\phi\phi}}\,v\cos\alpha+\Omega_{ZAMO},\\
\Psi =& \frac{\lambda\,\mathcal{L}}{\gamma\,\sqrt{g_{\theta\theta}\,g_{\phi\phi}}\,\cos\beta|\sin\beta|}\,.
\end{aligned}
\tag{4}
$$

where we use quantities expressed with related to free test particle and measured with respect to ZAMO frame (Bini et al., 2011), the Lorentz factor γ corresponds to

$$
\gamma=\frac{1}{\sqrt{1-v^2}},
\tag{5}
$$

the radial component of free test particle 4–acceleration $a^{\hat{r}}$, the radial component of shear vector $\Theta_{\hat{\phi}}$ and the radial component of associated Lie relative curvature vector $k^{\hat{r}}_{(lie)}$ are

$$
a^{\hat{r}}=\frac{\left(r^2+a^2\right)^2-4a^2r}{r^3\,\sqrt{\Delta}g_{\phi\phi}},
\tag{6}
$$

$$
\Theta_{\hat{\phi}}=-\frac{a\left(3r^2+a^2\right)}{r^3g_{\phi\phi}},
\tag{7}
$$

$$
k^{\hat{r}}_{(lie)}=-\frac{\Delta^{-1/2}(r^3-a^2)}{r^3g_{\phi\phi}}.
\tag{8}
$$

2.3 Critical radius

Even from non–relativistic description follows that small particle under influence of Poynting–Robertson effect cannot stay on stable circular orbit and has to either reach the surface of the radiating body or escape to infinity. However, for Schwarzschildcase one can find a radial distance r_{crit} where the radiation pressure and gravitational pull is balanced and particle ends its motion on this critical radius r_{crit} with $\nu_{crit} = 0$.

However, only in Schwarzschild spacetime (with $a = 0$) one can find the implicitly given value of the r_{crit} (Bini et al., 2009):

$$\frac{A}{MN} = \mathrm{sgn}(\sin\beta_0)\frac{1 - \frac{b^2}{Mr_{crit}}\left(1 - \frac{2M}{r_{crit}}\right)^2}{\left[1 - \frac{b^2}{r_{crit}^2}\left(1 - \frac{2M}{r_{crit}}\right)\right]^{\frac{3}{2}}}. \tag{9}$$

In other settings the r_{crit} can be easily found numerically.

The critical radius goes to infinity with $A = 1$, with low values of A it is very close to the event horizon. In very rare situations there can exist more than one critical radius, for example when the luminosity parameter extends value $A = 0.647$ and the impact parameter $b > 2$. The stability of such state is discussed in (Bini et al., 2009).

3 MOTION OF TEST PARTICLE

The motion of one test particle under the influence of Poynting–Robertson effect has unexpected properties. The particle is spiraling to the inner edge, however the radial component of its 4–velocity has remarkable profile with loops (figure 2). In some cases the radial component of 4–velocity can change the sign during the motion so particles are moving alternately inwards and outwards. At the radii corresponding to loops the particles spends more time. With high value of luminosity the trajectories can be significantly excentric as the radiation pressure pushes the particle far from the central body, yet due to loss of angular momentum the particle falls back.

In the structure of an accretion disc consisting of millions of such particles there are visible peaks of density at radii corresponding to loops in radial component of 4–velocity (figure 1). The structure of the disc is significantly different from structure of accretion disc consisting of particles on almost Keplerian orbits.

4 NUMERICAL IMPLEMENTATION

The numerical model approximates a thin accretion disc by non–interacting particles whose motion is driven by equations 4. The viscosity and scattering of radiation in the disc material are neglected. The inner edge r_{inner} of the disc is set to event horizon, the initial radial coordinate of particles r_0 is one of free parameters. The particles have initial velocity v_0 corresponding to Keplerian circular orbit without influence of radiation v_{kep} which

expressed in ZAMO frame is equal (Bini et al., 2009)

$$\nu_{kep} = \frac{a^2 \mp 2a\sqrt{Mr} + r^2}{\sqrt{\Delta}\left(a \pm r\sqrt{\frac{r}{M}}\right)}. \tag{10}$$

In some cases we are also simulating small randomization of initial parameters r_0 and ν_0 which are linked by $\frac{\Delta\nu_0}{\nu_0} = \frac{1}{2}\frac{\Delta r_0}{r_0}$.

Because the time scale of one particle falling to the inner edge is very short, the code needs to simulate constant inflow of particles. In every integration step is added a particle on the outer edge of area of interest.

For integration of motion the code using Runge–Kutta method of 8th order. The code is highly parallelised using *OpenMP* library, nevertheless the accretion disc consisting of hundreds thousands particles requires a considerable computational power.

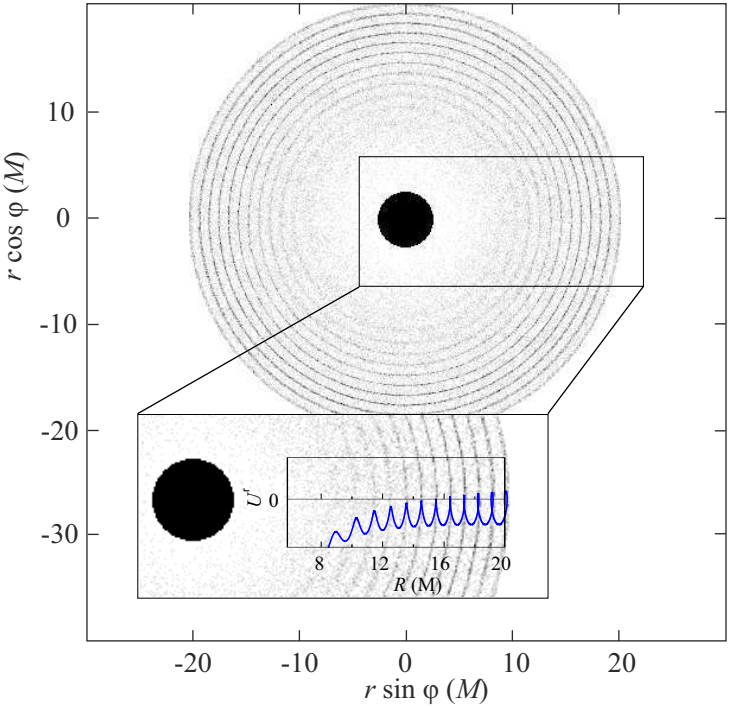

Figure 1. Structure of accretion disc consisting of particles driven by PR effect in comparation with radial component of 4–velocity of single particle. The peaks in density corresponds to the loops in 4–velocity. ($A/M = 0.01$, $a/M = 0.0$, $b/M = 0.0$,$R_0 = 20\,\mathrm{M}$)

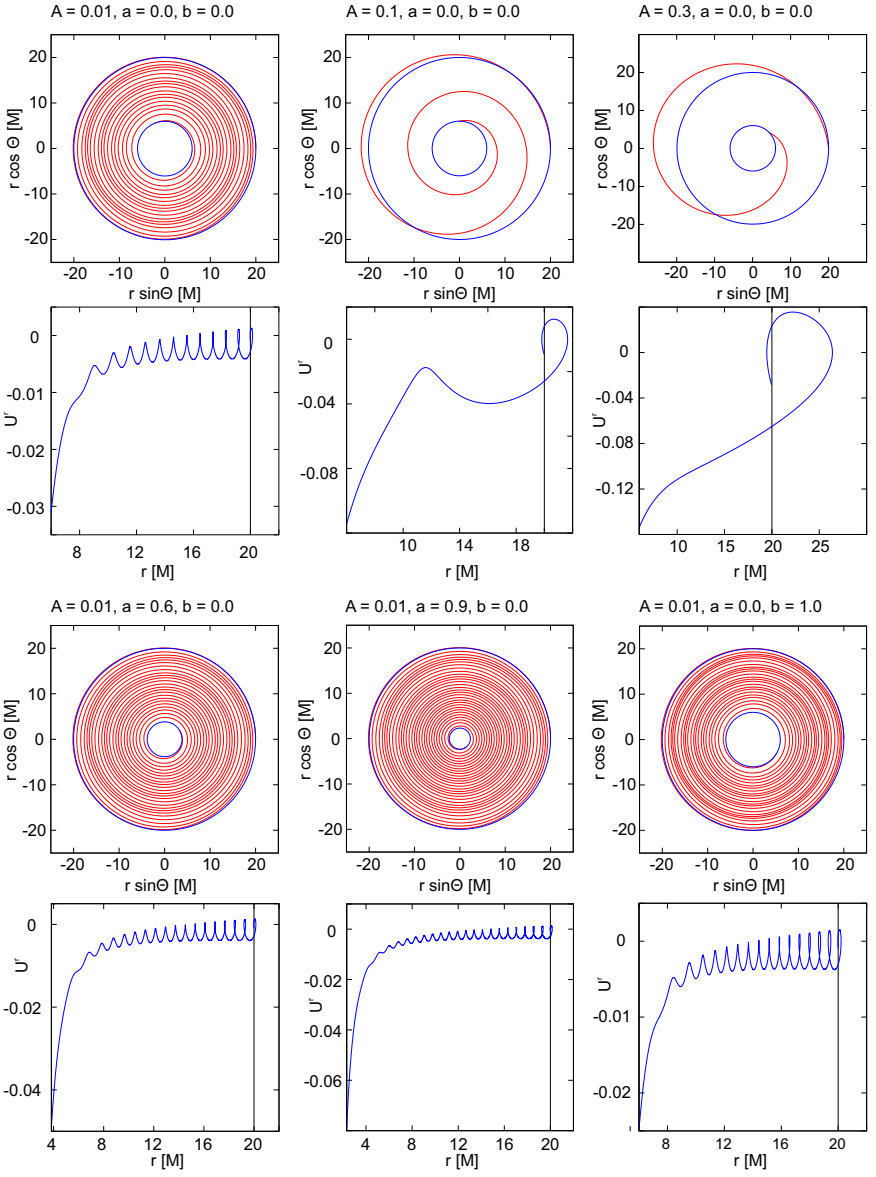

Figure 2. Examples of trajectories of single particle with different initial state and the evolution of it's radial component of 4–velocity. The initial radial coordinate is always $r_0 = 20\,\mathrm{M}$, the inner edge is on innermost stable circular orbit.

5 RESULTS

For study of behaviour of thin accretion disc the simulating code computes trajectories of many particles and in certain times printing their positions in Boyer–Lindquist coordinates. Due to the presence of radiation, distinctive pattern occurs in the structure of the accretion disc. On certain radii is the density of the disc matter is higher causing dark rings to appear. These structure in the disc reflex the changes in radial component of 4–velocity.The number and positions of this rings are very sensitive to initial state of the simulation.

With constant value of luminosity and with constant accretion inflow the disc reaches quasi–stable state although the particles are still rapidly falling to the central body. The distribution of matter in disc is henceforward unchanged.

The structure of the accretion disc depends significantly on the initial condition. Following figures shows selection of simulations result with different values of luminosity A, spin a, radiation field angular momentum b or with slightly scattered initial radial coordinate r_0 or velocity v_0.

6 CONCLUSION

The results of the simulations shows us significant influence of Poynting–Robertson effect on thin accretion discs. The radiation pressure causes inhomogeneous distribution of matter with significant peaks on certain radii, however the structure strongly depends on the initial parameters of simulation.

In further work we would like to also work on the influence of fast changes of luminosity on the structure of dust accretion disc, e.g. during the thermonuclear X-ray bursting on the surface neutron star.

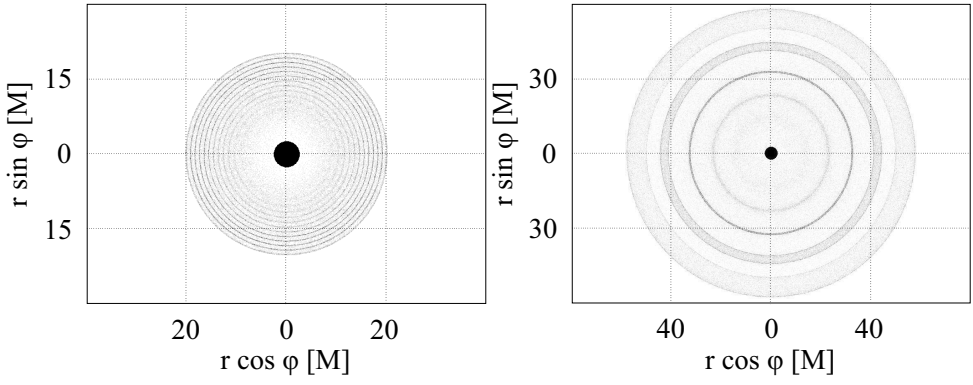

Figure 3. Different luminosities: Left $A/M = 0.01$, $a = 0.0$, $b = 0.0$, $r_0 = 20\,\mathrm{M}$, $v_0 = v_{kep}$. Right $A/M = 0.1$, $a = 0.0$, $b = 0.0$, $r_0 = 50\,\mathrm{M}$, $v_0 = v_{kep}$

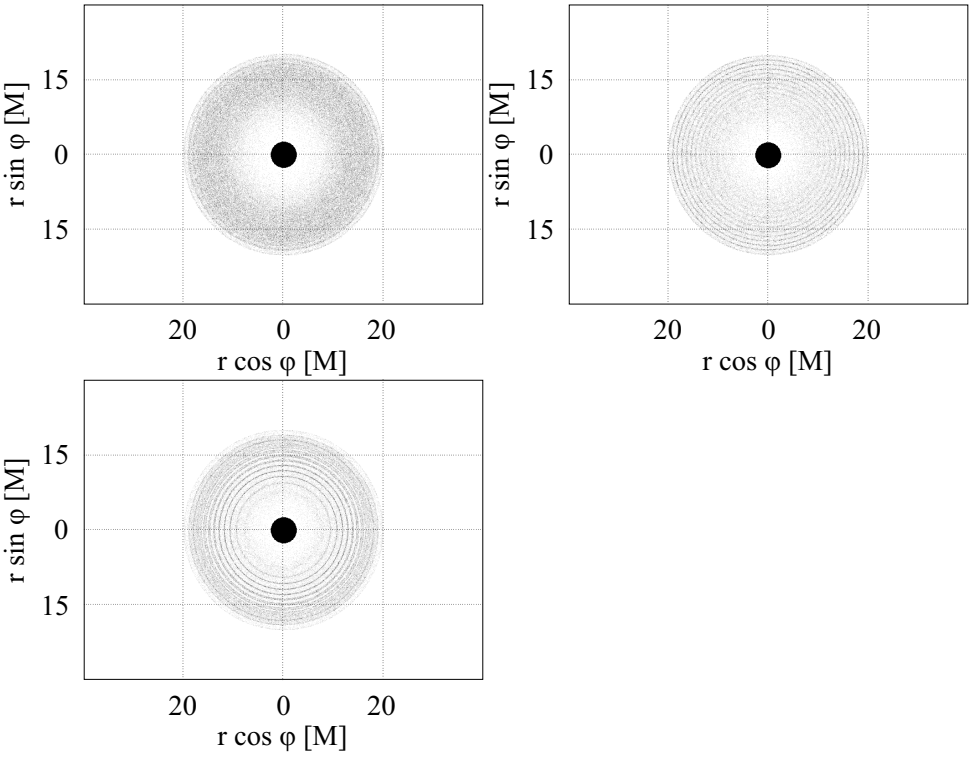

Figure 4. Randomization of initial parameters: $A/M = 0.01$, $a = 0.0$, $b = 0.0$,$r_0 = 20\,\mathrm{M}$, top left $\nu_0 = \nu_{kep} \pm 5\,\%$, top right $\nu_0 = \nu_{kep} \pm 1\,\%$, bottom $\nu_0 = \nu_{kep} \pm 1\,\%$, $r_0 = 20\,\mathrm{M} \pm 0.5\,\%$

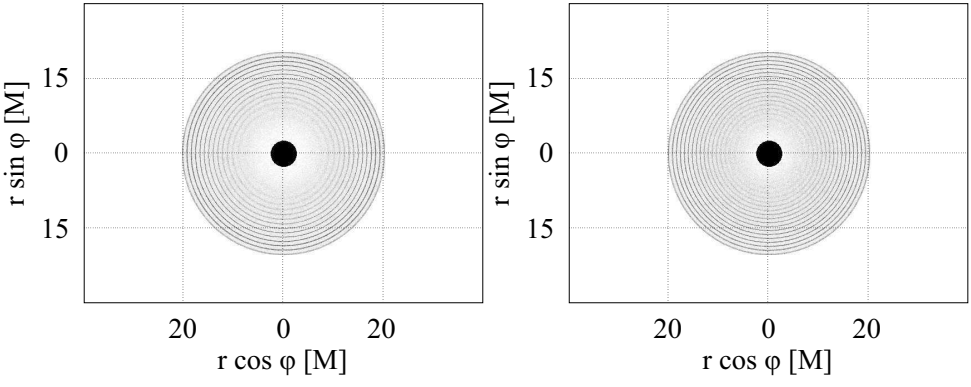

Figure 5. Non–zero spin: $A/M = 0.01$, $b = 0.0$, $r_0 = 20\,\mathrm{M}$, $\nu_0 = \nu_{kep}$, left $a = 0.2$, right $a = 0.6$

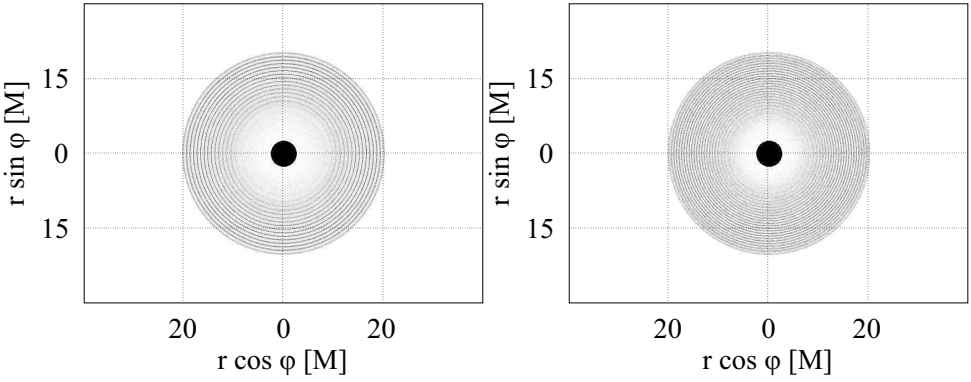

Figure 6. Non–zero radiation field angular momentum: $A/M = 0.01$, $a = 0.0$, $r_0 = 20\,\mathrm{M}$, $\nu_0 = \nu_{kep}$, left $b = 1.0$, right $b = 2.0$

ACKNOWLEDGEMENTS

We acknowledge the Czech Science Foundation (GAČR) grant No. 17–16287S, the internal grants of Silesian university SU SGS/15/2016 and IGS/1/2017, the inter and the MSK project 03788/2017/RRC. Computational resources were supplied by the Ministry of Education, Youth and Sports of the Czech Republic under the Projects CESNET (Project No. LM2015042) and CERIT-Scientific Cloud (Project No. LM2015085) provided within the program Projects of Large Research, Development and Innovations Infrastructures.

REFERENCES

Abramowicz, M. A., Ellis, G. F. R. and Lanza, A. (1990), Relativistic effects in superluminal jets and neutron star winds, *The Astrophysical Journal* , **361**, pp. 470–482.

Bini, D., Geralico, A., Jantzen, R. T., Semerák, O. and Stella, L. (2011), The general relativistic Poynting-Robertson effect: II. A photon flux with nonzero angular momentum, *Classical and Quantum Gravity*, **28**(3), 035008, arXiv: 1408.4945.

Bini, D., Jantzen, R. T. and Stella, L. (2009), The general relativistic Poynting Robertson effect, *Classical and Quantum Gravity*, **26**(5), 055009, arXiv: 0808.1083.

Miller, M. C. and Lamb, F. K. (2016), Observational constraints on neutron star masses and radii, *European Physical Journal A*, **52**, 63, arXiv: 1604.03894.

Miller, M. C., Lamb, F. K. and Psaltis, D. (1996), Sonic-Point Model of Kilohertz QPOs in LMXBs, in *American Astronomical Society Meeting Abstracts*, volume 28 of *Bulletin of the American Astronomical Society*, p. 1329.

Stahl, A., Kluźniak, W., Wielgus, M. and Abramowicz, M. (2013), Escape, capture, and levitation of matter in Eddington outbursts, *Astronomy and Astrophysics* , **555**, A114, arXiv: 1306.6556.

Stahl, A., Wielgus, M., Abramowicz, M., Kluźniak, W. and Yu, W. (2012), Eddington capture sphere around luminous stars, *Astronomy and Astrophysics* , **546**, A54, arXiv: 1208.2231.

Török, G., Bakala, P., Šrámková, E., Stuchlík, Z., Urbanec, M. and Goluchová, K. (2012), Mass-Angular-momentum Relations Implied by Models of Twin Peak Quasi-periodic Oscillations, *The Astrophysical Journal* , **760**, 138, arXiv: 1408.4220.

Proceedings of *RAGtime 17–19, 17–19/23–26 Oct., 1–5 Nov., 2015/2016/2017, Opava, Czech Republic*
Z. Stuchlík, G. Török and V. Karas, editors, Silesian University in Opava, 2017, pp. 137–152

Constraints on two accretion disks centered on the equatorial plane of a Kerr SMBH

Daniela Pugliese[1,a] and Zdeněk Stuchlík[1,b]

[1]Institute of Physics and Research Centre of Theoretical Physics and Astrophysics, Faculty of Philosophy & Science, Silesian University in Opava, Bezručovo náměstí 13, CZ-74601 Opava, Czech Republic
[a]d.pugliese.physics@gmail.com
[b]zdenek.stuchlik@physics.cz

ABSTRACT
The possibility that two toroidal accretion configurations may be orbiting around a super–massive Kerr black hole has been addressed. Such tori may be formed during different stages of the Kerr attractor accretion history. We consider the relative rotation of the tori and the corotation or counterrotation of a single torus with respect to the Kerr attractor. We give classification of the couples of accreting and non–accreting tori in dependence on the Kerr black hole dimensionless spin. We demonstrate that only in few cases a double accretion tori system may be formed under specific conditions.

Keywords: Accretion disks – accretion – jets – black hole physics – hydrodynamics

1 INTRODUCTION

Investigation of the issues concerning the attractor–accretion disks systems has led to question, if several toroidal orbiting structures may be formed around a single central super–massive attractor. The debate on the possible evidence of their existence eventually ended in the conjecture that the occurrence of the unstable phases of these structures may be important in the high–energy phenomena demonstrated, for example, in active galactic nuclei (AGNs). This possibility has been addressed over the years with different methods and considering different astrophysical contexts. Possible observational evidences of these configurations were already discussed in Karas and Sochora (2010); Sochora et al. (2011). Tori, strongly misaligned with respect to the central super–massive black hole (**BH**) spin, are considered in Nixon et al. (2012, 2013); Dunhill et al. (2014), where configurations around super–massive **BH** binaries are also addressed. Toroidal fluid configurations, tori, might be formed as remnants of several accretion regimes occurred in various phases of the **BH** life (Alig et al., 2013; King and Pringle, 2007, 2006; Krolik and Hawley, 2002). These sub–structures could be eventually reanimated in non isolated systems where the central attractor is interacting with the environment, or in some kinds of binary systems. Some additional matter could be supplied into the vicinity of the central black hole due

978-80-7510-257-7

to tidal distortion of a star(Miller et al., 2015), or if some cloud of interstellar matter is captured by the strong gravity. This issue has been faced in Pugliese and Montani (2015); Pugliese and Stuchlík (2015) and then in Pugliese and Stuchlík (2017b) in the framework of the "ringed accretion disk" (**RAD**). It has been directly considered that in modelling the evolution of super–massive **BH** in AGNs, both corotating and counterrotating accretion stages are mixed during various accretion periods Volonteri et al. (2003); Carmona-Loaiza et al. (2015); Dyda et al. (2015), tidally destroyed stars corotating or counterrotating with respect to the attractor could leave some remnants in the form of toroidal structures which then can give rise to individual accretion tori. The tori can be accreting or non–accreting (i.e. isolated in equilibrium state)[1]. By following general arguments implied by the geometric properties of the Kerr spacetimes, in the present analysis we discuss the existence of couples of toroidal configurations, identifying the situations where a doubled system of accretion tori may be formed in dependence on the **BH** spin. We consider couples of tori which are axis–symmetric and coplanar with the central Kerr **BH** as it is the simplest scenario adopted in the majority of the current analytical and numerical models of accretion configurations. We proved that the existence of couples of accretion tori orbiting around a central Kerr **BH** is strongly constrained and eventually only few coupled accretion tori systems are possible. We also identify the Kerr attractors around which such tori may be formed.

Finally Sec. (A) concerns with the construction and interpretation of special structures, graphs, representative of a couple of accretion tori and their evolution, within the constraints they are subjected to. These structures were introduced in Pugliese and Stuchlík (2016) and detailed in Pugliese and Stuchlík (2017b). Although the following analysis has been discussed independently from the graph formalism, graphs can be used also to quickly collect the different constraints on the tori existence and evolution. The use of these graphic schemes has been reveled to be crucial for the study and representation of the tori evolutionary paths.

2 KERR GEOMETRY AS GOVERNOR OF DOUBLED TORI SYSTEM

The toroidal configurations are governed by the Kerr geometry through the radial profile of the specific angular momentum of the circular geodesic motion

$$\ell_{\pm}(r;a) \equiv -\frac{p_\phi}{p_t} = \frac{a^3 M + aMr(3r-4M) \pm \sqrt{Mr^3\left[a^2+(r-2M)r\right]^2}}{\left[Ma^2-(r-2M)^2 r\right]M} \tag{1}$$

defined as ratio of the two constants of test particle motion, (p_ϕ, p_t), associated to the axial Killing field ξ_ϕ, and the Killing field ξ_t representing the stationarity of the Kerr geometry that is expressed in the Boyer–Lindquist coordinates $(\{t, r, \theta, \phi\})$, where M denotes the black hole mass parameter, and $a = J/M$ is the specific angular momentum of the black hole having intrinsic angular momentum J–(Pugliese and Stuchlík, 2015). The parameter

[1] Note that in Kerr–de Sitter spacetimes torii can be also excreting(Stuchlík et al., 2000; Slaný and Stuchlík, 2005; Stuchlík, 2005; Stuchlík et al., 2009).

$a/M = J/M^2 \in [0,1]$ is the dimensionless spin of the black hole – (Pugliese and Montani, 2013; Pugliese et al., 2013a). The relative properties of the functions $\ell_+(r;a)$ for the counterrotating and $\ell_-(r;a)$ for the corotating motions govern the possible existence of the double toroidal configurations (Pugliese and Stuchlík, 2015).

We consider two axially symmetric toroidal disks with symmetry plane coinciding with the equatorial plane of the central Kerr black hole. As fast (slow) attractors we will mean black holes with high (low) spin–mass ratio with respect to some limits provided on a/M by this analysis. The accretion tori corotate or counterrotate with respect to the central Kerr **BH**, for $\ell_- a > 0$ or $\ell_+ a < 0$, if $\ell_\pm$ is for example the fluid constant specific angular momentum. In the following we drop the notation $\mp$ when it will be not necessary to specify the fluid rotation. Considering the case of two orbiting tori, indicated by (i) and (o) respectively, we need to introduce the concept of *ℓcorotating* (ℓ**c**) tori, defined by the condition $\ell_i \ell_o > 0$, and *ℓcounterrotating* (ℓ**r**) tori, defined by the relations $\ell_i \ell_o < 0$. The two (ℓ**c**) couples can be both corotating, $\ell a > 0$, or counterrotating, $\ell a < 0$, with respect to the central Kerr attractor.

In the study of the accretion disk dynamics in the Kerr geometry, and in particular here for the (ℓ**r**) couples, it is important to consider the special radii, $R^\pm_{\mathbf{N}}$, determined by the geodesic characteristics of the Kerr spacetimes: the *marginally stable circular orbit*, $r^\pm_{mso}$, the *marginally bounded circular orbit*, $r^\pm_{mbo}$ and finally the *marginal circular orbit* $r^\pm_\gamma$ (which is also a photon circular orbit) (Pugliese et al., 2013b, 2011; Pugliese and Quevedo, 2015) – Fig. 1.

We assume **Condition 1**:

According to the symmetry conditions, the (stress) inner edge of the accretion torus is $r_\times \in]r_{mbo}, r_{mso}]$, while the torus is centered in $r_\odot > r_{mso}$, according to the geodesic structure determined by the attractor and the torus corotation or counterrotation with respect to this.

Condition 1 is consistent with most of the axially symmetric accretion torus models. Definition and constraints on the inner edge of the accretion torus and the center may be found in Krolik and Hawley (2002); Bromley et al. (1998); Abramowicz et al. (2010). The double system of accretion tori is then strongly constrained by the geodesic structure of the Kerr spacetimes. Solutions of the equations $r^\pm_i = r^\mp_j$ where $i \neq j$ and $r^\pm_i \in R^\pm_{\mathbf{N}}$ identify several notable spins $a_{\mathbf{N}}$ – see Fig. 1 – which distinguish several **BH** classes by some properties of the doubled torus system, as it will be discussed in Pugliese and Stuchlík (2017a). Here we introduce the system of special radii $\overline{R}^\pm_{\mathbf{N}} \equiv \{\overline{r}^\pm_{mbo}, \overline{r}^\pm_\gamma\}$ satisfying the equations $\ell^\pm_{mbo} \equiv \ell_\pm(r^\pm_{mbo}) = \ell_\pm(\overline{r}^\pm_{mbo})$, in other words is the second solution of the equation $\ell(r;a) = \ell^\pm_{mbo}$, similarly $\ell^\pm_\gamma \equiv \ell_\pm(r^\pm_\gamma) = \ell_\pm(\overline{r}^\pm_\gamma)$, which satisfies the relations $r^\pm_\gamma < r^\pm_{mbo} < r^\pm_{mso} < \overline{r}^\pm_{mbo} < \overline{r}^\pm_\gamma$–see Fig. (2). Accordingly, we introduce the three characteristic values of the spin: **(1)** $a_u \equiv 0.4740M : \overline{r}^+_{mbo} = \overline{r}^-_\gamma$, **(2)** $\tilde{a}_{\aleph} = 0.461854M : \overline{r}^-_{mbo} = r^+_{mso}$ and finally **(3)** $\check{a}_{\aleph} \equiv 0.73688M : \overline{r}^-_\gamma = r^+_{mso}$, which govern the relations of $\overline{R}^\pm_{\mathbf{N}}$ and $R^\pm_{\mathbf{N}}$.

While, according to **Condition 1**, there is $r_\times \in]r^\pm_{mbo}, r^\pm_{mso}[$, then, as demonstrated in Pugliese and Stuchlík (2015, 2016) for an accreting torusthere is $r^\pm_\odot \in]r^\pm_{mso}, \overline{r}^\pm_{mbo}[$. Whereas, for any "quiescent" torus, i.e. non accreting torus, there is $r_\odot > r_{mso}$, Figs 3,4. More detailed constraints of the location of $r_\times$ and $r_\odot$, particularly in the case of geometrically thick tori, are presented in Pugliese and Stuchlík (2015).

The **Condition 1** and the relations among $\overline{R}^\pm_{\mathbf{N}}$ imply the following statements.

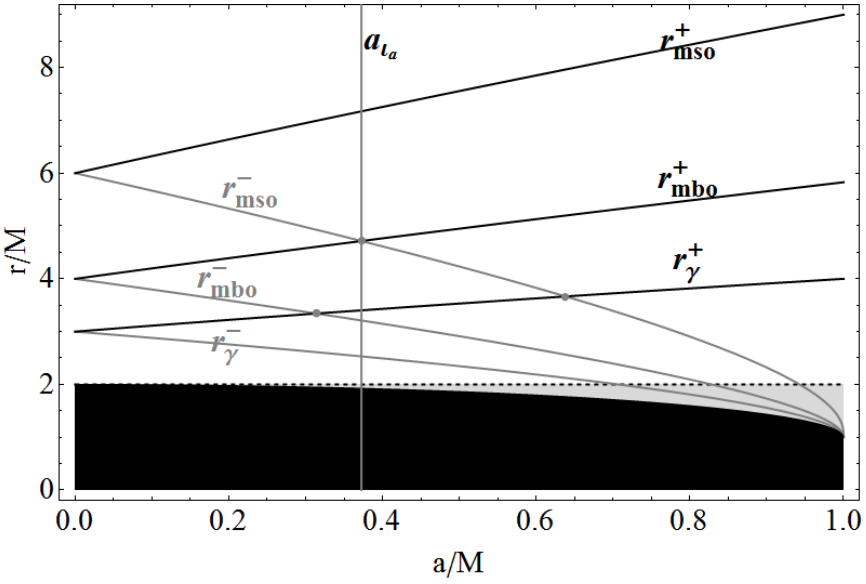

Figure 1. Geodesic structure of the Kerr geometry on the equatorial plane $\theta = \pi/2$. Radii $R^{\pm}_{\rm N} = \{r^{\pm}_{\gamma}, r^{\pm}_{mbo}, r^{\pm}_{mso}\}$ as function of the dimensionless spin $a/M \in [0, 1]$ of the central Kerr attractor: the marginally stable circular orbit $r^{\pm}_{mso}$, the *marginally bounded circular orbit* $r^{\pm}_{mbo}$ and finally the marginal (photon) circular orbit $r^{\pm}_{\gamma}$, for counterrotating (black curves) and corotating (gray curves) motion respectively. Black region is $r < r_+$, where r_+ is the outer Kerr horizon, gray region is the ergoregion or $r < r^+_{\epsilon}$, where $r^+_{\epsilon} = 2M$ (dashed line) is the outer ergosurface on the equatorial plane of the Kerr geometry.

3 ANALYSIS OF THE DOUBLE ACCRETION DISK SYSTEM

In the following, we present several statements that briefly represent results of our analysis of the doubled tori, while details on each of the presented cases will be provided elsewhere (Pugliese and Stuchlík, 2017a). We use the notation $\mathrm{C}^{\pm}$ for quiescent tori, $\mathrm{C}^{\pm}_{\times}$ for accreting tori, then $\mathrm{C}^{+}_{\times} < \mathrm{C}^{-}$ is the $(\ell\mathbf{r})$ couple of an inner counterrotating accreting torus and an outer corotating quiescent torus represented in Figs 3. We refer in the following to the analysis of Sec. (2) and particularly the **Condition I**.

Each torus is modeled by a perfect fluid, geometrically thick model, where the accretion phase (the start of accreting flow of matter towards the central **BH**) is driven by a the Paczynski-Wiita (P-W) mechanism of destabilization of gravo-dynamical equilibrium. This is a mechanism of violation of mechanical equilibrium of the tori, i.e. an instability in the balance of the gravitational and inertial forces and the pressure gradients in the fluid (Abramowicz and Fragile, 2013). The force balance in the tori is governed by the centrifugal, gravitational and pressure forces. A torus in accretion, $\mathrm{C}_{\times}$, is therefore as in Figs (3): the accretion onto the source occurs at the "cusp" $r_{\times}$ of the torus surface (the Boyer surface) where the hydrostatic pressure is vanishing and the particles fall freely under the action of the gravitational field towards the attractor. The cusp $r_{\times}$ is therefore the inner margin of the

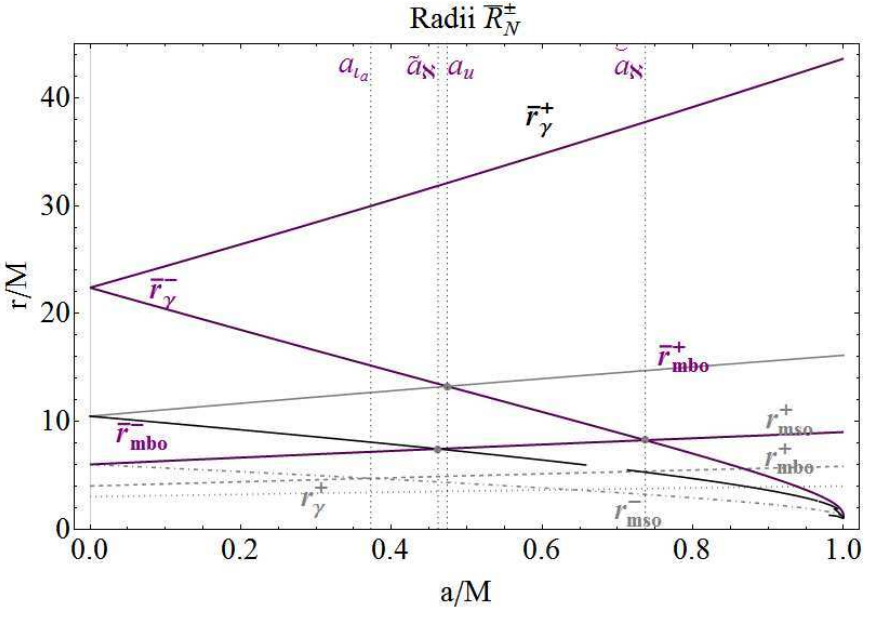

Figure 2. Radii $\bar{R}^{\pm}_{\mathbf{N}} = \{\bar{r}^{\pm}_{\gamma}, \bar{r}^{\pm}_{mbo}, \bar{r}^{\pm}_{mso}\}$ as function of the dimensionless spin $a/M \in [0, 1]$ of the central Kerr attractor, where $r^{+}_{\epsilon} = 2M$.

accreting tori. According to **Condition I** and following discussion in Sec. (2), the position of the torus with respect to the central **BH**, is regulated by the range of variation of the fluid angular momentum, which evidently regulates the centrifugal component of the torus force balance.

The larger is the fluid specific momentum magnitude, the far away from the central **BH** is the torus (i.e., the torus center $r_{\odot}$). Furthermore, a larger centrifugal component in the force balance acts in the sense to prevent the accretion, i.e. accretion is connected with a decrease in magnitude of the angular momentum of the fluid. This holds also for a general rotational law where, for example, dissipative effects as viscosity, resistivity, and the contribution of magnetic field are assumed. In the model adopted here for each torus, the centrifugal component is balanced with the gravitational and pressure components only. As such, in order the accretion instability to occur, the angular momentum magnitude has to be low "enough", namely $\mp\ell < \mp\ell^{\pm}_{mbo}$. We can also distinguish the emergence of accretion (unstable point $r_{\times}$) from the emergence of proto-jets, which are open cusped configurations not considered in this article–see Pugliese and Stuchlík (2016). For the low fluids angular momentum, $\mp\ell^{\pm} \in]\mp\ell^{\pm}_{mbo}, \mp\ell^{\pm}_{\gamma}[$, proto-jets appear as funnels of matter driven by the large centrifugal effects. Accretion occurs when $\ell \in [\ell_{mso}, \ell_{mbo}]$, with proper values of K parameter, which is related to the effective potential function regulating the fluid equilibrium. K is constrained according to the range of angular momentum. Because accretion occurs if $K = K_{\max} < 1$, where $K_{\max}$ corresponds to the maximum point of the associated effective potential (explicit definition can be found for example in Abramowicz and Fragile (2013);

Pugliese and Stuchlík (2015)), and the minimum point of the hydrostatic pressure. The larger is K, the bigger is the torus (the elongation in the equatorial plane).

For $r_\odot \gg r_{mso}$ there is $\ell > \ell_\gamma$ and the K parameter, related to the fluid elongation is bounded in the range $K < 1$, where $K = 1$ is the asymptotic value the effective potential. The gravo-hydrodynamic **P-W** instability cannot occur, and the Boyer surfaces are regular (absence of cusp)–see outer tori of Fig. (4). This situation corresponds to the absence of a minimum pressure point defining the unstable point of the torus from the point of view of the force balance condition. Concerning the location of the tori centers, in the development of the **RAD** model in Pugliese and Stuchlík (2015), radii $\bar{R}_N$ have been introduced. These radii, defined similarly to the set R_N, through the fluid angular momentum, set the location of tori centers according to the ranges of specific angular momentum and reflect the geodesic structure of the Kerr spacetime at greater distance.

Increasing the magnitude of the fluid specific angular momentum, the tori centers shift outwardly with respect to the black hole, the $\bar{R}_N$ are the boundaries of the regions where the centers are located according to given ℓ. Therefore, by considering $\bar{R}_N$, we can more precisely restrict the position of the torus center with respect to the central attractor. These conditions reflect of the geometrical structure of the Kerr spacetime and therefore they are describing purely general relativistic effect. Similar constraints are considered also in other models of accretion tori in presence of magnetic field or dissipative effects.

The main idea of the analysis presented below consists in verifying that the condition on force balance in the tori, is fulfilled for a couple of tori to form and for accretion from them to occur. Here we reduce the problem to the analysis of the set of parameters, ℓ and K,–details on this approach are thoroughly discussed in Pugliese and Stuchlík (2015, 2016); Pugliese and Stuchlik (2018); Pugliese and Stuchlík (2017b). A great advantage of this approach is that this makes the torus analysis simpler, providing an immediate way to fix constraints, and eventually to provide tori as initial configurations for more general GRMHD models. On the other side, *ranges* of variation for the specific angular momentum of the fluids and the parameter K are provided. Finally, from the methodological point of view, it is clear that given the **Conditions I**, part of the analysis refers to the geodesic structure of Kerr's geometry, defined by the radii $r_i^\pm \in R_{\mathbf{N}}^\pm$, limiting the location of the critical points of the hydrostatic pressure in the torus (this holds also for other torus models where the edge of the accretion torus is in the range $[r_{mso}, r_{mbo}]$). The angular momentum fixes also the constraints on K and therefore the outer edge of the torus. As the possibility for accretion to occur is regulated by the range of variation of fluid angular momentum, and the fluid angular momentum regulates also the location with respect to the central **BH**, of the radii $R_{\mathbf{N}}^\pm$, then, we may set constrains for accretion directly to the condition on $R_{\mathbf{N}}^\pm$ rather then to the angular momentum range. For an accurate description of how these procedures are applied we refer to Pugliese and Stuchlík (2017b). Further details, particularly on the role of the radii $R_{\mathbf{N}}^\pm$ could be found in Pugliese and Stuchlík (2016), while more discussion is in Pugliese and Stuchlik (2018).

(1) **Quiescent tori** Two equilibrium (quiescent) tori, ($\ell\mathbf{c}$) or ($\ell\mathbf{r}$), can exist in the spacetime of any Kerr attractor, if their specific angular momenta are properly related (Pugliese and Stuchlík, 2017a).

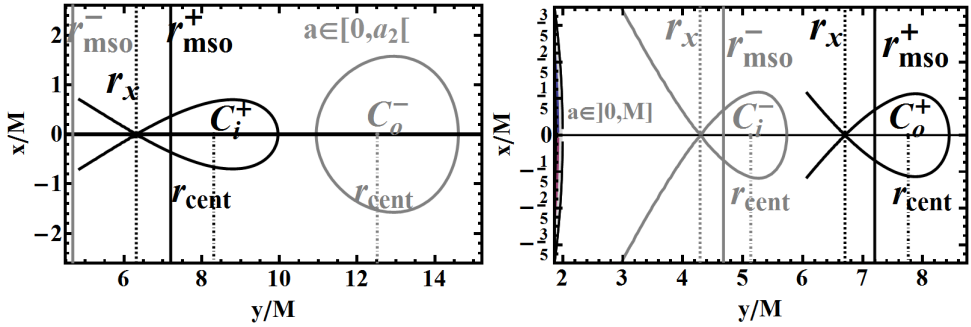

Figure 3. ℓcounterrotating couple of accretion torus orbiting a central Kerr black hole attractor with spin $a = 0.382M$. Cross sections on the equatorial plane of the Roche lobes corresponding to a couple made by an inner counterrotating torus C_i^+ in accretion and an outer corotating torus C_o^- (*left*), and a couple made by an inner corotating quiescent C_i^- torus and an outer counterrotating torus C_o^+, being in accretion (*right*). In couples (C_i^+, C_o^-) with an inner torus in accretion, an outer torus may be formed around any Kerr attractor with $a \in [0, M]$ but only for $a \in [0, \tilde{a}_{\aleph}[$, the outer corotating torus of the couple may reach the condition for instability. Couples (C_i^-, C_o^+) with one or both tori in accretion may exist around any Kerr attractor (excluding the Schwarzschild limit $a = 0$ for a static attractor). This illustrative case was obtained by integrating the equations for the Boyer surfaces in the general relativistic model of thick accretion tori in the Kerr geometry, with constant fluid specific angular momentum – see for example Pugliese and Stuchlík (2015, 2016): $r^{\pm}_{mso}$ are the marginally stable circular orbits for counterrotating and corotating matter respectively, $r_{\times} \in]r_{mbo}, r_{mso}[$ locates the inner edge of the accreting torus, r_{mbo} is the marginally bounded orbit, $r_{\odot}$ is the center of the correspondent Roche lobe (point of maximum hydrostatic pressure), and (x, y) are Cartesian coordinates. For the case of a couple (C_i^+, C_o^-) (*left*) accretion phase is possible *only* for the inner counterrotating torus (according to **Condition 1**). In the couple (C_i^-, C_o^+) (*right*) the inner C_i^- torus may accrete onto the attractor, or accretion may emerge from the outer counterrotating torus C_o^+, or both the tori can accrete, as shown in picture. Eventually in both cases, (C_i^+, C_o^-) and (C_i^-, C_o^+) collision between the Roche lobes of the tori is in general possible.

(2) **The Schwarzschild attractor and the corotating accreting torus: constraints** If a corotating toroidal disk is accreting onto the Kerr black hole, or if the attractor is *static* ($a = 0$), there *cannot* exist any inner (corotating or counterrotating) torus between the outer accreting torus and the attractor. Then an outer, quiescent corotating torus can exist as is illustrated in Fig. 4–*right* ((ℓ**c**)couples), or an outer counterrotating, quiescent or accreting disk can exist as illustrated in Fig. 3–*right*.

(3) **Kerr attractor and presence of a counterrotating accreting torus.** If the accreting torus is *counterrotating* with respect to the Kerr attractor, there is *no* inner (the closest to the attractor) counterrotating torus between the attractor and the outer accreting torus, only outer quiescent corotating and counterrotating torus can exist as illustrated in Fig. 3–*left* and Fig. 4–*left* respectively.

(4) **Location of the accreting torus: the Schwarzschild case and the (ℓc) versus (ℓr) cases.** For two (ℓ**c**) tori, or if the attractor is static, two orbiting tori cannot *both* be in accretion, neither the *outer* torus of the couple may be in accretion, only the inner torus can

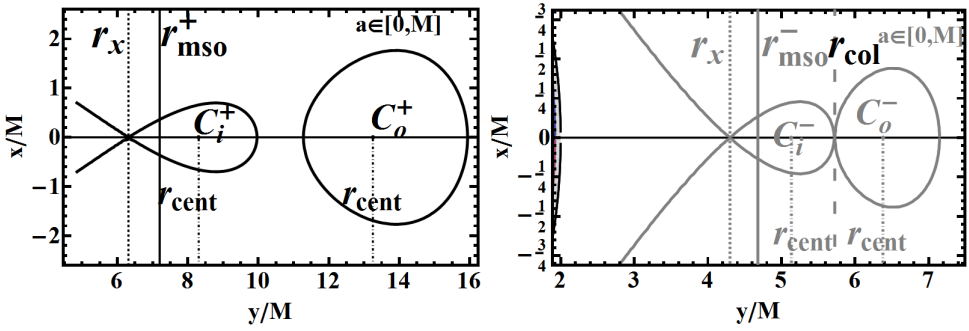

Figure 4. **ℓcorotating couple** of accretion torus orbiting a central Kerr black hole attractor with spin $a = 0.382M$. Cross sections on the equatorial plane of the Roche lobes correspondent to a couple of counterrotating tori (C^+_i, C^+_o) (*left*), and corotating tori (C^-_i, C^-_o) (*right*), (x, y) are Cartesian coordinates. These couples with inner accreting tori may be formed around any Kerr black hole central attractor. Roche lobes are obtained as solutions for Boyer equipotential surfaces in the general relativistic model of thick accretion tori in the Kerr geometry, with constant fluid specific angular momentum – see for example Pugliese and Stuchlík (2015, 2016): $r^{\pm}_{mso}$ are the marginally stable circular orbits for counterrotating and corotating matter respectively, r_{mbo} is the marginally bounded orbit, $r_{\odot}$ is the center of the Roche lobe (point of maximum hydrostatic pressure), $r_{\times} \in]r_{mbo}, r_{mso}[$ locates the inner edge of the accreting torus. For an **(ℓc)** couple accretion may emerge only from the inner torus. Collision between the Roche lobes of the tori, here shown for the couple (C^-_i, C^-_o) (*right*), may be possible in any **(ℓc)** couples.

be accreting as demonstrated in Fig. 4. In the **(ℓr)** couple, an accreting corotating torus *must be* the inner one of the couple. This implies that a possible outer torus may be corotating (non accreting), or counterrotating (which may be in accretion under proper conditions) with respect the central black hole – Fig. 3.

(5) **Focusing on the corotating torus of the couple.** A corotating torus can be the outer of a couple where the inner accreting torus is counterrotating with respect to the Kerr black hole – Fig. 3–*left*. In this case the outer corotating torus *cannot be* accreting, for *before* this occurs, the outer corotating torus starts to collide and eventually merges with the inner counterrotating torus.

(6) **The couple made by an inner accreting counterrotating torus and an outer corotating torus.** The system consisting of an inner accreting counterrotating torus and an outer equilibrium corotating torus may be formed in any spacetime, but the faster is the attractor, the farther away should be the outer torus. This also implies the outer torus has large specific angular momentum Pugliese and Stuchlík (2015, 2017b); Pugliese and Stuchlik (2018); Pugliese and Stuchlík (2017a). In this couple *only* the inner counterrotating torus can accrete onto the attractor – Fig. 3–*left*. We can particularize these arguments by saying that the corotating torus can be "close" to the phase of accretion (say here $r_{\times} \gtrapprox r^-_{mso}$), before the merge may occur, only in the geometries of attractors with dimensionless spin $a \lesssim \tilde{a}_{\aleph}$. Collision between the tori may occur if $a \approx \tilde{a}_{\aleph}$ – see Pugliese and Stuchlík (2017b).

(7) **Double accretion I: couple** $C_\times^- < C_\times^+$ If a counterrotating torus is accreting onto the central black hole there could be an inner corotating torus, which may even accrete onto the spinning attractor – see Fig. 3– *right*. However, the lower is the Kerr black hole dimensionless spin, say $a \lessapprox a_u$, the lower must be the corotating torus specific angular momentum (Pugliese and Stuchlík, 2017b).

(8) **Double accretion II** Remarkably, both the inner corotating torus of the couple and the outer counterrotating one of a couple can accrete onto the attractor. In an (ℓ**r**) couple, a corotating torus can be accreting onto the attractor only if it is the *inner* of the couple where the outer counterrotating torus can be in equilibrium or in accretion – Fig. 3–*right*. A counterrotating torus can therefore reach the instability being the inner or the outer torus of an (ℓ**r**) couple.

(9) **Summary: the situation for a torus in accretion** For a torus in accretion the following two cases may occur: **a)** for a *static* attractor only the *inner* torus may accrete, while the outer of the couple has to be in equilibrium. A torus collision occurs before the outer torus may accrete. This is the former point 2. **b)** if the torus is orbiting a Kerr attractor then we need to distinguish the case of a corotating torus from that of a counterrotating one. **b-I** If the accreting torus is corotating with respect to the central Kerr black hole then the following two cases may occur: **b-I-i)** The accreting corotating torus is the inner torus of a (ℓ**c**) couple, and the other corotating torus should be outer and in equilibrium – Fig. 4–*right*. **b-I-ii)** The accreting corotating torus can be the *inner* of an (ℓ**r**) couple where the outer torus is counterrotating and can be in equilibrium or in accretion – Fig. 3-*right*. **b-II)** If, on the other hand, the accreting torus is counterrotating, three situations may arise. **b-II-i)** The counterrotating accreting torus can be the inner of a (ℓ**c**) couple where the outer one is in equilibrium, as follows from point 3 – see Fig. 4–*left*. **b-II-ii)** the counterrotating accreting torus may be the inner of an (ℓ**r**) couple where the outer one, corotating with respect to the black hole, has to be in equilibrium – Fig. 3–*left*. The outer torus is close to the conditions for accretion only for slow attractors with $a < \tilde{a}_\aleph$. **b-II-iii)** The counterrotating accreting torus can be the *outer* of an (ℓ**r**) couple where the inner corotating torus may be in equilibrium or in accretion – Fig. 3–*right*.

(10) **Summary: the (ℓr) couples** Focusing on the (ℓ**r**) couples, suppose that a *counterrotating* torus will first be formed around a Kerr attractor. This could be therefore the inner torus of a possible couple. Then we know that *only* the inner torus may accrete onto the attractor, no outer corotating or counterrotating torus can reach the instable phase in this double system. In the geometries of the fast Kerr attractors, with dimensionless spin $a \gtrapprox \breve{a}_\aleph$, the outer corotating torus of the (ℓ**r**) couple should be far enough from the attractor to avoid collision (for example for the perfect fluid thick torus model this would imply $\ell > \ell_\gamma^-$ and $r_\odot > \overline{r_\gamma}$ – (Pugliese and Stuchlík, 2016)). The slower is the attractor, the closest can be the outer corotating torus (at generally lower specific angular momentum). If, on the other hand, an inner *corotating* torus will first be formed and it is accreting onto the central Kerr black hole, then an outer torus may be formed in any Kerr spacetime, it can be corotating or counterrotating. In this last case the outer torus can be also in accretion We have set out the range of location of the center $r_\odot$ through an assessment on the limits of variation of the specific angular momentum of the fluid, ℓ, that has been especially studied for the geometrically thick torus model. This boosted precision in the limiting spins serves us only as an example of application of these results – (Pugliese and Stuchlík, 2017b).

(11) **Emergence of the instability in a couple** Considering the emergence of possible accretion phase, in all $a \in [0, M]$ geometries collision is possible under appropriate constraints, but for some cases collision is inevitable following the emergence of the unstable phases of accretion of one or both configurations of the couples. For $a \in [0, M]$ ($\ell\mathbf{c}$) couples $\mathrm{C}^{\pm} < \mathrm{C}^{\pm}_{\times}$ cannot exist (merging with the outer equilibrium torus would precede the formation of this doubled system), while the ($\ell\mathbf{c}$) couples, $\mathrm{C}^{\pm}_{\times} < \mathrm{C}^{\pm}$ and $\mathrm{C}^{-}_{\times} < \mathrm{C}^{\pm}$ may be formed. The ($\ell\mathbf{r}$) couple $\mathrm{C}^{-}_{\times} < \mathrm{C}^{+}_{\times}$ is possible in $a \in]0, M]$: in the case of a static attractor, described by the Schwarzschild geometry, there is $R^{+}_{\mathbf{N}} = R^{-}_{\mathbf{N}}$ and the **($\ell\mathbf{r}$)** couples must fulfill the constraints of the ($\ell\mathbf{c}$) couples. In the geometries $]\tilde{a}_{\mathbf{N}}, M[$ only the ($\ell\mathbf{r}$) couples where $\mathrm{C}^{+}_{\times} < \mathrm{C}^{-}$ or $\mathrm{C}^{+} < \mathrm{C}^{-}$, with C^{-} close to accretion may exists .

(12) **Summary** To summarize our analysis, we identify two classes of Kerr attractors, distinguished according to the features of the orbiting **($\ell\mathbf{r}$)** couples: **a)** The fast attractors, with dimensionless spin $a \in]\tilde{a}_{\mathbf{N}}, M]$ where there are no **($\ell\mathbf{r}$)** couples, $\mathrm{C}^{+}_{\times} < \mathrm{C}^{-}$ or $\mathrm{C}^{+} < \mathrm{C}^{-}$, with an outer corotating torus close to the accretion phase – point 6 and Fig. 3–*left* The faster is the Kerr attractor ($a \gtrapprox \breve{a}_{\mathbf{N}}$) the farther away should be the outer torus with large specific angular momentum to prevent collision – point 9. The attractors with $a > a_u > \tilde{a}_{\mathbf{N}}$, where the outer counterrotating torus of the **($\ell\mathbf{r}$)** couples $\mathrm{C}^{-} < \mathrm{C}^{+}_{\times}$ are possible in different conditions on the fluid specific angular momentum and the inner torus may be in accretion, as in Fig. 3-*right*, or quiescent – see point 7. **b)**. The slow attractors, with dimensionless spin $a \in [0, \tilde{a}_{\mathbf{N}}[$: in these geometries an outer torus of a $\mathrm{C}^{+}_{\times} < \mathrm{C}^{-}$ couple may be close to the accretion phase–Fig. 3–*left* point 6. In the field of attractors with $a < a_u$ the outer counterrotating torus may form a $\mathrm{C}^{-} < \mathrm{C}^{+}_{\times}$ couple where the inner torus can be eventually in accretion – see Fig. 3–*right*, but with sufficiently low specific angular momentum. Finally, Schwarzschild attractors ($a = 0$) are characterized by **($\ell\mathbf{r}$)** or **($\ell\mathbf{c}$)** doubled systems where only the inner torus can be in accretion as illustrated in Figs 4 or Figs 3–*left*. In fact, the geometric properties of the static spacetimes do not differentiate doubled systems according to the relative rotation of the two tori (point 2).

4 CONCLUSIONS

We proved that only specific couples of toroidal accretion tori may orbit around a central Kerr black hole attractor: each torus is constrained by the presence of the second torus of the couple accordingly with the restriction provided by the Kerr background geometry. Analogously, collisions between tori and then merging arise, especially in the emergency of the unstable phases of the single torus evolution, which leads ultimately to the accretion into the central Kerr black hole. As a consequence of this the accretion of a single torus would in fact be preceded by a necessary merging with the torus companion. For all these reasons, the existence of the double torus systems appear to be in general strongly constrained and, ultimately, such a configurations are possible only in few situations and under specific circumstances. Essential in this respect is the relative rotation of the tori in the couple, and the rotation with the respect to the central attractor.

The torus couples may be formed during different stages of the black hole life, interacting with the surrounding matter for tidal disruption of a star or resulting from some gas clouds

(Nixon et al., 2012, 2013; Dunhill et al., 2014; Alig et al., 2013; King and Pringle, 2007, 2006; Krolik and Hawley, 2002; Miller et al., 2015).

The setup provided in this letter provides the necessary conditions for the formation of these doubled configurations, and we expect they could be the starting point for further analysis in future investigations which may focus on their formation and especially the associated phenomenology. The unstable phases of such configurations, we expect, may reveal of some significance for the high energy astrophysics related especially to accretion onto supermassive black holes, and the extremely energetic phenomena occurring in quasars and AGN that could be observable by the planned X–ray observatory ATHENA [2].

ACKNOWLEDGEMENTS

D. P. acknowledges support from the Junior GACR grant of the Czech Science Foundation No:16-03564Y.

Z. S. acknowledges the Albert Einstein Centre for Gravitation and Astrophysics supported by grant No. 14-37086G.

APPENDIX A: SOME NOTES ON THE GRAPHS FORMALISM

In this section we add some notes on the graph formalism introduced in Pugliese and Stuchlík (2016) and extensively used in Pugliese and Stuchlík (2017b,c); Pugliese and Stuchlik (2018); Pugliese and Stuchlík (2017a). The adoption of these schemes have proved to be an useful tool in the determination of the system states, as defined more precisely below, and especially in the investigation of tori evolutions as transition from different states: from the initial equilibrium (non accretion) state to accretion or collision or, eventually, tori collision where with one or two tori in accretion. Details concerning the graphs for a tori couple of Figs 4 and 3 have been extensively discussed in Pugliese and Stuchlík (2017b), here we discuss some general aspects of the graph formalism clarifying some relevant notions. As seen in Sec. (3), toroidal tori are related by boundary conditions dictated by the requirement of not penetration of matter (no tori overlapping) and by the geometric constraint for the equilibrium configurations determined by the geometric properties of the Kerr background. These conditions however have to be relaxed to consider the case of tori collision in the macro–structure. We distinguish four types of unstable couples of orbiting configurations (or unstable *states* of the macro–configurations): **(I)** the *proto jet–proto jet* systems, corresponding to couples of open cusped surfaces, **(II)** the *proto jet–accretion* systems, where the proto–jet can follow or precede the accretion point, and finally the **(III)** *accretion–accretion* systems, where matter can accrete onto the attractor from several instability points. However, not all these states can actually exist. We have proved that states formation and stability depend on the dimensionless spin of the attractor, the tori relative rotation respect to the central **BH**, and the relative rotation of the fluids in the tori (i.e. if they are ℓcorotating or ℓcounterrotating).

[2] http://the-athena-x-ray-observatory.eu/

The five fundamental states, constituted by the **(I)** − −**(II)** and **(III)** couples constituted by all unstable configurations, and **(IV)** *proto jet–non–accreting* configurations, **(V)** *accreting –non–accreting* tori can be combined for **RADs** made up by more that two tori. In this framework, the exploration of the internal dynamics of the macrostructure required the introduction of the notion of *geometrical correlation* between two configurations of a state, when the two surfaces may be in contact, in accordance with the constraints of the system (Pugliese and Stuchlík, 2016), then feeding or collision phenomena happen, leading eventually to a transition of the couple state and, in the end, of the entire macro–configuration. As a consequence of this, we face the problem of the *state evolution* i.e. the initial couple of configurations (starting state) evolves towards a transition from a stable solution to unstable one or viceversa. This analysis has lead to conclusion for example that in some cases equilibrium configurations can only lead to proto–jet configurations and not to the accretion.

More specifically, two sub–configurations of a **RAD** are said to be geometrically correlated if they may be in contact according to some constraints settled on their morphological or stability evolution. A part of the **RAD** analysis is therefore dedicated to establish the possible geometric correlation of tori in the macrostructure giving a number of features set in advance. It is clear that a geometrical correlation in a ringed structure induces a causal correlation in a couple, when the morphology of an element can be regarded as a result of that correlation, in the instability such as collision. On the other hand, causally correlated tori are tied by penetration of matter, which implies necessarily a geometric interaction between two sub–configurations.

Graph schemes essentially serve to represent the evolution of a couple, constituting the internal structure of a **RAD**, thus below we introduce two important concepts regarding the accretion torus dynamics in a state.

(a) the configuration sequentiality: the relative locations of the tori centers (the *sequentiality* of the centers), **(b)** the relative location of the possible instability points (the *sequentiality* of the maximum points of the effective potential).

It is useful then to use the schemes in Fig. A1, where five main states, with at least one unstable (with the cusp), are sketched. The different states for the ℓcorotating couples and the ℓcounterrotating ones are specified in Pugliese and Stuchlík (2017b), discussing the evolution of the possible individual configurations, from the initial state to a final one, following the *evolutive lines* of Fig. A1, which actually represent transitions between (main) states of the couple, which are represented by the *state lines* of Fig. A1. The analysis of **RAD** can be supported by the construction of these diagrams and the determination of the constraints of the *evolutive* and *state lines*. Not all the initial and final states are possible and not all the evolutive lines are actually possible for different attractors. Schemes of the main classes of Fig. A1 can be seen as *graphs* (see for example Trudeau (1993)), each of the five main classes being therefore featured in the graphs. More precisely each scheme is a vertex labeled graph that, we say, is *centered* on a main state (circle vertexes in Fig. A1) on which all the evolutive lines converge (point) or diverge. The evolutive lines are then oriented with the head and tail into two vertexes of the graph. There are two classes of lines: the evolutive lines which are oriented, and the state lines which are not oriented (in Fig. A1). Evolutive lines divide the graph into two parts centered around the center, namely in the *antecedent section*, from which the heads of the arrows converging at the center start,

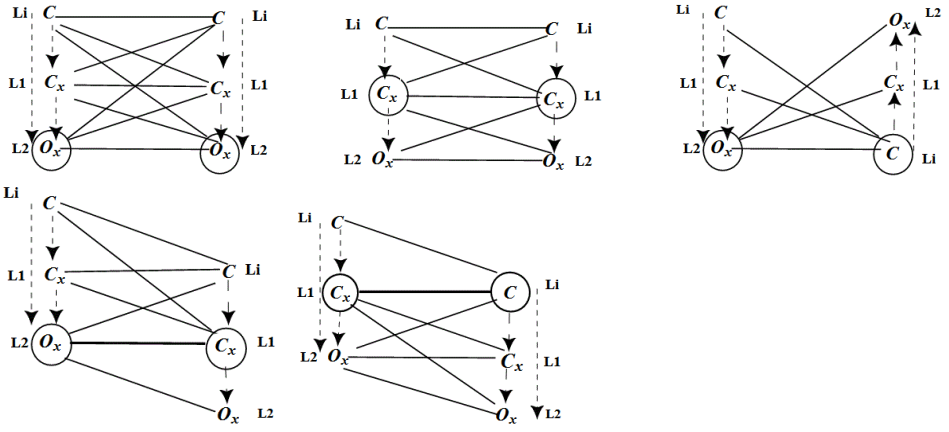

Figure A1. The five possible main states with at least one unstable configuration, for a couple (circled) of the classes C, O, O_x and C_x. The stability is fixed but not the rotation with respect to the black hole, nor the sequentiality, according to the location of the maximum pressure points (>). Dashed arrow–lines (evolutive lines) show the evolution of the possible individual configuration, and start from the initial main state and point to the ending. Black continuum lines indicate the status of the couple in a specific evolutionary phase of the couple. States with fixed sequentiality are represented by black lines with arrows, the direction of the arrow is in accordance to the sequentiality relation, in the order of configuration (and criticality). Where uniquely fixed, the region of specific angular momentum is indicated close to each configuration. All the possible initial and final states of the evolutive lines to and from the circled couple are shown.

and the *subsequent section* which is the one onto which the evolutive lines starting from the center of the graph or crossing the center, with head in the antecedent section, converge, see Fig. A1. Two vertices can be connected by two evolutive lines pointing in the same direction (section), with different paths (however we assume throughout this work that the specific angular momentum and the K–parameter, whose variations determine the transition from a stable to an unstable solution, do vary continuously). A graph may also have only one section, for example the first graph centered on the principal state of open configurations $O_x - O_x$, where the only existing section is the antecedent one and then all the evolutive lines converge at the central state. A vertex can also belong to the states, and therefore vertexes, of two different sections. That is, it can be connected to vertexes in a main state from which evolutive lines, having the opposite direction, start. However, an evolutionary line has only one possible orientation: an evolutionary loop that here means a return to a previous state for the same vertex is not considered (Pugliese and Stuchlík, 2016, 2017b). As discussed in the text, this process may be possible, for example transition $C \dashrightarrow C_x \dashrightarrow C$. Two vertexes can be connected by two evolutive lines, say one is a composition of (only) two evolutive lines connecting one vertex (the head) to a third vertex and the second line connecting this vertex to the second one (the tail), which is a composition of more lines representing different steps. State lines are not oriented in the graphs (of the main states). A state line has usually two possible ordinations, the sequen-

tiality, of minimum or maximum respectively, then the lines are directed and undirected in this sense. We note that symmetry relations are not generally possible in the state lines, as in details discussed Pugliese and Stuchlík (2016); Pugliese and Stuchlik (2018). For each center, the graph in Fig. A1 is the one with the maximum number of vertices and lines. Then, we shall often eliminate some evolutive and the state lines of the graphs in Fig. A1, because they are not permitted for example in accretion tori around particular classes of attractors. The vertices are not completely labeled because there is missing the information on the specific angular momentum, in the case of equilibrium. We allow here to decorate a graph, to specify the labels and other characteristics such as the line orientation. If all the possible information on the graph of a main state are provided, for example when we have identified a state element of the main state, the decorated graph is said saturated for complete decoration. In some cases the state of a system can remain indeterminate also after complete decoration – Fig. A1. All the vertices of the graphs are associated with lines. One can see the five graphs connected by state lines as a *macro–graph* connecting states. In fact, one can realize this just fixing up a center of a graph, and connect that to the other graphs looking for the same main state in the graphs centered in different states. All five graphs have degree or valency (i.e, number of vertices) six, vertex labels can be repeated for more vertex. The seed main states here have orders of composition $n = 2$, no loops through state lines are possible. It is not excluded that such loops may be introduced when one use the five classes as a seed of a decomposition of higher order. A vertex can be associated to one and only one value of sequentiality according to the maximum points and the minimum points of the effective potential. Thus these graphs are simple, i.e., not oriented according to the sequentiality of the state lines, but they are not simple according to the evolutive lines.

Eventually one can use the vertex colored graph notion combining two colors according to the signs of rotation relative to the attractor, a different chromaticity associated with a status line would correspond to a ℓcounterrotating couple, an equal chromaticity to a ℓcorotating couple. In this discussion, vertices connected or crossed by an evolutive line, pertain at an equal chromaticity. Thus if the center of the graph is monochrome then the entire graph is monochrome, and vice versa, if the center is dichromatic then the entire graph is dichromatic (intending the color of its vertices). Generally, we consider mixed graphs because we cannot always define the order to the state lines. On the other hand, since the different options of evolution are marked by different evolutive lines, this uncertainty is not rendered in a the mixed graph while remaining after the decoration. Instead, while not changing the stability during the evolution, one could think possible the evolutive line to change the sequentiality of the state line, but actually an evolutive line must represent transitions between monochromatic vertices (configurations), not changing, at fixed vertices, the sequentiality of the state line according to the minimum points of the effective potential, in fact this would imply an overlapping of matter and, similarly, in the evolution of a monochromatic state the sequentiality according to the instability points is conserved , but it not necessarily conserved for a dichromatic state as it is explained in Pugliese and Stuchlík (2015). Two vertices are not always connected neither by an evolutive line or by a state line, while the two sections of a graph are always connected by evolutive lines crossing its center.

To give an example of the mechanism, we concentrate on Fig. (A1) picturing a graph centered on the couple $C_{\times}^{-} < C\times^{+}$ featuring a double accretion. Here we specified the indication of the fluids rotation and accordingly, the sequentiality, following the analysis in Sec.(3) which constraints a double accretion to this specific couple only. This graph has an antecedent part represented by the vertices of two quiescent tori. The initial state can be represented according to constraints on fluids angular momentum and eventually the **BH** spin by any black line before the center, therefore the initial state may be formed by two quiescent tori or one quiescent torus and an accreting one of the center couple, different lines are for different sequentialities. Couple evolution follows according to the dashed lines, from one or two equilibrium tori to the state of two accreting tori. Eventually the center state may evolve towards the subsequent section of the graph, for a further transition. This graph-case may be found as colored graph in Pugliese and Stuchlík (2017b).

REFERENCES

Abramowicz, M. A. and Fragile, P. C. (2013), Foundations of Black Hole Accretion Disk Theory, *Living Rev. Rel.*, **16**, p. 1, arXiv: 1104.5499.

Abramowicz, M. A., Jaroszyński, M., Kato, S., Lasota, J.-P., Różańska, A. and Sądowski, A. (2010), Leaving the innermost stable circular orbit: the inner edge of a black-hole accretion disk at various luminosities, *Astronomy and Astrophysics* , **521**, A15, arXiv: 1003.3887.

Alig, C., Schartmann, M., Burkert, A. and Dolag, K. (2013), Numerical Simulations of the Possible Origin of the Two Sub-parsec Scale and Counterrotating Stellar Disks around SgrA*, *The Astrophysical Journal* , **771**, 119, arXiv: 1305.2953.

Bromley, B. C., Miller, W. A. and Pariev, V. I. (1998), The inner edge of the accretion disk around a supermassive black hole, *Nature* , **391**, p. 54.

Carmona-Loaiza, J. M., Colpi, M., Dotti, M. and Valdarnini, R. (2015), Overlapping inflows as catalysts of AGN activity - II. Relative importance of turbulence and inflow-disc interaction, *Monthly Notices of the Royal Astronomical Society* , **453**, pp. 1608–1618, arXiv: 1508.00022.

Dunhill, A. C., Alexander, R. D., Nixon, C. J. and King, A. R. (2014), Misaligned accretion on to supermassive black hole binaries, *Monthly Notices of the Royal Astronomical Society* , **445**, pp. 2285–2296, arXiv: 1409.3842.

Dyda, S., Lovelace, R. V. E., Ustyugova, G. V., Romanova, M. M. and Koldoba, A. V. (2015), Counter-rotating accretion discs, *Monthly Notices of the Royal Astronomical Society* , **446**, pp. 613–621, arXiv: 1408.5626.

Karas, V. and Sochora, V. (2010), Extremal Energy Shifts of Radiation from a Ring Near a Rotating Black Hole, *The Astrophysical Journal* , **725**, pp. 1507–1515, arXiv: 1010.5785.

King, A. R. and Pringle, J. E. (2006), Growing supermassive black holes by chaotic accretion, *Monthly Notices of the Royal Astronomical Society* , **373**, pp. L90–L92, arXiv: astro-ph/0609598.

King, A. R. and Pringle, J. E. (2007), Fuelling active galactic nuclei, *Monthly Notices of the Royal Astronomical Society* , **377**, pp. L25–L28, arXiv: astro-ph/0701679.

Krolik, J. H. and Hawley, J. F. (2002), Where Is the Inner Edge of an Accretion Disk around a Black Hole?, *The Astrophysical Journal* , **573**, pp. 754–763, arXiv: astro-ph/0203289.

Miller, J. M., Kaastra, J. S., Miller, M. C., Reynolds, M. T., Brown, G., Cenko, S. B., Drake, J. J., Gezari, S., Guillochon, J., Gultekin, K., Irwin, J., Levan, A., Maitra, D., Maksym, W. P., Mushotzky, R., O'Brien, P., Paerels, F., de Plaa, J., Ramirez-Ruiz, E., Strohmayer, T. and Tanvir,

N. (2015), Flows of X-ray gas reveal the disruption of a star by a massive black hole, *Nature* , **526**, pp. 542–545, arXiv: 1510.06348.

Nixon, C., King, A. and Price, D. (2013), Tearing up the disc: misaligned accretion on to a binary, *Monthly Notices of the Royal Astronomical Society* , **434**, pp. 1946–1954, arXiv: 1307.0010.

Nixon, C., King, A., Price, D. and Frank, J. (2012), Tearing up the Disk: How Black Holes Accrete, *Astrophysical Journal Letters* , **757**, L24, arXiv: 1209.1393.

Pugliese, D. and Montani, G. (2013), Squeezing of toroidal accretion disks, *EPL (Europhysics Letters)*, **101**, p. 19001, arXiv: 1301.1557.

Pugliese, D. and Montani, G. (2015), Relativistic thick accretion disks: Morphology and evolutionary parameters, *Phys. Rev. D* , **91**(8), 083011, arXiv: 1412.2100.

Pugliese, D., Montani, G. and Bernardini, M. G. (2013a), On the Polish doughnut accretion disc via the effective potential approach, *Monthly Notices of the Royal Astronomical Society* , **428**, pp. 952–982, arXiv: 1206.4009.

Pugliese, D. and Quevedo, H. (2015), The ergoregion in the Kerr spacetime: properties of the equatorial circular motion, *European Physical Journal C*, **75**, 234, arXiv: 1409.7652.

Pugliese, D., Quevedo, H. and Ruffini, R. (2011), Equatorial circular motion in Kerr spacetime, *Phys. Rev. D* , **84**(4), 044030, arXiv: 1105.2959.

Pugliese, D., Quevedo, H. and Ruffini, R. (2013b), Equatorial circular orbits of neutral test particles in the Kerr-Newman spacetime, *Phys. Rev. D* , **88**(2), 024042, arXiv: 1303.6250.

Pugliese, D. and Stuchlík, Z. (2015), Ringed Accretion Disks: Equilibrium Configurations, *The Astrophysical Journal Supplement*, **221**, 25, arXiv: 1510.03669.

Pugliese, D. and Stuchlík, Z. (2016), Ringed Accretion Disks: Instabilities, *The Astrophysical Journal Supplement*, **223**, 27, arXiv: 1603.00732.

Pugliese, D. and Stuchlík, Z. (2017a), Relating Kerr SMBHs in Active Galactic Nuclei to RADs configurations, submitted, .

Pugliese, D. and Stuchlík, Z. (2017b), Ringed Accretion Disks: Evolution of Double Toroidal Configurations, *The Astrophysical Journal Supplement*, **229**, 40, arXiv: 1704.04063.

Pugliese, D. and Stuchlík, Z. (2017c), submitted, .

Pugliese, D. and Stuchlik, Z. (2018), Tori sequences as remnants of multiple accreting periods of Kerr SMBHs, *JHEAp*, **17**, pp. 1–37, arXiv: 1711.04530.

Slaný, P. and Stuchlík, Z. (2005), Relativistic thick discs in the Kerr de Sitter backgrounds, *Classical and Quantum Gravity*, **22**, pp. 3623–3651.

Sochora, V., Karas, V., Svoboda, J. and Dovčiak, M. (2011), Black hole accretion rings revealed by future X-ray spectroscopy, *Monthly Notices of the Royal Astronomical Society* , **418**, pp. 276–283, arXiv: 1108.0545.

Stuchlík, Z. (2005), Influence of the RELICT Cosmological Constant on Accretion Discs, *Modern Physics Letters A*, **20**, pp. 561–575, arXiv: 0804.2266.

Stuchlík, Z., Slaný, P. and Hledík, S. (2000), Equilibrium configurations of perfect fluid orbiting Schwarzschild-de Sitter black holes, *Astronomy and Astrophysics* , **363**, pp. 425–439.

Stuchlík, Z., Slaný, P. and Kovář, J. (2009), Pseudo-Newtonian and general relativistic barotropic tori in Schwarzschild-de Sitter spacetimes, *Classical and Quantum Gravity*, **26**(21), 215013, arXiv: 0910.3184.

Trudeau, R. J. (1993), *Introduction to Graph Theory*, Dover Pub., ISBN 978-0486678702.

Volonteri, M., Haardt, F. and Madau, P. (2003), The Assembly and Merging History of Supermassive Black Holes in Hierarchical Models of Galaxy Formation, *The Astrophysical Journal* , **582**, pp. 559–573, arXiv: astro-ph/0207276.

Proceedings of *RAGtime 17–19, 17–19/23–26 Oct., 1–5 Nov., 2015/2016/2017, Opava, Czech Republic*
Z. Stuchlík, G. Török and V. Karas, editors, Silesian University in Opava, 2017, pp. 153–161

Modelling the bow–shock evolution along the DSO/G2 orbit in the Galactic centre

Lýdia Štofanová[1,a] Michal Zajaček[2,3] Devaky Kunneriath[4] Andreas Eckart[2,3] and Vladimír Karas[5]

[1] Astronomical Institute of Charles University, Faculty of Mathematics and Physics, V Holešovičkách 2, CZ-18000 Prague 8, Czech Republic
[2] I. Physikalisches Institut der Universität zu Köln, Zülpicher Straße 77, D-50937 Köln, Germany
[3] Max-Planck-Institut für Radioastronomie, Auf dem Hügel 69, D-53121 Bonn, Germany
[4] North American ALMA Science Center (NAASC), National Radio Astronomy Observatory (NRAO), 520 Edgemont Road, Charlottesville, Virginia 22903-2475, USA
[5] Astronomical Institute, Czech Academy of Sciences, Boční II 1401, CZ-141 00 Prague, Czech Republic
[a] lydiastofan@gmail.com

ABSTRACT
A radially directed flow of gaseous environment from a supermassive black hole affects the evolution of a bow–shock that develops along the orbit of an object passing through the pericentre. The bow–shock exhibits asymmetry between the approaching and receding phases, as can be seen in calculations of the bow-shock size, the velocity profile along the shocked layer, and the surface density of the bow–shock, and by emission-measure maps. We discuss these effects in the context of the recent pericentre transit of DSO/G2 near Sagittarius A*.

Keywords: Galactic center – Sagittarius A* – Astrophysical processes – Bow shocks – DSO – G2 – Interstellar medium

1 INTRODUCTION

A supermassive black hole (SMBH) resides in the centre of our Milky Way, at the distance of $\approx 8.19 \pm 0.11$ kpc (for a very recent exposition, see Parsa et al. 2017). The position of the Galactic center (GC) has been associated with the compact radio source, Sagittarius A* (Sgr A*). It is a highly variable radio, near–infrared, and X–ray source. It is believed that its mass is $M_\bullet \sim 4 \times 10^6 M_\odot$. Sgr A* is the nearest nucleus of an inactive galaxy to us – about two orders of magnitude closer to us than the next similar nucleus. Thanks to the rich morphology of different objects in mutual interaction, Sgr A* and its immediate neighbourhood are among the most interesting fields in the sky (Eckart et al., 2005; Sanders, 2014).

The Milky Way does not qualify as an active galaxy because the Galactic Center exhibits a very low level of accretion activity and the emerging electromagnetic signal is very weak compared to typical examples of active galactic nuclei, such as Seyfert galaxies and quasars. We can detect relatively weak events of enhanced emission. Recent multi-wavelength studies show that the current level of activity is low, although this might have been much higher in the past and it could rise in future, once the supply of accretion gas and dust is restored. This can be particularly well seen in X-rays and in NIR/mm wavelengths (Kunneriath et al., 2010).

The Galactic center activity manifests itself not only by the emission at various wavelengths, but also by the presence of streamers of gas within the innermost region with the size of a fraction of parsec. Shocks develop within the violently interacting, multi-temperature environment of gas, dust, stars, and the supermassive black hole (Karas et al., 2007). Stars of the Nuclear Star Cluster serve as probes of the gravitational potential, while their motion can be traced by studying the properties of bow-shocks that develop due to their super-sonic motion (Chatterjee and Cordes, 2002).

The transient component of the signal likely arises very close to the central supermassive black hole. It may thus enable us to study the 'plunge region' (about which very little is known), between the event horizon and its immediate vicinity where the accreting material performs the final inspiral. With the greatly enhanced spectral resolution and throughput, need arises for realistic theoretical models of the accretion flow emission and computational tools that are powerful enough to deal with complex models and to allow actual fitting of theoretical models to observational data. However, the current models available for fitting X-ray data are subject to various restrictions. These limitations became particularly problematic during the recent campaign on the G2/DSO event for which several interpretations have been put forward.

The Galactic centre is a dense region of gas, dust, and stars; variety of structures emerge in the immediate vicinity of SMBH. We concentrate our interest mainly in the DSO/G2 – a Dusty S-Cluster Object, which approached its nearest point to the SMBH (peri-bothron) in 2014. It was suggested to be a core-less gas and dust cloud (Eckart et al., 2014). After the pericentre passage, DSO/G2 stayed rather compact, not loosing matter as expected. A likely interpretation has thus emerged that DSO/G2 could be a young accreting star (Valencia-S. et al., 2015). Based on the polarimetry maps from Shahzamanian et al. (2015, 2016) DSO/G2 could also be a dustenshrouded young star with bipolar outflows that form a bow shock on its way to Sgr A*. Especially the bow–shock scenario (neglecting hydrodynamical instabilities) has been studied in Zajaček et al. (2015, 2016), Štofanová (2016), and Zajaček et al. (2017). Moreover, the hydrodynamical models and maps for DSO/G2 were examined in several recent papers (e.g. Ballone et al., 2013; De Colle et al., 2014; Christie et al., 2016; Ballone et al., 2017, and further references cited therein).

In the present paper we summarise the main aspects of stellar (supersonic) fly-by through the gaseous medium surrounding the central black hole, where bow-shock structures must develop and their morphology can help us to trace the physical properties of the ambient medium.

2 MODEL OF BOW–SHOCKS

Bow shock is a shock wave that is generated by a wind–blowing star moving supersonically with respect to the ambient medium. We model DSO/G2 as a bow–shock structure around a star orbiting the SMBH. Momentum-conserving bow-shock is described by an analytical model Wilkin (1996), where several assumptions are adopted, such as as an effective cooling process and the thin–shell limit (see Fig. 1). The internal momentum within the shell is conserved. At the point of the head–on collision between stellar wind and ISM one can get a formula for so called stand-off distance R_0 as

$$R_0 = \sqrt{\frac{\dot{m}_\mathrm{w} V_\mathrm{w}}{4\pi\rho_\mathrm{A} V^{\star 2}}}\,, \tag{1}$$

where $\dot{m}_\mathrm{w}$ is the mass rate of the isotropic stellar wind in the distance R_0 from the star, V_w is the velocity of the stellar wind, ρ_A is the density of the ambient medium (ISM) and $V^\star$ is the velocity of the star with respect to the ambient medium. Stand-off distance can be understood as a parameter which scales the size of the bow shock (it sets the length scale of the shell).

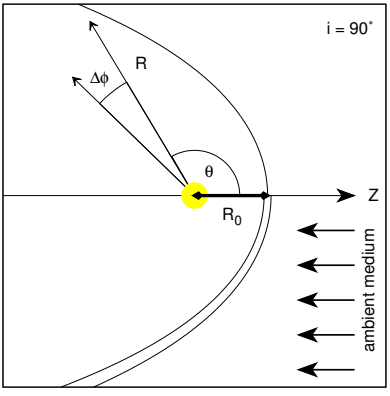

Figure 1. An illustration of the bow-shock shell given by eq. (2). In the star co-moving frame, the star (yellow dot) resides at the coordinate origin. The stellar wind blows in the radial direction, i.e., directed away from the star; z-axis is the symmetry axis of the shell. The ambient medium moves in the opposite direction of the axis z. Parameter R_0 stands for the stand-off distance given by eq. (1), $\Delta\phi$ is azimuthal angle about the symmetry axis, i is the inclination angle, R and θ are polar coordinates.

By assuming this very simple model (Wilkin, 1996) one can obtain an analytic solution for the shape of the bow–shock shell only as a function of polar coordinate

$$R(\theta) = R_0 \csc\theta \sqrt{3\,(1 - \theta\cot\theta)}\,. \tag{2}$$

The surface density and tangential velocity of shocked gas at all points in the shell (eqs. (3) and (4), respectively) can be derived as only a function of θ

$$\sigma(\theta) = R_0\rho_\mathrm{A} \frac{\left[2\alpha\,(1 - \cos\theta) + \varpi^2\right]^2}{2\varpi\sqrt{(\theta - \sin\theta\cos\theta)^2 + \left(\varpi^2 - \sin^2\theta\right)^2}}\,, \tag{3}$$

$$v_{\rm t}(\theta) = V^{\star} \frac{\sqrt{(\theta - \sin\theta\cos\theta)^2 + \left(\varpi^2 - \sin^2\theta\right)^2}}{2\alpha\,(1-\cos\theta) + \varpi^2}\,, \tag{4}$$

where $\alpha \equiv V^{\star}/V_{\rm w}$ is a non-dimensional parameter and $\varpi^2 = 3\,(1 - \theta\cot\theta)$ is a normalized cylindrical radius obtained from eq. (2).

From eq. (1) one can also obtain the ratio of stand-off distances in the apocentre and pericentre as a function of the eccentricity of the stellar orbit and γ,

$$n_{\rm A} = n_{\rm A0}\left(\frac{r_0}{r}\right)^{\gamma}\,, \tag{5}$$

where n stands for the number density and γ is a power-law index (Zajaček et al., 2016; Štofanová, 2016). Than the ratio of stand-off distances is

$$\frac{R_{0\rm Apo}}{R_{0\rm Per}} = \left(\frac{1+e}{1-e}\right)^{1+\gamma/2}\,. \tag{6}$$

Near the passage through the apocentre and pericentre, we should be able to estimate the behaviour of the number density of the ISM. If the ambient medium would be in the hydrostatical equilibrium, the number density should follow the profile Štofanová (2016)

$$n_{\rm a0} = \frac{n_{\rm A}(r)}{n_{\rm A}(r_{\rm s})} = \exp\left[-\frac{GM_{\bullet}m_{\rm H}\mu}{k_{\rm B}T_{\rm A}}\left(\frac{1}{r_{\rm s}} - \frac{1}{r}\right)\right]\,. \tag{7}$$

where $r_{\rm s} = 2GM_{\bullet}/c^2$; $M_{\bullet}$ is the mass of the SMBH, $n_{\rm A}$ stands for the number density of an ambient medium, G is a gravitational constant, c is the speed of light, $m_{\rm H}$ is the mass of hydrogen atom and μ is the relative molecular mass.

3 RESULTS

The results we present here are based on Štofanová (2016) and inspired by Zajaček et al. (2016) where the scenario assuming spherical outflow from the SMBH was taken into account. We give the detailed analysis of the shape of the bow–shock shell (in 2D), how it is changed along the orbit and how the profiles for the tangential velocity and mass surface density along the shell vary assuming four simple scenarios for the ISM movement: (a) without the presence of any gaseous medium emerging from or accreting onto the SMBH, (b) outflow from the SMBH, (c) the case of an inflow onto the SMBH, and finally (d) the combined model involving both an outflow and an inflow at the same time.

We neglected the relativistic effects mainly because, as seen in Fig. 2, the orbit of DSO/G2 object lies more than 10^3 r_s away from the SMBH in our Galactic centre. At the same time we can see that it should be moving with the supersonic velocity for the most of its orbit if not the whole (which depends on the temperature of the ambient medium T_a). In the models we have also included different density profiles for ISM (constant value of 1.67×10^{-21} g/cm^3 or a decreasing function of r); a sequence of values for the stellar wind

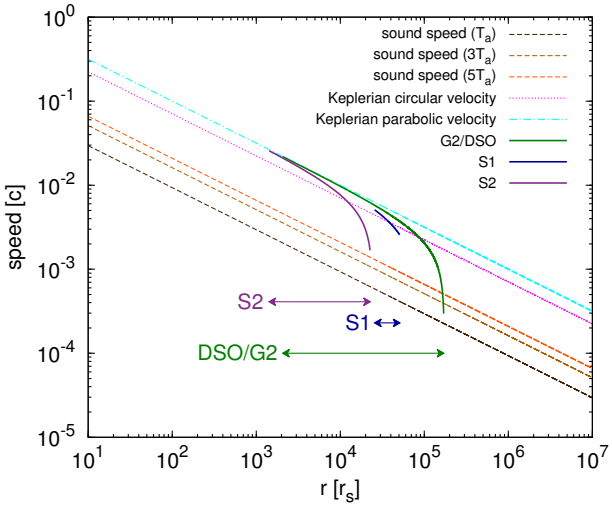

Figure 2. Comparison of Keplerian circular, parabolic and elliptic velocities of sources S1, S2 and DSO/G2 with speed of sound in central cavity (black, light brown and red dashed lines). All mentioned velocities are plotted as a function of distance r from the SMBH. Three lines for speed of sound vary through different temperatures of the ambient medium. All objects (S1, S2 and DSO/G2) are labelled with arrows (range of the arrows is between $r_{\rm apo}$ and $r_{\rm peri}$).

velocity: 20, 200, and 2000 km/s, and the ISM velocity 100, 500, 1000 and 2000 km/s, respectively.

Here we present only a combined model assuming that the Bondi accretion is a dominant process for the falling material onto SMBH and we set up the Bondi radius to 8000 au (in fact, for the Galactic centre Bondi radius is believed to be at $\simeq$ 33 000 a.u.; cf. Wang et al. 2013). Outside of this radius we assume that the material is moving in the direction away from SMBH. Exactly at the radius the ambient medium is at its rest. By following these assumptions one can get interesting results (see Sec. 4).

4 A COMBINED MODEL

Changes of orientation and the shape of the bow–shock shells due to different parameters can be seen in the Fig. 3 where is a graphical representation of its properties plotted in a cross-section with the orbital plane. One can see that with increasing velocity of the ambient medium the bow shocks are becoming smaller in size and they are being blown–off (outside Bondi radius) or dragged into the sphere of influence of SMBH.

Even more illustrative are the graphs plotted for the stand-off distance R_0 as a function of radius and time (see Fig. 4). The function is symmetric for zero velocity of ISM. As the ambient velocity increases, the function becomes distorted with respect to the pericentre passage (see the plot constructed for several viable scenarios that we had considered). We explored how these different schemes influence the tangential velocity and mass surface density profiles (for further details, see Štofanová 2016). Let us note that the asymmetrical bow-shock shapes are well-known from Pulsar Wind Nebulae (PWN; e.g. Romani et al., 2010; Bykov et al., 2017), where the angle between the magnetic moment and the rotation axis stands as the most decisive parameter. In our case, in addition to orientation of the intrinsic magnetic field, it is the enormous speed of translational motion of the star with

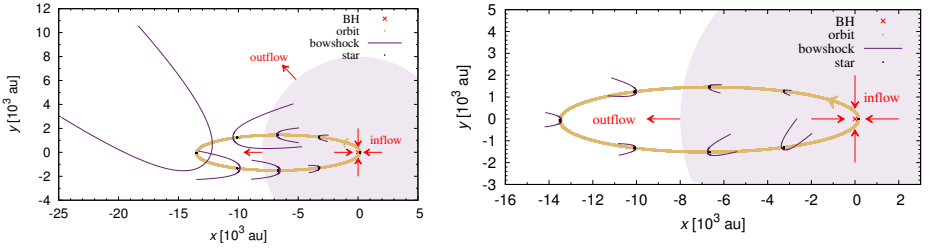

Figure 3. The geometrical shape and orientation of bow–shock shells that are plotted along the orbit for the combined model of an outflow from the SMBH and an inflow onto the SMBH. Graphs vary by the velocity of the outflow V_0, which was set to 100 km/s (left figure) and 2000 km/s (right figure). The parameter of the stellar wind V_w is fixed to 200 km/s. Light purple circle marks the area of Bondi radius (Štofanová, 2016).

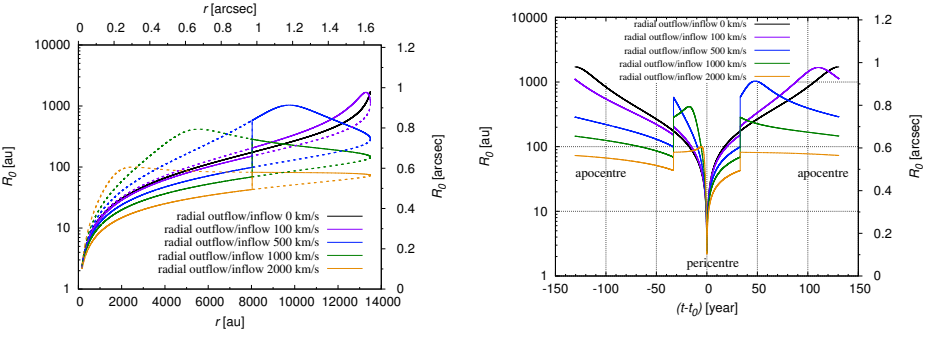

Figure 4. Dependence of the stand-off distance R_0 on the distance r from the SMBH (left panel) and on the time interval $(t - t_0)$ (right panel) for the ambient medium at rest (black line) and for different velocities of the outflow/inflow from/onto the SMBH (colour lines). The time t_0 of the apocentre passage is $\simeq$ 131 years. Solid lines represent post-pericentre phase and dashed lines correspond to pre-pericentre phase.

respect to the inflow/outflow transition of the SMBH accretion flow which have the main impact on the shock morphology. The above-mentioned combined model exhibits the most asymmetrical behaviour.

5 CONCLUSIONS

While DSO/G2 is a recently discovered object, numerous scenarios have been developed to point out its disputable origin. Here we assumed it was a star moving supersonically with respect to the ambient medium and as a consequence of this supersonic motion it creates a bow–shock structure. The aim was to find out how the bow–shock shell can change its properties along the orbit for different scenarios of the ambient medium surrounding the SMBH in our Galactic centre.

We found the combined model to be the most interesting case of all above-assumed scenarios as showing the most asymmetrical morphology in terms of the behaviour of the stand-off distance and star velocity as the functions of the distance and time. One can see that R_0 is the smallest in the pericentre for all considered velocities and with increasing velocity of an outflow/inflow the local maximum is decreasing after the pericentre passage. At the Bondi radius the solution exhibits a jump, which can be made smooth by employing a more realistic scheme for the density of ISM at the transition radius.

Here we presented only thin axisymmetric bow shocks in two dimensions. The bow shocks in three dimensions (with luminosity maps) could improve our models and make them more realistic by including a possibility of more general solutions for anisotropic stellar wind and non-axisymmetric bow-shock structure (Wilkin, 2000; Romani et al., 2010). The progress of a combined model could be formulated by employing self–consistent inflow/outflow accretion scheme, which can avoid somewhat artificial discontinuities at the Bondi radius, seen in our current plots.

ACKNOWLEDGEMENTS

The authors thank the Czech Science Foundation for continued support in the framework of "Albert Einstein Center for Gravitation and Astrophysics" (ref. 14-37086G), and the Ministry of Education Youth and Sports project Kontakt II (ref. LTAUSA17095), titled "Spectral and Timing Properties of Cosmic Black Holes", aimed to support international collaboration of the team members.

REFERENCES

Ballone, A., Schartmann, M., Burkert, A., Gillessen, S., Genzel, R., Fritz, T. K., Eisenhauer, F., Pfuhl, O. and Ott, T. (2013), Hydrodynamical Simulations of a Compact Source Scenario for the Galactic Center Cloud G2, *ApJ*, **776**, 13, arXiv: 1305.7238.

Ballone, A., Schartmann, M., Burkert, A., Gillessen, S., Plewa, P. M., Genzel, R., Pfuhl, O., Eisenhauer, F., Habibi, M., Ott, T. and George, E. M. (2017), 3D AMR hydrosimulations of a compact source scenario for the Galactic Centre cloud G2, *ArXiv e-prints*, arXiv: 1706.08547.

Bykov, A. M., Amato, E., Petrov, A. E., Krassilchtchikov, A. M. and Levenfish, K. P. (2017), Pulsar Wind Nebulae with Bow Shocks: Non-thermal Radiation and Cosmic Ray Leptons, *Space Science Reviews*, **207**, pp. 235–290, arXiv: 1705.00950.

Chatterjee, S. and Cordes, J. M. (2002), Bow Shocks from Neutron Stars: Scaling Laws and Hubble Space Telescope Observations of the Guitar Nebula, *ApJ*, **575**, pp. 407–418, arXiv: astro-ph/0201062.

Christie, I. M., Petropoulou, M., Mimica, P. and Giannios, D. (2016), Modelling accretion disc and stellar wind interactions: the case of Sgr A*, *MNRAS*, **459**, pp. 2420–2431.

De Colle, F., Raga, A. C., Contreras-Torres, F. F. and Toledo-Roy, J. C. (2014), A Stellar Wind Origin for the G2 Cloud: Three-dimensional Numerical Simulations, *ApJL*, **789**, L33, arXiv: 1406.1188.

Eckart, A., Horrobin, M., Britzen, S., Zamaninasab, M., Mužić, K., Sabha, N., Shahzamanian, B., Yazici, S., Moser, L., García-Marin, M., Valencia-S., M., Borkar, A., Bursa, M., Karssen, G., Karas, V., Zajaček, M., Bronfman, L., Finger, R., Jalali, B., Vitale, M., Rauch, C., Kunneriath, D., Moultaka, J., Straubmeier, C., Rashed, Y. E., Markakis, K. and Zensus, A. (2014), The infrared

K-band identification of the DSO/G2 source from VLT and Keck data, in L. O. Sjouwerman, C. C. Lang and J. Ott, editors, *The Galactic Center: Feeding and Feedback in a Normal Galactic Nucleus*, volume 303 of *IAU Symposium*, pp. 269–273, arXiv: 1311.2753.

Eckart, A., Schödel, R. and Straubmeier, C. (2005), *The black hole at the center of the Milky Way*, London: Imperial College Press.

Karas, V., Dovčiak, M., Eckart, A. and Meyer, L. (2007), Flares from spiral waves by lensing and time-delay amplification?, in S. Hledík and Z. Stuchlík, editors, *Proceedings of RAGtime 8/9: Workshops on Black Holes and Neutron Stars*, pp. 99–108, arXiv: 0709.3836.

Kunneriath, D., Witzel, G., Eckart, A., Zamaninasab, M., Gießübel, R., Schödel, R., Baganoff, F. K., Morris, M. R., Dovčiak, M., Duschl, W. J., García-Marín, M., Karas, V., König, S., Krichbaum, T. P., Krips, M., Lu, R.-S., Mauerhan, J., Moultaka, J., Mužić, K., Sabha, N., Najarro, F., Pott, J.-U., Schuster, K. F., Sjouwerman, L. O., Straubmeier, C., Thum, C., Vogel, S. N., Teuben, P., Weiss, A., Wiesemeyer, H. and Zensus, J. A. (2010), Coordinated NIR/mm observations of flare emission from Sagittarius A*, *A&A*, **517**, A46, arXiv: 1008.1560.

Parsa, M., Eckart, A., Shahzamanian, B., Karas, V., Zajaček, M., Zensus, J. A. and Straubmeier, C. (2017), Investigating the Relativistic Motion of the Stars Near the Supermassive Black Hole in the Galactic Center, *ApJ*, **845**, 22, arXiv: 1708.03507.

Romani, R. W., Shaw, M. S., Camilo, F., Cotter, G. and Sivakoff, G. R. (2010), The Balmer-dominated Bow Shock and Wind Nebula Structure of γ-ray Pulsar PSR J1741-2054, *ApJ*, **724**, pp. 908–914, arXiv: 1009.5310.

Sanders, R. H. (2014), *Revealing the Heart of the Galaxy*, Cambridge, UK: Cambridge University Press.

Shahzamanian, B., Eckart, A., Valencia-S., M., Witzel, G., Zamaninasab, M., Zajaček, M., Sabha, N., García-Marín, M., Karas, V., Peissker, F., Karssen, G. D., Parsa, M., Grosso, N., Mossoux, E., Porquet, D., Jalali, B., Horrobin, M., Buchholz, R., Dovčiak, M., Kunneriath, D., Bursa, M., Zensus, A., Schödel, R., Moultaka, J. and Straubmeier, C. (2015), Variable and Polarised Near-infrared Emission from the Galactic Centre, *The Messenger*, **159**, pp. 41–45.

Shahzamanian, B., Eckart, A., Zajaček, M., Valencia-S., M., Sabha, N., Moser, L., Parsa, M., Peissker, F. and Straubmeier, C. (2016), Polarized near-infrared light of the Dusty S-cluster Object (DSO/G2) at the Galactic center, *A&A*, **593**, A131, arXiv: 1607.04568.

Štofanová, L. (2016), Bachelor Thesis, *Faculty of Mathematics and Physics, Charles University in Prague, 60 pp. (2016).*

Valencia-S., M., Eckart, A., Zajaček, M., Peissker, F., Parsa, M., Grosso, N., Mossoux, E., Porquet, D., Jalali, B., Karas, V., Yazici, S., Shahzamanian, B., Sabha, N., Saalfeld, R., Smajic, S., Grellmann, R., Moser, L., Horrobin, M., Borkar, A., García-Marín, M., Dovčiak, M., Kunneriath, D., Karssen, G. D., Bursa, M., Straubmeier, C. and Bushouse, H. (2015), Monitoring the Dusty S-cluster Object (DSO/G2) on its Orbit toward the Galactic Center Black Hole, *ApJ*, **800**, 125, arXiv: 1410.8731.

Wang, Q. D., Nowak, M. A., Markoff, S. B., Baganoff, F. K., Nayakshin, S., Yuan, F., Cuadra, J., Davis, J., Dexter, J., Fabian, A. C., Grosso, N., Haggard, D., Houck, J., Ji, L., Li, Z., Neilsen, J., Porquet, D., Ripple, F. and Shcherbakov, R. V. (2013), Dissecting X-ray-Emitting Gas Around the Center of Our Galaxy, *Science*, **341**, pp. 981–983, arXiv: 1307.5845.

Wilkin, F. P. (1996), Exact analytic solutions for stellar wind bow shocks, *ApJL*, **459**(1), p. L31, URL http://stacks.iop.org/1538-4357/459/i=1/a=L31.

Wilkin, F. P. (2000), Modeling nonaxisymmetric bow shocks: Solution method and exact analytic solutions, *ApJ*, **532**(1), p. 400, URL http://stacks.iop.org/0004-637X/532/i=1/a=400.

Zajaček, M., Britzen, S., Eckart, A., Shahzamanian, B., Busch, G., Karas, V., Parsa, M., Peissker, F., Dovčiak, M., Subroweit, M., Dinnbier, F. and Zensus, J. A. (2017), Nature of the Galactic centre NIR-excess sources. I. What can we learn from the continuum observations of the DSO/G2 source?, *A&A*, **602**, A121, arXiv: 1704.03699.

Zajaček, M., Eckart, A., Karas, V., Kunneriath, D., Shahzamanian, B., Sabha, N., Mužić, K. and Valencia-S., M. (2016), Effect of an isotropic outflow from the Galactic Centre on the bow-shock evolution along the orbit, *MNRAS*, **455**, pp. 1257–1274, arXiv: 1510.02285.

Zajaček, M., Eckart, A., Peissker, F., Karssen, G. D. and Karas, V. (2015), Infrared-excess Source DSO/G2 Near the Galactic Center: Theory vs. Observations, in *Proceedings of the 24th Annual Conference of Doctoral Students - WDS 2015 - Physics (eds. J. Safrankova and J. Pavlu), Prague, Matfyzpress, pp. 27-35, 2015; ISBN 978-80-7378-311-2*, pp. 27–35, arXiv: 1507.00237.

Proceedings of *RAGtime 17–19, 17–19/23–26 Oct., 1–5 Nov., 2015/2016/2017, Opava, Czech Republic*
Z. Stuchlík, G. Török and V. Karas, editors, Silesian University in Opava, 2017, pp. 163–176

Hysteresis behavior of shocks in low angular momentum flows

Petra Suková

Astronomical Institute of the CAS, Fričova 298, CZ-251 65 Ondřejov, Czech Republic
petra.sukova@asu.cas.cz

ABSTRACT
In this work we present the GRMHD 1D simulations of accreting matter with variable angular momentum. We focus on the existence and behaviour of the shock in the flow. We show that the location of the shock front responds to the change of the angular momentum, which also causes the accretion rate onto the black hole to vary on different time scales. We study the possible hysteresis behaviour of the shock front during the time evolution of the flow. We discuss the potential observational effects of this phenomenon.

Keywords: black hole – microquasars – accretion flows – shocks

1 INTRODUCTION

During the last decades, the observational data keep confirming the existence of extremely powerful sources of energy ranging on a very broad mass, power, and time scales. Although initially sounding surprisingly, these events are now being theoretically explained as the products of mass accretion on compact objects – neutron stars and black holes. The accretion of matter can proceed in several different regimes which leave observational traces in the measured spectra and lightcurves and which are accompanied by some interesting phenomena, like e.g. jets.

The matter essentially flows into black hole with the speed of light, while the sound speed at maximum can reach $c/\sqrt{3}$. Hence, every accretion flows must have transonic nature. The viscous accretion flow with transonic solution based on the alpha-disk model were first studied by Paczyński and Bisnovatyi-Kogan (1981) and Muchotrzeb and Paczynski (1982). After that, Abramowicz and Kato (1989) examined the stability and structure of transonic disks. The possibility of collimation of jets by thick accretion tori was proposed by, e.g., Sikora and Wilson (1981).

In respect of the value of angular momentum there are two main regimes of accretion, the Bondi accretion, which refers to spherical accretion of gas without any angular momentum, and the disk-like accretion with Keplerian distribution of angular momentum. If we consider the same polytropic index and sound speed at infinity of the gas, then in the case of the former, the sonic point is located far away from the compact object and the flow is

978-80-7510-257-7

supersonic downstream of it. In the latter case, the flow becomes supersonic quite close to the compact object. For gas with a low value of constant angular momentum, hence belonging in between these two regimes, the equations allow for the existence of two sonic points of both types.

The possible existence of shocks in low angular momentum flows connected with the presence of multiple critical points in the phase space has been studied from different points of view during the last thirty years. However, the theoretical works which describe the fundamental properties of the low angular momentum accretion flow and which usually treat the steady solution of the equations, has so far been carried only for non-magnetized and usually also non-viscous flows. Quasi-spherical distribution of the gas endowed by constant specific angular momentum λ and the arisen bistability was studied already by Abramowicz and Zurek (1981). Later, the significance of this phenomenon related to the variability of some X-ray sources has been pointed out by Jufu and Abramowicz (1988) and soon after, the possibility of the shock existence together with shock conditions in different types of geometries was discussed by Abramowicz and Chakrabarti (1990). More recently, the shock existence was found also in the disc-like structure with low angular momentum in hydrostatic equilibrium both in pseudo-Newtonian potential Das (2002) and in full relativistic approach Das and Czerny (2012). Regarding the sequence of steady solutions with different values of specific angular momentum, the hysteresis-like behaviour of the shock front was proposed by the latter.

Further development of this topic includes numerical simulations of low angular momentum flows in different kinds of geometrical setup. Hydrodynamical models of the low angular momentum accretion flows have been studied already in two and three dimensions, e.g. by Proga and Begelman (2003), Janiuk et al. (2008) and Janiuk et al. (2009). In those simulations, a single, constant value of the specific angular momentum was assumed, while the variability of the flows occurred due to e.g. non-spherical or non-axisymmetric distribution of the matter. The level of this variability was also dependent on the adiabatic index. However, these studies have not concentrated on the existence of the standing shocks as predicted by the theoretical works mentioned above.

Recently, we have carried out simulations of one-dimensional hydrodynamical model of shocked quasi-spherical accretion flow, which confirm the shape of the steady solution and also the dependence of this solution on the leading parameters (angular momentum λ, energy ϵ and adiabatic index γ). These simulations were held in the pseudo-Newtonian framework using the computational code ZEUS (Stone and Norman, 1992; Hayes and Norman, 2003).

The simulations yield the shock front unstable for a subset of parameters which leads to oscillation of the shock front around the position given by the steady solution with frequency depending on the distance to the center (Suková and Janiuk, 2015). Since the shock front is thought to be the source of radiation, this mechanism could be connected with the QPOs with evolving frequency reported from several microquasars (e.g. GX 339-4 (Nandi et al., 2012) or XTE J1550-564 (Chakrabarti et al., 2009)). Moreover, we also show the evolution of the flow with changing angular momentum and reported the repeating creation and disappearance of the shock front due to the hysteresis loop. In another words, we have seen for the first time, that during the dynamical evolution of the accretion flow, the shock was repeatedly created and accreted.

In this work we are reexamining this issue with the general relativistic hydrodynamical simulations done in the Kerr spacetime with both non-spinning and spinning black hole.

2 STANDING SHOCKS IN FLOWS WITH LOW CONSTANT ANGULAR MOMENTUM

In the previous work we studied the behaviour of shocks in low angular momentum flows in the pseudo-Newtonian framework using the Paczynski-Wiita potential to mimic the strong gravity effects near the black hole (Suková and Janiuk, 2015). Because we will use the semi-analytical solution as the initial conditions for our GRMHD simulations, we will shortly repeat here the main equations and derivation.

We assume one dimensional quasi-spherical flow of polytropic gas (with EOS of the form $p = K\rho^{\gamma}$), which posses constant angular momentum λ and accretes with constant accretion rate $\dot{M}$. From the continuity equation we can express the mass accretion rate in the form

$$\dot{M} = u\rho r^2 = \text{const}, \tag{1}$$

where u is the inward radial speed of the gas and ρ is its density.

Further, we can write the energy conservation for the steady state in the form

$$\epsilon = \frac{1}{2}u^2 + \frac{a^2}{\gamma - 1} + \frac{\lambda^2}{2r^2} + \Phi(r), \tag{2}$$

where a is the local sound speed and the term $\Phi(r) = -\frac{1}{2(r-1)}$ represents the Paczynski-Wiita gravitational potential (Paczyński and Wiita, 1980), so that r is given in the units of $r_g = 2GM/c^2$.

From these equations we can derive the relation for the radial gradient of the flow velocity

$$\frac{\mathrm{d}u}{\mathrm{d}r} = \frac{\frac{\lambda^2}{r^3} - \frac{\mathrm{d}\Phi(r)}{\mathrm{d}r} + \frac{2a^2}{r}}{u - \frac{a^2}{u}} = \frac{\frac{\lambda^2}{r^3} - \frac{1}{2(r-1)^2} + \frac{2a^2}{r}}{u - \frac{a^2}{u}}. \tag{3}$$

Our aim is to describe the smooth flow, which is subsonic far away from the compact object and which accretes inward onto the compact object. Therefore, at the point, where the denominator of equation (3) equals to zero, the numerator also has to be equal to zero. We call such points the critical points, which have to satisfied the two conditions

$$u_c = a_c, \tag{4}$$

$$a_c = \sqrt{\frac{r_c}{2}\frac{\mathrm{d}\Phi(r_c)}{\mathrm{d}r_c} - \frac{\lambda^2}{2r_c^2}} = \sqrt{\frac{r_c}{4(r_c-1)^2} - \frac{\lambda^2}{2r_c^2}}. \tag{5}$$

We can see that in our settings the critical points coincide with the location of the possible sonic points in the flow (the points, where the radial inward speed equals to the local sound

speed $u = a$, hence the radial Mach number $\mathfrak{M} = u/a = 1$). Using these relations, the position of the critical point can be found by solving the equation

$$\epsilon - \frac{\lambda^2}{2r_c^2} + \frac{1}{2(r_c-1)} - \frac{\gamma+1}{2(\gamma-1)}\left(\frac{r_c}{4(r_c-1)^2} - \frac{\lambda^2}{2r_c^2}\right) = 0, \tag{6}$$

After we have found the position of the critical point together with values of $u(r_c)$ and $a(r_c)$, we can integrate equation (3) downwards and upwards and obtain the whole solution.

Important property of the set of equations is that for a subset of parameters, there exist more critical points. In fact, there are three critical points, from which two are of a saddle type and one is of a center type. The topology of the solution in space spanned by r and $\mathfrak{M}$ for spinning black hole was studied by Das and Czerny (2012) and differs for different values of parameters. They showed, that there is set of parameters, for which two global solutions are possible. In this case we have two branches of solution, which passes through the inner and outer saddle critical point. The transonic solution required by the aforementioned boundary conditions, which is the solution having low subsonic velocity far away from the compact object ($\mathfrak{M} < 1$) and supersonic velocity very near to the horizon ($\mathfrak{M} > 1$), thus can locally pass only through the outer or both sonic points. The latter is globally achieved due to the shock formation between the two critical points. So, either the accretion proceeds through the outer sonic point and it is supersonic downwards to the black hole (we call this solution the "Bondi-like type", because the profile of radial Mach number is similar to the Bondi case) or shock can appear at a given radius r_s and connects the two branches, while the entropy accretion rate is increased at the shock location. We call this subspace of the parameter space the shock-existence region.

The possibility of the shock existence is given by the requirement, that the Rankine-Hugoniot shock conditions, which express the conservation of mass, energy and momentum at the shock front are satisfied at some radius r_s. We can write them in the form

$$\frac{\left(\frac{1}{\mathfrak{M}_{\mathtt{in}}} + \gamma\mathfrak{M}_{\mathtt{in}}\right)^2}{\mathfrak{M}_{\mathtt{in}}^2(\gamma-1)+2} = \frac{\left(\frac{1}{\mathfrak{M}_{\mathtt{out}}} + \gamma\mathfrak{M}_{\mathtt{out}}\right)^2}{\mathfrak{M}_{\mathtt{out}}^2(\gamma-1)+2}, \tag{7}$$

which has to hold at the radius r_s. Here, $\mathfrak{M}_{\mathtt{out}}$ and $\mathfrak{M}_{\mathtt{in}}$ is the radial Mach number of the preshock and postshock gas, respectively.

Previously, we run the simulations of the accretion flow behaviour in this framework using the code ZEUS (Suková and Janiuk, 2015) and we confirmed the existence of the stationary shocks, as well as we reported the oscillations of the shock front for lower energies and higher angular momentum of the flow. Later we repeated the study with the GRMHD simulation in the Kerr spacetime (Suková et al., 2016; Suková et al., 2017) using the computational code `Einstein Toolkit` (Löffler et al., 2012) and HARMPI[1] (Ressler et al., 2015, 2017; McKinney et al., 2012; Tchekhovskoy et al., 2007; Mignone and McKinney, 2007) based on the original HARM code (Gammie et al., 2003; McKinney and Gammie, 2004; Noble et al., 2006; Janiuk et al., 2013; Janiuk, 2017). We confirmed the qualitative findings of the earlier study and we pointed out some quantitative differences.

[1] e.g., see `https://github.com/atchekho/harmpi`

In this work we focus on the issue of the hysteresis behaviour of the flow with the GRMHD 1D simulations using the code HARMPI.

3 SIMULATION SETUP

For our GRMHD simulations we set the initial conditions according to the semi-analytical solution (eqns (3) and (6)) with the shock front connecting the two branches placed at an arbitrary position. This solution is not the steady state solution, but the flow quickly settles itself into the real solution after short transient time at the beginning of the computation. For higher values of spin of the black hole a, we use different λ^s for the semi-analytical solution and different λ_g, which governs the rotation of the flow, because the shock-existence region exists for much lower values of angular momentum of the gas.

To study the hysteresis behaviour, we have to change at least one of the leading parameters across the shock-existence region. Physically meaningful is the change of the angular momentum of the incoming matter, which can happen due to the change of conditions in the neighborhood of the black hole, e.g. winds from orbiting stars, matter from magnetic trap held by magnetic companion, gas cloud which passes around the black hole etc. can have slightly different angular momentum in different regions.

The exact time dependence of the angular momentum at the outer boundary depends on the particular physical situation, which causes this change. However, we can assume, that for some time the angular momentum will increase or decrease, that such change will be slow and that the monotonic trend has to stop at some point. We are also interested in the case, when the angular momentum will change periodically (e.g. as a consequence of the orbital or rotational motion of the companion) to see the impact of such behaviour on the flow. Hence, we choose angular momentum as the leading parameter and we run the simulations, in which the angular momentum of the gas incoming through the outer boundary is changed periodically in time according to simple relation

$$\lambda(t) = \lambda(0) - A \sin(t/P), \tag{8}$$

where P is the period and A is the amplitude of the oscillations.

The fiducial value of the polytropic index used in our computations is $\gamma = 4/3$.

4 RESULTS

We run several 1D simulations with changing angular momentum of the incoming gas. We follow the position of the shock and also the mass accretion rate onto the black hole. In fact, we are looking on the mass flux through the inner boundary of our grid, which is placed bellow the horizon of the black hole.

At first we can confirm our earlier results, which show, that the choice between the Bondi-like type of accretion and accretion flow with shock depends on the history of the flow and especially on the presence of the inner sonic point in the flow. Hence we showed that both of the solutions are plausible solutions, which can exist under certain circumstances, and the accretion flow can switch between them during the dynamical evolution of the system.

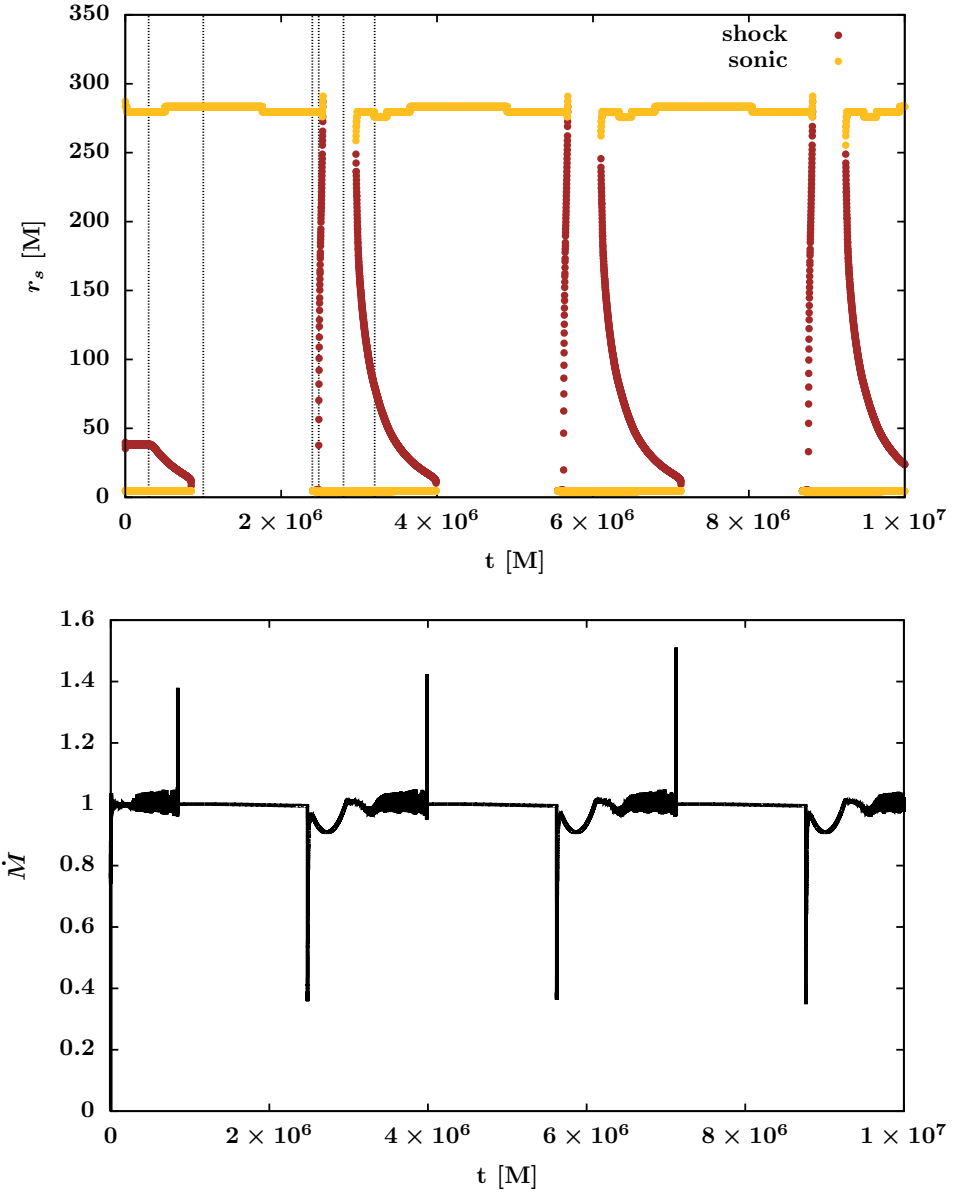

Figure 1. Top panel: Location of the sonic points and the shock front in the flow during the simulation. The vertical lines show the times of the snapshots shown in Fig. 2. Bottom panel: Time dependence of the mass accretion rate through the inner boundary. Parameters of the simulation are $\lambda(0) = 3.55$M, $\epsilon = 0.0025, A = 0.12$M, $P = 5 \cdot 10^5$M.

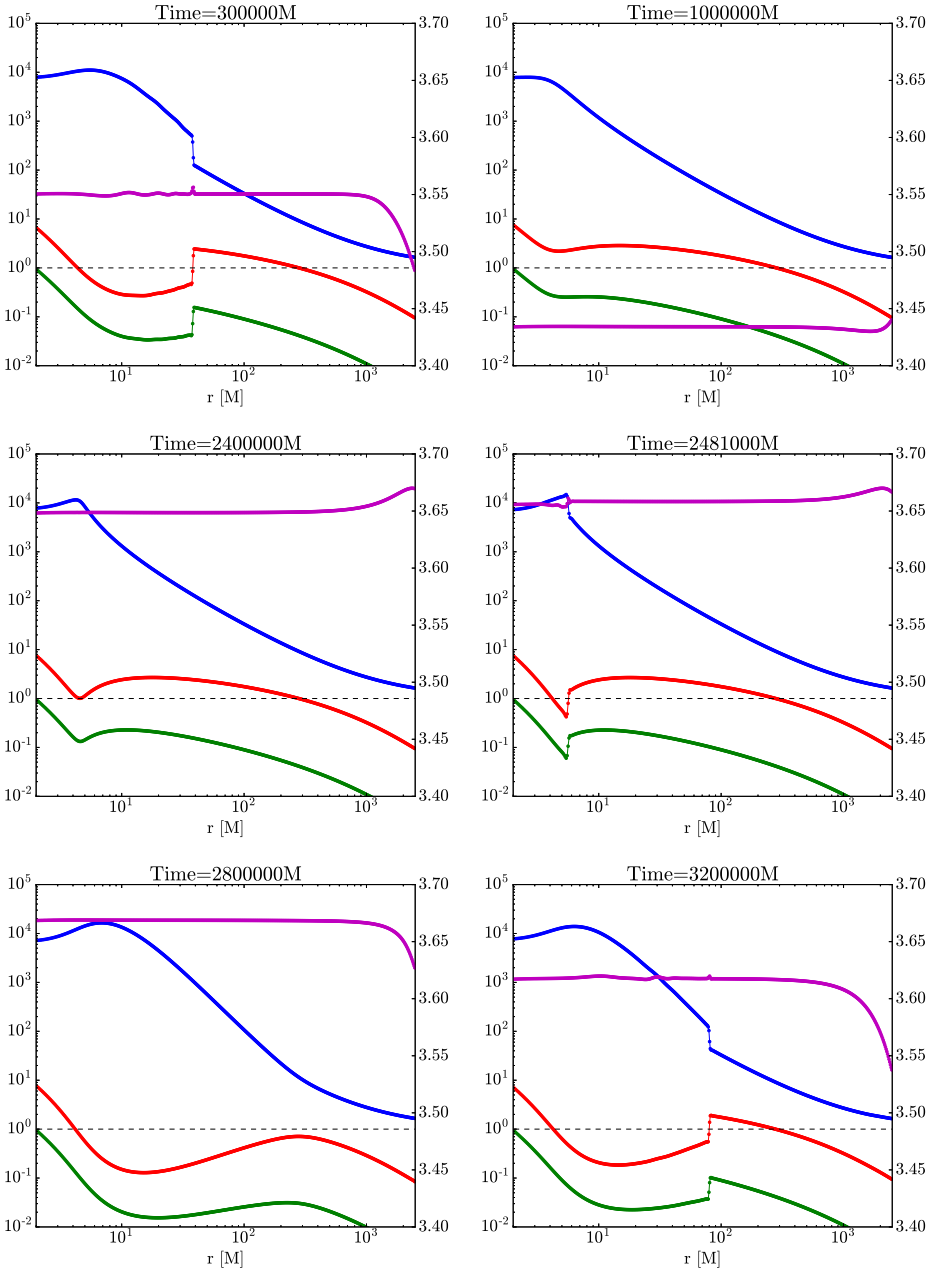

Figure 2. Snapshots from the simulation showing profiles of radial velocity of the gas $u^r_{\rm BL}$ (green) in units of c, Mach number $\mathfrak{M} = -u^r_{\rm BL}/a$ (red) and density ρ in arbitrary units (blue) on the left y-axis and the angular momentum λ [M] (purple) on the right y-axis. Parameters of the simulation are $\epsilon = 0.0025$, $\lambda(0) = 3.55$M, $A = 0.12$M, $P = 5 \cdot 10^5$M.

In Fig. 1 we can see three full hysteresis cycles of the flow and in Fig. 2 six snapshots taken during the first cycle are shown. We can see, that after the change of the angular momentum propagates inside from the outer boundary of the grid, the shock location starts to slowly decrease (first panel in Fig. 2, $t = 3 \cdot 10^5$M). At the moment, when the shock front reaches the minimal stable shock location, it is accreted on the advection time scale. Afterwards, the flow follows the Bondi-like type of solution, where only the outer sonic point exists (second panel in Fig. 2, $t = 10^6$M). When the angular momentum increases back to the shock-existence region, the shock does not form, only the profile of Mach number bends towards $\mathfrak{M} = 1$ in the innermost part of the accretion flow due to the centrifugal barrier (third panel in Fig. 2, $t = 2.4 \cdot 10^6$M). However, at the point, where the angular momentum increases above the shock-existence region, hence the outer sonic point does not exist and the Bondi-like type of solution is not possible anymore, the shock front detaches from the inner sonic point and very quickly expands outwards towards the outer sonic point, with which it merges (fourth panel in Fig. 2, $t = 2.481 \cdot 10^6$M). After that the flow follows the disc-like type of accretion with only the inner sonic point present (fifth panel in Fig. 2, $t = 2.8 \cdot 10^6$M), until the moment, when the angular momentum returns back into the shock-existence region. At that moment shock is created close to the outer sonic point and moves slowly inward (depending on the rate of the angular momentum change given by A and P) and the hysteresis cycle is completed (sixth panel in Fig. 2, $t = 3.2 \cdot 10^6$M).

Simultaneously with the evolution of the shock front position we can also notice the changes in mass accretion rate onto the black hole. When the shock is building in the flow, the radial inward speed decreases and the mass accretion rate drops down. While the shock front location is changing, we can notice some oscillations of the mass accretion rate. At the moment of the abrupt accretion of the shock front from the minimal stable shock position sharp peak occurs in the mass accretion rate. Because the mass accretion rate is a proxy to the luminosity of the source, we can speculate that partially the variability, which we observe in accreting black hole systems, can be induced by the change of the angular momentum of the accreting matter. Considering that these shocks exist in gas with low angular momentum, which gains high energy while falling on the compact object, this conclusion holds especially for the variability in harder spectral bands, above the energy corresponding to the disc black body radiation.

To show the generality of our findings, we performed a set of simulations with different spin of the black hole. Parameters of the runs are $\epsilon = 0.0025, P = 4 \cdot 10^4$M; A) $a = 0, \lambda(0) = 3.55$M$, A = 0.13$M; B) $a = 0.3, \lambda(0) = 3.3M, A = 0.15$M; C) $a = 0.5, \lambda(0) = 3.1M, A = 0.13$M; D) $a = 0.8, \lambda(0) = 2.67M, A = 0.13$M.

In Fig. 3 the mass accretion rate for the four different spins is given. In all cases, we can see similar features, which are the sharp peaks when the shock front is accreted and the decrease of accretion rate followed by oscillations and a broad peak. The time scale of the broad features are given by our chosen rate of change of the angular momentum (P and A). The amplitude of the oscillations and the overall variability is higher for higher spin of the black hole. However, the time scale of the sharp peak is determined by the position of the minimal stable shock position, which is given mostly by value of the polytropic index γ (see Suková and Janiuk (2015) for details in pseudo-newtonian framework), and it does depend on other parameters only slightly. That is illustrated on the second panel of Fig. 3, where we shift the time of each run such that the peak occurs at $t = 1000$M. The height

of the peak increases with increasing spin of the black hole, but the time profile is very similar in every case. Duration of the peak is of the order of few hundreds of M, which is in agreement with the X-ray flares seen from Sgr A* (Nowak et al., 2012).

Our last example in Fig. 4 shows the behaviour of the gas with lower energy $\epsilon = 0.0005$. The three runs are set with $P = 2 \cdot 10^5$M; A) $a = 0, \lambda(0) = 3.66$M$, A = 0.23$M; B) $a = 0.3, \lambda(0) = 3.36M, A = 0.25$M; C) $a = 0.5, \lambda(0) = 3.05M, A = 0.33$M. We adjusted the time in such a way, that one cycle of the hysteresis loop is shown and that the broad peaks coincide. The overall evolution during the cycle agrees with the above described behaviour. The main difference from the previous example is the higher amplitude of the peaks and dips and the fact, that the broad peak is now higher than the sharp peak. The shape and time scale of the sharp peak is however very similar as for the higher energy, hence this feature seems to be quite universal for wide range of parameters.

5 CONCLUSIONS

In the present work we examined the behaviour of the accretion flow with changing angular momentum of the incoming matter. We studied the hysteresis cycle of the shock front location and the induced variability of the accretion rate onto the black hole. In comparison with the previous results, we provided the simulations for spinning black hole with wide range of spins of the black hole. We also varied the value of the energy of the gas. We noted the similarities and differences of the individual runs.

Our numerical results shows that the change of the angular momentum of the matter far away from the black hole (at the outer boundary of our grid) can induce the movement of the shock location in the flow. This can provide the explanation of the shock front motion, which is fitted from the change of the low frequency QPOs seen in some microquasars during the onset and decline of their outburst with the phenomenological propagating oscillatory shock (POS) model (Chakrabarti et al., 2008, 2009; Nandi et al., 2012; Debnath et al., 2013; Debnath et al., 2014).

In case, that the angular momentum crosses the boundary of the shock-existence region in the parameter space (keeping other parameters constant) the shock front can disappear suddenly (abrupt accretion of the shock front) or can be created and expand quickly through the flow. If the parameter exceeds the shock-existence region from both sides, the hysteresis cycle in the shock location appears.

The changes of the flow in response to the different angular momentum of the gas lead to the variable accretion rate onto the black hole. Depending on the value and on the rate of change of λ we can observe oscillatory behaviour with changing frequency, longer dips and peaks connected with the time scale of the oscillations of λ and sharp peaks determined by the minimal stable shock position.

These features can be connected with some of the variability seen in microquasars and also some low luminous AGNs like Sgr A* in the center of our Galaxy. This conclusion is strengthen by our study of non-linear features found in the lightcurves of several microquasars (Suková et al., 2016), detailed study of the microquasar XTE J1550-564 discusses also the possible outburst scenario (Suková and Janiuk, 2016). However, our method can-

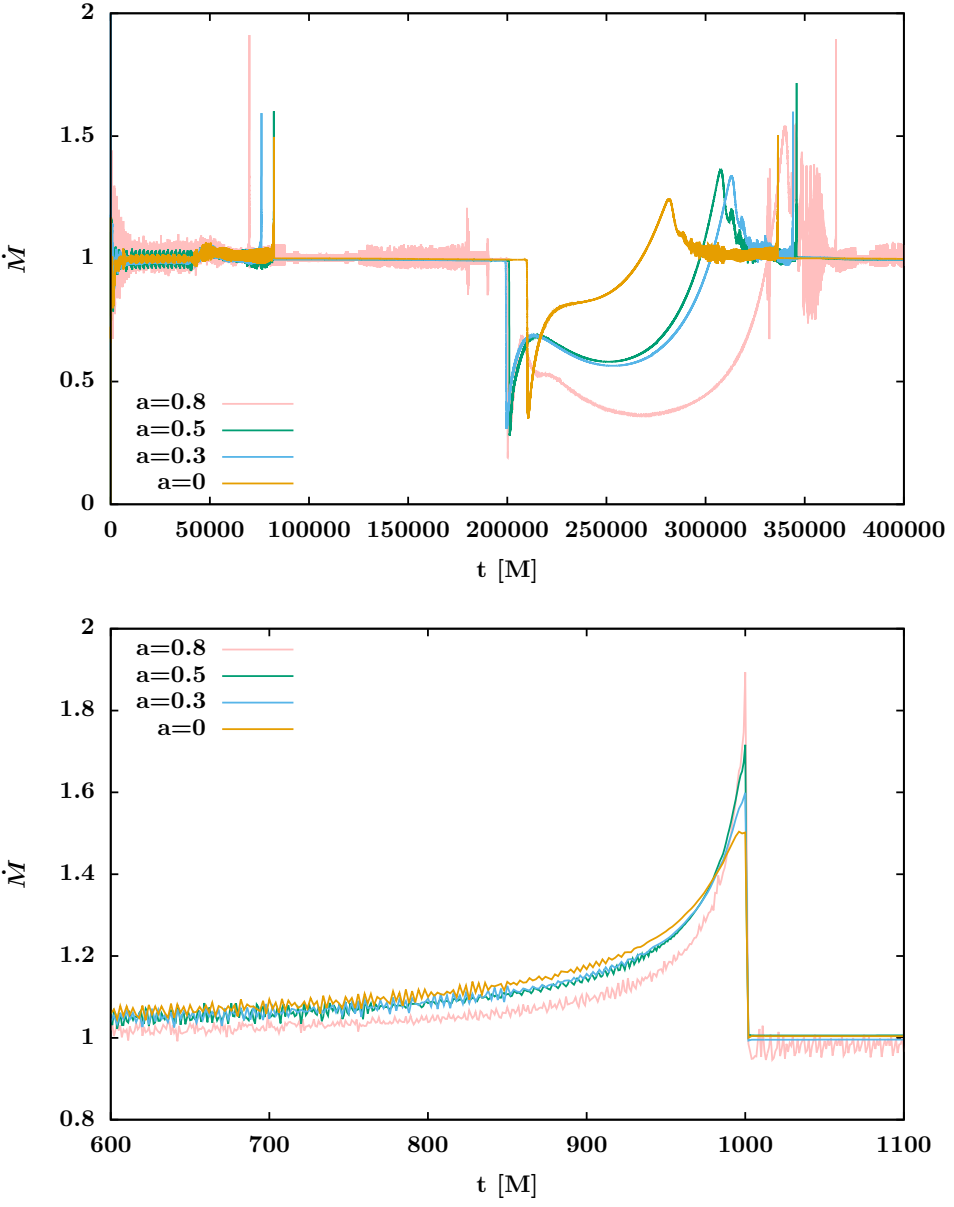

Figure 3. Time dependence of the mass accretion rate through the inner boundary for simulations with changing spin. Parameters of the runs are described in the text.

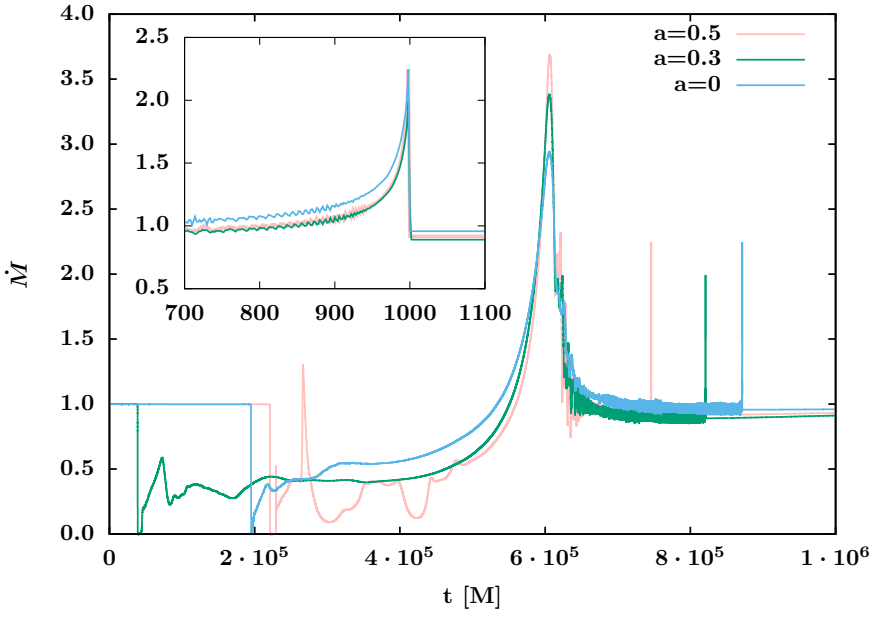

Figure 4. Time dependence of the mass accretion rate through the inner boundary for simulations with changing spin and lower energy $\epsilon = 0.0005$. The time is adjusted so that the broad peaks of all runs coincide. The inset plot shows the sharp peaks, which are aligned to $t = 1000$M. Parameters of the runs are described in the text.

not distinguish between different non-linear mechanisms of the emission and thus it cannot rule out the other possible scenarios.

Hence, more elaborate models, which include also the radiation transfer and possibly also other physical processes (e.g. the magnetic field, the two temperature accretion flows, etc.), are needed to study the observational consequences of this phenomenon, which can be directly compared to the experimental data.

ACKNOWLEDGEMENTS

The present work was supported by the Czech Grant GACR-17-06962Y.

REFERENCES

Abramowicz, M. A. and Chakrabarti, S. K. (1990), Standing shocks in adiabatic black hole accretion of rotating matter, *ApJ*, **350**, pp. 281–287.

Abramowicz, M. A. and Kato, S. (1989), Constraints for transonic black hole accretion, *ApJ*, **336**, pp. 304–312.

Abramowicz, M. A. and Zurek, W. H. (1981), Rotation-induced bistability of transonic accretion onto a black hole, *ApJ*, **246**, pp. 314–320.

Chakrabarti, S. K., Debnath, D., Nandi, A. and Pal, P. S. (2008), Evolution of the quasi-periodic oscillation frequency in GRO J1655-40 - Implications for accretion disk dynamics, *ApJ*, **489**, pp. L41–L44, arXiv: 0809.0876.

Chakrabarti, S. K., Dutta, B. G. and Pal, P. S. (2009), Accretion flow behaviour during the evolution of the quasi-periodic oscillation frequency of xte j1550-564 in 1998 outburst, *MNRAS*, **394**(3), pp. 1463–1468, URL http://mnras.oxfordjournals.org/content/394/3/1463.abstract.

Chakrabarti, S. K., Dutta, B. G. and Pal, P. S. (2009), Accretion flow behaviour during the evolution of the quasi-periodic oscillation frequency of XTE J1550-564 in 1998 outburst, *MNRAS*, **394**, pp. 1463–1468, arXiv: 0906.5068.

Das, T. K. (2002), Generalized Shock Solutions for Hydrodynamic Black Hole Accretion, *ApJ*, **577**, pp. 880–892, arXiv: astro-ph/0212119.

Das, T. K. and Czerny, B. (2012), Hysteresis effects and diagnostics of the shock formation in low angular momentum axisymmetric accretion in the Kerr metric, *NA*, **17**, pp. 254–271, arXiv: 0906.4559.

Debnath, D., Chakrabarti, S. K. and Mondal, S. (2014), Implementation of two-component advective flow solution in xspec, *Monthly Notices of the Royal Astronomical Society: Letters*, **440**(1), p. L121, URL +http://dx.doi.org/10.1093/mnrasl/slu024.

Debnath, D., Mondal, S. and Chakrabarti, S. K. (2013), Characterization of GX 339-4 outburst of 2010-11: Analysis by XSPEC using Two Component Advective Flow model, *Preprint*, **1306.3745 [astro-ph.HE]**, arXiv: 1306.3745.

Gammie, C. F., McKinney, J. C. and Tth, G. (2003), Harm: A numerical scheme for general relativistic magnetohydrodynamics, *ApJ*, **589**(1), p. 444, URL http://stacks.iop.org/0004-637X/589/i=1/a=444.

Hayes, J. C. and Norman, M. L. (2003), Beyond Flux-limited Diffusion: Parallel Algorithms for Multidimensional Radiation Hydrodynamics, *ApJS*, **147**, pp. 197–220, arXiv: astro-ph/0207260.

Janiuk, A. (2017), Microphysics in the Gamma-Ray Burst Central Engine, *ApJ*, **837**, 39, arXiv: 1609.09361.

Janiuk, A., Mioduszewski, P. and Moscibrodzka, M. (2013), Accretion and Outflow from a Magnetized, Neutrino Cooled Torus around the Gamma-Ray Burst Central Engine, *ApJ*, **776**, 105, arXiv: 1308.4823.

Janiuk, A., Proga, D. and Kurosawa, R. (2008), Nonaxisymmetric Effects in Black Hole Accretion Inviscid Hydrodynamics: Formation and Evolution of a Tilted Torus, *ApJ*, **681**, pp. 58–72, arXiv: 0803.2087.

Janiuk, A., Sznajder, M., Mościbrodzka, M. and Proga, D. (2009), Time Evolution of the Three-Dimensional Accretion Flows: Effects of the Adiabatic Index and Outer Boundary Condition, *ApJ*, **705**, pp. 1503–1521, arXiv: 0909.5572.

Jufu, L. and Abramowicz, M. A. (1988), Bimodal character of black hole accretion, *ChA&A*, **12**, pp. 119–128.

Löffler, F., Faber, J., Bentivegna, E., Bode, T., Diener, P., Haas, R., Hinder, I., Mundim, B. C., Ott, C. D., Schnetter, E., Allen, G., Campanelli, M. and Laguna, P. (2012), The Einstein Toolkit: a community computational infrastructure for relativistic astrophysics, *Classical and Quantum Gravity*, **29**(11), 115001.

McKinney, J. C. and Gammie, C. F. (2004), A measurement of the electromagnetic luminosity of a kerr black hole, *The Astrophysical Journal*, **611**(2), p. 977, URL http://stacks.iop.org/0004-637X/611/i=2/a=977.

McKinney, J. C., Tchekhovskoy, A. and Blandford, R. D. (2012), General relativistic magnetohydrodynamic simulations of magnetically choked accretion flows around black holes, *MNRAS*, **423**, pp. 3083–3117, arXiv: 1201.4163.

Mignone, A. and McKinney, J. C. (2007), Equation of state in relativistic magnetohydrodynamics: variable versus constant adiabatic index, *MNRAS*, **378**, pp. 1118–1130, arXiv: 0704.1679.

Muchotrzeb, B. and Paczynski, B. (1982), Transonic accretion flow in a thin disk around a black hole, *Acta Astron.*, **32**, pp. 1–11.

Nandi, A., Debnath, D., Mandal, S. and Chakrabarti, S. K. (2012), Accretion flow dynamics during the evolution of timing and spectral properties of GX 339-4 during its 2010-11 outburst, *A&A*, **542**, A56, arXiv: 1204.5044.

Noble, S. C., Gammie, C. F., McKinney, J. C. and Del Zanna, L. (2006), Primitive Variable Solvers for Conservative General Relativistic Magnetohydrodynamics, *ApJ*, **641**, pp. 626–637, arXiv: astro-ph/0512420.

Nowak, M. A., Neilsen, J., Markoff, S. B., Baganoff, F. K., Porquet, D., Grosso, N., Levin, Y., Houck, J., Eckart, A., Falcke, H., Ji, L., Miller, J. M. and Wang, Q. D. (2012), Chandra/HETGS Observations of the Brightest Flare Seen from Sgr A*, *ApJ*, **759**, 95, arXiv: 1209.6354.

Paczyński, B. and Bisnovatyi-Kogan, G. (1981), A Model of a Thin Accretion Disk around a Black Hole, *Acta Astron.*, **31**, p. 283.

Paczyński, B. and Wiita, P. J. (1980), Thick accretion disks and supercritical luminosities, *A&A*, **88**, pp. 23–31.

Proga, D. and Begelman, M. C. (2003), Accretion of Low Angular Momentum Material onto Black Holes: Two-dimensional Hydrodynamical Inviscid Case, *ApJ*, **582**, pp. 69–81, arXiv: astro-ph/0208517.

Ressler, S. M., Tchekhovskoy, A., Quataert, E., Chandra, M. and Gammie, C. F. (2015), Electron thermodynamics in GRMHD simulations of low-luminosity black hole accretion, *MNRAS*, **454**, pp. 1848–1870, arXiv: 1509.04717.

Ressler, S. M., Tchekhovskoy, A., Quataert, E. and Gammie, C. F. (2017), The disc-jet symbiosis emerges: modelling the emission of Sagittarius A* with electron thermodynamics, *MNRAS*, **467**, pp. 3604–3619, arXiv: 1611.09365.

Sikora, M. and Wilson, D. B. (1981), The collimation of particle beams from thick accretion discs, *MNRAS*, **197**, pp. 529–541.

Stone, J. M. and Norman, M. L. (1992), ZEUS-2D: A radiation magnetohydrodynamics code for astrophysical flows in two space dimensions. I - The hydrodynamic algorithms and tests., *ApJS*, **80**, pp. 753–790.

Suková, P., Charzyński, S. and Janiuk, A. (2016), Relativistic low angular momentum accretion in 3D, in A. Różańska and M. Bejger, editors, *37th Meeting of the Polish Astronomical Society*, volume 3, pp. 150–153, arXiv: 1602.07215.

Suková, P., Charzyński, S. and Janiuk, A. (2017), Shocks in the relativistic transonic accretion with low angular momentum, *Monthly Notices of the Royal Astronomical Society*, **472**(4), pp. 4327–4342, URL +http://dx.doi.org/10.1093/mnras/stx2254.

Suková, P., Grzedzielski, M. and Janiuk, A. (2016), Chaotic and stochastic processes in the accretion flows of the black hole x-ray binaries revealed by recurrence analysis, *A&A*, **586**, p. A143, URL http://dx.doi.org/10.1051/0004-6361/201526692.

Suková, P. and Janiuk, A. (2015), Oscillating shocks in the low angular momentum flows as a source of variability of accreting black holes, *MNRAS*, **447**(2), pp. 1565–1579, URL http://mnras.oxfordjournals.org/content/447/2/1565.abstract.

Suková, P. and Janiuk, A. (2016), Non-linear behaviour of xte j1550-564 during its 1998-1999 outburst, revealed by recurrence analysis, *A&A*, **591**, p. A77, URL https://doi.org/10.1051/0004-6361/201628428.

Tchekhovskoy, A., McKinney, J. C. and Narayan, R. (2007), WHAM: a WENO-based general relativistic numerical scheme - I. Hydrodynamics, *MNRAS*, **379**, pp. 469–497, arXiv: 0704.2608.

Proceedings of *RAGtime 17–19, 17–19/23–26 Oct., 1–5 Nov., 2015/2016/2017, Opava, Czech Republic*
Z. Stuchlík, G. Török and V. Karas, editors, Silesian University in Opava, 2017, pp. 177–193

A one-parametric formula relating the frequencies of twin-peak quasi-periodic oscillations

Gabriel Török[1,a] Kateřina Goluchová[1] Eva Šrámková[1]
Jiří Horák[2] Pavel Bakala[1] and Martin Urbanec[1]

[1] Institute of Physics and Research Centre for Computational Physics and Data Processing, Faculty of Philosophy & Science, Silesian University in Opava, Bezručovo nám. 13, CZ-746 01 Opava, Czech Republic
[2] Astronomical Institute, Boční II 1401/2a, CZ-14131 Praha 4 - Spořilov, Czech Republic
[a] gabriel.torok@gmail.com

ABSTRACT
Timing analysis of X-ray flux in more than a dozen low-mass X-ray binary systems containing a neutron star reveals remarkable correlations between frequencies of two characteristic peaks present in the power-density spectra. We find a simple analytic relation that well reproduces all these individual correlations. We link this relation to a physical model which involves accretion rate modulation caused by an oscillating torus.

Keywords: X-Rays: Binaries — Accretion, Accretion Disks — Stars: Neutron

1 INTRODUCTION

Low-mass X-ray binaries (LMXBs) provide a unique opportunity to probe the effects associated with strong gravity. The way electromagnetic radiation propagates in space, its time variability, and shape of lines in its energetic spectrum, are all invaluable tools for exploring physical behaviour of matter in strong gravitational field around black holes (BHs) and neutron stars (NSs). A systematic study of NS properties similarly allows for exploration of the supra-dense matter (Lewin et al., 1997).

High-frequency quasi-periodic oscillations (HF QPOs) appear in the X-ray flux of several LMXBs. In NS sources they commonly occur in pairs, therefore being called twin-peak HF QPOs (van der Klis, 2006). The Rossi X-ray timing explorer (RXTE Bradt et al., 1993), which operated from 1995 to 2012, has provided a large amount of NS data. Timing analysis of the X-ray flux in more than a dozen NS systems reveals remarkable correlations between frequencies of two characteristic peaks present in the power-density spectra. In Figure 1 we illustrate these correlations in terms of the upper and lower QPO frequency, ν_U and ν_L, for a group of 14 sources. The Figure comprehends a major part of the available twin-peak QPO measurements in 8 atoll sources, 5 Z sources, and one mili-second X-ray

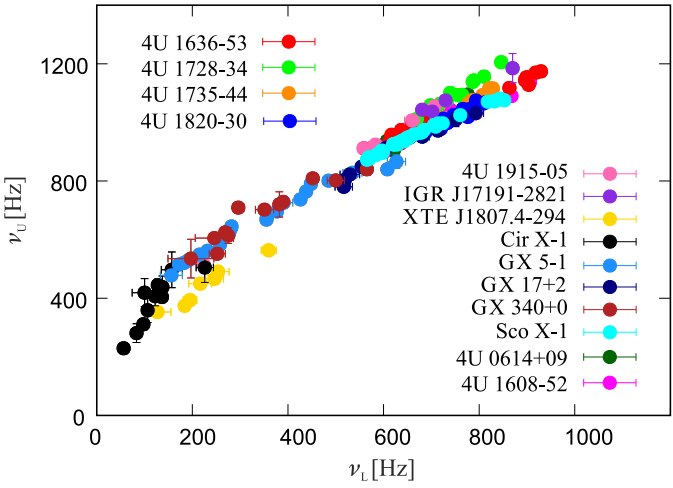

Figure 1. Correlations between frequencies of twin-peak QPOs observed in 14 sources. Properties of these sources and relevant references are given in Table 1.

pulsar (see Table 1 for the list of sources and references). A great number of various theories has been proposed to explain the observed phenomenon. Most often, QPOs are related to orbital motion in strong gravity. Many astrophysicists believe that observations of QPOs may be beneficial in studying the properties of NSs and strong gravitational field, e.g., utilizing QPO frequency correlations (Alpar and Shaham, 1985; Lamb et al., 1985; Miller et al., 1998; Psaltis et al., 1999; Stella and Vietri, 2001; Wagoner et al., 2001; Kluźniak and Abramowicz, 2001; Kato, 2001; Titarchuk and Wood, 2002; Abramowicz et al., 2003; Rezzolla et al., 2003; Kluźniak et al., 2004; Zhang, 2004; Pétri, 2005; Bursa, 2005; Čadež et al., 2008; Mukhopadhyay, 2009; Stuchlík et al., 2013).

2 A ONE-PARAMETRIC RELATION

Up to this date most researchers have been unsuccessful in their attempt to model the individual observed correlations using simple formulae based on geodesic orbital motion (e.g., Lin et al., 2011; Török et al., 2016b and references therein).

2.1 Physical arguments for one-parametric relation

In the series of works (Török et al., 2010, 2012, 2016b) the authors discussed the effective degeneracy between various parameters of the relativistic precession (RP) model as well as several other orbital QPO models. Within this degeneracy, each combination of NS mass M, angular momentum j and quadrupole moment q corresponds to a certain value of

Table 1. List of sources and references, and parameters resulting from matching the observed correlations between twin-peak QPO frequencies by the linear relation, $\nu_U = a\nu_L + b$. The goodness of fits is formally characterized by the χ^2 values. The uncertainties displayed here correspond to standard errors.

Source No./ Type[a]	Name	a	$b[Hz]$	$\frac{\chi^2_{lin}}{d.o.f.}$	Data-points
1/A	4U 1608-52	$0.75^{\pm 0.01}$	$458^{\pm 6}$	30	12
2/A	4U 1636-53	$0.72^{\pm 0.01}$	$505^{\pm 3}$	35	22
3/A	4U 1735-44	$0.91^{\pm 0.01}$	$362^{\pm 4}$	6	8
4/A	4U 1915-05	$1.15^{\pm 0.01}$	$256^{\pm 4}$	1	5
5/A	IGR J17191-2821	$0.73^{\pm 0.02}$	$540^{\pm 10}$	1	4
6/Z	GX 17+2	$0.90^{\pm 0.02}$	$342^{\pm 9}$	10	10
7/Z	Sco X-1	$0.75^{\pm 0.01}$	$456^{\pm 1}$	85	39
8/Z	Cir X-1	$2.39^{\pm 0.14}$	$97^{\pm 16}$	11	11
9/P	XTE J1807.4-294	$1.10^{\pm 0.05}$	$183^{\pm 12}$	5	7
10/A	4U 1728-34	$0.97^{\pm 0.01}$	$370^{\pm 5}$	37	15
11/A	4U 0614+09	$1.02^{\pm 0.1}$	$303^{\pm 4}$	11	13
12/A	4U 1820-30	$0.89^{\pm 0.01}$	$353^{\pm 2}$	74	23
13/Z	GX 340+0	$0.84^{\pm 0.04}$	$402^{\pm 14}$	23	12
14/Z	GX 5-1	$0.86^{\pm 0.02}$	$372^{\pm 7}$	49	21

[a] A - atoll, Z - Z, P - pulsar.

References: (1)–(3), (10) – (12) - Barret et al. (2005a,b, 2006), (4) - Boirin et al. (2000), (5) - Altamirano et al. (2010), (6) - Homan et al. (2002), (7) - van der Klis et al. (1997), (8) - Boutloukos et al. (2006), (9) - Linares et al. (2005), (13) - Jonker et al. (2000), (14) - Jonker et al. (2002).

a single generalized parameter $\mathcal{M}$, e.g., non-rotating NS mass. This degeneracy seems to be a generic property of geodesic QPO models,

$$\nu_L = \nu_L(\nu_U, \mathcal{M}), \; \nu_U = \nu_U(\nu_L, \mathcal{M}). \tag{1}$$

2.2 Observational evidence of one-parametric relation

Fitting of QPO frequencies with ad-hoc (phenomenological) relations has been discussed in a number of studies. In several cases the fits are reliable when two free parameters specific for each source are considered (e.g., Psaltis et al., 1998; Abramowicz et al., 2005b,a; Zhang et al., 2006). We investigate parameters of various fitting relations and find that these parameters are strongly correlated.

It has been noticed by Abramowicz et al. (2005a,b) that the slope a and intercept b of the linear fits ($\nu_U = a\nu_L + b$) are roughly related as $a \approx 1.5 - 0.0015b$. We find that similar behaviour arises for the quadratic relation, $\nu_U = a\nu_L^2 + b$, the square-root relation, $\nu_U = a\sqrt{\nu_L} + b$, and the power-law relation $\nu_U = b(1\nu_L)^a$. Detailed outcomes of data fitting are shown in Tables 1–4 and illustrated in Figure 2.

Table 2. Parameters resulting from matching the observed correlations between twin-peak QPO frequencies by the quadratic relation, $\nu_U = a\nu_L^2 + b$.

Source No./ Type	Name	$a \times 10^4$	$b[Hz]$	$\frac{\chi^2}{d.o.f.}$	Data-points
1/A	4U 1608-52	$5.3^{\pm 0.2}$	$716^{\pm 4}$	45	12
2/A	4U 1636-53	$4.8^{\pm 0.1}$	$764^{\pm 3}$	44	22
3/A	4U 1735-44	$5.9^{\pm 0.1}$	$712^{\pm 3}$	5	8
4/A	4U 1915-05	$13.7^{\pm 0.8}$	$445^{\pm 7}$	8	5
5/A	IGR J17191-2821	$4.9^{\pm 0.2}$	$811^{\pm 9}$	1	4
6/Z	GX 17+2	$7.5^{\pm 0.3}$	$607^{\pm 11}$	17	10
7/Z	Sco X-1	$5.5^{\pm 0.1}$	$708^{\pm 3}$	211	39
8/Z	Cir X-1	$121.3^{\pm 15.8}$	$202^{\pm 19}$	17	11
9/P	XTE J1807.4-294	$22.9^{\pm 2.8}$	$305^{\pm 12}$	8	7
10/A	4U 1728-34	$6.6^{\pm 0.1}$	$725^{\pm 5}$	36	15
11/A	4U 0614+09	$7.5^{\pm 0.1}$	$647^{\pm 4}$	12	13
12/A	4U 1820-30	$6.2^{\pm 0.1}$	$671^{\pm 2}$	74	23
13/Z	GX 340+0	$11.1^{\pm 1.2}$	$551^{\pm 12}$	36	12
14/Z	GX 5-1	$12.1^{\pm 1.0}$	$505^{\pm 12}$	160	21

Table 3. Parameters resulting from matching the observed correlations between twin-peak QPO frequencies by the square-root relation, $\nu_U = a\sqrt{\nu_L} + b$.

Source No./ Type	Name	a	$b[Hz]$	$\frac{\chi^2}{d.o.f.}$	Data-points
1/A	4U 1608-52	$40^{\pm 1}$	$-71^{\pm 6}$	26	12
2/A	4U 1636-53	$40^{\pm 1}$	$-47^{\pm 3}$	37	22
3/A	4U 1735-44	$51^{\pm 1}$	$-352^{\pm 6}$	6	8
4/A	4U 1915-05	$46^{\pm 1}$	$-175^{\pm 3}$	1	5
5/A	IGR J17191-2821	$40^{\pm 1}$	$-7^{\pm 10}$	2	4
6/Z	GX 17+2	$45^{\pm 1}$	$-217^{\pm 8}$	8	10
7/Z	Sco X-1	$39^{\pm 1}$	$-50^{\pm 2}$	51	39
8/Z	Cir X-1	$47^{\pm 2}$	$-127^{\pm 14}$	10	11
9/P	XTE J1807.4-294	$35^{\pm 1}$	$-90^{\pm 11}$	4	7
10/A	4U 1728-34	$53^{\pm 1}$	$-354^{\pm 5}$	37	15
11/A	4U 0614+09	$53^{\pm 1}$	$-383^{\pm 4}$	12	13
12/A	4U 1820-30	$51^{\pm 1}$	$-377^{\pm 2}$	73	23
13/Z	GX 340+0	$32^{\pm 1}$	$102^{\pm 12}$	19	12
14/Z	GX 5-1	$32^{\pm 1}$	$85^{\pm 6}$	30	21

These findings imply that (the one) relation between the QPO frequencies should be based mostly on a single $\mathcal{M}$ parameter.

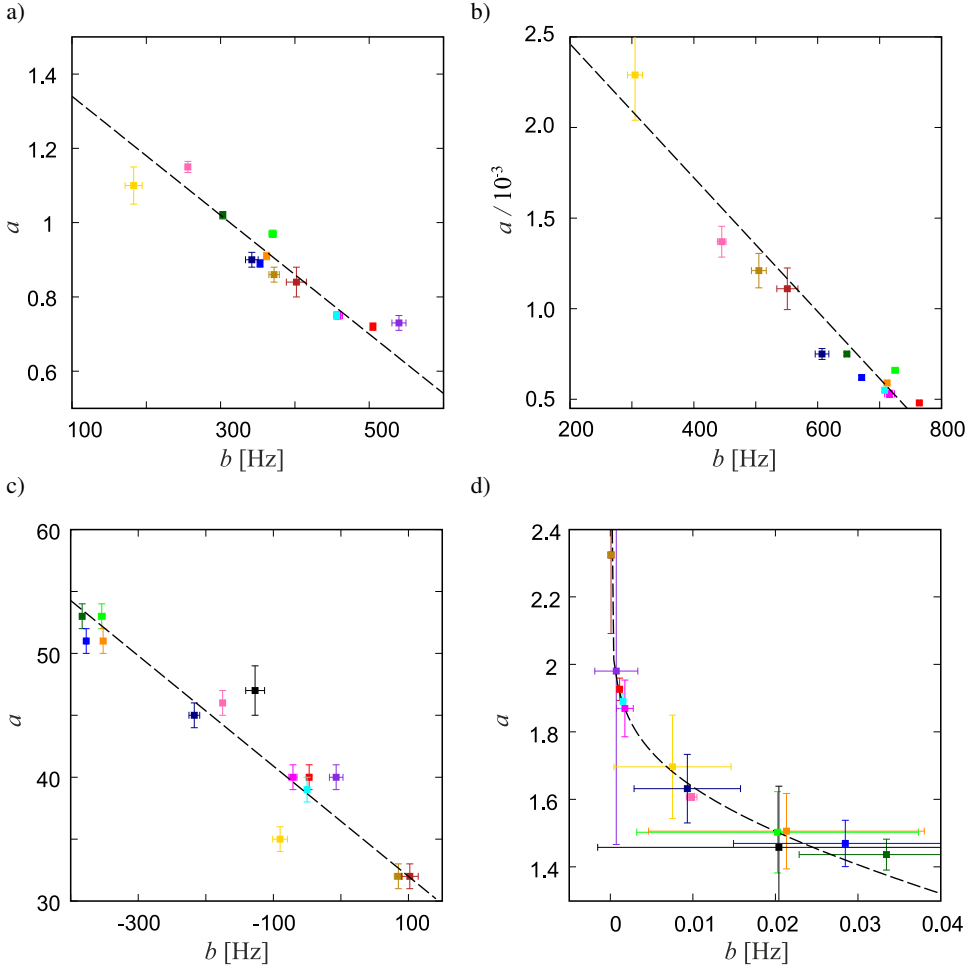

Figure 2. The fitting relations parameters obtained for the individual sources. a) The linear relation. b) The quadratic relation. c) The square-root relation. d) The power-law relation. In all the four panels the dashed line indicates the character of the $a(b)$ dependence.

Table 4. Parameters resulting from matching the observed correlations between twin-peak QPO frequencies by the power-law relation, $\nu_U = b(1\nu_L)^a$.

Source No./ Type	Name	a	$b[Hz]$	$\frac{\chi^2}{d.o.f.}$	Data-points
1/A	4U 1608-52	$0.0018^{\pm 0.0010}$	$1.87^{\pm 0.0841}$	20	12
2/A	4U 1636-53	$0.0011^{\pm 0.0003}$	$1.93^{\pm 0.0332}$	35	22
3/A	4U 1735-44	$0.0213^{\pm 0.0167}$	$1.51^{\pm 0.1118}$	6	8
4/A	4U 1915-05	$0.0099^{\pm 0.0006}$	$1.61^{\pm 0.0101}$	1	5
5/A	IGR J17191-2821	$0.0007^{\pm 0.0026}$	$1.98^{\pm 0.5138}$	1	4
6/Z	GX 17+2	$0.0093^{\pm 0.0064}$	$1.63^{\pm 0.1015}$	8	10
7/Z	Sco X-1	$0.0015^{\pm 0.0002}$	$1.89^{\pm 0.0220}$	51	39
8/Z	Cir X-1	$0.0204^{\pm 0.0219}$	$1.46^{\pm 0.1812}$	10	11
9/P	XTE J1807.4-294	$0.0075^{\pm 0.0071}$	$1.70^{\pm 0.1531}$	4	7
10/A	4U 1728-34	$0.0203^{\pm 0.0171}$	$1.50^{\pm 0.1205}$	32	15
11/A	4U 0614+09	$0.0335^{\pm 0.0106}$	$1.44^{\pm 0.0458}$	11	13
12/A	4U 1820-30	$0.0285^{\pm 0.01355}$	$1.47^{\pm 0.0686}$	69	23
13/Z	GX 340+0	$0.0001^{\pm 0.0001}$	$2.32^{\pm 0.2325}$	18	12
14/Z	GX 5-1	$0.0001^{\pm 0.0001}$	$2.32^{\pm 0.0073}$	29	21

3 GLOBAL MODES OF ACCRETED FLUID MOTION

Török et al. (2016a) explored a model of an oscillating torus. In this model (in next referred to as the CT model), the torus is assumed to form a cusp by filling up the critical equipotential volume. The observed HF QPO frequencies are here identified with the frequencies of global modes of the accreted fluid motion. The upper HF QPO frequency is assumed to be the Keplerian orbital frequency of the fluid defined at the centre of the torus where both pressure and density peak, and from which most of the torus radiation emerges. The lower HF QPO corresponds to the non-axisymmetric $m = -1$ radial epicyclic mode. Overall, we may write

$$\nu_U \equiv \nu_K(r_0), \tag{2}$$

$$\nu_L \equiv \nu_{\mathrm{r},-1}(r_0, \beta). \tag{3}$$

The QPO frequencies therefore strongly depend on the position of the centre of the torus r_0 and its thickness β. The configuration of a torus with cusp is defined by

$$\beta(r_0) \doteq \beta_{\mathrm{c}}(r_0). \tag{4}$$

In other words, we expect that for a given r_0 the torus is always close to its maximal possible size filling its 'Roche-like' lobe (see Figure 3 for illustration). For a given accreting central compact object our model predicts that the QPO frequencies are functions of a sin-

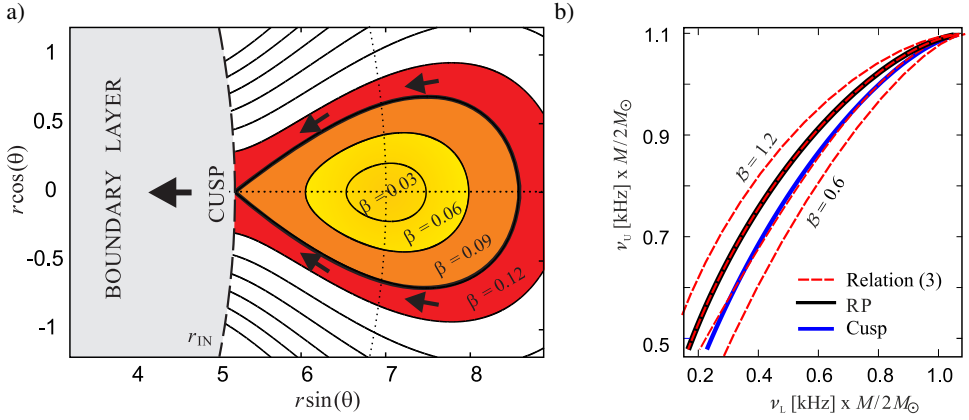

Figure 3. The CT model and its relation to formula (9). The β (panel a) and $\mathcal{B}$ (panel b) symbols denote different physical quantities. a) An illustration of equipotential surfaces of an accretion torus. The yellow colour denotes a non-accreting equilibrium torus. The thick black curve which bounds the orange region signifies the critical equipotential surface corresponding to a torus with cusp. b) A comparison between shapes of the $\nu_U(\nu_L)$ curves predicted by the RP model (the black line), CT model (the blue line) and relation (9) for $\mathcal{B} \in \{0.6,\ 0.8,\ 1.0,\ 1.2\}$ (the dashed red lines). The RP model curve coincides with those given by relation (9) for $\mathcal{B} = 1$ while the CT model curve nearly overlaps with those given by relation (9) for $\mathcal{B} = 0.8$.

gle parameter r_0,

$$\nu_U \equiv \nu_K(r_0), \tag{5}$$

$$\nu_L \equiv \nu_{\mathrm{r},-1}\left[r_0, \beta_c(r_0)\right] . \tag{6}$$

Rather long analytic formulae that define $\nu_{\mathrm{r},-1}$ can be found in Straub and Šrámková (2009). In Török et al. (2016a) the authors numerically calculated the $\nu_L(\nu_U)$ correlation following from relations (5) and (6). Assuming this correlation they obtained good match of data in the case of the atoll source 4U 1636-53 for NS mass of $M_0 = 1.7 M_\odot$.

4 ANALYTIC RELATION THAT WELL MATCHES THE DATA

In Török et al. (2017) we have suggested that frequency relations $\nu_L(\nu_U)$ are scaled as

$$\nu_L = \nu_U \left(1 - \mathcal{B}\sqrt{1 - (\nu_U/\nu_0)^{2/3}}\right), \tag{7}$$

where ν_0 represents the highest possible QPO frequency, $\nu_0 \geq \nu_U \geq \nu_L$. For orbital QPO models, ν_0 is the characteristic frequency of the orbital motion. When ν_0 equals the Keplerian orbital frequency at the innermost stable circular orbit around a non-rotating NS

with gravitational mass M_0, it can be expressed in the units of Hz as (e.g., Kluzniak and Wagoner, 1985; Kluzniak et al., 1990)

$$\nu_0 = \nu_{ISCO} = \frac{1}{6^{3/2}} \frac{c^3}{2\pi G} \frac{1}{M} = 2198 \frac{M_\odot}{M_0} = 2198 \frac{1}{\mathcal{M}}. \tag{8}$$

Hence relation (7) can be written in the form

$$\nu_L = \nu_U \left(1 - \mathcal{B} \sqrt{1 - 0.0059 (\nu_U \mathcal{M})^{2/3}}\right). \tag{9}$$

For $\mathcal{B} = 1$, relation (9) merges with the frequency relation implied by the RP model. This is illustrated in Figure 3 where we plot the curve predicted by the RP model along with the curves given by relation (9) for $\mathcal{B} \in \{(0.6,\ 0.8,\ 1.0,\ 1.2\}$. In the same Figure we include the curve calculated using the CT model. One can see that the CT model prediction is well approximated by relation (9) for $\mathcal{B} = 0.8$,

$$\nu_L = \nu_U \left(1 - 0.8 \sqrt{1 - 0.0059 (\nu_U \mathcal{M})^{2/3}}\right). \tag{10}$$

5 APPLICATIONS

Assuming non-rotating NSs we calculate the sequences of equipotential contours of tori with cusp that provide the best matches to data of the individual sources. This can be done for the following 9 sources - 4U 1608-52, 4U 1636-53, 4U 1735-44, 4U 1915-05, IGR J17191-2821, GX 17+2, Sco X-1, Cir X-1 and XTE J1807.4-294. For these sources we find good agreement between the model and the data. In each case there is $0.5 < \chi^2/\text{d.o.f.} \lesssim 2$. We note that these sources span the approximate range of $\nu_L \in (200,\ 900)$Hz and include the atoll source 4U 1915-05 which itself covers a large range of frequencies, $\nu_L \in (200,\ 800)$Hz. We plot the relevant sequences of equipotential contours as well as the best data fits in Figures 4–6. These data fits are compared to the best fits obtained for the RP model. In all these sources the CT model matches the observed trend better than is done by the RP model. For the sake of clarity we also compare the relevant values of the torus thickness β to the exact values corresponding to the critical cusp torus configuration (see Török et al., 2016a for details). This is done in panels c) of Figures 4–6.

For the other 5 sources - 4U 1728-34, 4U 0614+09, 4U 1820-30, GX 340+0 and GX 5-1 - we cannot fit the data due to the model limitations discussed by Török et al. (2016a). For each of the 14 considered sources we compare the data and relation (9) for $\mathcal{B} = 0.8$. The resulting best fits are shown in Figure 7 along with the best fits obtained for the RP model. We furthermore perform fitting by relation (9) assuming $\mathcal{B}$ as a free parameter. In such case relation (9) matches the data in each of the 14 sources. This finding is illustrated in Figure 8.

The above mentioned outcomes of data fitting are summarized in Tables 5 and 6.

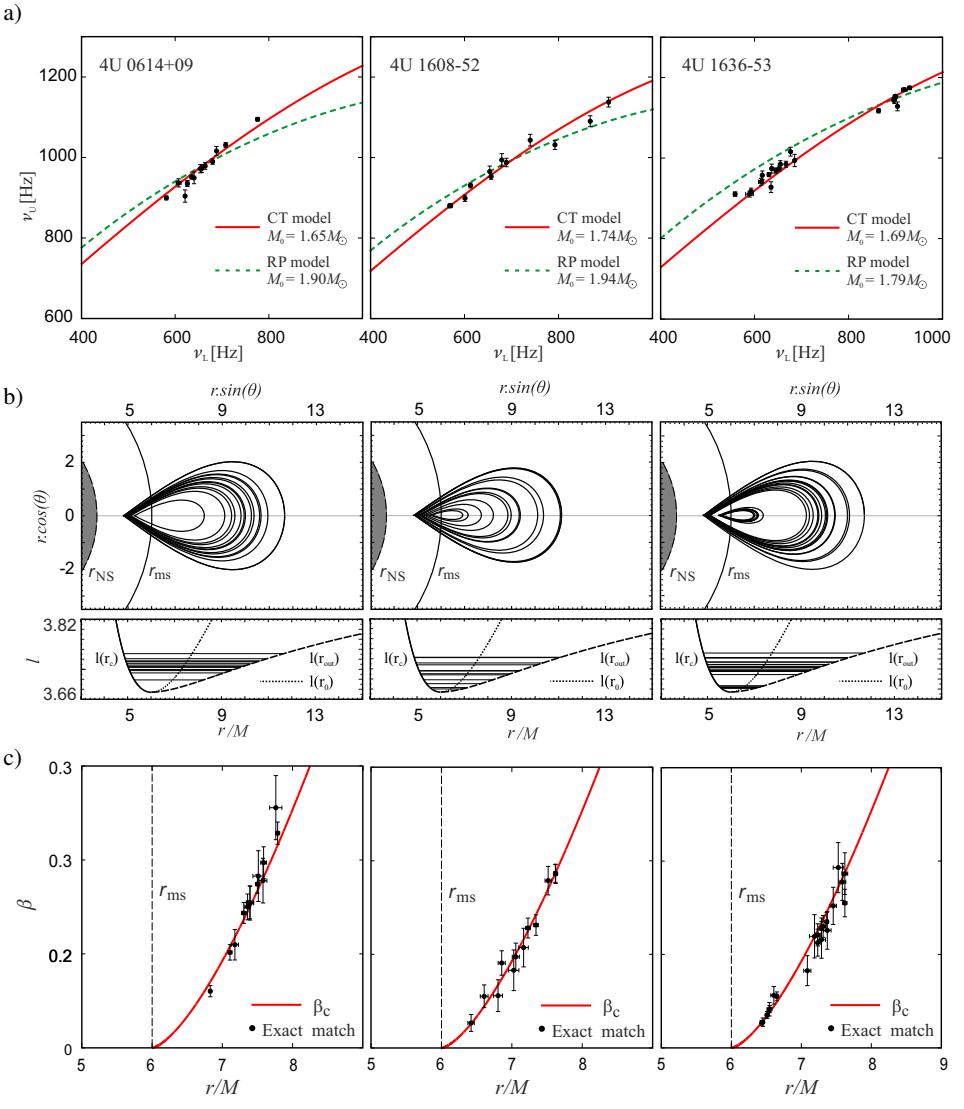

Figure 4. A comparison between the results obtained for the CT and the RP model. We consider here the three following sources - 4U 1608-52, 4U 1636-53 and 4U 1735-44. a) A sequence of tori with a cusp corresponding to a one-parametric data fit ($j = 0$). The bottom sub-panel always indicates the angular momentum behaviour along with the positions of the torus centre r_0 and both the inner and outer edge, r_c and r_{out}. b) The corresponding frequency relation plotted together with the datapoints. We also present the best fit implied by the RP model ($j = 0$). c) A consideration of the β and r combinations that exactly match the individual datapoints for the two chosen combinations of mass and angular momentum (see the paper of Török et al., 2016a). The red line denotes the numerically calculated CT model relation.

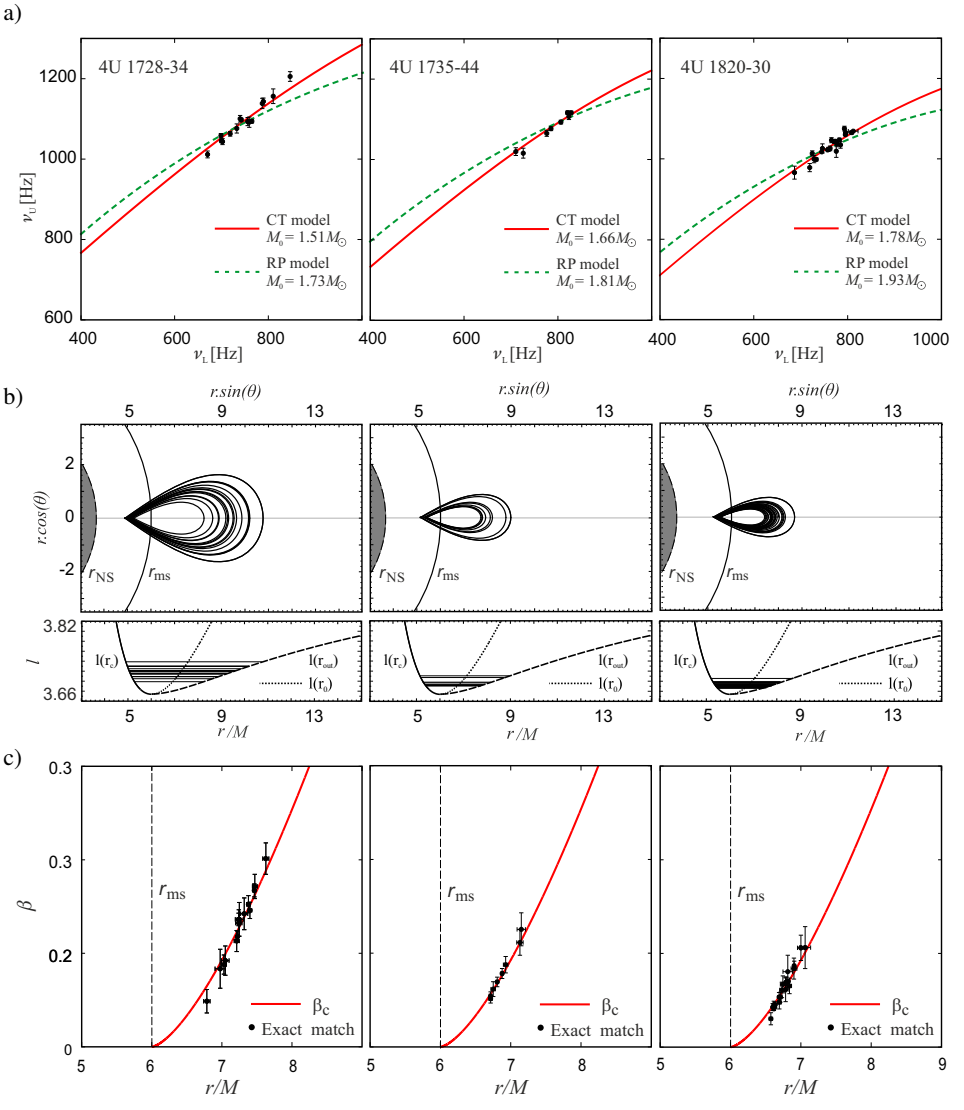

Figure 5. A comparison between the results obtained for the CT and the RP model. We consider here the three following sources - 4U 1728-34, 4U 1735-44 and 4U 1820-30. a) A sequence of tori with a cusp corresponding to a one-parametric data fit ($j = 0$). The bottom sub-panel always indicates the angular momentum behaviour along with the positions of the torus centre r_0 and both the inner and outer edge, r_c and r_{out}. b) The corresponding frequency relation plotted together with the datapoints. We also present the best fit implied by the RP model ($j = 0$). c) A consideration of the β and r combinations that exactly match the individual datapoints for the two chosen combinations of mass and angular momentum (see the paper of Török et al., 2016a). The red line denotes the numerically calculated CT model relation.

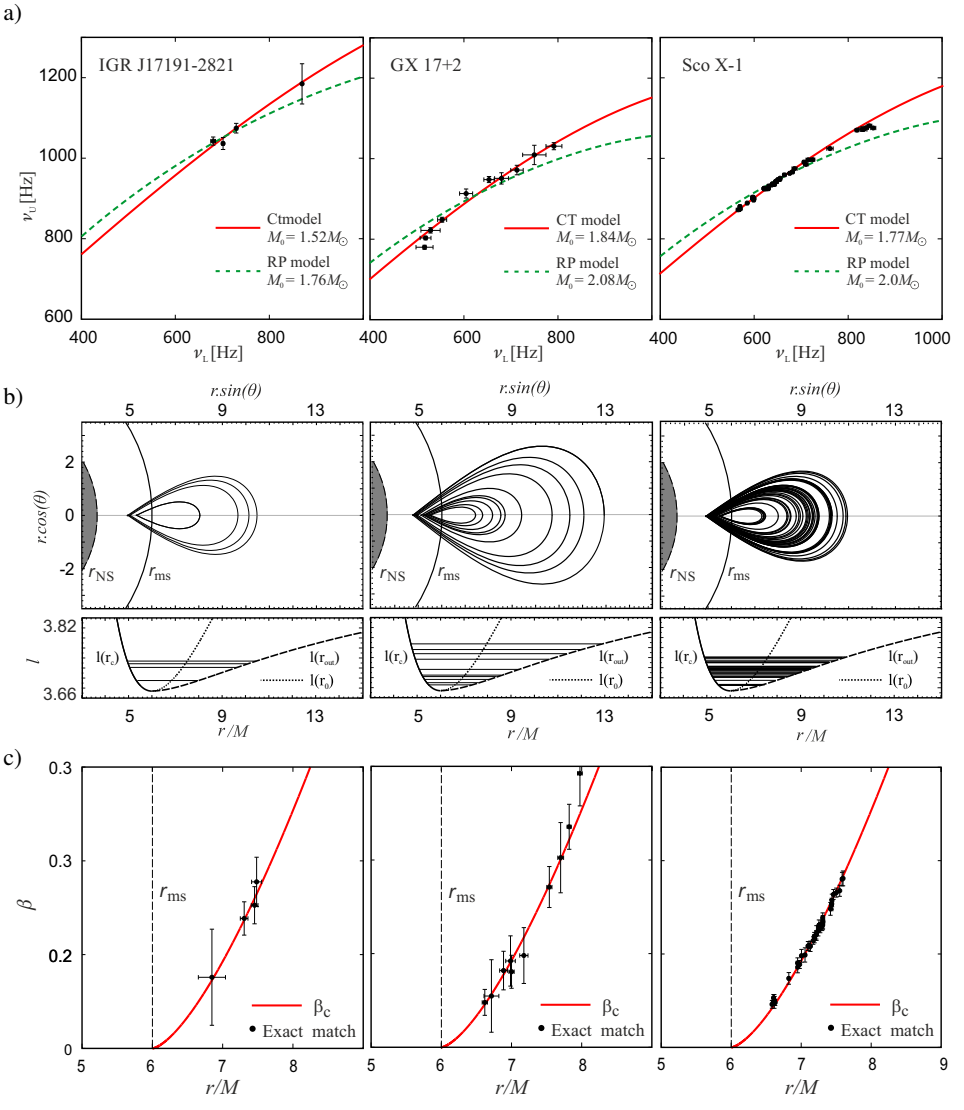

Figure 6. A comparison between the results obtained for the CT and the RP model. We consider here the three following sources - IGR J17191-2821, GX 17+2 and Sco X-1. a) A sequence of tori with a cusp corresponding to a one-parametric data fit ($j = 0$). The bottom sub-panel always indicates the angular momentum behaviour along with the positions of the torus centre r_0 and both the inner and outer edge, r_c and r_{out}. b) The corresponding frequency relation plotted together with the datapoints. We also present the best fit implied by the RP model ($j = 0$). c) A consideration of the β and r combinations that exactly match the individual datapoints for the two chosen combinations of mass and angular momentum (see the paper of Török et al., 2016a). The red line denotes the numerically calculated CT model relation.

Table 5. Parameters obtained through data matching - RP model and CT model.

Source No./ Type[a]	Name	$\frac{M_{\rm RP}}{M_\odot}$	$\frac{\chi^2_{\rm RP}}{d.o.f.}$	$\frac{M_{\rm CUSP}}{M_\odot}$	$\frac{\chi^2_{\rm CUSP}}{d.o.f.}$	Data-points
1/A	4U 1608-52	1.94	10.1	$1.74^{\pm 0.01}$	1.9	12
2/A	4U 1636-53	1.79	17.4	$1.69^{\pm 0.01}$	3.4	22
3/A	4U 1735-44	1.81	5.1	$1.66^{\pm 0.01}$	1.4	8
4/A	4U 1915-05	2.09	28.6	–[a]	–[a]	5
5/A	IGR J17191-2821	1.76	0.6	$1.52^{\pm 0.02}$	0.6	4
6/Z	GX 17+2	2.08	5.5	$1.83^{\pm 0.02}$	0.9	10
7/Z	Sco X-1	2.0	24.2	$1.76^{\pm 0.01}$	2.3	39
8/Z	Cir X-1	2.23	1.3	–[a]	–[a]	11
9/P	XTE J1807.4-294	3.27	1.4	–[a]	–[a]	7
10/A	4U 1728-34	1.74	5.7	$1.51^{\pm 0.01}$	2.8	15
11/A	4U 0614+09	1.90	14.7	$1.65^{\pm 0.01}$	3.4	13
12/A	4U 1820-30	1.93	24.2	$1.78^{\pm 0.01}$	6.4	23
13/Z	GX 340+0	2.07	1.8	–[a]	–[a]	12
14/Z	GX 5-1	2.13	3.1	–[a]	–[a]	21

[a] The observed frequencies extend below the expected range of physical applicability of the CT model discussed by Török et al. (2016a).

Table 6. Parameters obtained through data matching - relation (9) in its one- and two- parametric form.

Source No./Type	Name	$\mathcal{M}$	$\frac{\chi^2}{d.o.f.}$	$\mathcal{M}(\mathcal{B})$	$\mathcal{B}$	$\frac{\chi^2_{\mathcal{M}(\mathcal{B})}}{d.o.f.}$	Data-points
1/A	4U 1608-52	$1.80^{\pm 0.01}$	1.6	$1.79^{\pm 0.04}$	$0.79^{\pm 0.03}$	1.7	12
2/A	4U 1636-53	$1.70^{\pm 0.01}$	2.0	$1.70^{\pm 0.01}$	$0.8^{\pm 0.01}$	2.1	22
3/A	4U 1735-44	$1.69^{\pm 0.01}$	2.1	$1.48^{\pm 0.10}$	$0.61^{\pm 0.06}$	1.0	8
4/A	4U 1915-05	$1.58^{\pm 0.03}$	0.8	$1.65^{\pm 0.03}$	$0.82^{\pm 0.01}$	0.2	5
5/A	IGR J17191	$1.58^{\pm 0.02}$	0.6	$1.63^{\pm 0.20}$	$0.85^{\pm 0.2}$	0.8	4
6/Z	GX 17+2	$1.89^{\pm 0.02}$	1.2	$1.77^{\pm 0.07}$	$0.72^{\pm 0.04}$	0.8	10
7/Z	Sco X-1	$1.82^{\pm 0.01}$	1.0	$1.81^{\pm 0.01}$	$0.8^{\pm 0.01}$	1.0	39
8/Z	Cir X-1	$0.74^{\pm 0.10}$	1.2	$1.42^{\pm 0.5}$	$0.89^{\pm 0.06}$	1.1	11
9/P	XTE J1807.4	$2.61^{\pm 0.11}$	0.8	$2.85^{\pm 0.25}$	$0.86^{\pm 0.07}$	0.8	7
10/A	4U 1728-34	$1.57^{\pm 0.01}$	3.2	$1.35^{\pm 0.12}$	$0.65^{\pm 0.06}$	2.5	15
11/A	4U 0614+09	$1.71^{\pm 0.02}$	5.1	$1.39^{\pm 0.06}$	$0.62^{\pm 0.02}$	1.1	13
12/A	4U 1820-30	$1.81^{\pm 0.01}$	9.3	$1.53^{\pm 0.07}$	$0.58^{\pm 0.03}$	3.2	23
13/Z	GX 340+0	$1.62^{\pm 0.08}$	4.2	$2.23^{\pm 0.10}$	$1.10^{\pm 0.08}$	1.6	12
14/Z	GX 5-1	$1.65^{\pm 0.10}$	16.7	$2.31^{\pm 0.04}$	$1.11^{\pm 0.02}$	1.5	21

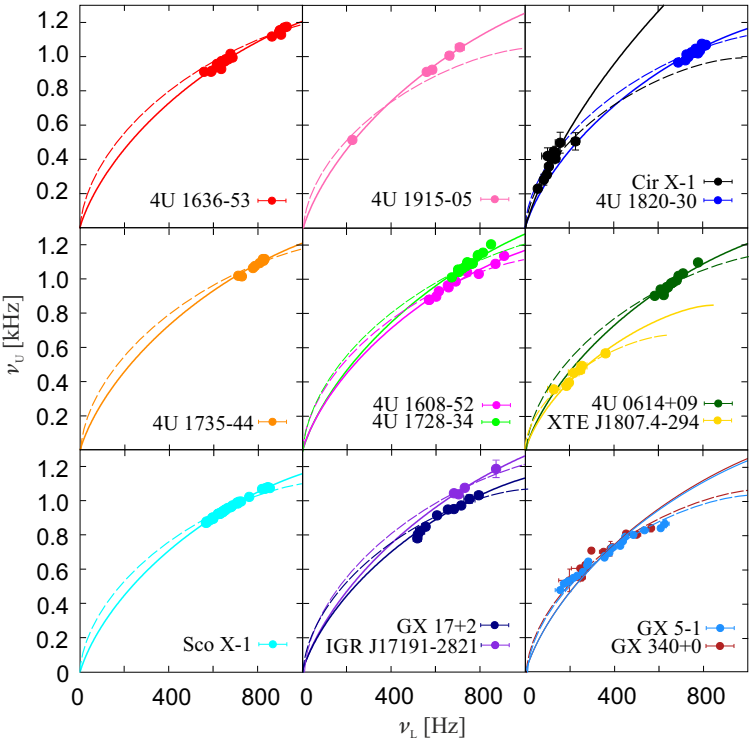

Figure 7. The best fits obtained using relation (9) for $\mathcal{B} = 0.8$ in each of the 14 sources (the solid lines). The best fits carried out for the RP model are shown as well (the dashed lines).

6 DISCUSSION AND CONCLUSIONS

We suggest that relation (9) is likely related to global modes of orbital motion (see the studies of Rezzolla et al., 2003; Abramowicz et al., 2006; Šrámková et al., 2007; Ingram and Done, 2010; Fragile et al., 2016; Török et al., 2016a; Mishra et al., 2017; Parthasarathy et al., 2017; de Avellar et al., 2017 and references therein).

We conclude that for $\mathcal{B} = 0.8$ the CT model as well as relation (9) well reproduce the data of 9 sources. When $\mathcal{B}$ is considered as a free parameter, we obtain good fits for each of the 14 considered sources. Within the CT model framework, larger deviations from the case of $\mathcal{B} = 0.8$ can have a direct physical interpretation. They may be caused by further non-geodesic effects acting on the torus formation induced by, e.g., the influence of magnetic field. This would agree with the general interpretation, in which the $\mathcal{M}$ parameter represents the main parameter which reflects the spacetime geometry given by the NS mass and spin, while the $\mathcal{B}$ parameter reflects the additional stable factors.

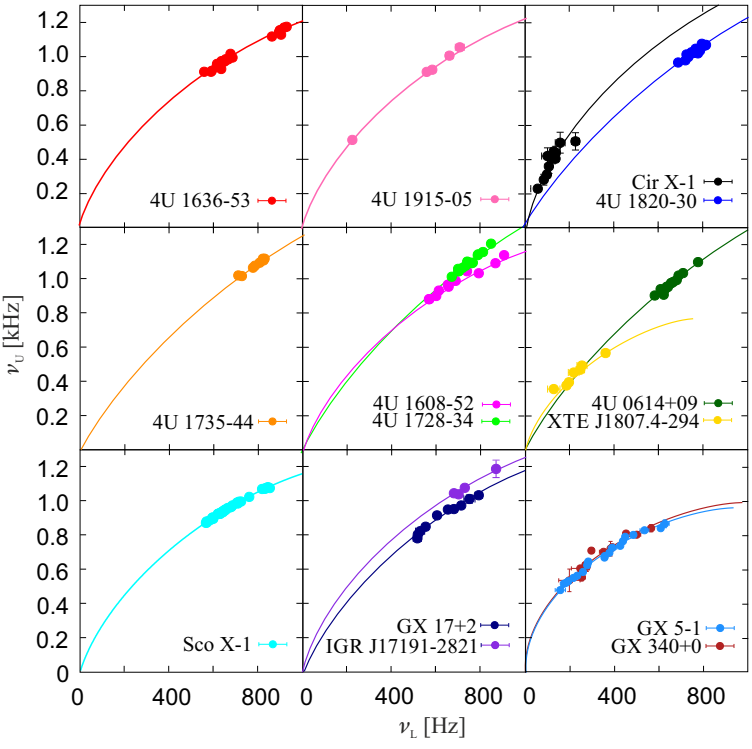

Figure 8. The best fits obtained using relation (9) while assuming $\mathcal{B}$ as a free parameter in each of the 14 sources.

ACKNOWLEDGEMENTS

We would like to acknowledge the Czech Science Foundation grant No. 17-16287S, the INTER-EXCELLENCE project No. LTI17018 aimed to support collaboration between the Silesian University in Opava (SU) and the Astronomical Institute in Prague (ASU), and the internal SU grant No. SGS/15/2016. We are grateful to Marek Abramowicz (SU) and Omer Blaes (University of California in Santa Barbara - UCSB) for useful discussions. Last but not least we would like to acknowledge the hospitality of UCSB and to express our thanks to concierges of Mlýnská hotel in Uherské Hradiště, Czech Republic for their participation in organizing frequent workshops of SU and ASU.

REFERENCES

Abramowicz, M. A., Barret, D., Bursa, M., Horák, J., Kluźniak, W., Rebusco, P. and Török, G. (2005a), A note on the slope-shift anticorrelation in the neutron star kHz QPOs data, in S. Hledík

and Z. Stuchlík, editors, *RAGtime 6/7: Workshops on black holes and neutron stars*, pp. 1–9.

Abramowicz, M. A., Barret, D., Bursa, M., Horák, J., Kluźniak, W., Rebusco, P. and Török, G. (2005b), The correlations and anticorrelations in QPO data, *Astronomische Nachrichten*, **326**, pp. 864–866, arXiv: astro-ph/0510462.

Abramowicz, M. A., Blaes, O. M., Horák, J., Kluźniak, W. and Rebusco, P. (2006), Epicyclic oscillations of fluid bodies: II. Strong gravity, *Classical and Quantum Gravity*, **23**, pp. 1689–1696, arXiv: astro-ph/0511375.

Abramowicz, M. A., Karas, V., Kluźniak, W., Lee, W. H. and Rebusco, P. (2003), Non-Linear Resonance in Nearly Geodesic Motion in Low-Mass X-Ray Binaries, *PASJ*, **55**, pp. 467–466, arXiv: astro-ph/0302183.

Alpar, M. A. and Shaham, J. (1985), Is GX5 - 1 a millisecond pulsar?, *Nature*, **316**, pp. 239–241.

Altamirano, D., Linares, M., Patruno, A., Degenaar, N., Wijnands, R., Klein-Wolt, M., van der Klis, M., Markwardt, C. and Swank, J. (2010), Type I X-ray bursts, burst oscillations and kHz quasi-periodic oscillations in the neutron star system IGRJ17191-2821, *MNRAS*, **401**, pp. 223–230, arXiv: 0908.4039.

Barret, D., Olive, J.-F. and Miller, M. C. (2005a), An abrupt drop in the coherence of the lower kHz quasi-periodic oscillations in 4U 1636-536, *MNRAS*, **361**, pp. 855–860, arXiv: astro-ph/0505402.

Barret, D., Olive, J.-F. and Miller, M. C. (2005b), Drop of coherence of the lower kilo-Hz QPO in neutron stars: Is there a link with the innermost stable circular orbit?, *Astronomische Nachrichten*, **326**, pp. 808–811, arXiv: astro-ph/0510094.

Barret, D., Olive, J.-F. and Miller, M. C. (2006), The coherence of kilohertz quasi-periodic oscillations in the X-rays from accreting neutron stars, *MNRAS*, **370**, pp. 1140–1146, arXiv: astro-ph/0605486.

Boirin, L., Barret, D., Olive, J. F., Bloser, P. F. and Grindlay, J. E. (2000), Low and high frequency quasi-periodic oscillations in 4U1915-05, *Astronomy and Astrophysics*, **361**, pp. 121–138, arXiv: astro-ph/0007071.

Boutloukos, S., van der Klis, M., Altamirano, D., Klein-Wolt, M., Wijnands, R., Jonker, P. G. and Fender, R. P. (2006), Discovery of Twin kHz QPOs in the Peculiar X-Ray Binary Circinus X-1, *APJ*, **653**, pp. 1435–1444, arXiv: astro-ph/0608089.

Bradt, H. V., Rothschild, R. E. and Swank, J. H. (1993), X-ray timing explorer mission, *ApJ Supp.*, **97**, pp. 355–360.

Bursa, M. (2005), High-frequency QPOs in GRO J1655-40: Constraints on resonance models by spectral fits, in S. Hledík and Z. Stuchlík, editors, *RAGtime 6/7: Workshops on black holes and neutron stars*, pp. 39–45.

de Avellar, M. G., Porth, O., Younsi, Z. and Rezzolla, L. (2017), The kilo Hertz quasi-periodic oscillations in neutron star low-mass X-ray binaries as tori oscillation modes. I, *ArXiv e-prints*, arXiv: 1709.07706.

Fragile, P. C., Straub, O. and Blaes, O. (2016), High-frequency and type-C QPOs from oscillating, precessing hot, thick flow, *MNRAS*, **461**, pp. 1356–1362, arXiv: 1602.08082.

Homan, J., van der Klis, M., Jonker, P. G., Wijnands, R., Kuulkers, E., Méndez, M. and Lewin, W. H. G. (2002), RXTE Observations of the Neutron Star Low-Mass X-Ray Binary GX 17+2: Correlated X-Ray Spectral and Timing Behavior, *The Astrophysical Journal*, **568**, pp. 878–900, arXiv: astro-ph/0104323.

Ingram, A. and Done, C. (2010), A physical interpretation of the variability power spectral components in accreting neutron stars, *MNRAS*, **405**, pp. 2447–2452, arXiv: 0907.5485.

Jonker, P. G., van der Klis, M., Homan, J., Méndez, M., Lewin, W. H. G., Wijnands, R. and Zhang,

W. (2002), Low- and high-frequency variability as a function of spectral properties in the bright X-ray binary GX 5-1, *MNRAS*, **333**, pp. 665–678, arXiv: astro-ph/0202420.

Jonker, P. G., van der Klis, M., Wijnands, R., Homan, J., van Paradijs, J., Méndez, M., Ford, E. C., Kuulkers, E. and Lamb, F. K. (2000), The Power Spectral Properties of the Z Source GX 340+0, *The Astrophysical Journal*, **537**, pp. 374–386, arXiv: astro-ph/0002022.

Kato, S. (2001), Basic Properties of Thin-Disk Oscillations, *PASJ*, **53**, pp. 1–24.

Kluźniak, W. and Abramowicz, M. A. (2001), The physics of kHz QPOs—strong gravity's coupled anharmonic oscillators, *ArXiv Astrophysics e-prints*, arXiv: astro-ph/0105057.

Kluźniak, W., Abramowicz, M. A., Kato, S., Lee, W. H. and Stergioulas, N. (2004), Nonlinear Resonance in the Accretion Disk of a Millisecond Pulsar, *AJ*, **603**, pp. L89–L92, arXiv: astro-ph/0308035.

Kluzniak, W., Michelson, P. and Wagoner, R. V. (1990), Determining the properties of accretion-gap neutron stars, *ApJ*, **358**, pp. 538–544.

Kluzniak, W. and Wagoner, R. V. (1985), Evolution of the innermost stable orbits around accreting neutron stars, *ApJ*, **297**, pp. 548–554.

Lamb, F. K., Shibazaki, N., Alpar, M. A. and Shaham, J. (1985), Quasi-periodic oscillations in bright galactic-bulge X-ray sources, *Nature*, **317**, pp. 681–687.

Lewin, W. H. G., van Paradijs, J. and van den Heuvel, E. P. J. (1997), *X-ray Binaries*, Cambridge University Press.

Lin, Y.-F., Boutelier, M., Barret, D. and Zhang, S.-N. (2011), Studying Frequency Relationships of Kilohertz Quasi-periodic Oscillations for 4U 1636-53 and Sco X-1: Observations Confront Theories, *The Astrophysical Journal*, **726**, 74, arXiv: 1010.6198.

Linares, M., van der Klis, M., Altamirano, D. and Markwardt, C. B. (2005), Discovery of Kilohertz Quasi-periodic Oscillations and Shifted Frequency Correlations in the Accreting Millisecond Pulsar XTE J1807-294, *The Astrophysical Journal*, **634**, pp. 1250–1260, arXiv: astro-ph/0509011.

Miller, M. C., Lamb, F. K. and Psaltis, D. (1998), Sonic-Point Model of Kilohertz Quasi-periodic Brightness Oscillations in Low-Mass X-Ray Binaries, *AJ*, **508**, pp. 791–830, arXiv: astro-ph/9609157.

Mishra, B., Vincent, F. H., Manousakis, A., Fragile, P. C., Paumard, T. and Kluźniak, W. (2017), Quasi-periodic oscillations from relativistic ray-traced hydrodynamical tori, *MNRAS*, **467**, pp. 4036–4049.

Mukhopadhyay, B. (2009), Higher-Order Nonlinearity in Accretion Disks: Quasi-Periodic Oscillations of Black Hole and Neutron Star Sources and Their Spin, *AJ*, **694**, pp. 387–395, arXiv: 0811.2033.

Parthasarathy, V., Kluzniak, W. and Cemeljic, M. (2017), MHD simulations of oscillating cusp-filling tori around neutron stars – missing upper kHz QPO, *ArXiv e-prints*, arXiv: 1703.05036.

Pétri, J. (2005), An explanation for the kHz-QPO twin peaks separation in slow and fast rotators, *A&A*, **439**, pp. L27–L30, arXiv: astro-ph/0507167.

Psaltis, D., Méndez, M., Wijnands, R., Homan, J., Jonker, P. G., van der Klis, M., Lamb, F. K., Kuulkers, E., van Paradijs, J. and Lewin, W. H. G. (1998), The Beat-Frequency Interpretation of Kilohertz Quasi-periodic Oscillations in Neutron Star Low-Mass X-Ray Binaries, *ApJ Lett.*, **501**, pp. L95–L99, arXiv: astro-ph/9805084.

Psaltis, D., Wijnands, R., Homan, J., Jonker, P. G., van der Klis, M., Miller, M. C., Lamb, F. K., Kuulkers, E., van Paradijs, J. and Lewin, W. H. G. (1999), On the Magnetospheric Beat-Frequency and Lense-Thirring Interpretations of the Horizontal-Branch Oscillation in the Z Sources, *AJ*, **520**, pp. 763–775, arXiv: astro-ph/9903105.

Rezzolla, L., Yoshida, S. and Zanotti, O. (2003), Oscillations of vertically integrated relativistic

tori - I. Axisymmetric modes in a Schwarzschild space-time, *MNRAS*, **344**, pp. 978–992, arXiv: astro-ph/0307488.

Šrámková, E., Torkelsson, U. and Abramowicz, M. A. (2007), Oscillations of tori in the pseudo-Newtonian potential, *A&A*, **467**, pp. 641–646, arXiv: 0802.3856.

Stella, L. and Vietri, M. (2001), Quasi-Periodic Oscillations from Low-Mass X-ray Binaries and Strong Field Gravity, in R. Giacconi, S. Serio and L. Stella, editors, *X-ray Astronomy 2000*, volume 234 of *Astronomical Society of the Pacific Conference Series*, p. 213.

Straub, O. and Šrámková, E. (2009), Epicyclic oscillations of non-slender fluid tori around Kerr black holes, *Classical and Quantum Gravity*, **26**(5), 055011, arXiv: 0901.1635.

Stuchlík, Z., Kotrlová, A. and Török, G. (2013), Multi-resonance orbital model of high-frequency quasi-periodic oscillations: possible high-precision determination of black hole and neutron star spin, *A&A*, **552**, A10, arXiv: 1305.3552.

Titarchuk, L. and Wood, K. (2002), On the Low and High Frequency Correlation in Quasi-periodic Oscillations among White Dwarf, Neutron Star, and Black Hole Binaries, *AJ*, **577**, pp. L23–L26, arXiv: astro-ph/0208212.

Török, G., Bakala, P., Šrámková, E., Stuchlík, Z. and Urbanec, M. (2010), On Mass Constraints Implied by the Relativistic Precession Model of Twin-peak Quasi-periodic Oscillations in Circinus X-1, *AJ*, **714**, pp. 748–757, arXiv: 1008.0088.

Török, G., Bakala, P., Šrámková, E., Stuchlík, Z., Urbanec, M. and Goluchová, K. (2012), Mass-Angular-momentum Relations Implied by Models of Twin Peak Quasi-periodic Oscillations, *ApJ*, **760**, 138, arXiv: 1408.4220.

Török, G., Goluchová, K., Horák, J., Šrámková, E., Urbanec, M., Pecháček, T. and Bakala, P. (2016a), Twin peak quasi-periodic oscillations as signature of oscillating cusp torus, *MNRAS*, **457**, pp. L19–L23, arXiv: 1512.03841.

Török, G., Goluchová, K., Urbanec, M., Šrámková, E., Adámek, K., Urbancová, G., Pecháček, T., Bakala, P., Stuchlík, Z., Horák, J. and Juryšek, J. (2016b), Constraining Models of Twin-Peak Quasi-periodic Oscillations with Realistic Neutron Star Equations of State, *The Astrophysical Journal*, **833**, 273, arXiv: 1611.06087.

Török, G., Goluchová, K., Šrámková, E., Horák, J., Bakala, P. and Urbanec, M. (2017), On one-parametric formula relating the frequencies of twin-peak quasi-periodic oscillations, *ArXiv e-prints*, accepted for publication in MNRAS, arXiv: 1710.10901.

Čadež, A., Calvani, M. and Kostić, U. (2008), On the tidal evolution of the orbits of low-mass satellites around black holes, *A&A*, **487**, pp. 527–532, arXiv: 0809.1783.

van der Klis, M. (2006), *Rapid X-ray Variability*, pp. 39–112, Cambridge University Press.

van der Klis, M., Wijnands, R. A. D., Horne, K. and Chen, W. (1997), Kilohertz Quasi-Periodic Oscillation Peak Separation Is Not Constant in Scorpius X-1, *APJL*, **481**, pp. L97–L100, arXiv: astro-ph/9703025.

Wagoner, R. V., Silbergleit, A. S. and Ortega-Rodríguez, M. (2001), "Stable" Quasi-periodic Oscillations and Black Hole Properties from Diskoseismology, *AJ*, **559**, pp. L25–L28, arXiv: astro-ph/0107168.

Zhang, C. (2004), The MHD Alfven wave oscillation model of kHz Quasi Periodic Oscillations of Accreting X-ray binaries, *A&A*, **423**, pp. 401–404, arXiv: astro-ph/0402028.

Zhang, C. M., Yin, H. X., Zhao, Y. H., Zhang, F. and Song, L. M. (2006), The correlations between the twin kHz quasi-periodic oscillation frequencies of low-mass X-ray binaries, *MNRAS*, **366**, pp. 1373–1377, arXiv: astro-ph/0601318.

Proceedings of *RAGtime 17–19, 17–19/23–26 Oct., 1–5 Nov., 2015/2016/2017, Opava, Czech Republic*
Z. Stuchlík, G. Török and V. Karas, editors, Silesian University in Opava, 2017, pp. 195–199

Note on the character of the generic rotating charged regular black holes in general relativity coupled to nonlinear electrodynamics

Bobir Toshmatov[1,a] Zdeněk Stuchlík[1,b]
and Bobomurat Ahmedov[2,c]

[1]Institute of Physics and Research Centre of Theoretical Physics and Astrophysics,
Faculty of Philosophy & Science, Silesian University in Opava,
Bezručovo náměstí 13, CZ-74601 Opava, Czech Republic
[2]Ulugh Beg Astronomical Institute, Astronomicheskaya 33, Tashkent 100052, Uzbekistan
[a]bobir.toshmatov@fpf.slu.cz [b]zdenek.stuchlik@fpf.slu.cz
[c]ahmedov@astrin.uz

ABSTRACT
We demonstrate that the generic charged rotating regular black hole solutions of general relativity coupled to non-linear electrodynamics, obtained by using the alternate Newman-Janis algorithm, introduces only small (on level 10^{-2}) inconsistency in the behaviour of the electrodynamics Lagrangian. This approves application of these analytic and simple solutions as astrophysically relevant, sufficiently precise approximate solutions describing rotating regular black holes.

Keywords: nonlinear electrodynamics – regular black holes – Newman-Janis algorithm

1 INTRODUCTION

Starting by the Bardeen geometry (Bardeen, 1968), regular black hole solutions attract extended attention till present times. A special focus is devoted to the regular black hole solutions in general relativity combined with the nonlinear electrodynamic models (Hayward, 2006; Ayón-Beato and García, 1998; Neves, 2015). The spherically symmetric solutions were studied in variety of works (Bronnikov and Fabris, 2006; Stuchlík and Schee, 2015), recently generic black hole solutions of general relativity coupled to the Born-Infeld electrodynamics were introduced in (Fan and Wang, 2016) that could cover many of the previously introduced solutions. The rotating regular black hole solutions are usually generated by the Newman-Janis algorithm (NJA) (Newman and Janis, 1965), or by its modification (Azreg-Aïnou, 2014). The modified NJA was applied in the case of the generic rotating charged black holes in (Toshmatov et al., 2017). However, an inconsistency related to the behaviour of the Lagrangian of the nonlinear electrodynamics has been noticed

978-80-7510-257-7

in (Rodrigues and Junior, 2017). Here we shortly estimate this inconsistency and its implication on the relevance of the generic rotating regular solutions presented in (Toshmatov et al., 2017).

2 INCONSISTENCY OF THE GENERIC ROTATING BLACK HOLE SOLUTION IN (TOSHMATOV ET AL., 2017)

In the paper (Toshmatov et al., 2017) we had recently obtained the following solution which is one of the possible candidates for the rotating regular black hole solution of general relativity coupled to nonlinear electrodynamic field, converting the spherically symmetric regular black hole solution (Fan and Wang, 2016) by using the alternate NJA. The spacetime geometry of this solution reads

$$ds^2 = -\left(1-\frac{2\rho r}{\Sigma}\right)dt^2 + \frac{\Sigma}{\Delta}dr^2 - 2a\sin^2\theta\frac{2\rho r}{\Sigma}d\phi dt + \Sigma d\theta^2 + \sin^2\theta\frac{(r^2+a^2)^2 - a^2\Delta\sin^2\theta}{\Sigma}d\phi^2 , \quad (1)$$

with

$$\Sigma = r^2 + a^2\cos^2\theta, \qquad 2\rho = r(1-f),$$
$$\Delta = r^2 f + a^2 = r^2 - 2\rho r + a^2 . \quad (2)$$

where ρ is the mass function which depends on radial coordinate and electrodynamic field parameters and f is determined by the spherically symmetric class of solutions of the theory. These solutions can take the form of the Bardeen-like, Hayward-like, and Maxwell-like spacetimes. The generic solution (1) had been obtained analytically and it satisfies the Einstein equations in the tetrad frame – see (Toshmatov et al., 2017) for details. However, the NJA does not always lead to true precise solutions of the whole set of field equations of the theory under consideration, i.e, the energy-momentum tensor of the rotating regular black hole solution generated by the NJA is not exactly fulfilling the equations of nonlinear electrodynamics in some cases, as explicitly demonstrated in (Toshmatov et al., 2017; Rodrigues and Junior, 2017).

In the case of the nonrotating black holes with total magnetic charge Q_m, considered in nonlinear electrodynamics, the Lagrangian density of the nonlinear electrodynamic field is defined in terms of ρ as (Fan and Wang, 2016)

$$\mathscr{L} = \frac{4\rho'}{r^2} , \qquad \mathscr{L}_F \equiv \frac{\partial\mathscr{L}}{\partial F} = \frac{r^2(2\rho' - r\rho'')}{2Q_m^2} . \quad (3)$$

where the electromagnetic field strength is $F = 2Q_m^2/r^4$. As a rule, introduction of the rotation parameter by the NJA must change the form of the Lagrangian density (3), and the gauge of the field as well. The new gauge can be easily found (for details – see (Toshmatov et al., 2017)). However, we cannot apply the NJA directly to (3). The only way to find the Lagrangian density of the rotating black hole in nonlinear electrodynamics, is to solve

the Einstein field equations, $G_{\mu\nu} = T_{\mu\nu}$, with respect to $\mathscr{L}$ and $\mathscr{L}_F$ in the background (1). Here, the energy-momentum tensor of the nonlinear electrodynamic field is given by

$$T_{\mu\nu} = 2\left(\mathscr{L}_F F^{\alpha}_{\mu} F_{\nu\alpha} - \frac{1}{4} g_{\mu\nu}\mathscr{L}\right), \tag{4}$$

Thus, the Einstein equations give five independent equations with two unknowns $\mathscr{L}$ and $\mathscr{L}_F$, which cannot be solved simultaneously. Therefore, in the paper (Toshmatov et al., 2017) we had not solved the whole set of equations, instead, we solved just three of them simultaneously, and obtained the expressions for $\mathscr{L}$ and $\mathscr{L}_F$ in the form

$$\mathscr{L} = \frac{r^2\left(15a^4 - 8a^2r^2 + 8r^4 + 4a^2(5a^2 - 2r^2)\cos 2\theta + 5a^4\cos 4\theta\right)\rho'}{2\Sigma^4} + \frac{8a^2r^3\cos^2\theta\rho''}{\Sigma^3}, \tag{5}$$

$$\mathscr{L}_F = \frac{2(r^2 - a^2\cos^2\theta)\rho' - r\Sigma\rho''}{2Q_m^2}, \tag{6}$$

where the electromagnetic field strength F in the rotating case takes the following form (Toshmatov et al., 2017)

$$F = \frac{Q_m^2[a^4(3 - \cos 4\theta) + 4(6a^2r^2 + 2r^4 + a^2(a^2 - 6r^2)\cos 2\theta)]}{4\Sigma^4}. \tag{7}$$

In the nonrotating limit, $a = 0$, we recover the expressions (3). Obviously, these obtained expressions of $\mathscr{L}$, Eq. (5), and $\mathscr{L}_F$, Eq. (6), do not exactly satisfy the remaining two equations. Therefore, as it has been shown in the paper (Rodrigues and Junior, 2017), the total derivative of $\mathscr{L}$ with respect to F is not equal to $\mathscr{L}_F$. The difference can be written as

$$\Delta\mathscr{L}_F = \mathscr{L}_F - \frac{\partial\mathscr{L}}{\partial F} \equiv \mathscr{L}_F - \frac{\partial\mathscr{L}}{\partial r}\frac{\partial r}{\partial F} - \frac{\partial\mathscr{L}}{\partial\theta}\frac{\partial\theta}{\partial F} \neq 0. \tag{8}$$

However, we are able to demonstrate explicitly that the values of $\mathscr{L}_F$ and $\partial\mathscr{L}/\partial F$ are very close and thus, the remaining equations can be considered as being approximately fulfilled, as the value of $\Delta\mathscr{L}_F$ is close to zero. In Fig. 1 we present the radial profile of this difference, $\Delta\mathscr{L}_F$, for the typical values of the Bardeen-like, Hayward-like and Maxwell-like rotating regular black holes. One can see from Fig. 1 that the inconsistency in the rotating regular black hole solution is very small, on the level of 10^{-2}. Therefore, our results can be considered in the same spirit as many results obtained in relation to the so called dirty Kerr-like spacetime metrics, where the relation to the mass stress energy tensor is not considered at all, but the results are considered as relevant for estimations of the astrophysical phenomena related to uncharged matter. Of course, in the case of the behaviour of charged matter in the charged rotating regular black hole backgrounds, we have to be very careful due to the small inconsistency related to the electrodynamic part of the theory.

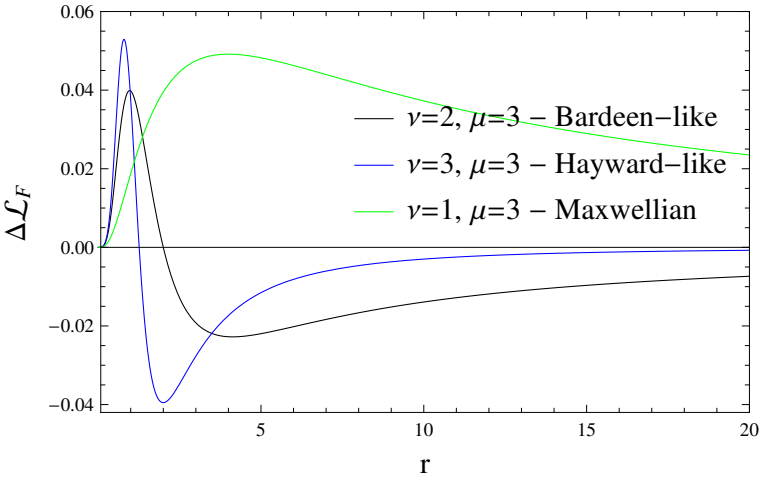

Figure 1. Plot illustrates a change of difference (estimation of inconsistency) $\Delta\mathscr{L}_F = \mathscr{L}_F - \partial\mathscr{L}/\partial F$ with the radial coordinate r at the equatorial plane of the rotating regular black holes presented by Toshmatov et al. (2017) for $q = 1$, $a = 0.5$.

3 CONCLUSION

In general situations, for generic regular charged black hole spherically symmetric solutions of general relativity combined with the nonlinear electrodynamics, it is very difficult to find corresponding rotating black hole solutions in an analytic and fully precise form. Probably, the exact and consistent solutions could be constructed only by numerical procedures. However, the generic rotating charged black hole solutions obtained by using the alternate NJA in (Toshmatov et al., 2017) are analytic and simple solutions that are precise enough for exploring such solutions in astrophysical situations involving uncharged matter.

ACKNOWLEDGEMENTS

This work is supported by the internal student grant of the Silesian University (Grant No. SGS/14/2016) and the Albert Einstein Centre for Gravitation and Astrophysics under the Czech Science Foundation (Grant No. 14-37086G).

REFERENCES

Ayón-Beato, E. and García, A. (1998), Regular Black Hole in General Relativity Coupled to Nonlinear Electrodynamics, *Phys. Rev. Lett.*, **80**, pp. 5056–5059, arXiv: gr-qc/9911046.

Azreg-Aïnou, M. (2014), Generating rotating regular black hole solutions without complexification, *Phys. Rev. D*, **90**(6), 064041, arXiv: 1405.2569.

Bardeen, J. (1968), in *Proceedings of GR5*, p. 174, Tbilisi, USSR.

Bronnikov, K. A. and Fabris, J. C. (2006), Regular Phantom Black Holes, *Phys. Rev. Lett.*, **96**(25), 251101, arXiv: gr-qc/0511109.

Fan, Z.-Y. and Wang, X. (2016), Construction of regular black holes in general relativity, *Phys. Rev. D*, **94**(12), 124027, arXiv: 1610.02636.

Hayward, S. A. (2006), Formation and Evaporation of Nonsingular Black Holes, *Phys. Rev. Lett.*, **96**(3), 031103, arXiv: gr-qc/0506126.

Neves, J. C. S. (2015), Note on regular black holes in a brane world, *Phys. Rev. D*, **92**(8), 084015, arXiv: 1508.03615.

Newman, E. T. and Janis, A. I. (1965), Note on the Kerr Spinning-Particle Metric, *J. Math. Phys.*, **6**, pp. 915–917.

Rodrigues, M. E. and Junior, E. L. B. (2017), Comment on "Generic rotating regular black holes in general relativity coupled to non-linear electrodynamics", *Phys. Rev. D*, in press.

Stuchlík, Z. and Schee, J. (2015), Circular geodesic of Bardeen and Ayon-Beato-Garcia regular black-hole and no-horizon spacetimes, *Int. J. Mod. Phys. D*, **24**, 1550020, arXiv: 1501.00015.

Toshmatov, B., Stuchlík, Z. and Ahmedov, B. (2017), Generic rotating regular black holes in general relativity coupled to nonlinear electrodynamics, *Phys. Rev. D*, **95**(8), 084037, arXiv: 1704.07300.

Proceedings of *RAGtime 17–19, 17–19/23–26 Oct., 1–5 Nov., 2015/2016/2017, Opava, Czech Republic*
Z. Stuchlík, G. Török and V. Karas, editors, Silesian University in Opava, 2017, pp. 201–209

Gravitational field energy of rotating brany black hole

Bobur Turimov[1,a] Javlon Rayimbaev[1,b]
and Azam Rakhmatov[2,c]

[1] Ulugh Beg Astronomical Institute, Astronomicheskaya 33,
Tashkent 100052, Uzbekistan
[2] National University of Uzbekistan, Tashkent,100174, Uzbekistan
[a] bturimov@astrin.uz
[b] javlon@astrin.uz

ABSTRACT
In the present paper we investigate the gravitational field energy associated with the rotating brany black hole by using Tolman's and Landau-Lifshitz's approaches. It is shown that both approaches give exactly the same results and the total gravitational energy is found to be shared by its interior as well as exterior spacetime of the black hole. Switching off the brane parameter (i.e., $Q^* = 0$) one finds that there is no energy shared by the exterior of the rotating brany black hole. Thus the gravitational field seems to have a remarkable difference in comparison the electromagnetic field as the energy in the latter case is shared by the interior as well as exterior of the system producing the electromagnetic field .

Keywords: Brany black hole – Energy associated – Gravitational energy

1 INTRODUCTION

One of the important properties of black holes is their energy associated with exterior spacetime. Using Tolman's definition one can find an expression of the energy associated with a general non-static spherically symmetric spacetime, which is enable to get the energy of radiating Schwarszchild and brany black hole spacetimes. The calculation demonstrates that the energy of a nonlocal system is shared by its exterior as well as interior but for a purely gravitating system the entire energy is confined to its interior.

In the papers Lynden-Bell and Katz (1985); Dadhich and Chellathurai (1986) it has been studied a coordinate-independent definition of the gravitational field energy of the static spherically symmetric spacetime and then it has been shown that the entire gravitational field energy of a Schwarzschild and Reissner-Nordström black hole remains outside the hole. Although there is no unique way of defining energy in curved spacetime, that is why in order to compute the energy one have to work on Cartesian spacetimes. In the paper Virbhadra (1990) it has been evaluated the energy associated with the Kerr-Newman

978-80-7510-257-7

spacetime (charged Kerr spacetime) correction; though and has found that the charge of the black hole strongly depends on the energy associated.

In this paper we are interested in study of the gravitational field energy of the black hole in one of the alternate theories of gravity, in which braneworld model proposed by Randall and Sundrum (1999). In this model the matter is confined to a three dimensional braneworld space, embedded in a larger space so-called bulk in which only gravitation interaction can propagate. The static and spherically symmetric exterior solution of the brane world models has been obtained in Dadhich et al. (2000) in astrophysical scale, which exactly coincides with the Reissner-Nordström solution with the only difference that the brane parameter Q^* stands instead of the square of the electric charge Q^2.

In the present work we will show the effect of the brane parameter in the energy associated with exterior spacetime of the rotating brany black hole and its gravitational energy. First we will show cal calculation of the energy associated with with exterior spacetime the rotating brany black hole in two different ways, such that by using Tolman's and Landau-Lifshitz's approach, then we will compute the gravitational field energy by the exterior spacetime of the brany black hole. Throughout this paper we have used signatures $(-,+,+,+)$ for the spacetime and geometrized unit system $G = c = 1$. Latin indexes run from $1, 2, 3$ and Greek ones from 0 to 3.

2 THE ROTATING BRANY BLACK HOLE

In this section we will briefly mention about the spacetime of the rotating brany balck hole and give a definition of the energy associated by the black hole through its external spacetime. In the spherical coordinate (t, r, θ, ϕ) the spacetime geometry of the rotating brany black hole can be given by the following line element

$$\begin{aligned} ds^2 =& \frac{\Sigma}{\Delta}dr^2 + \Sigma d\theta^2 + \frac{1}{\Sigma}\left[(\Sigma + a^2\sin^2\theta)^2 - \Delta a^2\sin^2\theta\right]d\phi^2 \\ &- \frac{2}{\Sigma}\left[\Sigma + a^2\sin^2\theta - \Delta\right]d\phi dt - \frac{1}{\Sigma}\left[\Delta - a^2\sin^2\theta\right]dt^2 , \end{aligned} \tag{1}$$

where $\Delta = r^2 - 2Mr + a^2 + Q^*$, $\Sigma = r^2 + a^2\cos^2\theta$, and M is the total mass and a is the specific angular momentum of the brany black hole or the spin parameter. The quantity Q^* is the brane charge parameter which is negatively defined $Q^* \leq 0$. One can easily see that the metric in the expression (1) is very similar with Kerr-Newman solution, difference is the square of the electric charge is replaced by brane charge parameter. The Kerr solution can be obtained in the case when the brane charge parameter vanishes $Q^* = 0$.

Since the brane charge parameter takes negative value the radius of the horizon can be found as

$$r_+ = M\left(1 + \sqrt{1 - \frac{a^2}{M^2} + \frac{|Q^*|}{M^2}}\right) \tag{2}$$

from equation (2) one can easily see that spin parameter a of the brany black hole can be greater than its mass as $0 \leq a \leq \sqrt{M^2 + |Q^*|}$. In the paper Turimov et al. (2017) it is found

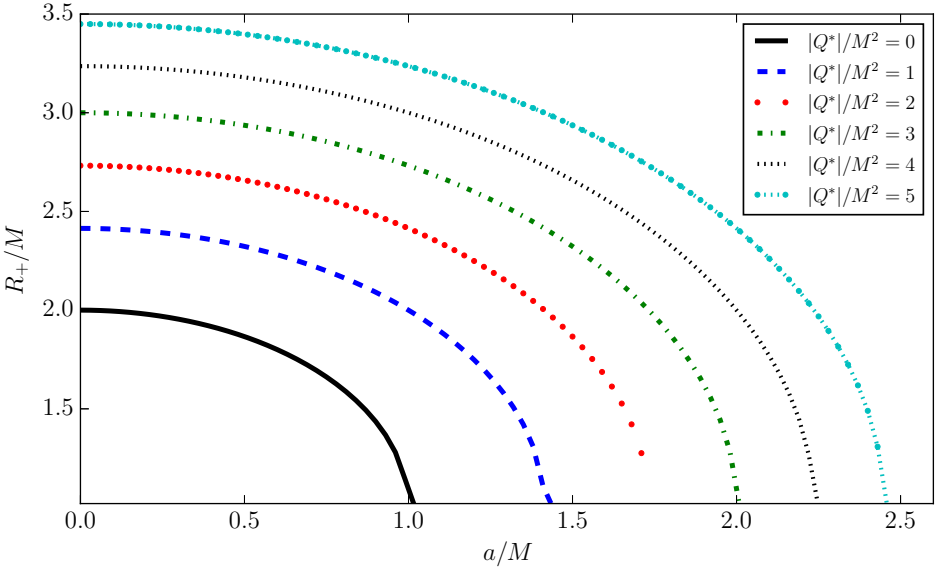

Figure 1. Dependence of the radius of the horizon on the spin parameter for different values of the brane charge parameter.

the upper limit for the value of the brane charge parameter is approximately $|Q^*| \lesssim 8M^2$, that means the spin of the black hole $0 \leq a \leq 3M$. In Fig.1 dependence of the radius of the horizon on the spin parameter for the different values of the brane parameter is shown. One can easily see that the spin of the black hole can take the value up $a \lesssim 3M$. While Figure 2 draws dependence of the radius of the horizon on the brane parameter for the different values of the spin parameter is shown. One can easily see that the size of the brany black hole larger than that in Kerr black hole.

In the present research our aim is investigating the gravitational field energy of the brany black hole, such a work performed by Lynden-Bell and Katz, that main idea is the total energy $E_0 = M$ (in the unit $c = 1$) of the the black hole is sum of the matter energy E_m and the gravitational field energy E_f that can be expressed as Lynden-Bell and Katz (1985); Dadhich and Chellathurai (1986)

$$E_0 = M = E_m + E_f \tag{3}$$

In order to calculate the gravitational energy one have to compute the energy associated with exterior spacetime of the black hole that can be evaluated in the following form

$$E_m = \int d^3x \sqrt{-g}\, T^{00} \tag{4}$$

where $T^{\mu\nu}$ is the energy-momentum tensor that could be found from Einstein field equations for given metric.

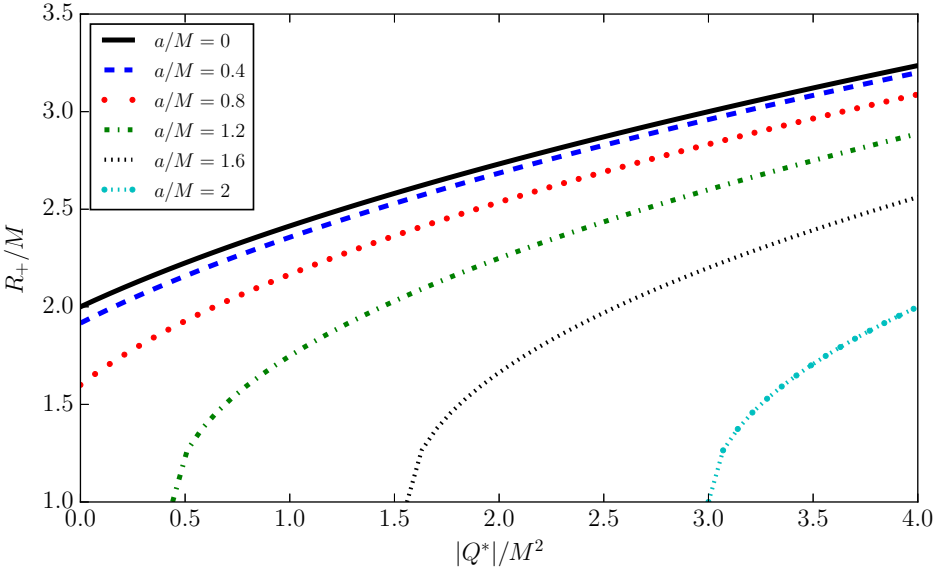

Figure 2. Dependence of the radius of the horizon on the brane charge parameter for different values of the spin parameter.

In the present work we will show the calculation of the gravitational field energy in two different ways: (i) Tolman's approach and (ii) Landau and Lifshitz's approach. In both approaches it is required that to get correct value of the energy the spacetime around the black hole should be considered in Cartesian coordinates (t, x, y, z), that the metric around rotating brany black hole (1) can expressed as

$$ds^2 = -dt^2 + dx^2 + dy^2 + dz^2 + \frac{(2Mr_0 - Q^*)r_0^2}{r_0^4 + a^2z^2} \times \left[dt + \frac{z}{r_0}dz + \frac{xr_0 - ya}{r_0^2 + a^2}dx + \frac{yr_0 + xa}{r_0^2 + a^2}dy\right]^2 , \tag{5}$$

where

$$r_0^4 - r_0^2(x^2 + y^2 + z^2 - a^2) - a^2z^2 = 0 . \tag{6}$$

3 TOLMAN'S APPROACH

In this section we will show the calculation of the energy associated by the brany black hole in Tolman's approach and the definition of the energy E_m associated with arbitrary

space-time is written in the form Tolman (1930)

$$E_m = \frac{1}{8\pi}\int \partial_\nu \left(U_0^{0\nu}\right) d^3x\,, \tag{7}$$

here the pseudotensor $U_\mu^{\alpha\beta}$ is defined as

$$U_\mu^{\alpha\beta} = \sqrt{-g}\left(-g^{\nu\alpha}V_{\beta\nu}^{\beta} + \frac{1}{2}g_\mu^\alpha\, g^{\nu\sigma}V_{\nu\sigma}^{\beta}\right) \tag{8}$$

with

$$V_{\alpha\beta}^{\mu} = -\Gamma_{\alpha\beta}^{\mu} + \frac{1}{2}g_\alpha^\mu\,\Gamma_{\nu\beta}^{\nu} + \frac{1}{2}g_\beta^\mu\,\Gamma_{\nu\alpha}^{\nu} \tag{9}$$

where $\Gamma_{\alpha\beta}^{\mu}$ Cristoffel symbol. Before we mentioned that the energy associated in Tolman's approach can be evaluated in Cartesian coordinates only, obviously without any approximation the calculation will be complicated. That is why we assume that spin parameter quantitatively very small for most physical situations and to be convenience we consider terms containing powers of a up to a^3 only. Since we are interested in calculating the energy associated with the exterior of the rotating brany black hole, the mass of the black hole M and the brane charge parameter Q^* are constants. Now we evaluate all the required components of affine connection, neglecting terms containing powers of a greater than 3.

Nonzero components of affine connection U_0^{0i} (i=1,3) are

$$U_0^{01} = \frac{2Mx}{r^3} - \frac{Q^*x}{r^4} - \frac{aMy}{r^4} + \frac{2a^2Q^*x}{r^6}\left(\frac{3z^2}{r^2}-1\right) - \frac{2a^2Mx}{r^5}\left(\frac{5z^2}{r^2}-1\right) - \frac{a^3My}{r^6}\left(\frac{3z^2}{r^2}-1\right), \tag{10a}$$

$$U_0^{02} = \frac{2My}{r^3} - \frac{Q^*y}{r^4} + \frac{aMx}{r^4} + \frac{2a^2Q^*y}{r^6}\left(\frac{3z^2}{r^2}-1\right) - \frac{2a^2My}{r^5}\left(\frac{5z^2}{r^2}-1\right) - \frac{a^3Mx}{r^6}\left(\frac{3z^2}{r^2}-1\right), \tag{10b}$$

$$U_0^{03} = \frac{2Mz}{r^3} - \frac{Q^*z}{r^4} + \frac{aMx}{r^4} + \frac{2a^2Q^*z}{r^6}\left(\frac{3z^2}{r^2}-1\right) - \frac{2a^2Mz}{r^5}\left(\frac{5z^2}{r^2}-1\right), \tag{10c}$$

Further inserting equation (10) into (7) and then transforming it in spherical coordinates one can get following expression

$$E_m = \frac{1}{8\pi}\int_0^{2\pi} d\phi \int_0^{\pi} \sin\theta d\theta \int_{r_+}^{\infty} dr\left[\frac{2a^2Q^*}{r^4}(3\cos^2\theta - 1) + \frac{Q^*}{r^2}\right] \tag{11}$$

After calculating the integral in the equation (11) one can find the energy associated with exterior rotating brany black hole in Tolman's approach

$$E_m = -\frac{|Q^*|}{2r_+}\left(1 + \frac{2a^2}{3r_+^2}\right), \tag{12}$$

where r_+ is the radius of the horizon of the rotating brany black hole which is given in the equation (2). From the expression (12) one can see that the energy associated with exterior spacetime rotating brany black hole should be also negative.

4 LANDAU-LIFSHITZ'S APPROACH

Another way of computing the energy associated with exterior spacetime of the black hole has been performed by Landau-Lifshitz, which is much more easy to work out in comparison with that in Tolman's way of calculation. In this approach Einstein's field equations can be written in the form Landau and Lifshitz (2004)

$$\partial_\alpha\partial_\beta\mathcal{H}^{\mu\alpha\nu\beta} = 16\pi\mathcal{T}^{\mu\nu} \tag{13}$$

where $\mathcal{T}_{\mu\nu}$ is the energy-momentum tensor of matter and $\mathcal{H}_{\mu\nu\alpha\beta}$ is the Riemann tensor which is defined by in the following form

$$\mathcal{H}^{\mu\alpha\nu\beta} = \mathbf{g}^{\mu\nu}\mathbf{g}^{\alpha\beta} - \mathbf{g}^{\mu\beta}\mathbf{g}^{\alpha\nu} \tag{14}$$

where $\mathbf{g}^{\mu\nu} = \sqrt{-g}\, g^{\mu\nu}$. The energy associated by the black hole is calculated by

$$E_m = \int \mathcal{T}^{00} d^3x \tag{15}$$

These integral also have the meaning of the energy only if it is evaluated in Cartesian coordinates. Considering the terms containing powers of the spin parameter up to a^3 and evaluating nonzero components of the tensor $\mathcal{H}^{0i0j}$ one can rewrite equation (15) in the following form

$$E_m = \frac{1}{8\pi}\int_0^{2\pi} d\phi \int_0^{\pi} \sin\theta d\theta \int_{r_+}^{\infty} dr \left[\frac{2a^2Q^*}{r^4}(3\cos^2\theta - 1) + \frac{Q^*}{r^2}\right] \tag{16}$$

which has exactly same form with equation (11), obviously one can easily see that the energy contained by the exterior spacetime of the rotating brany black hole in the following form

$$E_{\mathrm{m}} = -\frac{|Q^*|}{2r_+}\left(1 + \frac{2a^2}{3r_+^2}\right). \tag{17}$$

Comparing the expressions (12) and (17) one easily see that the energy associated by the rotating black hole have exactly same form in both Tolman's and Landau-Lifshitz's approach.

5 DISCUSSION

By using a definition of the full field energy of the black hole in the equation (3) one can easily obtain following expression for the gravitational energy of the the rotating brany

black hole in the following form Lynden-Bell and Katz (1985); Dadhich and Chellathurai (1986)

$$E_f = M + \frac{|Q^*|}{2r_+}\left(1 + \frac{2a^2}{3r_+^2}\right), \tag{18}$$

from the equation (18) one can easily see that gravitational energy is positive (i.e., $E_f \geq 0$) for the brany black hole. Introducing the new dimensionless definitions for the brane charge parameter $\beta = |Q^*|/M^2$ and the spin parameter $\alpha = a/M$ of the black hole one can have the expression for the dimensionless gravitational energy in the following form

$$\mathcal{E}_f = \frac{E_f}{M} = 1 + \frac{\beta}{2\left(1 + \sqrt{1-\alpha^2+\beta}\right)}\left[1 + \frac{2\alpha^2}{3\left(1 + \sqrt{1-\alpha^2+\beta}\right)^2}\right], \tag{19}$$

In the case of non-rotating brany black hole (i.e., $\alpha = 0$) the gravitational energy will be

$$\begin{aligned}\mathcal{E}_f =& 1 + \frac{\beta}{2\left(1 + \sqrt{1+\beta}\right)} \\ =& \frac{1}{2}(1 + \sqrt{1+\beta}),\end{aligned} \tag{20}$$

For the Kerr black hole (i.e., $\beta = 0$) the dimensionless gravitational energy will be $\mathcal{E}_f = 1$. Figure 3 draws dependence of the gravitational field energy on the brane charge parameter for different values of the spin parameter. One can easily see that the gravitational field energy increase when the brane charge parameter increase.

6 SUMMARY

In the present research we meanly target on the calculation of the energy associated with exterior the rotating brany black hole and its the gravitational energy. We find that the expressions for the energy associated and gravitational energy are exactly the same in Tolman's as well as Landau-Lifshitz's approach. Switching off the brane charge parameter (i.e., $Q^* = 0$) one finds that no energy is contained by the exterior Kerr black hole (i.e., $T^{00} = 0$) and hence the entire energy is confined to its interior only. Although we have evaluated the energy neglecting the terms containing the spin parameter a beyond its third power. We construct the following heuristic arguments in favor of our conclusion. Firstly, once one starts with a definition of energy which demands the entire energy of a Schwarzschild black hole confined to its interior only, we argue that merely the introduction of an intrinsic rotation parameter cannot cause its exterior to share its energy as one must remember that the black hole under investigation is isolated, having no medium surrounding it to propagate its rotational energy to its exterior. Secondly, the rotational energy of the system is proportional to a and in this calculation we have retained terms up to a^3 . So if at all the energy would have been shared by the exterior of the Kerr black hole, it should have certainly appeared in our result. The energy associated with the spacetime of

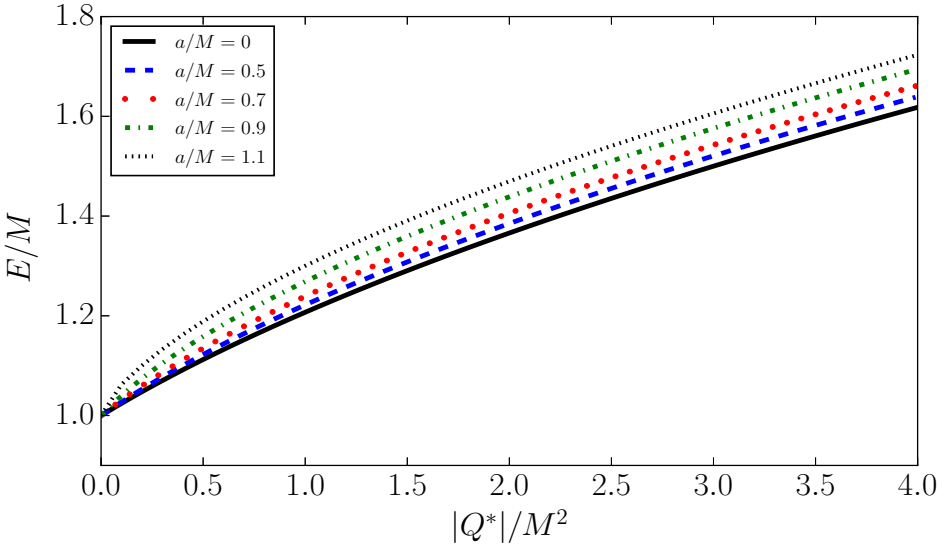

Figure 3. The associated energy dependence of the brane parameter.

the brany black hole of the ($a = 0$) is shared by its interior as well as exterior. Thus one finds a remarkable distinction that Tolman's as well as Landau-Lifshitz's definitions of energy provide between a gravitational field and an electromagnetic field. The entire energy of a gravitational field is confined to its interior only while for the latter case the energy is shared by its interior as well as exterior. In the case of nonrotating black hole (i. e., $a = 0$) we get the energy associated with the spacetime of the brany black hole like metric which is similar the same as found in Virbhadra (1990).

ACKNOWLEDGEMENTS

B.T. thanks B. Ahmedov for very useful comments and discussions. This research is supported by Grant No. VA-FA-F-2- 008, of the Uzbekistan Agency for Science and Technology. This research is partially supported by an Erasmus+exchange grant between SU and NUUz.

REFERENCES

Dadhich, N. and Chellathurai, V. (1986), On gravitational field energy of a charged black hole, *Mon. Not. R. Astron. Soc.*, **220**, pp. 555–558.

Dadhich, N., Maartens, R., Papadopoulos, P. and Rezania, V. (2000), Black holes on the brane, *Physics Letters B*, **487**, pp. 1–6, arXiv: hep-th/0003061.

Landau, L. D. and Lifshitz, E. M. (2004), *The Classical Theory of Fields, Course of Theoretical Physics, Volume 2*, Elsevier Butterworth-Heinemann, Oxford.

Lynden-Bell, D. and Katz, J. (1985), Gravitational field energy density for spheres and black holes, *Mon. Not. R. Astron. Soc.*, **213**, pp. 21P–25P.

Randall, L. and Sundrum, R. (1999), Large Mass Hierarchy from a Small Extra Dimension, *Physical Review Letters*, **83**, pp. 3370–3373, arXiv: hep-ph/9905221.

Tolman, R. C. (1930), On the Use of the Energy-Momentum Principle in General Relativity, *Physical Review*, **35**, pp. 875–895.

Turimov, B. V., Ahmedov, B. J. and Hakimov, A. A. (2017), Stationary electromagnetic fields of slowly rotating relativistic magnetized star in the braneworld, *Physical Review D*, **96**(10), 104001.

Virbhadra, K. S. (1990), Energy associated with a Kerr-Newman black hole, *Physical Review D*, **41**, pp. 1086–1090.

Proceedings of *RAGtime 17–19, 17–19/23–26 Oct., 1–5 Nov., 2015/2016/2017, Opava, Czech Republic*
Z. Stuchlík, G. Török and V. Karas, editors, Silesian University in Opava, 2017, pp. 211–221

On the synchrotron radiation reaction in external magnetic field

Arman Tursunov[a] and Martin Kološ[b]

Institute of Physics, Faculty of Philosophy & Science, Silesian University in Opava,
Bezručovo nám. 13, CZ-746 01 Opava, Czech Republic
[a]Arman.Tursunov@fpf.slu.cz [b]Martin.Kolos@fpf.slu.cz

ABSTRACT
We study the dynamics of point electric charges undergoing radiation reaction force due to synchrotron radiation in the presence of external uniform magnetic field. The radiation reaction force cannot be neglected in many physical situations and its presence modifies the equations of motion significantly. The exact form of the equation of motion known as the Lorentz-Dirac equation contains higher order Schott term which leads to the appearance of the runaway solutions. We demonstrate effective computational ways to avoid such unphysical solutions and perform numerical integration of the dynamical equations. We show that in the ultrarelativistic case the Schott term is small and does not have considerable effect to the trajectory of a particle. We compare results with the covariant Landau-Lifshitz equation which is the first iteration of the Lorentz-Dirac equation. Even though the Landau-Lifshitz equation is thought to be approximative solution, we show that in realistic scenarios both approaches lead to identical results.

Keywords: radiation reaction – point charge – magnetic field

1 INTRODUCTION

Recent developments in accelerators and laser techniques with high intensities opened up many new phenomena which requires the inclusion of radiation reaction force into equations of motion of charged particles. Estimates confirm that in many physically relevant scenarios the radiation reaction force cannot be neglected. The study of the problem of the motion of electric charges with the effects of the radiation reaction force started more than century ago for nonrelativistic particles by Abraham and Föppl (1905), Lorentz (2003) and generalized by Dirac (1938) for relativistic case (for historical review, see Hammond (2010)). The exact form of equations plagues from the runaway solutions due to the presence of higher order term and may violate causality. The recent study of the radiation reaction in flat spacetime can be found in Gal'tsov and Spirin (2006) where the explicit derivation of the third-order Schott term was given along the lines of the Teitelboim idea to associate it with the Coulomb part of the electromagnetic field of the point charge. According to Teitelboim (1970) the Schott term arises from the derivative of the bound elec-

978-80-7510-257-7

tromagnetic momentum of the charge. The problem of the contribution of Schott term to the radiation reaction force still remains the source of discussion (see e.g. Poisson (2004)). In the present paper we will re-examine the relevance of this term too.

In order to avoid the non-physical solutions, Landau and Lifshitz (1975) proposed the iterated formula for the radiation reaction force. Their reduced order equation become first successful attempt to keep off the runaway solutions without violation of the principle of inertia (see discussions in Rohrlich (2001); Poisson (1999)).

In the present paper we are aimed to compare these two main approaches to the problem of the radiation reaction in the presence of external magnetic field. For doing so, we start from the general case and later solve the equations of motion numerically. For simplified scenario of the uniform magnetic field we find explicit trajectories of the charged particles together with the cooling times and related rates of the energy-momentum loss.

Generalizations of the radiation reaction to higher dimensions are given in Gal'tsov (2002); Gal'tsov and Spirin (2007). Radiation from hypothetical massless charges was studied in Gal'tsov (2015). The self force of point particles with mass, scalar and electric charges, has been reviewed in Poisson (2004). The electromagnetic radiation-reaction of extended classical charged particles has been studied in Cremaschini and Tessarotto (2011), its quantum approach is discussed in Cremaschini and Tessarotto (2015). Statistical treatment of the self-force is studied in Cremaschini and Tessarotto (2013). Nevertheless, despite the active interest in topic and broad bibliographical reviews, the successful attempts to integrate the equations of motion in realistic cases and presence of external electromagnetic fields is quite rare.

Throughout the paper we use the spacelike signature $(-,+,+,+)$, and the system of units with $c = 1$. However, for expressions having a physical relevance we use the constants explicitly. Greek indices are taken to run from 0 to 3.

2 SELF-FORCE OF A POINT CHARGE

Accelerated particles emit electromagnetic radiation leading to the radiation reaction force. In case of the circular motion the particle spirals down to the center of the motion due to the loss of energy and momentum. Generally, the charged particle equations of motion contain two forces

$$\frac{\mathrm{d}u^\mu}{\mathrm{d}\tau} = f^\mu_L + f^\mu_R, \tag{1}$$

where $f^\mu_L = (q/m)F^{\mu\nu}u_\nu$ is the Lorentz force reflected by the external electromagnetic tensor $F^{\mu\nu} = \partial^\mu A^\nu - \partial^\nu A^\mu$ and $u^\mu(\tau) = dx^\mu/d\tau$ is a four-velocity of the particle. The last term is the radiation reaction force. In this section we introduce Lorentz-Dirac and Landau-Lifshitz equations for the self-force of point charge. The comparison of two approaches and integration of equations of motion are given in section 3.

2.1 Lorentz-Dirac equation

The radiation reaction force in the non-relativistic case is given by the expression $\frac{3q^2}{2m}\frac{d^2u^\alpha}{d\tau^2}$. In the relativistic case, any force vector has to satisfy the condition $f^\mu_R u_\mu = 0$. This implies

that the correct covariant form of the expression for the radiation reaction force is

$$f_R^\mu = \frac{2q^2}{3m}\left(\frac{d^2u^\mu}{d\tau} + u^\mu u_\nu \frac{d^2u^\nu}{d\tau}\right). \tag{2}$$

This expression was found by Dirac and sometimes called as Lorentz-Abraham-Dirac or Lorentz-Dirac (LD) equation. The first term in the parentheses, also known as Schott term arises from the particle electromagnetic momentum. The second term in parentheses is the radiation recoil term which corresponds to the relativistic corrections of the radiation reaction force. The equation of motion of radiating particle is thus a third order differential equation in coordinates, rather than habitual second order. Equation (2) can be simplified reducing the order of the last term in the parentheses using the normalization condition. The four-velocity of the charged particle satisfies the following equations

$$u_\alpha u^\alpha = -1, \quad u_\alpha \dot{u}^\alpha = 0, \quad u_\alpha \ddot{u}^\alpha = -\dot{u}_\alpha \dot{u}^\alpha. \tag{3}$$

Substituting the last equality of (3) to the self-force (2) we get

$$f_R^\mu = \frac{2q^2}{3m}\left(\frac{d^2u^\mu}{d\tau} - u^\mu \frac{du_\nu}{d\tau}\frac{du^\nu}{d\tau}\right). \tag{4}$$

Since the Schott term is still of the third order in coordinates the expression (2) leads to the well known problem of the classical electrodynamics - the existence of so called runaway solutions which violate causality. Unphysical solutions appear due to the possible presence of the pre-acceleration in the absence of external forces. Even though the unphysical solutions can be removed by properly chosen values of initial conditions, the exact form of equations of motion (1) and (2) is inconvenient to solve due to the presence of higher order term which exponentially increases the computational error in practical calculations.

2.1.1 Synchrotron radiation without self-force

The Lorentz-Dirac equation can lead to the following interesting consequence. Introducing the four acceleration as $a^\mu = du^\mu/d\tau$ for a particle moving in Minkowski space one can write the rate of radiated four-momentum from particle and the radiation reaction force acting on a particle in the following form

$$\frac{dP^\mu}{d\tau} = \frac{2q^2}{3} a^\alpha a_\alpha u^\mu. \tag{5}$$

$$f_R^\mu = \frac{2q^2}{3m}\left(\frac{da^\mu}{d\tau} + u^\mu u_\nu \frac{da^\nu}{d\tau}\right). \tag{6}$$

Equation (5) also allows to find the rate of energy and angular momentum loses, alternatively from the way derived in the later sections, where the cooling rates are found directly from the equations of motion. One can notice that the radiation reaction force vanishes in case of uniform acceleration while radiated power remains non-zero. This leads to the energy loss with conserved angular momentum. Thus, the radiating charged particle may or

may not feel the radiation reaction force. However, this case corresponds to the full form of Eq.(6) which as pointed above leads to the appearance of the runaway solutions and, moreover, corresponds to the improper choice of initial conditions. In case when the initial acceleration of a particle is chosen to be zero, which as we will see below corresponds to the only reasonable choice of initial conditions, then the problem described in this subsection disappears. Equivalently, when the reduction of order procedure is applied to the equations of motion, then any radiating accelerated particle with uniform or non-uniform acceleration will radiate the synchrotron radiation and undergo the radiation reaction force.

2.2 Landau-Lifshitz equation

In order to exclude the unphysical solutions and find equations of motion in usual second order form, it was proposed by Landau and Lifshitz to rewrite the radiation reaction force in terms of the external force and the four-velocity performing the iteration of the Lorentz-Dirac equation. Substituting in (2) instead of the higher order terms the derivatives of the Lorentz force, we get the following equation of motion for the charged particle

$$\frac{\mathrm{d}u^\mu}{\mathrm{d}\tau} = f_L^\mu + \frac{2q^2}{3m}\left(\delta^\mu_\alpha + u^\mu u_\alpha\right)\frac{df_L^\alpha}{d\tau}. \tag{7}$$

This equation does not contain runaway solutions and has been proved to be useful in e.g. Landau and Lifshitz (1975), Poisson (1999). The important consequence of the equation above that it is of a second order, does not violate the principle of inertia and in the absence of the Lorentz force, the radiation reaction force vanishes as well Rohrlich (2001). The self-contained derivation of the equation (7) in terms of retarded potentials is given in Poisson et al. (2011). The equation (7) has more general property and can be applied for the cases with any external force acting on a charged particle instead of the Lorentz force. In case when $f_L^\mu = \frac{q}{m}F^{\mu\nu}u_\nu$, the radiation reaction force can be rewritten in the form

$$f_R^\mu = k\tilde{q}\left(F^{\mu\nu}{}_{,\alpha}u^\alpha u_\nu + \tilde{q}(F^{\mu\nu}F_{\nu\rho} - F^{\beta\alpha}F_{\beta\rho}u_\alpha u^\mu)u^\rho\right), \tag{8}$$

where $\tilde{q} = q/m$ is a specific charge of the particle, $k = (2/3)\,\tilde{q}\,q$, and the comma in the first term denotes the partial derivative with respect to the coordinate x^α. The characteristics of the motion of radiating charged particle undergoing a radiation reaction force (8) in particular representative case is studied in the following section.

3 INTEGRATION OF EQUATIONS AND RELATED TRAJECTORIES

One can basically find the trajectory of the radiating charged particle in two ways, either solving the third order equations (4) or using the iterated formula (8). Below we solve both equations numerically and compare results.

Let us consider a simple case of the motion of charged particle in flat spacetime filled with a homogeneous magnetic field aligned along z-axis, $\boldsymbol{B} = (0, 0, B)$. The tensor of electromagnetic field $F_{\alpha\beta}$ in this case will have only two nonzero components $F_{xy} = -F_{yx} = B$. Since the magnetic field B enters to the equations of motion together with the specific charge of charged particle one can introduce the new parameter in the form $\mathcal{B} = qB/(2m)$.

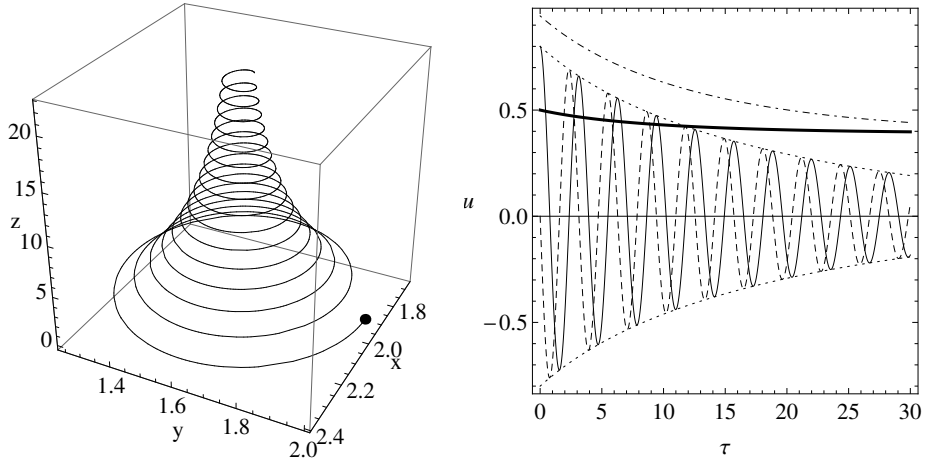

Figure 1. Motion of radiating charged particle in flat spacetime. Left figure represents an example of 3D trajectory of charged particle. Middle plot represents the evolution of different components of 3-velocity in proper time τ: the damping harmonic oscillations correspond to u^x (solid thin) and u^y (dashed) components of velocity, tangential to them (dotted) is a plane velocity of a particle $v_\perp$ orthogonal to z axis, vertical u^z component of velocity is shown by solid thick line and dot-dashed curve of the middle plot shows the evolution of 3-velocity ($\sqrt{u_x^2+u_y^2+u_z^2}$). Right figure shows the change of the energy, angular momentum and gyroradius of charged particle in time t with respect to observer at rest. corresponding to the trajectory illustrated in Fig.1. Energy decreases up to the nonzero irredusible energy level, while angular momentum and radius of gyration asymptotically tend to zero. For illustrative purposes we have set the radiation parameter k to the value much larger than in realistic situations.

Below, we define the proper velocity of a particle as $u^\alpha = dx^\alpha/d\tau$ and coordinate velocity (velocity measured by observer at rest) by $v^\alpha = dx^\alpha/dt$.

3.1 Integration of Lorentz-Dirac equations

The equations of motion (1) and (4) can be written explicitly in the form

$$\frac{du^x}{d\tau} = 2\mathcal{B}u^y - k\,a^2u^x + k\frac{d^2u^x}{d\tau^2}, \tag{9}$$

$$\frac{du^y}{d\tau} = -2\mathcal{B}u^x - k\,a^2u^y + k\frac{d^2u^y}{d\tau^2}, \tag{10}$$

$$\frac{du^z}{d\tau} = -k\,a^2u^z + k\frac{d^2u^z}{d\tau^2}, \tag{11}$$

$$\frac{du^t}{d\tau} = -k\,a^2u^t + k\frac{d^2u^t}{d\tau^2},. \tag{12}$$

where we used the notation

$$a^2 \equiv a_\alpha a^\alpha = -\left(\frac{du^t}{d\tau}\right)^2 + \left(\frac{du^x}{d\tau}\right)^2 + \left(\frac{du^y}{d\tau}\right)^2 + \left(\frac{du^z}{d\tau}\right)^2. \quad (13)$$

In order to eliminate the unphysical solutions of the equations (9) - (12) one needs to choose the initial conditions of a charged particle properly. As for any third order ordinary differential equations in Minkowski spacetime, one needs to set the values of 9 constants - arbitrary independent components of initial position, velocity and the acceleration of the charged particle. The three other constants can be identified by normalization condition (3). The values of initial conditions which satisfy the physical solutions of equations of motion are those in which all components of initial acceleration are vanishing. However, the direct integration of higher order equations leads to the exponential increase of the computational error in very short times. We have found that the problem of the time dispersion error can be greatly reduced by integrating equations of motion backward in time. Similar method of solving higher order equations has been proposed in the past by Huschilt and Baylis (1976). The result of integration of equations of motion are shown in Fig. 1. It is interesting to note that the same result has been obtained using the Landau-Lifshitz approach, which is discussed below. We also leave the discussion of Fig. 1 to the following subsection. Proposed by Landau and Lifshitz (1975) as an approximative solution to the third order LD equations, it was more recently argued by Rohrlich (2001), that the reduced form of the equations of motion are exact, rather than approximative. In our calculations, corresponding to Fig.(1) the difference between two methods appears to be negligible.

3.2 Integration of Landau-Lifshitz equations

For the motion in a uniform magnetic field, the reduced-order equations of motion (7) of radiating charged particle can be written explicitly in the form

$$\frac{du^x}{d\tau} = 2\mathcal{B}u^y - 4k\mathcal{B}^2\left(1+u_\perp^2\right)u^x, \quad (14)$$

$$\frac{du^y}{d\tau} = -2\mathcal{B}u^x - 4k\mathcal{B}^2\left(1+u_\perp^2\right)u^y, \quad (15)$$

$$\frac{du^z}{d\tau} = -4k\mathcal{B}^2u_\perp^2u^z, \quad (16)$$

$$\frac{du^t}{d\tau} = -4k\mathcal{B}^2u_\perp^2u^t,. \quad (17)$$

Here $u_\perp^2 = (u^x)^2 + (u^y)^2$ is a square of plane velocity of a particle orthogonal to the magnetic field and z axis, $k = (2/3)\tilde{q}q$ is the parameter responsible for the radiation reaction. The representative view of corresponding trajectories is shown in Fig.1, which coincides with the results of integrations of the Lorentz-Dirac equations (see previous subsection). The particle starts its motion with the initial plane velocity $u_{\perp 0} = 0.8c$ and the vertical velocity $u_0^z = 0.5c$. Due to combined effects of the Lorentz force and the radiation reaction force, the charged particle spirals down to the center. It occurs due to the loss of energy and angular momentum of a particle and correspondingly, the plane velocity of a particle decreases by

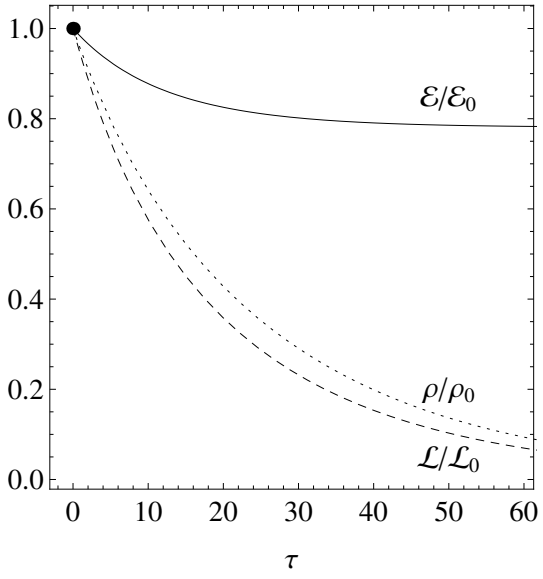

Figure 2. Figure shows the evolution of the energy, angular momentum and gyroradius corresponding to the trajectory illustrated in Fig.1. Energy decreases up to the nonzero irredusible energy level, while angular momentum and radius of gyration asymptotically tend to zero.

the law given as the solution of equations (14) and (15) or equivalently as solutions of (9) and (10). However, if one looks to the motion along z axis shown in Fig.1 (solid thick in the right plot), one can notice that the proper velocity of a charged particle $u^\alpha = dx^\alpha/d\tau$ undergoes small nonzero deceleration in the direction parallel to the magnetic field which coincides with z axis, while there are no external forces in z direction. This contradiction with the common sense occurs due to the reason that the system of radiating particle is non-conservative. The problem, however, vanishes if we measure the velocity of a radiating charged particle with respect to the static observer $v^\alpha = dx^\alpha/dt \equiv u^z/u^t = const$, where the motion appears to be uniform in the direction orthogonal to the action of the Lorentz force.

3.3 Energy and momentum loss

The rate of the energy loss of a particle can be easily evaluated from Eq.(12) or (17). However, one needs to note that it is more convenient to use the equation (17) as it is ordinary second order differential equation. Modifying it for a static observer we get

$$\frac{dE}{dt} = -kB^2\tilde{q}^2 u_\perp(t)^2. \tag{18}$$

Integrating this equation one can obtain the energy of a particle in a given moment of time. The representative plot of the evolution of the energy in time is given in Fig.2. Thus the energy loss will be given only by the change of the plane velocity $u_\perp$ in time, while the

linear component of the velocity of a particle in z-direction will be conserved. This implies that the part of kinetic energy of a charged particle related to the linear motion along z axis is conserved as well. Writing the normalization condition $u^\alpha u_\alpha = -1$ explicitly and reminding that the particle specific energy is $\mathcal{E} = E/m = -u_t$, we get the formal decomposition of the total energy of the particle in the form

$$\mathcal{E}^2 = 1 + u_\perp^2 + u_z^2 \equiv 1 + \mathcal{E}_\perp^2 + \mathcal{E}_z^2, \tag{19}$$

where $u_\perp^2 = u_x^2 + u_y^2$. The final state of the particle is defined by the first and the last terms of the right hand side of Eq.(19). This implies that there exists an irreducible energy of radiating charged particle which corresponds to the final state of a particle having the following simple form

$$\mathcal{E}_{\rm irr} = \left(1 - (v_0^z)^2\right)^{-\frac{1}{2}}, \tag{20}$$

where v_0^z is the vertical velocity of the particle along the z-axis measured by static observer which is constant during the radiation process.

In order to find the rate of the angular momentum loss one can concentrate attention only on the motion in a fixed plane by taking $u^z = 0$. Thus, we have $u_\perp$ component of 3-velocity only. Angular momentum, in general, for the motion in plane is defined by formula $L = m\rho^2 d\phi/d\tau + qA_\phi$, where ρ is gyroradius of the particle trajectory. Reminding that $d\phi/d\tau = u_\perp\gamma/\rho$ and $\rho = u_\perp/\omega_L$, where $\omega_L = qB/m \equiv 2\mathcal{B}$ is the Larmor frequency, one can write the angular momentum of radiating charged particle in the given moment of time in the form

$$L = \frac{mu_\perp(\tau)^2}{4\mathcal{B}}\left[2\gamma(\tau) + 1\right], \quad \gamma = (1 - u_\perp^2)^{-\frac{1}{2}}. \tag{21}$$

Solving first two equations of motion (14) and (15) and substituting into Eq.(21) we get the evolution of angular momentum in time, which is represented in Fig.2. Unlike the energy of a particle, the angular momentum asymptotically tends to zero for large τ. This occurs due to the reason that the gyroradius ρ of a charged particle tends to zero as well, while L is proportional to ρ. The relative evolutions of the energy, angular momentum and gyroradius are illustrated in Fig.2.

One can find the ratio between the angular momentum loss $\dot{L} = dL/dt$ and energy loss $\dot{E} = dE/dt$ as

$$\frac{\dot{L}}{\dot{E}} = r^2\Omega\frac{u_\perp^2 + 1}{u_\perp^2}. \tag{22}$$

where Ω is an angular velocity of the charged particle measured by observer at rest. In Cartesian coordinates Ω takes the form

$$\Omega = \frac{x\dot{y} - y\dot{x}}{x^2 + y^2}, \tag{23}$$

where dots denote the derivative with respect to the coordinate time t. One can see from Eq.(22) that in the processes connected with the synchrotron radiation the angular momentum loss of a radiating particle cannot be neglected.

B (Gauss)	τ_e (s)	τ_p (s)
10^{12}	10^{-16}	10^{-6}
10^{8}	10^{-8}	10^{2}
10^{4}	1	10^{10}
1	10^{8}	10^{1}
10^{-4}	10^{16}	10^{26}

Table 1. Typical decay times of ultrarelativistic electrons τ_e and protons τ_p for different values of magnetic field B.

3.4 Cooling time

One can find the cooling time of a radiating charged particle in the following way. Since the velocity in the magnetic field direction is constant one can consider the motion of a particle in plane only by taking $u^z = 0$. This implies, that according to condition $u_\alpha u^\alpha = -1$ we get $u_\perp^2 = (u^t)^2 - 1$. Thus, the equation (17) can be rewritten in the form

$$\frac{d\mathcal{E}}{d\tau} = -\mathcal{K}\left(\mathcal{E}^3 - \mathcal{E}\right), \quad \mathcal{K} = 4k\mathcal{B}^2 \equiv \frac{2q^4B^2}{3m^3c^5}. \tag{24}$$

Integrating above equation we get the energy of a particle in a given moment of time

$$\mathcal{E}(\mathcal{T}) = \frac{\mathcal{E}_0 e^{\mathcal{K}\mathcal{T}}}{\sqrt{1 + \mathcal{E}_0^2\,(e^{2\mathcal{K}\mathcal{T}} - 1)}}, \tag{25}$$

where the integration constant $\mathcal{E}_0$ is the initial energy of the particle and $\mathcal{E}(\mathcal{T})$ is the energy in a given moment of time, which is an exponentially decreasing function of time $\mathcal{T}$. Asymptotically in time the energy tends to the particle rest energy, being equal to 1. Thus, from (25) we find the cooling time during which the energy will be lowered from $\mathcal{E}_0$ to $\mathcal{E}_f$ due to radiation in the following form

$$\mathcal{T} = \frac{1}{2\mathcal{K}} \ln \frac{\mathcal{E}_f^2(\mathcal{E}_0^2 - 1)}{\mathcal{E}_0^2(\mathcal{E}_f^2 - 1)}. \tag{26}$$

For example, the time required to decay the half of the initial energy of the particle ($\mathcal{E}_f = \mathcal{E}_0/2$) is

$$\mathcal{T}_{1/2} = \frac{1}{2\mathcal{K}} \ln \frac{\mathcal{E}_0^2 - 1}{\mathcal{E}_0^2 - 4}. \tag{27}$$

One can estimate the timescale of the decay of charged particle energy as follows. Assuming the ultrarelativistic particle with initial and final energies: $\mathcal{E}_0 \gg 1$ and $\mathcal{E} \approx 1$, the logarithm in (26) can be approximately taken to be unity. Then, the timescale of cooling of the charge is simply $\mathcal{T} \approx 1/\mathcal{K}$. Typical orders of magnitude of the oscillation decay time

of an electron and proton are shown in Tab.1. The radiation reaction and related cooling time of charges can have a significant effect in plasma, when the decay time of charged particle becomes smaller than the average time between collisions of particles in plasma. For typical hydrogen plasma with the temperature $T = 10^8$K and concentration $n = 10^{14}$cm^{-3} the timescales of electron-electron, electron-ion and ion-ion collisions take the values

$$t_{ee} \approx 6.4 \times 10^{-4}\text{s}, \quad t_{ei} \approx 4.5 \times 10^{-4}\text{s}, \quad t_{ii} \approx 4.1 \times 10^{-2}\text{s}. \tag{28}$$

Thus, comparing (28) with Tab.1, one can conclude that in many physically relevant scenarios the radiation-reaction force cannot be neglected.

4 CONCLUSIONS

We have studied the problem of radiation reaction of charged particle using two main approaches, given by the Lorentz-Dirac and Landau-Lifshitz equations. Comparing results in case of the uniform magnetic field we have found that the difference between two approaches is negligibly small. In order to solve the Lorentz-Dirac equations which are of the third order in coordinates we have performed the integration of dynamical equations backward in time. We have found that the physical solutions of Lorentz-Dirac equations are those which correspond to the initial conditions with zero initial acceleration or equivalently those where the acceleration is zero in an arbitrary given moment of time. We have also found that in ultrarelativistic case the contribution of Schott term is considerably small. Together with the numerical solutions of the dynamical equations of charged particle we have obtained analytical expressions for the energy and angular momentum loss of the particle and the corresponding cooling time. The solution of Landau-Lifshitz equations is straightforward and more convenient since the equations contain the physical solutions only and do not violate causality. Small difference between Lorentz-Dirac and Landau-Lifshitz approaches imply that in the most physically relevant situations one can use the Landau-Lifshitz equation instead of Lorentz-Dirac one. It was pointed out by Spohn (2000) that using the Landau-Lifshitz equation is identical to imposing Dirac's asymptotic condition $\lim_{\tau\to\infty} \dot{u}^\mu = 0$ to the Lorentz-Dirac equation. This implies that the Landau-Lifshitz equation is exact, rather than approximative. One can conclude that this statement is correct at least in the case when the Schott term is small, which is exactly the case we have shown.

ACKNOWLEDGEMENTS

The present work was supported by the Czech Science Foundation Grant No. 16-03564Y.

REFERENCES

Abraham, M. and Föppl, A. (1905), *Theorie der Elektrizität*, number . 2 in Theorie der Elektrizität, B.G. Teubner, URL https://books.google.com.pk/books?id=b3ZCAAAAIAAJ.

Cremaschini, C. and Tessarotto, M. (2011), Exact solution of the EM radiation-reaction problem for classical finite-size and Lorentzian charged particles, *European Physical Journal Plus*, **126**, 42, arXiv: 1201.1817.

Cremaschini, C. and Tessarotto, M. (2013), Statistical treatment of the electromagnetic radiation-reaction problem: Evaluation of the relativistic Boltzmann-Shannon entropy, *Phys. Rev. E* , **87**(3), 032107.

Cremaschini, C. and Tessarotto, M. (2015), Quantum theory of extended particle dynamics in the presence of EM radiation-reaction, *European Physical Journal Plus*, **130**, 166.

Dirac, P. A. M. (1938), Classical Theory of Radiating Electrons, *Proceedings of the Royal Society of London Series A*, **167**, pp. 148–169.

Gal'tsov, D. V. (2002), Radiation reaction in various dimensions, *Phys. Rev. D* , **66**(2), 025016, arXiv: hep-th/0112110.

Gal'tsov, D. V. (2015), Synchrotron radiation from massless charge, *Physics Letters B*, **747**, pp. 400–405, arXiv: 1505.06775.

Gal'tsov, D. V. and Spirin, P. A. (2006), Radiation reaction reexamined: bound momentum and the Schott term, *Gravitation and Cosmology*, **12**, pp. 1–10, arXiv: hep-th/0405121.

Gal'tsov, D. V. and Spirin, P. A. (2007), Radiation reaction in curved even-dimensional spacetime, *Gravitation and Cosmology*, **13**, pp. 241–252, arXiv: 1012.3085.

Hammond, R. T. (2010), Relativistic Particle Motion and Radiation Reaction in Electrodynamics, *Electronic Journal of Theoretical Physics*, **7**(23), pp. 221–258.

Huschilt, J. and Baylis, W. E. (1976), Numerical solutions to two-body problems in classical electrodynamics: Head-on collisions with retarded fields and radiation reaction. I. Repulsive case, *Phys. Rev. D* , **13**, pp. 3256–3261.

Landau, L. D. and Lifshitz, E. M. (1975), *The classical theory of fields*.

Lorentz, H. (2003), *The Theory of Electrons and Its Applications to the Phenomena of Light and Radiant Heat*, Dover books on physics, Dover Publications, ISBN 9780486495583, URL https://books.google.de/books?id=-BAvOT4La5UC.

Poisson, E. (1999), An introduction to the Lorentz-Dirac equation, *ArXiv General Relativity and Quantum Cosmology e-prints*, arXiv: gr-qc/9912045.

Poisson, E. (2004), The Motion of Point Particles in Curved Spacetime, *Living Reviews in Relativity*, **7**, 6, arXiv: gr-qc/0306052.

Poisson, E., Pound, A. and Vega, I. (2011), The Motion of Point Particles in Curved Spacetime, *Living Reviews in Relativity*, **14**, 7, arXiv: 1102.0529.

Rohrlich, F. (2001), The correct equation of motion of a classical point charge, *Physics Letters A*, **283**, pp. 276–278.

Spohn, H. (2000), The critical manifold of the Lorentz-Dirac equation, *EPL (Europhysics Letters)*, **50**, pp. 287–292, arXiv: physics/9911027.

Teitelboim, C. (1970), Splitting of the Maxwell Tensor: Radiation Reaction without Advanced Fields, *Phys. Rev. D* , **1**, pp. 1572–1582.

Proceedings of *RAGtime 17–19, 17–19/23–26 Oct., 1–5 Nov., 2015/2016/2017, Opava, Czech Republic*
Z. Stuchlík, G. Török and V. Karas, editors, Silesian University in Opava, 2017, pp. 223–235

Escape cones of null-geodesics from the interior of rotating compact stars

Jaroslav Vrba,[1a+] Martin Urbanec[1b] and Zdeněk Stuchlík[1a]

[1]Institute of Physics, Faculty of Philosophy & Science, Silesian University in Opava
Bezručovo nám. 13, CZ-746 01 Opava, Czech Republic
[a]Research Centre for Theoretical Physics and Astrophysics
[b]Research Centre for Computational Physics and Data Processing
[+]jaroslav.vrba@fpf.slu.cz

ABSTRACT
In this work we present investigation of the escape cones of null-geodesics from the interior of rotating homogeneous compact stars in the model, where only terms linear in the star's rotational frequency are assumed. We focus on the single model of the star with particular radius $R = 2.8M$ (using units in which $c = G = 1$) rotating with different values of angular momentum J. We vary the position of the isotropically radiating source both in radial and latitudinal direction and we show the impact of the position and the rotational rate on the shape of the escape cone of null-geodesics. We find that even for small rotational rate corresponding to $j = J/M^2 = 0.1$ the impact on the escape cones is rather strong. The escape cones are no longer symmetrical around radial direction, and it is clearly seen that the radiation in the direction of the rotation can easily reach the infinity. On the other hand, the radiation in the direction opposite to the rotation will be trapped in the interior of the star. We discuss possible astrophysical relevance of our results.

Keywords: Compact object – axially symmetric spacetime – trapped null-geodesic – effective potential – escape cone

1 INTRODUCTION

Compact stars are general-relativistic objects with internal structure where general relativity plays key role in governing both their structure and astrophysical phenomena in their surroundings. Their central densities reach values that are not achievable in any terrestrial experiment and they serve as unique laboratories for nuclear physics and gravitational physics. Usually by compact stars we mean either neutron stars or strange stars. Neutron stars are made of neutrons, protons and electrons that are in $\beta-$equilibrium (see e.g. S.L. Shapiro and S.A. Teukolsky, (1983)), while strange stars are consisting of up, down and strange quarks that are deconfined (Witten, 1984). Different descriptions of microphysics of the interior matter transform into different global properties of the star for the same values of central density. Main gross properties of the compact star are its gravitational mass M, radius R and if the star is rotating with given angular velocity Ω, also its

978-80-7510-257-7

angular momentum J and quadrupole moment Q (see e.g. Urbanec et al. (2013) for impact of equation of state on the gross properties of the compact star).

Null-geodesics and their trapping have been investigated in various contexts in many previous works (Abramowicz et al., 1997; Stuchlík et al., 2009, 2011, 2012; Novotný et al., 2017; Völkel and Kokkotas, 2017). In the non-rotating case, the null-geodesics can be trapped in the interior of the star if the star's radius R is bellow the position of circular photon orbit, i.e. if $R < 3M$[1]. However, most of the models of neutron stars calculated using realistic equations of state are having radius $R > 3M$ (see e.g. Figure 1 in Urbanec et al. (2013)). Rotation of the compact star is going to affect external space-time and therefore the position of the photon orbit.

Within this work we are going to focus on the very simple model, where the star is homogeneous with constant energy-density ρ and the rotation is taken as a perturbation of spherically symmetric Schwarzschild metric. We are going to keep the terms that are linear in the star's angular velocity Ω only. This is the same approach as the linearization of the Hartle-Thorne model (Hartle and Thorne, 1968). We first study the effective potential inside and close-to compact object for star with $R = 2.8M$ to demonstrate the impact of rotation. Later we use the concept of the escape cones introduced in Schee et al. (2005); Stuchlík and Schee (2010) to demonstrate directions of the null-geodesics that are trapped by the gravity of a compact object.

Relevance of this research has increased after the first detection of gravitational-wave signal from merging neutron stars (Abbott et al., 2017b) that has been observed with its optical counterparts (Abbott et al., 2017a,c). Both gravitational-waves and electromagnetic-waves are moving along null geodesics and if the neutron star is formed after the coalescence, it may be very heavy and may rotate very rapidly. Combination of high mass and high rotational rate will lead to the existence of counter-rotating circular photon orbit in the exterior space-time of the compact star causing part of the geodesics (and therefore gravitational waves) to be trapped in the interior of the compact star.

The paper is organized as follows. In Section 2, we focus on the spherically symmetric case. We present effective potential and the trapping of null-geodesics in the similar way as in Stuchlík et al. (2009), and we introduce escape cones in Section 2 as well. In Section 3 we investigate the influence of rotation on possible trapping of null-geodesics using both the profiles of effective potential and the escape cones. Section 4 contains our conclusions.

2 SPHERICALLY SYMMETRIC SPACETIME

In this section we recap main concepts of Stuchlík et al. (2009) and we introduce the escape cones of null-geodesics in this context. This work deals with model of the homogeneous compact star.

We are interested in the toy model to be able to perform most of the calculations analytically and to use it in the future as a testbed for more advanced calculations.

[1] We are using units in which $c = G = 1$ thorough this paper.

Line element of spherically symmetric space-time can be written in spherical coordinates as (Schwarzschild, 1999)

$$\mathrm{d}s^2 = -e^{2\Phi(r)}\mathrm{d}t^2 + e^{2\Psi(r)}\mathrm{d}r^2 + r^2(\mathrm{d}\theta^2 + \sin^2\theta\mathrm{d}\phi^2). \tag{1}$$

Assuming constant energy-density ρ, we can write the metric coefficients in the form

$$(-g_{tt})^{1/2} = e^{\Phi} = \frac{3}{2}Y_1 - \frac{1}{2}Y(r), \qquad (g_{rr})^{1/2} = e^{\Psi} = \frac{1}{Y(r)}, \tag{2}$$

where

$$Y(r) = \sqrt{1 - \frac{r^2}{a^2}}, \qquad Y_1 = Y(R) = \sqrt{1 - \frac{R^2}{a^2}}, \tag{3}$$

$$\frac{1}{a^2} = \frac{3}{8}\pi\rho = \frac{2M}{R^3}, \tag{4}$$

and M and R are the mass and the radius of the compact star.

It is convenient to use the tetrad formalism. We can rewrite Equations (1)-(4) as

$$\mathrm{d}s^2 = [\omega^{(t)}]^2 + [\omega^{(r)}]^2 + [\omega^{(\theta)}]^2 + [\omega^{(\phi)}]^2, \tag{5}$$

where

$$\omega^{(t)} = e^{\Phi}\mathrm{d}t, \quad \omega^{(r)} = e^{\Psi}\mathrm{d}r, \quad \omega^{(\theta)} = r\mathrm{d}\theta, \quad \omega^{(\phi)} = r\sin\theta\mathrm{d}\phi. \tag{6}$$

Relations between vectors and co-vectors are written as

$$\omega^{(\alpha)}_{\mu}e^{\mu}_{(\beta)} = \delta^{(\alpha)}_{(\beta)} \quad \text{and} \quad e^{\mu}_{(\alpha)}\omega^{(\alpha)}_{\nu} = \delta^{\mu}_{\nu}. \tag{7}$$

We use this formalism to project 4-momentum of the mass-less particle k^{μ} to the local frame as $k^{(\alpha)} = k^{\mu}\omega^{(\alpha)}_{\mu}$, $k_{(\alpha)} = k_{\mu}e^{\mu}_{(\alpha)}$.

2.1 Effective potential

The motion along null-geodesics is described by the equation of motion

$$\frac{\mathrm{D}k^{\mu}}{\mathrm{d}\tau} = 0 \qquad \text{and} \qquad k_{\mu}k^{\mu} = 0, \tag{8}$$

where τ is the proper time. We can find two Killing fields ($\frac{\partial}{\partial t}$ and $\frac{\partial}{\partial\phi}$) and relate them to the constants of motion E and L as

$$k_t = -E \qquad \text{and} \qquad k_{\phi} = L. \tag{9}$$

In the spherically symmetric case, the motion takes place in a single plane that can be identified with the equatorial one and we can therefore set $\theta = \pi/2$ and $k^{\theta} = 0$. Combining (8) and (9) we then get

$$(k^r)^2 = \frac{1}{g_{tt}g_{rr}}E^2\left(1 - g_{tt}\frac{\lambda^2}{r^2}\right), \tag{10}$$

where we introduced the impact parameter $\lambda = L/E$. The term in the brackets in the formula above needs to non-negative and this condition can be written as

$$\lambda^2 \leq V_{\rm eff} = -\frac{r^2}{g_{tt}}, \tag{11}$$

where we have defined the effective potential $V_{\rm eff}$.

The effective potential for the star with $R/M = 2.8$ is plotted in Figure 1. On the right panel of Figure 1 we see that there can be distinguished two kinds of trapping that are visualized by darker and lighter areas. If the null geodesic is described by the impact parameter $\lambda > \lambda_{\rm crit} = \sqrt{V_{\rm eff}(r = 3M)}$ the geodesic will be trapped under the circular photon orbit $r_{\rm ph} = 3M$, the particle moving along it will leave the star, hit the potential barrier and will be reflected back and will enter the star later (lighter area of right panel of Figure 1). If the $\lambda > \sqrt{V_{\rm eff}(r = R)}$ the geodesic will stay in the interior of the star permanently (darker area of right panel of Figure 1). We also see that if the particle is radiated from the radius $r < r_{\rm b}$ there is no potential barrier for it and it will escape to the infinity. Therefore we see that the trapping of geodesics take place only in limited area of the star and that only limited part of the mass-less particles radiated from this are will be trapped. For the purpose of this work we will distinguish only between geodesics that are trapped and geodesics that can reach the infinity. A more detailed discussion of trapped areas can be found in Stuchlík et al. (2009).

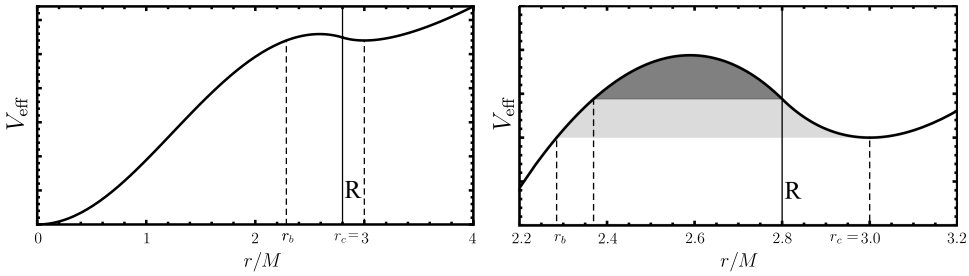

Figure 1. Effective potential of star with $R/M = 2.8$. Schematic depiction of the trapped area (right). See text for details.

2.2 Escape cones

Escape cones has been presented e.g. in Schee et al. (2005); Stuchlík and Schee (2010) and we are going to use similar approach here. Four-momentum of mass-less particles radiated from given position in the compact star can be written using directional angles (see Figure 2)

$$k^{(t)} = -k_{(t)} = 1, \tag{12}$$

$$k^{(r)} = k_{(r)} = \cos\alpha, \tag{13}$$

$$k^{(\theta)} = k_{(\theta)} = \sin\alpha\cos\beta, \tag{14}$$

$$k^{(\phi)} = k_{(\phi)} = \sin\alpha \sin\beta = \cos\gamma. \tag{15}$$

We can see that two angles are sufficient to determine the direction of the null-geodesic at the radiation point.

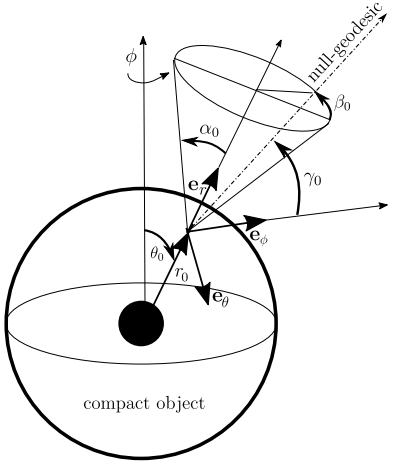

Figure 2. The definition of directional angles of null-geodesic radiated from the point with coordinates r_0, θ_0.

Now let us say we have a point emitter which emits mass-less particles that are moving along null-geodesics. The escape cone determines directions of null-geodesics which can travel to infinity. Complementary directions correspond to null-geodesics that are trapped by the gravitational field. These directions are described by angles $[\alpha,\beta]$, defined in Figure 2 and they may be plotted to a polar graph of escape cone where α is the 'radial' coordinate ($\alpha \in \langle 0,\pi\rangle$) and β is the 'polar' coordinate ($\beta \in \langle 0, 2\pi\rangle$). The position of the emitter is determined by $[r_0, \theta_0]$. For instance, if we sit at any r in the equatorial plane, i.e., $[r_0, \pi/2]$ the direction (a) $[\alpha,\beta]$=[0,whatever], points radially to infinity, (b) $[\alpha,\beta]$=[π,whatever], points directly to the center and (c) $[\alpha,\beta]$=$[\pi/2, \pi/2]$, points perpendicularly to the radial direction in the equatorial plane in direction of the rotation (if the star would be rotating).

The typical escape cone for non-rotating objects is shown in Figure 3. This particular one has been constructed in the equatorial plane and at the radial coordinate r corresponding to the position of the maxima of the effective potential. We see that dark are that is corresponding to the trapped geodesics is symmetrical around $\alpha = \pi/2$ that is corresponding to the radiation in the direction perpendicular to the radial direction and we also see, that there is no dependency on the angle β being given by the spherically symmetric space-time.

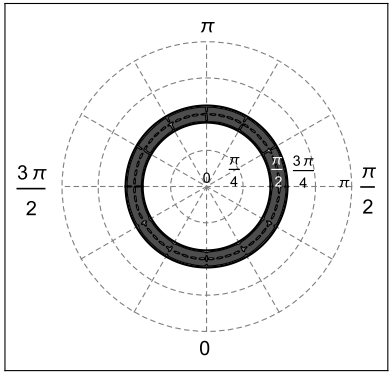

Figure 3. The escape cone produced at the maximum of the effective potential for $R/M = 2.8$. A shaded area depicts directional angles α, β for which the null-geodesics is trapped trapped .

3 AXIALLY SYMMETRIC SPACE-TIME

The main goal of this section is to examine escape cones produced in various points in the interior of the slowly and rigidly rotating compact star. We model rotating compact stars taking into account corrections up to the first order in the angular velocity of the star Ω. For description of the rotating body we will use dimension-less specific angular momentum $j = J/M^2$, where J is angular momentum of the body.

The rotating star within this approximation is described by the Lense-Thirring metric (Lense and Thirring, 1918)

$$g_{t\phi} = g_{\phi t} = -\omega(r) r^2 \sin^2(\theta), \tag{16}$$

where the diagonal components of the metric tensor $g_{\mu\mu}$ are the same as in the non-rotating case (1-4), and in addition there are cross terms that can be written as

$$\mathrm{d}s^2 = -e^{2\Phi(r)}\mathrm{d}t^2 + e^{2\Psi(r)}\mathrm{d}r^2 + r^2(\mathrm{d}\theta^2 + \sin^2\theta \mathrm{d}\phi^2) + 2g_{t\phi}\mathrm{d}t\mathrm{d}\phi, \tag{17}$$

where the function $\omega(r)$ represents angular velocity of the locally non-rotating frame (LNRF). It can be calculated from relations for the angular velocity of the matter with respect to the angular velocity of LNRF $\bar{\omega}(r) = \Omega - \omega(r)$. Equation for $\bar{\omega}(r)$ is the same as in the Hartle-Thorne model (Hartle and Thorne, 1968)

$$\frac{1}{4}\frac{\mathrm{d}}{\mathrm{d}r}\left(r^4 j(r)\frac{\mathrm{d}\bar{\omega}}{\mathrm{d}r}\right) + \frac{4}{r}\frac{\mathrm{d}j(r)}{\mathrm{d}r}\bar{\omega} = 0, \tag{18}$$

where

$$j(r) = \sqrt{\frac{-1}{g_{tt}g_{rr}}}. \tag{19}$$

For deeper analysis of the problem and inclusion of higher order terms see Hartle (1967) and Hartle and Thorne (1968).

3.1 Tetrad formalism

The tetrad formalism is very useful for the case of rotating object. The LNRF frame is in this formalism given by relations

$$\omega^{(t)} = \left\{ \sqrt{-\omega(r) g_{\phi t} - g_{tt}}, 0, 0, 0 \right\}, \tag{20}$$

$$\omega^{(r)} = \{0, \sqrt{g_{rr}}, 0, 0\}, \tag{21}$$

$$\omega^{(\theta)} = \{0, 0, \sqrt{g_{\theta\theta}}, 0\}, \tag{22}$$

$$\omega^{(\varphi)} = \left\{ -\omega(r) \sqrt{g_{\phi\phi}} \sin\theta, 0, 0, \sqrt{g_{\phi\phi}} \right\}. \tag{23}$$

We transform it using the Lorentz transformation Λ to the frame rotating with the object (with angular velocity Ω).

$$\mathbf{\Lambda}(\bar{\omega}) = \begin{pmatrix} \gamma & 0 & 0 & -\gamma\bar{\omega} \\ 0 & 1 & 0 & 0 \\ 0 & 0 & 1 & 0 \\ -\gamma\bar{\omega} & 0 & 0 & \gamma \end{pmatrix}, \tag{24}$$

where $\gamma = 1/\sqrt{1 - \bar{\omega}^2}$ is Lorentz factor. We can finally write $\bar{\omega}$ as[2]

$$\bar{\omega} = \frac{U^{(\phi)}}{U^{(t)}} = \frac{\omega^{(\phi)}_{\mu} U^{\mu}}{\omega^{(t)}_{\mu} U^{\mu}}. \tag{25}$$

3.2 Effective potential

The effective potential related to null-geodesics in the space-time described by line-element (17) can be derived using the Lagrangian (see e.g. Chandrasekhar (1983))

$$2\mathcal{L} = g_{tt}\dot{t}^2 + g_{rr}\dot{r}^2 + g_{\theta\theta}\dot{\theta}^2 + g_{\phi\phi}\dot{\phi}^2 + 2g_{t\phi}\dot{\phi}\dot{t}. \tag{26}$$

The radial part of the effective potential reads

$$V_{\mathrm{Reff}} = 2g^{t\phi} g_{\theta\theta}\lambda - g^{tt} g_{\theta\theta}, \tag{27}$$

and the latitudinal part takes the form

$$V_{\mathrm{Teff}} = \frac{\lambda^2}{\sin^2\theta}, \tag{28}$$

where we use the impact parameter

$$\lambda = \frac{L}{E} = \frac{k_{\phi}}{-k_t} = \frac{\omega^{(\mu)}_{\phi} k_{(\mu)}}{-\omega^{(\mu)}_{t} k_{(\mu)}}. \tag{29}$$

[2] Index in bracket is expressed in local frame.

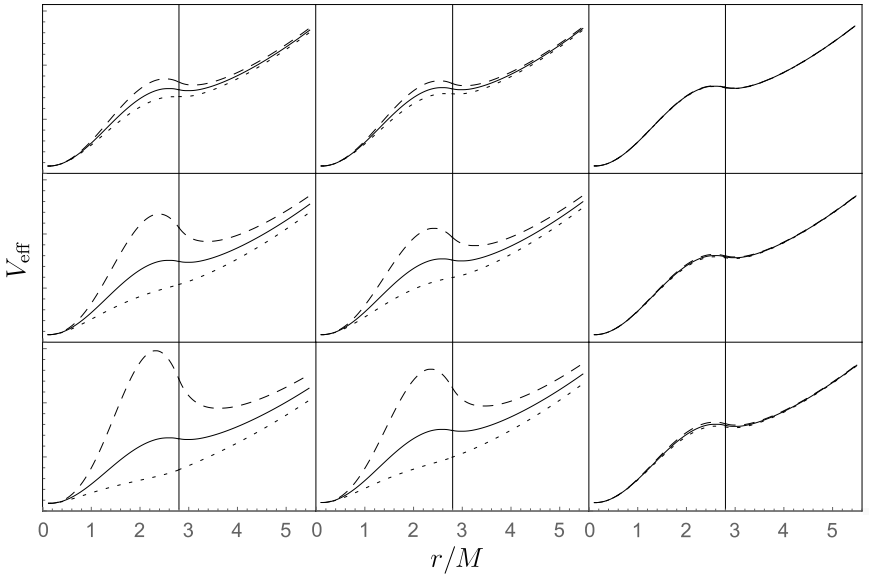

Figure 4. Effective potentials of the radial part of null-geodesic for configuration with $R/M = 2.8$. First column corresponds to $\theta = \pi/2$, second to $\pi/4$, and third to $\pi/1000$. In first row specific angular momentum of the star is $j = 0.1$ in the second row $j = 0.4$ and in the third row $j = 0.7$. Dashed lines are corresponding to counter-rotating geodesics while the dotted lines to co-rotating ones. Full lines are plotted for comparison and they correspond to the non-rotating case, where $j = 0$.

We can notice that if the rotation vanishes (i.e $g_{t\phi} = 0$), effective potentials given by Eqs. (11) and (27) are identical. The resulting effective potentials are illustrated in Figure 4, where we plot the effective potential separately for co-rotating particles (dotted line) and for counter-rotating particles (dashed line). For comparison, we plot effective potential for non-rotating configuration as well (solid line).

3.3 Escape cones

Detailed description of a construction of the light escape cones for Kerr black holes and naked singularities can be found in Schee et al. (2005); Stuchlík and Schee (2010). Here, we adopt the main idea of it in the context of slowly-rotating compact stars. Constants of motion (9) fully determine the direction angles as they were defined in Figure 2. The relation (29) connects constant λ and angle γ. For trapped geodesics the constant λ is limited by the condition $V_{\rm Reff} > V_{\rm Teff}$, coming from the separation of equations of motion. Using relation

$$\cos\alpha = \frac{k^{(r)}}{k^{(t)}} = \frac{\omega^{(r)}_{\mu} k^{\mu}}{\omega^{(t)}_{\mu} k^{\mu}}, \tag{30}$$

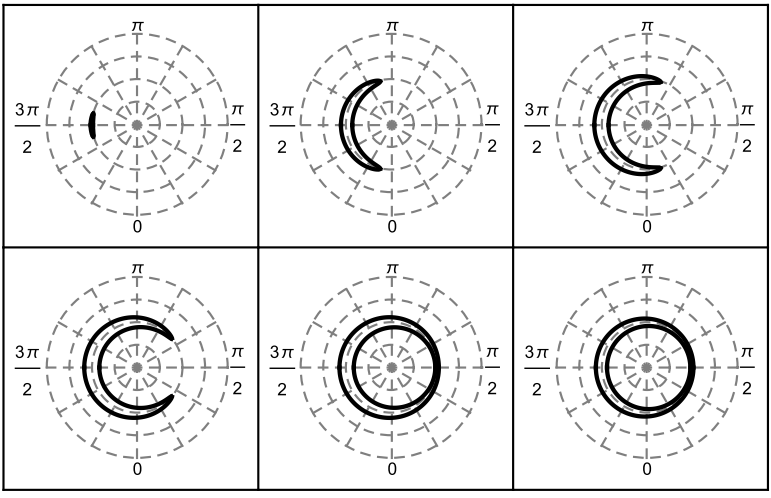

Figure 5. Escape cones of configuration with $R/M = 2.8$ and specific angular momentum $j = 0.1$. Cones are produced at $\theta_0 = \pi/2$ and at points where $r_0 = \{2.285, 2.388, 2.491, 2.594, 2.697, 2.8\}M$.

that relates directional angles α and γ. In order to null-geodesic being trapped, the value of λ^2 has to be in the shaded region in Figure 1 (see also Eq. (27)), i.e. λ^2 has to be bigger than the minimum of the effective potential in the exterior space-time. The condition when λ^2 is equal to the value of minimum of effective potential determines a critical value of angle α separating the trapped null-geodesics and null-geodesics that can reach infinity. An angle β is determined from Eq. (15).

This procedure is repeated for all allowed values of λ and values $[\alpha, \beta]$ are plotted in a graph as the escape cone.

We now create a set of escape cones in different positions r_0 of the rotating body. We vary rotating rate and initial r_0 in the equatorial plane ($\theta = \pi/2$) for the compact star with $R/M = 2.8$ rotating with $j = 0.1,\ 0.4$ and $j = 0.7$ and we plot the resulting escape cones in Figures 5–7. We can see that even for very low rotational rate, the impact on the escape cones is rather strong. We see that the trapped areas are more dominant in the left half of the escape cones, corresponding to the geodesics radiated in the opposite direction with respect to the rotation. We also see that with increasing rotational rate the smallest selected values of r_0 (corresponding to the top left escape-cone) is decreasing ($r_0 = 2.285M$ for $j = 0.1$, while $r_0 = 1.68M$ for $j = 0.7$). This is corresponding to the situation that is clearly seen of Figure 4 bottom, left, where we see that counter-rotating geodesics are trapped for much smaller values r_0 and that co-rotating geodesics can not be trapped for such a high values of rotational rate.

We will now investigate impact of latitudinal coordinate θ_0 on the escape cones of null-geodesics. We present the results on Figures 8, 9. We can see that as we are decreasing θ, i.e. as we are approaching the rotational axis, the escape cones of null-geodesics are

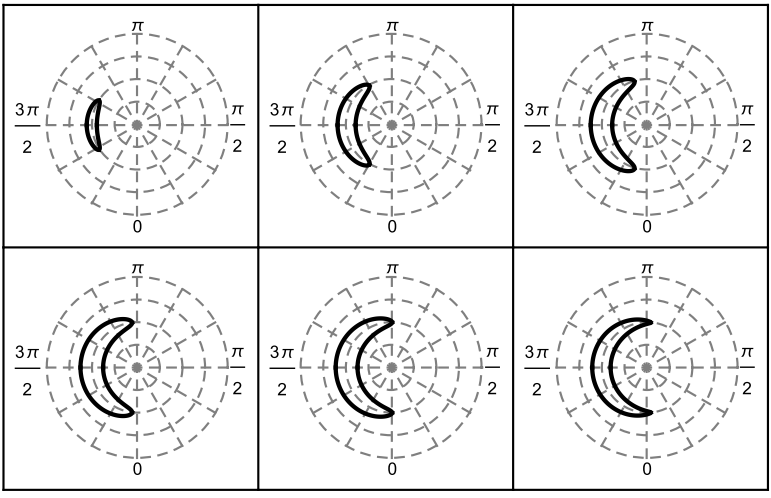

Figure 6. Escape cones of configuration with $R/M = 2.8$ and specific angular momentum $j = 0.4$. Cones are produced at $\theta_0 = \pi/2$ and at points where $r_0 = \{1.785, 1.988, 2.191, 2.394, 2.597, 2.8\}M$.

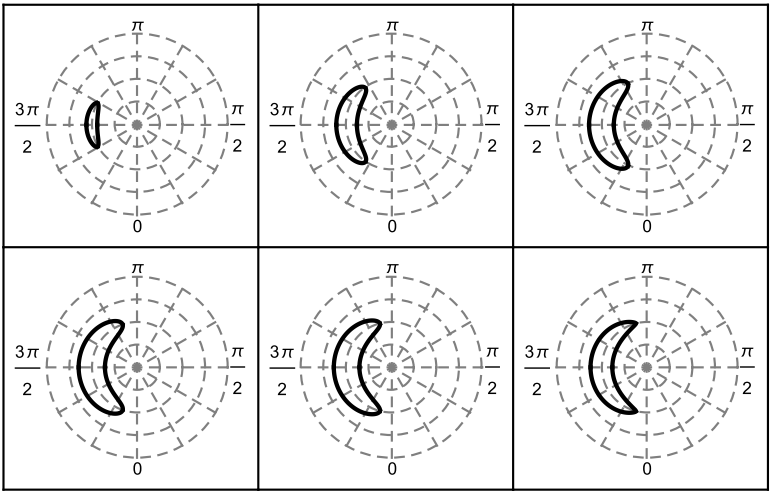

Figure 7. Escape cones of configuration with $R/M = 2.8$ and specific angular momentum $j = 0.7$. Cones are produced at $\theta_0 = \pi/2$ and at points where $r_0 = \{1.68, 1.904, 2.128, 2.352, 2.576, 2.8\}M$.

becoming more symmetrical as expected. This is of course natural result since the impact of rotation is becoming negligible as one is approaching the rotational axis.

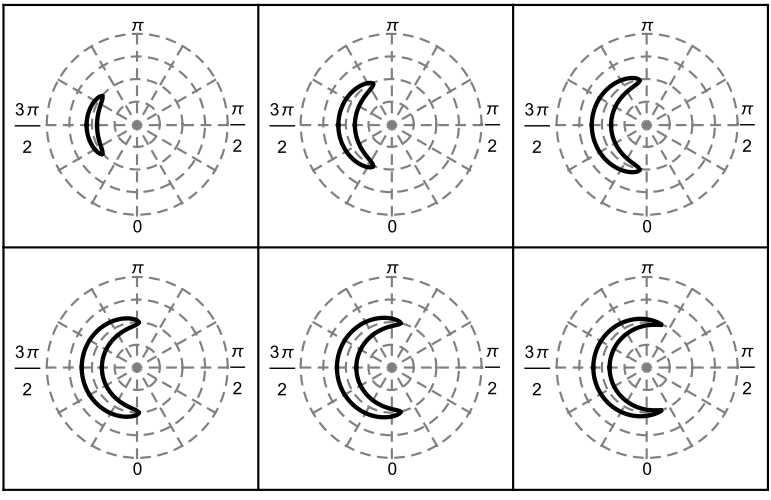

Figure 8. Escape cones of configuration with $R/M = 2.8$ and specific angular momentum $j = 0.4$. Cones are produced at $\theta_0 = \pi/4$ and at points where $r_0 = \{1.889, 2.071, 2.253, 2.435, 2.617, 2.8\}M$.

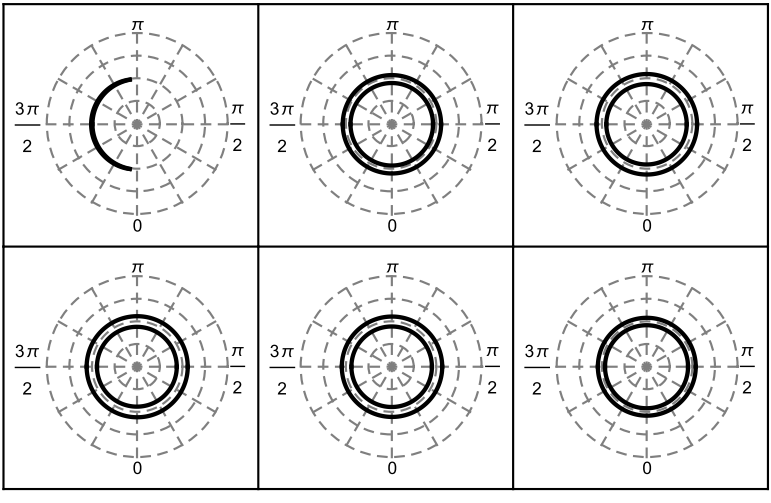

Figure 9. Escape cones of configuration with $R/M = 2.8$ and specific angular momentum $j = 0.4$. Cones are produced at $\theta_0 = \pi/1000$ and at points where $r_0 = \{2.285, 2.388, 2.491, 2.594, 2.697, 2.8\}M$.

4 CONCLUSIONS

We studied escape cones of null-geodesics from the interior of the rotating homogeneous compact stars in the limit of slow rotation. We have shown that the rotation has significant

impact on the existence and on the shape of the escape cones. Rotation separates the null-geodesics into two families - the ones that are directing in the same direction as the rotation (co-rotating ones) and the ones that are directing in the opposite direction (counter-rotating ones). The mass-less particles that will move in the co-rotating direction can easily escape the gravitational field than the particles moving in the counter-rotating direction. This may lead to additional slow-down of the rotating compact-star.

We also investigated the impact of the position of the radiating source on the escape cones of null-geodesics. We plotted escape cones of null-geodesics for positions at various radial and latitudinal coordinate. We have seen, that as one is approaching the rotational axis, the impact of rotation is becoming less important.

Our main motivation was to see the impact of rotation on the trapping of null-geodesics inside the rotating compact star. Rotation allow the trapping for stars having radius $R > 3M$ because the position of the counter-rotating circular photon orbit is shifted and can therefore be relevant for models of compact stars with realistic equations of state. More studies in this field are planned in the future and model presented in this paper will be used as testbed for more sophisticated calculations.

ACKNOWLEDGEMENTS

J.V. acknowledges the support from SGS/15/2016. M.U. acknowledges Czech Science Foundation grant No. 17-16287S. Z.S. acknowledges the Albert Einstein Centre for Gravitation and Astrophysics supported by Czech Science Foundation grant No. 14-37086G.

REFERENCES

Abbott, B. P., Abbott, R., Abbott, T. D., Acernese, F., Ackley, K., Adams, C., Adams, T., Addesso, P., Adhikari, R. X., Adya, V. B. and et al. (2017a), Gravitational Waves and Gamma-Rays from a Binary Neutron Star Merger: GW170817 and GRB 170817A, *Astrophys. J. Lett.*, **848**, L13, arXiv: 1710.05834.

Abbott, B. P., Abbott, R., Abbott, T. D., Acernese, F., Ackley, K., Adams, C., Adams, T., Addesso, P., Adhikari, R. X., Adya, V. B. and et al. (2017b), GW170817: Observation of Gravitational Waves from a Binary Neutron Star Inspiral, *Physical Review Letters*, **119**(16), 161101, arXiv: 1710.05832.

Abbott, B. P., Abbott, R., Abbott, T. D., Acernese, F., Ackley, K., Adams, C., Adams, T., Addesso, P., Adhikari, R. X., Adya, V. B. and et al. (2017c), Multi-messenger Observations of a Binary Neutron Star Merger, *Astrophys. J. Lett.*, **848**, L12, arXiv: 1710.05833.

Abramowicz, M. A., Andersson, N., Bruni, M., Ghosh, P. and Sonego, S. (1997), LETTER TO THE EDITOR: Gravitational waves from ultracompact stars: the optical geometry view of trapped modes, *Classical and Quantum Gravity*, **14**, pp. L189–L194.

Chandrasekhar, S. (1983), *The mathematical theory of black holes*, Oxford/New York, Clarendon Press/Oxford University Press.

Hartle, J. B. (1967), Slowly Rotating Relativistic Stars. I. Equations of Structure, *The Astrophysical Journal*, **150**, pp. 1005–+.

Hartle, J. B. and Thorne, K. S. (1968), Slowly Rotating Relativistic Stars. II. Models for Neutron Stars and Supermassive Stars, *The Astrophysical Journal*, **153**, pp. 807–+.

Lense, J. and Thirring, H. (1918), Über den Einfluß der Eigenrotation der Zentralkörper auf die Bewegung der Planeten und Monde nach der Einsteinschen Gravitationstheorie, *Physikalische Zeitschrift*, **19**.

Novotný, J., Hladík, J. and Stuchlík, Z. (2017), Polytropic spheres containing regions of trapped null geodesics, *Phys. Rev. D*, **95**(4), 043009, arXiv: 1703.04604.

Schee, J., Stuchlík, Z. and Jurán, J. (2005), Light escape cones and raytracing in Kerr geometry, in S. Hledík and Z. Stuchlík, editors, *RAGtime 6/7: Workshops on black holes and neutron stars*, pp. 143–155.

Schwarzschild, K. (1999), On the gravitational field of a sphere of incompressible fluid according to Einstein's theory, *ArXiv Physics e-prints*, arXiv: physics/9912033.

S.L. Shapiro and S.A. Teukolsky, (1983), *Black holes, white dwarfs and neutron stars*, John Wilery and Sons, New York.

Stuchlík, Z., Hladík, J. and Urbanec, M. (2011), Neutrino trapping in braneworld extremely compact stars, *General Relativity and Gravitation*, **43**, pp. 3163–3190, arXiv: 1108.5767.

Stuchlík, Z., Hladík, J., Urbanec, M. and Török, G. (2012), Neutrino trapping in extremely compact objects described by the internal Schwarzschild-(anti-)de Sitter spacetimes, *General Relativity and Gravitation*, **44**, pp. 1393–1417.

Stuchlík, Z. and Schee, J. (2010), Appearance of Keplerian discs orbiting Kerr superspinars, *Classical and Quantum Gravity*, **27**(21), 215017, arXiv: 1101.3569.

Stuchlík, Z., Török, G., Hledík, S. and Urbanec, M. (2009), Neutrino trapping in extremely compact objects: I. Efficiency of trapping in the internal Schwarzschild spacetimes, *Classical and Quantum Gravity*, **26**(3), pp. 035003–+.

Urbanec, M., Miller, J. C. and Stuchlík, Z. (2013), Quadrupole moments of rotating neutron stars and strange stars, *MNRAS*, **433**, pp. 1903–1909, arXiv: 1301.5925.

Völkel, S. H. and Kokkotas, K. D. (2017), Ultra compact stars: reconstructing the perturbation potential, *Classical and Quantum Gravity*, **34**(17), 175015, arXiv: 1704.07517.

Witten, E. (1984), Cosmic separation of phases, *Phys. Rev. D*, **30**, pp. 272–285.

Proceedings of *RAGtime 17–19, 17–19/23–26 Oct., 1–5 Nov., 2015/2016/2017, Opava, Czech Republic*
Z. Stuchlík, G. Török and V. Karas, editors, Silesian University in Opava, 2017, pp. 237–252

Polarization properties of bow shock sources close to the Galactic centre

M. Zajaček[1,2,3,a], V. Karas[3], E. Hosseini[2,1], A. Eckart[2,1], B. Shahzamanian[2], M. Valencia-S.[2], F. Peissker[2], G. Busch[2], S. Britzen[1] and J. A. Zensus[1]

[1] Max-Planck-Institut für Radioastronomie (MPIfR), Auf dem Hügel 69, D-53121 Bonn, Germany
[2] I. Physikalisches Institut der Universität zu Köln, Zülpicher Strasse 77, D-50937 Köln, Germany
[3] Astronomical Institute, Academy of Sciences, Boční II 1401, CZ-14131 Prague, Czech Republic
[a] zajacek@ph1.uni-koeln.de

ABSTRACT
Several bow shock sources were detected and resolved in the innermost parsec from the supermassive black hole in the Galactic centre. They show several distinct characteristics, including an excess towards mid-infrared wavelengths and a significant linear polarization as well as a characteristic prolonged bow-shock shape. These features give hints about the presence of a non-spherical dusty envelope generated by the bow shock. The Dusty S-cluster Object (also denoted as G2) shows similar characteristics and it is a candidate for the closest bow shock with a detected proper motion in the vicinity of Sgr A*, with the pericentre distance of only approx. 2000 Schwarzschild radii. However, in the continuum emission it is a point-like source and hence we use Monte Carlo radiative transfer modeling to reveal its possible three-dimensional structure. Alongside the spectral energy distribution, the detection of polarized continuum emission in the near-infrared K_s-band (2.2 micrometers) puts additional constraints on the geometry of the source.

Keywords: black hole physics – Galaxy: centre – radiative transfer – polarization – stars: pre-main-sequence

1 BOW SHOCKS CLOSE TO THE GALACTIC CENTRE

The Galactic centre region serves as a unique laboratory to study the mutual interaction of stars with the ambient gaseous-dusty medium (Genzel et al., 2010; Mužić et al., 2010). Inside the sphere of gravitational influence of the supermassive black hole (hereafter SMBH) of $M_\bullet \simeq 4 \times 10^6\, M_\odot$ (Parsa et al., 2017), which is associated with the compact radio source

Sgr A*, stars exhibit a Keplerian rise (Eckart and Genzel, 1996, 1997) in orbital velocities $v_\star \propto r^{-1/2}$, with the typical Keplerian velocities as large as

$$v_\star \simeq 415 \left(\frac{M_\bullet}{4\times10^6\,M_\odot}\right)^{1/2}\left(\frac{r}{0.1\,\mathrm{pc}}\right)^{-1/2}\ \mathrm{km\,s^{-1}}\ \text{for}\ r \lesssim r_{\mathrm{inf}}, \tag{1}$$

where r is the radial distance from the SMBH. The radius of the gravitational influence of the SMBH represents the length-scale on which the gravitational potential of the SMBH prevails over the potential of the Nuclear Star Cluster, which is proportional to the square of the one-dimensional stellar velocity dispersion $\sigma_\star$ (see e.g. Schneider, 2006; Merritt, 2013; Generozov et al., 2015),

$$r_{\mathrm{inf}} \simeq GM_\bullet/\sigma_\star^2 = 1.7\left(\frac{M_\bullet}{4\times10^6\,M_\odot}\right)\left(\frac{\sigma_\star}{100\,\mathrm{km\,s^{-1}}}\right)^{-2}\ \mathrm{pc}\,. \tag{2}$$

Using the empirical SMBH mass–velocity disperion correlation $M_\bullet - \sigma_\star$ (Ferrarese and Merritt, 2000; McConnell et al., 2011) in the form (McConnell et al., 2011)

$$M_\bullet \simeq 2\times10^8\left(\frac{\sigma_\star}{200\,\mathrm{km\,s^{-1}}}\right)^{5.1}\ M_\odot\,, \tag{3}$$

the influence radius (2) can be expressed as a function of the SMBH mass only,

$$r_{\mathrm{inf}} \simeq 2\left(\frac{M_\bullet}{4\times10^6\,M_\odot}\right)^{0.6}\ \mathrm{pc}\,, \tag{4}$$

which keeps the influence radius at about 2 pc for the Galactic centre region. Inside this radius the inner rim of the atomic and the molecular circum-nuclear ring (CND) is located, which has an inner radius at $\sim$ 1.5 pc (Harada et al., 2015). Further in towards the SMBH, there is a cavity that is filled mostly with rarefied diffuse ionized gas (Becklin et al., 1982; Montero-Castaño et al., 2009). A distinct feature is the minispiral that represents a denser concentration of colder ionized and neutral gas and dust and its dynamics is represented by three bundles of quasi-Keplerian orbits (see Moser et al., 2017and references therein). The rest of the gas is mostly supplied by the winds of massive OB/Wolf-Rayet stars and its dynamics can be approximated by the radial inflow/outflow towards/from the SMBH (Cuadra et al., 2006). The gas supplied by stars is bound to the SMBH inside the Bondi radius r_{B}, inside which the gravitational potential of the SMBH overcomes the pressure of the gas,

$$r_{\mathrm{B}} \simeq \frac{2GM_\bullet}{c_{\mathrm{s}}^2} \approx 0.15\left(\frac{M_\bullet}{4\times10^6\,M_\odot}\right)\left(\frac{\mu_{\mathrm{HII}}}{0.5}\right)\left(\frac{\gamma}{1.4}\right)^{-1}\left(\frac{T_{\mathrm{a}}}{10^7\,\mathrm{K}}\right)^{-1}\ \mathrm{pc}\,, \tag{5}$$

where the mean molecular weight is scaled to $\mu_{\mathrm{HII}} = 0.5$, which corresponds to the fully ionized HII region (Lang, 1978). The temperature of the ambient medium is expressed in 10^7 K, which is based on the thermal bremsstrahlung emission of hot ionized plasma in the central parsec. The fit of the bremsstrahlung emissivity to the observed surface brightness profile yields the electron temperature of $k_{\mathrm{B}}T_{\mathrm{e}} \in [1; 2; 3.5\,\mathrm{keV}]$ ($T_{\mathrm{e}} = 11.6 - 40.6\times10^6$ K)

at the Bondi radius based on different dynamical models – radiatively inefficient accretion flow (RIAF) (Wang et al., 2013), stellar outflows (Shcherbakov and Baganoff, 2010), and the spherical steady Bondi flow (Różańska et al., 2015), respectively. Depending on whether the flow is adiabatic ($\gamma = 5/3$) or isothermal ($\gamma = 1$), the Bondi radius can extend from ~ 0.1 pc up to ~ 0.2 pc within the uncertainties of adopted parameters, respectively. The steady inflow-outflow flow solution in the Galactic centre region is illustrated in Fig. 2. In general the structure of the flow inside the classical Bondi radius is expected to be more complex, possibly non-spherical. This is hinted by the fact that the accretion rate at the Bondi radius is $\dot{M}_{\rm B} = 1 \times 10^{-5}\,{\rm M}_{\odot}\,{\rm yr}^{-1}$ (Baganoff et al., 2003), whereas the SMBH associated with Sgr A* was inferred to accrete at much smaller rate based on the Faraday rotation measurements, $\dot{M}_{\rm SgrA*} = 2\times10^{-9} - 2\times10^{-7}{\rm M}_{\odot}\,{\rm yr}^{-1}$ (Marrone et al., 2007), which implies a significant outflow even inside the Bondi sphere. However, the steady spherical inflow-outflow structure is still a relevant approximation of the Galactic centre processes and we will adopt it further for analytical and semi-analytical estimates of the star–ambient medium interaction.

The radial distance in Eq. (1) is scaled to the length-scale of 0.1 pc, which is within the distance range where ~ 200 young, massive stars of spectral type OB are located (~ 0.04-0.5 pc Buchholz et al., 2009; Bartko et al., 2010). These recently formed luminous stars provide a significant fraction of the kinetic energy and material via their fast outflows and due to their large orbital velocities given by Eq. (1), they are observed to interact with the ambient medium in the form of *bow shocks* (Mužić et al., 2010; Rauch et al., 2013; Sanchez-Bermudez et al., 2014). These are clearly detected as extended non-spherical dusty shells in infrared bands that exhibit a thermal excess towards mid-infrared bands as well as an intrinsic linearly polarized emission (Buchholz et al., 2011, 2013).

The basic condition for the formation of shocks in the interstellar medium (ISM) is that the relative velocity of the source $\mathbf{v}_{\rm rel}$ (star, cloud) with respect to the ambient medium is supersonic. The bow shock that forms is aligned with respect to the relative velocity vector $\mathbf{v}_{\rm rel} = \mathbf{v}_{\star} - \mathbf{v}_{\rm a}$. In case the ionized gas is non-magnetized, the perturbations and signals in the medium move at the sound speed $c_{\rm s}$,

$$c_{\rm s} = 482 \left(\frac{\gamma}{1.4}\right)^{1/2} \left(\frac{T_{\rm a}}{10^7\,{\rm K}}\right)^{1/2} \left(\frac{\mu_{\rm HII}}{0.5}\right)^{-1/2} \,{\rm km\,s^{-1}}, \tag{6}$$

which means that the Mach number $\mathcal{M} \equiv v_{\rm rel}/c_{\rm s}$ at the Bondi radius is close to unity for a non-magnetized medium since the orbital velocity and the sound speed are comparable, see Eqs. (1) and (6).

Based on the multi-frequency observations of the Galactic centre magnetar (Eatough et al., 2013), a large, dynamical important magnetic field intensity was found based on the Faraday rotation measurements, $B \geq 50\,\mu$G on the projected radial scales of $\sim 3'' = 0.12$ pc. Combined with the inferred electron number density of $n_{\rm e}^{\rm out} = 18.3\pm0.1\,{\rm cm}^{-3}$ at the Bondi radius (Różańska et al., 2015), one can estimate the Alfvén velocity that represents the speed at which hydrodynamic waves propagate in the magnetized plasma,

$$v_{\rm A} = \sqrt{\frac{B^2}{\mu_0 \mu m_{\rm H} n_{\rm e}^{\rm out}}} \approx 36 \left(\frac{B}{50\,\mu G}\right) \left(\frac{\mu_{\rm HII}}{0.5}\right)^{-1/2} \left(\frac{n_{\rm e}^{\rm out}}{18.3\,{\rm cm}^{-3}}\right)^{-1/2}, \tag{7}$$

which implies the Alfvénic Mach number $\mathcal{M}_{\rm A} \equiv v_{\rm rel}/v_{\rm A}$ larger than unity and thus supersonic velocities of stars at the Bondi radius in case the plasma is magnetically dominated.

The formation of the shock is given by the interaction between the pressure of the stellar outflow and the ambient ram pressure due to the linear stellar motion. The open bow shock is formed for supersonic relative velocities, when the shock driven into the ambient medium and the shocked stellar wind are separated by the contact discontinuity located at the stand-off distance $R_{\rm bw}$ from the star. However, for fast stellar outflows, the prolonged cavity surrounded by the shocked stellar wind is formed even for subsonic velocities (Christie et al., 2016). In general, it is instructive to look at the distance range in the Galactic centre where the bow shocks can form, which is in general given by the condition $\mathcal{M} \gtrsim 1$ for a non-magnetized plasma or $\mathcal{M}_{\rm A} \gtrsim 1$ for the magnetically dominated environment. For simplicity, we assume that stars move on circular Keplerian orbits and they can interact with stationary medium or inflow/outflow with the ambient velocity $v_{\rm a}^{\rm r} = 1000, 2000,$ and $3000\,{\rm km\,s^{-1}}$. For the ambient medium, we take the radial density and temperature profile as calculated for Bondi spherical flow (Różańska et al., 2015) and RIAF-based flow (Psaltis, 2012). In addition, we consider the profile of the Alfvén velocity calculated according to Eq. (7), where we calculate the magnetic field intensity $B^2 = 8\pi P_{\rm gas}/\beta$, where β is the plasma parameter. We take $\beta = 100$ so that the Alfvén velocity is consistent with the Faraday rotation measurements at the projected distance of $3''$ (Eatough et al., 2013; Różańska et al., 2015).

The occurrence of bow-shock structures in the Galactic centre is expected on a large spatial scale according to Fig. 1 – depending on the ambient temperature profile of the hot diffuse plasma as well as the presence and the velocity of the inflow/outflow, which both affect the Mach number at the given radius $\mathcal{M}(r) = v_{\rm rel}/c_{\rm s}(r)$. The conditions for bow-shock formation inside the sphere of influence are not quite isotropic, mainly because of the presence of the denser and the cooler arms of the Minispiral with the gas temperature in the range of $\sim$ 1000 K–10 000 K (Kunneriath et al., 2012; Moser et al., 2017), which puts the sound speed well below the expected Keplerian velocities of stars. It is thus not a coincidence that several bright bow-shock sources are detected along and close to the Minispiral arms (Wolf-Rayet stars IRS5, IRS1W, IRS10W, IRS21 Sanchez-Bermudez et al., 2014).

2 AMBIENT MEDIUM AND SCALING OF BOW SHOCK SIZES AND LUMINOSITIES

Inside the influence radius, the ambient medium in the Galactic centre is neither stationary nor homogeneous. In fact, it represents a multi-phase medium (Barai et al., 2012; Różańska et al., 2014, 2017) with a complex inflow-outflow structure, see Fig. 2, which is partially represented by radiatively inefficient accretion flows (RIAFs, Yuan and Narayan, 2014) or spherical Bondi solutions (Różańska et al., 2015). In case of a purely hydrodynamical accretion, transonic behaviour is typical for black hole inflows at small radii, where the inward-directed speed of the medium reaches and exceeds the speed of sound (e.g., Chakrabarti, 1990; Das et al., 2015). This is also the case of accretion onto a rotating black hole; unlike the case of accretion onto a non-rotating black hole, in a rapidly rotating case

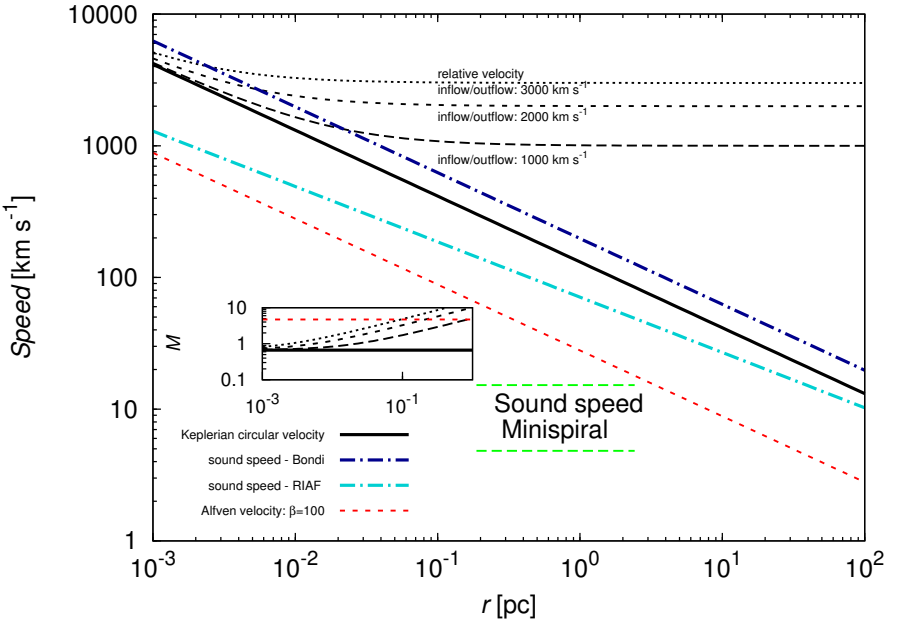

Figure 1. The radial profile of the Keplerian circular velocity, the sound speed for the Bondi flow and RIAF, the relative velocity of the circular stellar motion with respect to the ambient outflow/inflow. There is a lower sound speed in the denser and cooler Minispiral arms, which is shown by green dashed lines. The profile of the Alfvén velocity is also depicted for the plasma parameter $\beta = 100$. The plot inset shows the Mach numbers for the Keplerian circular velocity and corresponding relative velocities with respect to the sound speed and the Alfvén velocity in the Bondi flow (Różańska et al., 2015).

the medium acquires azimuthal velocity in the course of infall (Pariev, 1996). This arises due to the effect of frame dragging, which occurs at small radii just above the black hole ergosphere.

Unlike the classical purely hydrodynamical Bondi spherical accretion, where no additional energy input (heat or mechanical driving by winds) is available, in the case of Sgr A* there are indeed such sources present due to stars of the Nuclear Stellar Cluster (Silich et al., 2008). This can act against the gravitational pull of the central black hole and reverse the direction of the medium inflow in the inner regions to outflow above a transitional, so-called stagnation radius. In consequence, the bow-shock interaction with the ambient medium of changing velocity will affect the orientation and the overall shape of the bow-shock. The motion of the ambient medium can be revealed either by the combination of the stellar proper motion and bow-shock orientation for extended sources or by the detection of polarized emission for unresolved sources.

It is instructive to calculate the change of the bow-shock size as well as the overall thermal luminosity of the bow shock along the orbit. This is possible under the assumption

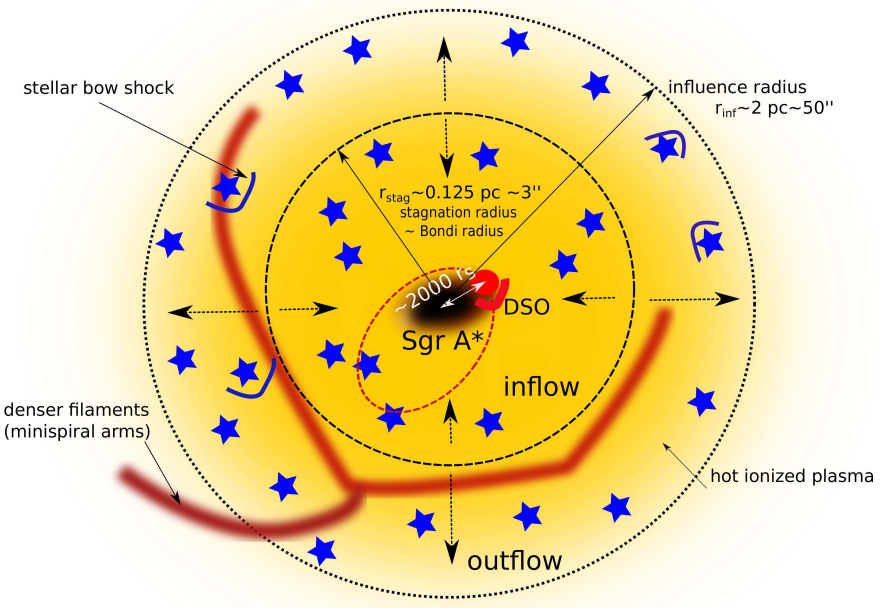

Figure 2. Illustration of the Galactic centre region within the sphere of influence. Two main regions may be distinguished: inside the stagnation radius the inflow of gas takes place, outside it the gas flows out. Stars of the Nuclear Star Cluster are located in both regions. When the relative velocity of the star is larger than the local sound speed, the bow shock forms. Its size and gas and dust density depend on both stellar parameters (the stellar mass-loss rate $\dot{m}_{\rm w}$ and the terminal stellar wind velocity $v_{\rm w}$) and the local ambient density $\rho_{\rm a}$ as well as the relative velocity $v_{\rm rel}$.

of the Keplerian motion around the SMBH (Sgr A*) and the prescription for the radial density profile, $n_{\rm a} = n_{\rm a0}(r/r_0)^{-\nu}$, where $n_{\rm a0}$ is the ambient density at the distance r_0 from the SMBH and ν denotes the index of the power-law ambient density. The relations between two positions along the orbit are especially simple and elegant for an elliptic orbit, which is valid for most of the stars in the innermost S cluster (Zajaček et al., 2016), and under the assumption that $\mathbf{v}_{\rm rel} = \mathbf{v}_\star$, i.e. the motion of the ambient medium is negligible, which is especially the case at and close to the stagnation radius $r_{\rm stag}$, where the radial gas velocity passes through zero.

The relation for the stagnation radius can be found within a one-dimensional steady-state inflow-outflow model of the gas in the vicinity of a galactic nucleus (Generozov et al., 2015). The gas supplied to the interstellar medium by stellar winds flows towards the black hole inside $r_{\rm stag}$ and a fraction of the matter is accreted into the SMBH, while the gas outside $r_{\rm stag}$ forms a radial outflow, see Fig 2. When considering bright massive OB stars in the inner parsec of the Galactic centre (Paumard et al., 2006; Bartko et al., 2010), the heating rate due to their fast outflows $v_{\rm w}$ is typically larger than the stellar velocity dispersion $\sigma_\star$ of the cluster, $v_{\rm w} \gg \sigma_\star$. In this case, the stagnation radius can be approximately expressed

as (Generozov et al., 2015),

$$r_{\rm stag} \approx \left(\frac{13+8\Gamma}{4+2\Gamma} - \frac{3\nu_{\rm stag}}{2+\Gamma}\right)\frac{GM_\bullet}{\nu_{\rm stag}v_{\rm w}^2} \approx \begin{cases} 0.30\left(\frac{M_\bullet}{4\times10^6\,M_\odot}\right)\left(\frac{v_{\rm w}}{500\,{\rm km\,s^{-1}}}\right)^{-2}\,{\rm pc} & ,{\rm core}\ \ (\Gamma=0.1)\,, \\ 0.16\left(\frac{M_\bullet}{4\times10^6\,M_\odot}\right)\left(\frac{v_{\rm w}}{500\,{\rm km\,s^{-1}}}\right)^{-2}\,{\rm pc} & ,{\rm cusp}\ \ (\Gamma=0.8)\,, \end{cases} \tag{8}$$

where Γ is the power-law index of the inner stellar brightness profile. For estimative purposes, we consider two limiting cases, the core profile with $\Gamma = 0.1$ and the stellar cusp with $\Gamma = 0.8$. The quantity $\nu_{\rm stag} = -{\rm d}n_{\rm a}/{\rm d}r|_{r_{\rm stag}}$ is the gas density power-law slope at $r_{\rm stag}$, which according to the numerical analysis of Generozov et al. (2015) is $\nu_{\rm stag} \approx 1/6[(4\Gamma+3)]$. According to the estimates in Eq. (8), the stagnation radius is expected to be located close to the Bondi radius with an offset given by the numerical factor (Generozov et al., 2015)

$$\frac{r_{\rm stag}}{r_{\rm B}} \approx \frac{13+8\Gamma}{(2+\Gamma)(3+4\Gamma)}\,, \tag{9}$$

which is of the order of unity. This is also illustrated in the two-zone scheme in Fig. 2.

Under the assumption that the stellar-wind pressure is at the equilibrium with the ram pressure and the thermal pressure of the medium $P_{\rm w} = P_{\rm ram} + P_{\rm th} = P_{\rm ram}(1+\alpha)$, where $\alpha = P_{\rm th}/P_{\rm ram}$, one can express the characteristic length-scale – or stand-off distance R_0 – using the following generalized formula (Wilkin, 1996; Zhang and Zheng, 1997; Christie et al., 2016),

$$R_0 = \left(\frac{\dot{m}_{\rm w}v_{\rm w}}{\Omega_{\rm w}\rho_{\rm a}v_{\rm rel}^2(1+\alpha)}\right)^{1/2} \simeq C_\star\rho_{\rm a}^{-1/2}v_{\rm rel}^{-1}\,, \tag{10}$$

where $\dot{m}_{\rm w}$ is the stellar mass-loss rate, $v_{\rm w}$ is the terminal wind velocity, and $\Omega_{\rm w}$ is the solid angle into which the stellar wind is blown (for the isotropic case that is often assumed, $\Omega_{\rm w} = 4\pi$). The last equality in Eq. 10 is valid in case the ratio of the thermal pressure to the ram pressure α is negligible, which is for highly supersonic motion, $\mathcal{M} = v_{\rm rel}/c_{\rm s} = 1/\sqrt{\gamma\alpha} \gg 1$ when $\alpha \to 0$. The quantity $C_\star^2 = \dot{m}_{\rm w}v_{\rm w}/\Omega_{\rm w}$ is the momentum flux of the stellar wind per unit solid angle. It can be assumed to be constant per several orbital periods of a star around the SMBH. For the brightest star in the S-cluster S2 star (Martins et al., 2008), the momentum flux can be evaluated as

$$C_\star^2 = 7.85\times10^{-5}\left(\frac{\dot{m}_{\rm w}}{10^{-7}\,M_\odot\,{\rm yr^{-1}}}\right)\left(\frac{v_{\rm w}}{1000\,{\rm km\,s^{-1}}}\right)\,M_\odot\,{\rm km\,s^{-1}\,yr^{-1}\,sr^{-1}}\,. \tag{11}$$

Under the assumption that the motion of ambient medium is negligible, we can relate the relative velocity to the orbital velocity of the star $v_{\rm rel} \simeq v_\star = \sqrt{GM_\bullet(2/r - 1/a)}$, where we assumed the Keplerian motion of a star around the SMBH with semi-major axis a and we applied the *vis-viva* equation. When we neglect the thermal pressure, we can relate the bow-shock length-scales R_{01} and R_{02} between two respective positions r_1 and r_2 ($r_1 > r_2$) as follows,

$$\frac{R_{01}(r_1)}{R_{02}(r_2)} = \left(\frac{n_{\rm a2}}{n_{\rm a1}}\right)^{1/2}\left(\frac{v_{\rm rel2}}{v_{\rm rel1}}\right) = \left(\frac{r_1}{r_2}\right)^{\nu/2}\left(\frac{v_{\star2}}{v_{\star1}}\right)\,. \tag{12}$$

Using the *vis-viva* integral, we can express the ratio in Eq. (12) as a function of four variables,

$$\frac{R_{01}}{R_{02}}(r_1, r_2, a, \nu) = \left(\frac{r_1}{r_2}\right)^{(\nu+1)/2} \left(\frac{2a - r_2}{2a - r_1}\right)^{1/2} . \tag{13}$$

Even simpler relations can be obtained when evaluating the ratio in Eq. (13) at special points along the elliptical orbit, e.g. between the apobothron and the peribothron of a star orbiting the SMBH,

$$\frac{R_{\rm A}}{R_{\rm P}}(e, \nu) = \left(\frac{1+e}{1-e}\right)^{\frac{\nu}{2}+1} , \tag{14}$$

or between semi-latus rectum (the true anomaly of 90°) and the peribothron,

$$\frac{R_{90}}{R_{\rm P}}(e, \nu) = \frac{(1+e)^{\nu/2+1}}{(1+e^2)^{1/2}} . \tag{15}$$

Since the star on a bound elliptical orbit around the SMBH changes its relative velocity (because of both the change in the orbital velocity and the ambient flow velocity), the bow-shock luminosity is also expected to change. The upper limit for the thermal bow-shock luminosity $L_{\rm th}$ can be obtained from the sum of the kinetic terms of the flow that are assumed to become fully thermalized (Wilkin et al., 1997),

$$L_{\rm th} = \frac{1}{2}\dot{m}_{\rm w}(v_{\rm rel}^2 + v_{\rm w}^2) \simeq \frac{1}{2}\dot{m}_{\rm w}(v_\star^2 + v_{\rm w}^2) . \tag{16}$$

The ratio of the bow-shock luminosities at two different radii along the elliptical orbit may be then simply calculated according to,

$$\frac{L_{\rm th1}}{L_{\rm th2}} = \frac{\beta_1^2 + 1}{\beta_2^2 + 1} , \tag{17}$$

where $\beta = v_{\rm rel}/v_{\rm w} \simeq v_\star/v_{\rm w}$.

In Table 1, we calculate both the ratio of bow-shock sizes according to Eq. (14) and luminosities according to Eq. (17) between the apocentre and the pericentre for different values of the density power-law index ν as well as different orbital eccentricities e. As a prototype of B-type stars in the innermost arcsecond in the S cluster, we take the brightest S2 star with $a \simeq 0.126''$, $e \simeq 0.884$, $\dot{m}_{\rm w} \simeq 10^{-7}\, M_\odot {\rm yr}^{-1}$, and $v_{\rm w} \simeq 1000\,{\rm km\,s}^{-1}$ (Martins et al., 2008; Parsa et al., 2017).

3 MODELLING POLARIZED BOW-SHOCK EMISSION: DUSTY S-CLUSTER OBJECT (DSO/G2) AS A SPECIAL CASE OF UNRESOLVED BOW SHOCK CLOSE TO THE BLACK HOLE

Of special interest is a stellar bow shock located in the direct vicinity of the SMBH. The Galactic centre is the only nucleus where we can study the individual proper motion of

e	ν	R_A/R_P	L^A_{th}/L^P_{th} (S2 star)
0.0	≥ 0	1.0	1.0
0.50	0.0	3.00	0.19
0.50	0.5	3.95	0.19
0.50	1.0	5.20	0.19
0.50	2.0	9.00	0.19
0.90	0.0	19.00	1.8×10^{-2}
0.90	0.5	39.67	1.8×10^{-2}
0.90	1.0	82.82	1.8×10^{-2}
0.90	2.0	361.00	1.8×10^{-2}
0.95	0.0	39.00	8.1×10^{-3}
0.95	0.5	97.46	8.1×10^{-3}
0.95	1.0	243.55	8.1×10^{-3}
0.95	2.0	1521.00	8.1×10^{-3}

Table 1. The ratio of bow-shock sizes R_A/R_P as well as the ratio of thermal bow-shock luminosities L^A_{th}/L^P_{th} between the apocentre and the pericentre of the orbit for different orbital eccentricities and the power-law indices of the gas density profile. We adopted the parameters of S2 star, $a \simeq 0.126''$, $e \simeq 0.884$, $\dot{m}_w \simeq 10^{-7}\, M_\odot \mathrm{yr}^{-1}$, and $v_w \simeq 1000\,\mathrm{km\,s}^{-1}$ (Martins et al., 2008; Parsa et al., 2017), for the calculation of the ratio of bow-shock luminosities.

stars as well as study the interaction of stars with their environment. Although currently there is no bow shock detected on the scale of $\sim$ 10–100 Schwarzschild radii, on which some of the strong-gravity effects could be studied (Dovčiak et al., 2004), Dusty S-cluster Object (DSO/G2; Gillessen et al., 2012; Eckart et al., 2013; Phifer et al., 2013; Witzel et al., 2014; Valencia-S. et al., 2015) shows several signs of an unresolved bow-shock source with the closest distance to the SMBH at $\sim$ 2000 Schwarzschild radii. The main properties of DSO/G2 are the following,

- observed as a bright L'-band (3.8 μm) source. The fitted single-temperature black-body yields the radius of the optically thick photosphere of $R_{DSO} = (0.31 \pm 0.07)$ AU and the temperature of $T_{DSO} = (874 \pm 54)$ K (Zajaček et al., 2017),
- clear infrared-excess (in comparison with main-sequence stars; Eckart et al., 2013; Shahzamanian et al., 2016; Zajaček et al., 2017), which implies the presence of dust,
- a strong emission line of Brγ (but also HeI and Paα), which implies the presence of either inflow or outflow to/from the star (Valencia-S. et al., 2015),
- a significant linearly polarized continuum emission in K_s-band (2.2 μm) with the polarization degree of $p_L = (30 \pm 15)\%$ and a variable polarization angle (Shahzamanian et al., 2016). In continuum, the source is point-like (Witzel et al., 2014; Shahzamanian et al., 2016), and hence the overall non-zero polarization implies a non-spherical nature.

In order to set-up a three-dimensional model of the Dusty S-cluster Object (DSO) – a star with non-spherical dusty envelope – in terms of the continuum emission, we used the Monte Carlo Radiative Transfer code (MCRT) `Hyperion` (Robitaille, 2011). The MCRT

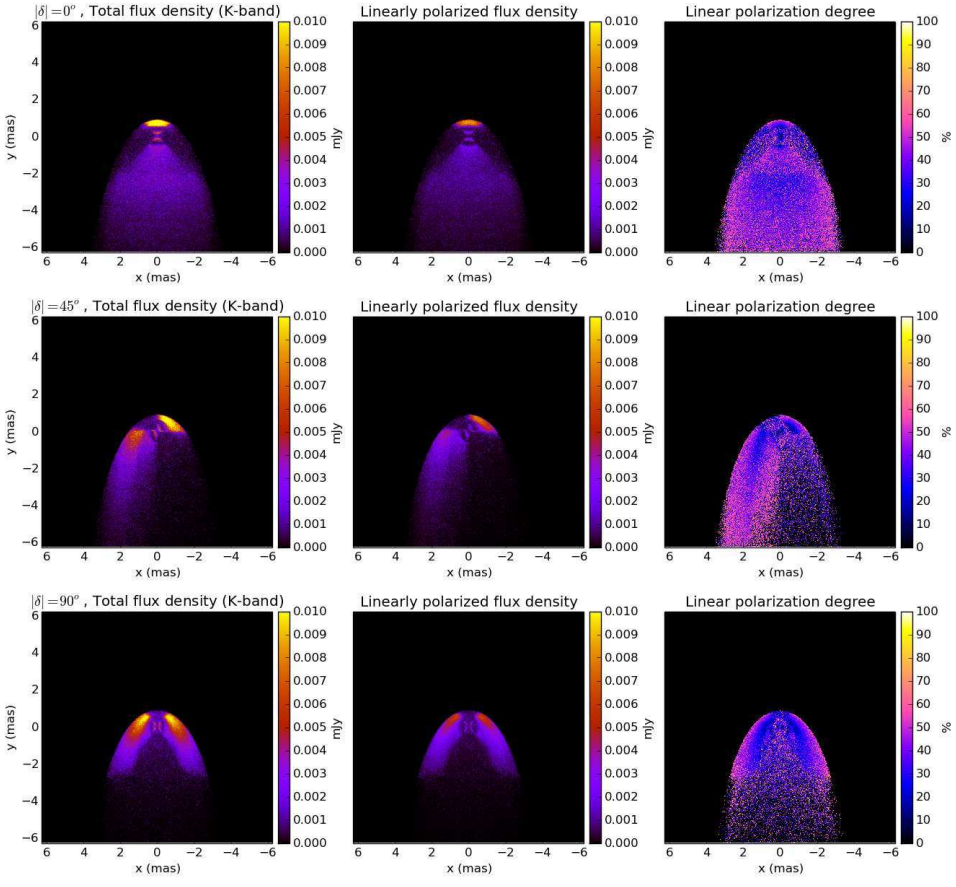

Figure 3. Individual rows represent simulated images of the Dusty S-cluster Object (DSO/G2) for different position angles of the bipolar outflow with respect to the bow-shock symmetry axis: $\delta = 0°$ – top row (the bow shock and the bipolar outflow are aligned), $\delta = 45°$ – middle row, and $\delta = 90°$ – bottom row. In the left column, figures show simulated images in K_s-band (2.2 μm), figures in the middle panel show linearly polarized continuum emission in the same band, and in the right column, images show the maps of the polarization degree.

mimics real observations in a sense that it allows to track photons from their emission by a source, through their propagation through a density field in the medium, until they reach the observer. For the fundamental theory of radiative transfer, first one needs to define the specific intensity I_ν of a beam of light that passes through surface area of dA at an angle of θ to the surface normal within a solid angle dΩ in a time interval dt and a frequency range of dν,

$$I_\nu = \frac{\mathrm{d}E_\nu}{\mathrm{d}A\cos\theta\mathrm{d}\nu\mathrm{d}\Omega\mathrm{d}t}\,. \tag{18}$$

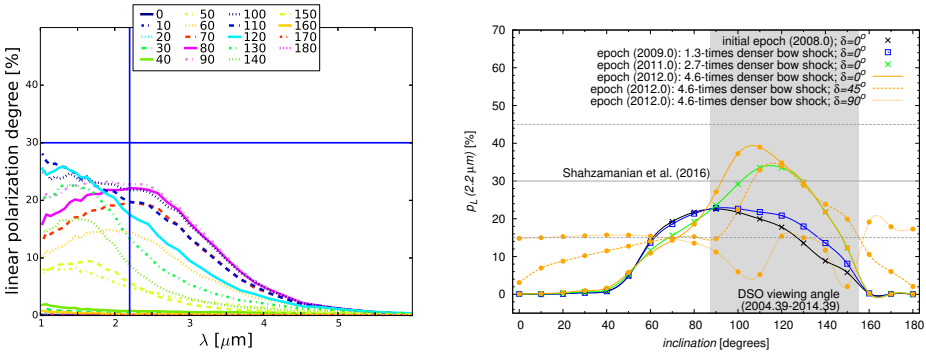

Figure 4. Left panel: The dependency of the linear polarization degree $p_{\rm L}$ $K_{\rm s}$-band (2.2 μm) on the wavelength λ expressed in μm. Different lines correspond to different viewing angles with respect to the observer (0° represents the front view of the bow shock, 90° the side view, and 180° the tail view of the bow shock). The vertical line represents the wavelength of 2.2 μm and the horizontal line stands for the polarization degree of 30%. **Right panel:** The dependency of the linear polarization degree $p_{\rm L}$ in $K_{\rm s}$-band (2.2 μm) on the viewing angle (using the same definition as in the left panel). Different lines correspond to different bow-shock densities as the DSO approached Sgr A* (according to the legend). In addition, for one epoch we also plot the dependencies for different position angles of the bipolar outflow with respect to the bow shock. The dark-gray dashed horizontal lines mark the polarization degree of $p_{\rm L} \simeq (30 \pm 15)\%$ as inferred by Shahzamanian et al. (2016).

The change of the specific intensity through the medium segment dl is governed by the equation of the radiative transfer,

$$\frac{{\rm d}I_\nu}{{\rm d}l} = -\kappa_\nu \rho I_\nu + j_\nu \rho \,, \tag{19}$$

where κ_ν is the opacity of the medium and j_ν is the emissivity, which are both complex functions of the composition and dynamics of the medium as well as of the radiation frequency ν. Eq. (19) can be rewritten in terms of the optical depth τ_ν along the line of sight L,

$$\tau_\nu = -\int_0^L \kappa_\nu \rho {\rm d}l \,, \tag{20}$$

into the form

$$\frac{{\rm d}I_\nu}{{\rm d}\tau_\nu} = I_\nu - S_\nu \,, \tag{21}$$

where $S_\nu = j_\nu/\kappa_\nu$ is the source function of the medium. The transfer equation can be analytically solved only for a certain set of simple problems, e.g. homogeneous plan-parallel layers or isotropic spherical problems. For more complicated cases, it must be solved numerically. In case of three-dimensional dusty stellar atmospheres and envelopes, the MCRT method is currently applied as it can handle the calculation of both total as well as polarized continuum spectral energy distributions and images (Robitaille, 2011).

When a photon interacts with the gaseous-dusty medium, it can either be scattered or absorbed (and emitted in other direction and different wavelength). The scattering probability is given by the *albedo function a*, which can be expressed as follows,

$$a = \frac{n_{\rm s}\sigma_{\rm s}}{n_{\rm s}\sigma_{\rm s} + n_{\rm a}\sigma_{\rm a}}\,, \tag{22}$$

where $n_{\rm s}$ and $n_{\rm a}$ are number densities of scatterers and absorbers, respectively, and $\sigma_{\rm s}$ and $\sigma_{\rm a}$ are cross-sections for scattering and absorbing, respectively.

The scattering of a photon, e.g. by a dust particle, is described by the angular phase function $P(\cos\theta)$. For an isotropic scattering, we have $P(\cos\theta) = 1/2$ and for Rayleigh scattering $P(\cos\theta) = 3/8(1 + \cos^2\theta)$.

The probability that a photon interacts on the length-scale x is given by

$$P(\tau) = 1 - \exp(-\tau)\,, \tag{23}$$

where $\tau = -\int_0^x \kappa\rho {\rm d}x'$. The MCRT then proceeds in three basic steps:

(1) The emission of N photon packets that further propagate through the medium.

(2) The site of the interaction of the photon packet in the medium is found by sampling the optical depth τ_ν from the probability distribution given by Eq. (23). The character of interaction (scattering or absorption) is determined by sampling from albedo and angular phase functions, Eq. (22).

(3) Photons that escape the medium (are not absorbed, but can be scattered) are counted on an image plane (mimicking CCD detectors for real observations) or are binned in frequency intervals for calculating spectral energy distributions.

The advantage of the MCRT is that it describes individual photon packets with the full Stokes vector $\mathbf{S} = (I, Q, U, V)$, which allows us to easily construct polarization maps of the source as well as to calculate the total polarization degree as well as the angle. It was thus possible to compare the radiative properties of the DSO model with the observational analysis of Shahzamanian et al. (2016), who detected a significant polarized emission in the NIR $K_{\rm s}$ for the DSO. The model of the DSO included a young stellar object of class I that is still embedded in the optically thick dusty envelope within its tidal Hill radius. The source exhibits a relatively large polarization degree of $p_{\rm L} \sim 30\%$, which is most probably caused by the presence of bipolar outflows as well as a bow-shock dusty layer. These components significantly break the spherical symmetry (see Zajaček et al., 2017 for a detailed analysis and discussion). In Fig. 3, we show the simulated images of the DSO model, in which one can clearly see the bow-shock layer. From the left to the right panels, images of the continuum, polarized emission as well as the polarization degree in $K_{\rm s}$-band, respectively, are presented. In the left panel of Fig. 4, the polarization degree as a function of wavelength is depicted for different viewing angles. The polarization degree as a function of the viewing angle is specifically shown in the right panel of Fig. 4, where the shaded area is the viewing angle for the years when the DSO was intensively monitored. In our model, we can obtain the polarization degree as large as $\sim 30\%$ depending on the density of the bow shock, which is expected to increase as the DSO approaches the SMBH.

4 CONCLUSIONS

We presented an introductory analysis of the inflow-outflow structure of the Galactic centre environment in the sphere of gravitational influence of the SMBH. The focus was put on the analysis of conditions under which stellar bow shocks can develop. We found that these structures are expected to be present across the broad spatial scale of the Nuclear Star Cluster, which is further supported by the detection and analysis of several bright bow-shock sources in the NIR and MIR-bands. In addition, we derived useful formulae for the scaling of bow-shock sizes as well as thermal luminosities in the vicinity of the SMBH.

In the end, we presented the theoretical basics for Monte Carlo modelling of radiative properties of bow-shock sources and non-spherical circumstellar envelopes in general. We applied the MCRT to the case of the NIR-excess source DSO. The comparison of observations with the MCRT model allows us to draw the conclusion that the NIR continuum characteristics of the DSO are consistent with a young stellar object of class I surrounded by an optically thick dusty envelope dissected by bipolar cavities. Since the DSO is expected to move mildly supersonically close to its peribothron, it should develop a bow shock whose properties can vary along the orbit, depending on the relative velocity of the source as well as the density gradient of the ambient medium.

ACKNOWLEDGEMENTS

We received funding from the European Union Seventh Framework Program (FP7/2013 – 2017) under grant agreement no 312789 - Strong gravity: Probing Strong Gravity by Black Holes Across the Range of Masses. This work was supported in part by the Deutsche Forschungsgemeinschaft (DFG) via the Cologne Bonn Graduate School (BCGS), the Max Planck Society through the International Max Planck Research School (IMPRS) for Astronomy and Astrophysics, as well as special funds through the University of Cologne and SFB 956 Conditions and Impact of Star Formation. M. Zajaček and E. Hosseini are members of the International Max Planck Research School at the Universities of Cologne and Bonn. The authors thank the Czech Ministry of Education Youth and Sports project INTER-INFORM, ref. LTI17018, in cooperation with Silesian University in Opava.

REFERENCES

Baganoff, F. K., Maeda, Y., Morris, M., Bautz, M. W., Brandt, W. N., Cui, W., Doty, J. P., Feigelson, E. D., Garmire, G. P., Pravdo, S. H., Ricker, G. R. and Townsley, L. K. (2003), Chandra X-Ray Spectroscopic Imaging of Sagittarius A* and the Central Parsec of the Galaxy, *ApJ*, **591**, pp. 891–915, arXiv: arXiv:astro-ph/0102151.

Barai, P., Proga, D. and Nagamine, K. (2012), Multiphase, non-spherical gas accretion on to a black hole, *MNRAS*, **424**, pp. 728–746, arXiv: 1112.5483.

Bartko, H., Martins, F., Trippe, S., Fritz, T. K., Genzel, R., Ott, T., Eisenhauer, F., Gillessen, S., Paumard, T., Alexander, T., Dodds-Eden, K., Gerhard, O., Levin, Y., Mascetti, L., Nayakshin, S., Perets, H. B., Perrin, G., Pfuhl, O., Reid, M. J., Rouan, D., Zilka, M. and Sternberg, A. (2010), An Extremely Top-Heavy Initial Mass Function in the Galactic Center Stellar Disks, *ApJ*, **708**, pp. 834–840, arXiv: 0908.2177.

Becklin, E. E., Gatley, I. and Werner, M. W. (1982), Far-infrared observations of Sagittarius A - The luminosity and dust density in the central parsec of the Galaxy, *ApJ*, **258**, pp. 135–142.

Buchholz, R. M., Schödel, R. and Eckart, A. (2009), Composition of the galactic center star cluster. Population analysis from adaptive optics narrow band spectral energy distributions, *A&A*, **499**, pp. 483–501, arXiv: 0903.2135.

Buchholz, R. M., Witzel, G., Schödel, R. and Eckart, A. (2013), Ks- and Lp-band polarimetry on stellar and bow-shock sources in the Galactic center, *A&A*, **557**, A82, arXiv: 1308.0956.

Buchholz, R. M., Witzel, G., Schödel, R., Eckart, A., Bremer, M. and Mužić, K. (2011), Adaptive-optics assisted near-infrared polarization measurements of sources in the Galactic center, *A&A*, **534**, A117, arXiv: 1107.3781.

Chakrabarti, S. K. (1990), *Theory of Transonic Astrophysical Flows*, World Scientific Publishing Co.

Christie, I. M., Petropoulou, M., Mimica, P. and Giannios, D. (2016), Modelling accretion disc and stellar wind interactions: the case of Sgr A*, *MNRAS*, **459**, pp. 2420–2431, arXiv: 1601.07432.

Cuadra, J., Nayakshin, S., Springel, V. and Di Matteo, T. (2006), Galactic Centre stellar winds and Sgr A* accretion, *MNRAS*, **366**, pp. 358–372, arXiv: astro-ph/0505382.

Das, T. K., Nag, S., Hegde, S., Bhattacharya, S., Maity, I., Czerny, B., Barai, P., Wiita, P. J., Karas, V. and Naskar, T. (2015), Black hole spin dependence of general relativistic multi-transonic accretion close to the horizon, *NewA*, **37**, pp. 81–104, arXiv: 1211.6952.

Dovčiak, M., Karas, V. and Yaqoob, T. (2004), An Extended Scheme for Fitting X-Ray Data with Accretion Disk Spectra in the Strong Gravity Regime, *ApJS*, **153**, pp. 205–221, arXiv: astro-ph/0403541.

Eatough, R. P., Falcke, H., Karuppusamy, R., Lee, K. J., Champion, D. J., Keane, E. F., Desvignes, G., Schnitzeler, D. H. F. M., Spitler, L. G., Kramer, M., Klein, B., Bassa, C., Bower, G. C., Brunthaler, A., Cognard, I., Deller, A. T., Demorest, P. B., Freire, P. C. C., Kraus, A., Lyne, A. G., Noutsos, A., Stappers, B. and Wex, N. (2013), A strong magnetic field around the supermassive black hole at the centre of the Galaxy, *Nature*, **501**, pp. 391–394, arXiv: 1308.3147.

Eckart, A. and Genzel, R. (1996), Observations of stellar proper motions near the Galactic Centre, *Nature*, **383**, pp. 415–417.

Eckart, A. and Genzel, R. (1997), Stellar proper motions in the central 0.1 PC of the Galaxy, *MNRAS*, **284**, pp. 576–598.

Eckart, A., Mužić, K., Yazici, S., Sabha, N., Shahzamanian, B., Witzel, G., Moser, L., Garcia-Marin, M., Valencia-S., M., Jalali, B., Bremer, M., Straubmeier, C., Rauch, C., Buchholz, R., Kunneriath, D. and Moultaka, J. (2013), Near-infrared proper motions and spectroscopy of infrared excess sources at the Galactic center, *A&A*, **551**, A18, arXiv: 1208.1907.

Ferrarese, L. and Merritt, D. (2000), A Fundamental Relation between Supermassive Black Holes and Their Host Galaxies, *ApJL*, **539**, pp. L9–L12, arXiv: astro-ph/0006053.

Generozov, A., Stone, N. C. and Metzger, B. D. (2015), Circumnuclear media of quiescent supermassive black holes, *MNRAS*, **453**, pp. 775–796, arXiv: 1505.00268.

Genzel, R., Eisenhauer, F. and Gillessen, S. (2010), The Galactic Center massive black hole and nuclear star cluster, *Reviews of Modern Physics*, **82**, pp. 3121–3195, arXiv: 1006.0064.

Gillessen, S., Genzel, R., Fritz, T. K., Quataert, E., Alig, C., Burkert, A., Cuadra, J., Eisenhauer, F., Pfuhl, O., Dodds-Eden, K., Gammie, C. F. and Ott, T. (2012), A gas cloud on its way towards the supermassive black hole at the Galactic Centre, *Nature*, **481**, pp. 51–54, arXiv: 1112.3264.

Harada, N., Riquelme, D., Viti, S., Jiménez-Serra, I., Requena-Torres, M. A., Menten, K. M., Martín, S., Aladro, R., Martin-Pintado, J. and Hochgürtel, S. (2015), Chemical features in the circumnuclear disk of the Galactic center, *A&A*, **584**, A102, arXiv: 1510.02904.

Kunneriath, D., Eckart, A., Vogel, S. N., Teuben, P., Mužić, K., Schödel, R., García-Marín, M.,

Moultaka, J., Staguhn, J., Straubmeier, C., Zensus, J. A., Valencia-S., M. and Karas, V. (2012), The Galactic centre mini-spiral in the mm-regime, *A&A*, **538**, A127, arXiv: 1201.2362.

Lang, K. R. (1978), *Astrophysical formulae. A compendium for the physicist and astrophysicist (Berlin: Springer)*.

Marrone, D. P., Moran, J. M., Zhao, J.-H. and Rao, R. (2007), An Unambiguous Detection of Faraday Rotation in Sagittarius A*, *ApJL*, **654**, pp. L57–L60, arXiv: astro-ph/0611791.

Martins, F., Gillessen, S., Eisenhauer, F., Genzel, R., Ott, T. and Trippe, S. (2008), On the Nature of the Fast-Moving Star S2 in the Galactic Center, *ApJL*, **672**, pp. L119–L122, arXiv: 0711.3344.

McConnell, N. J., Ma, C.-P., Gebhardt, K., Wright, S. A., Murphy, J. D., Lauer, T. R., Graham, J. R. and Richstone, D. O. (2011), Two ten-billion-solar-mass black holes at the centres of giant elliptical galaxies, *Nature*, **480**, pp. 215–218, arXiv: 1112.1078.

Merritt, D. (2013), *Dynamics and Evolution of Galactic Nuclei (Princeton: Princeton University Press)*.

Montero-Castaño, M., Herrnstein, R. M. and Ho, P. T. P. (2009), Gas Infall Toward Sgr A* from the Clumpy Circumnuclear Disk, *ApJ*, **695**, pp. 1477–1494, arXiv: 0903.0886.

Moser, L., Sánchez-Monge, Á., Eckart, A., Requena-Torres, M. A., García-Marin, M., Kunneriath, D., Zensus, A., Britzen, S., Sabha, N., Shahzamanian, B., Borkar, A. and Fischer, S. (2017), Approaching hell's kitchen: Molecular daredevil clouds in the vicinity of Sagittarius A*, *A&A*, **603**, A68, arXiv: 1603.00801.

Mužić, K., Eckart, A., Schödel, R., Buchholz, R., Zamaninasab, M. and Witzel, G. (2010), Comet-shaped sources at the Galactic center. Evidence of a wind from the central 0.2 pc, *A&A*, **521**, A13, arXiv: 1006.0909.

Pariev, V. I. (1996), Hydrodynamic accretion on to a rapidly rotating Kerr black hole, *MNRAS*, **283**, pp. 1264–1280, arXiv: astro-ph/9510008.

Parsa, M., Eckart, A., Shahzamanian, B., Karas, V., Zajaček, M., Zensus, J. A. and Straubmeier, C. (2017), Investigating the Relativistic Motion of the Stars Near the Supermassive Black Hole in the Galactic Center, *ApJ*, **845**, 22, arXiv: 1708.03507.

Paumard, T., Genzel, R., Martins, F., Nayakshin, S., Beloborodov, A. M., Levin, Y., Trippe, S., Eisenhauer, F., Ott, T., Gillessen, S., Abuter, R., Cuadra, J., Alexander, T. and Sternberg, A. (2006), The Two Young Star Disks in the Central Parsec of the Galaxy: Properties, Dynamics, and Formation, *ApJ*, **643**, pp. 1011–1035, arXiv: arXiv:astro-ph/0601268.

Phifer, K., Do, T., Meyer, L., Ghez, A. M., Witzel, G., Yelda, S., Boehle, A., Lu, J. R., Morris, M. R., Becklin, E. E. and Matthews, K. (2013), Keck Observations of the Galactic Center Source G2: Gas Cloud or Star?, *ApJL*, **773**, L13, arXiv: 1304.5280.

Psaltis, D. (2012), The Influence of Gas Dynamics on Measuring the Properties of the Black Hole in the Center of the Milky Way with Stellar Orbits and Pulsars, *ApJ*, **759**, 130, arXiv: 1112.0026.

Rauch, C., Mužić, K., Eckart, A., Buchholz, R. M., García-Marín, M., Sabha, N., Straubmeier, C., Valencia-S., M. and Yazici, S. (2013), A peek behind the dusty curtain: K_S-band polarization photometry and bow shock models of the Galactic center source IRS 8, *A&A*, **551**, A35.

Robitaille, T. P. (2011), HYPERION: an open-source parallelized three-dimensional dust continuum radiative transfer code, *A&A*, **536**, A79, arXiv: 1112.1071.

Różańska, A., Czerny, B., Kunneriath, D., Adhikari, T. P., Karas, V. and Mościbrodzka, M. (2014), Conditions for thermal instability in the Galactic Centre mini-spiral region, *MNRAS*, **445**, pp. 4385–4394, arXiv: 1410.0397.

Różańska, A., Kunneriath, D., Czerny, B., Adhikari, T. P. and Karas, V. (2017), Multiphase environment of compact galactic nuclei: the role of the nuclear star cluster, *MNRAS*, **464**, pp. 2090–2102, arXiv: 1609.08834.

Różańska, A., Mróz, P., Mościbrodzka, M., Sobolewska, M. and Adhikari, T. P. (2015), X-ray observations of the hot phase in Sagittarius A*, *A&A*, **581**, A64, arXiv: 1507.01798.

Sanchez-Bermudez, J., Schödel, R., Alberdi, A., Muzić, K., Hummel, C. A. and Pott, J.-U. (2014), Properties of bow-shock sources at the Galactic center, *A&A*, **567**, A21, arXiv: 1405.4528.

Schneider, P. (2006), *Extragalactic Astronomy and Cosmology (Berlin: Springer)*.

Shahzamanian, B., Eckart, A., Zajaček, M., Valencia-S., M., Sabha, N., Moser, L., Parsa, M., Peissker, F. and Straubmeier, C. (2016), Polarized near-infrared light of the Dusty S-cluster Object (DSO/G2) at the Galactic center, *A&A*, **593**, A131, arXiv: 1607.04568.

Shcherbakov, R. V. and Baganoff, F. K. (2010), Inflow-Outflow Model with Conduction and Self-consistent Feeding for Sgr A*, *ApJ*, **716**, pp. 504–509, arXiv: 1004.0702.

Silich, S., Tenorio-Tagle, G. and Hueyotl-Zahuantitla, F. (2008), Spherically Symmetric Accretion onto a Black Hole at the Center of a Young Stellar Cluster, *ApJ*, **686**, 172-180, arXiv: 0806.3054.

Valencia-S., M., Eckart, A., Zajaček, M., Peissker, F., Parsa, M., Grosso, N., Mossoux, E., Porquet, D., Jalali, B., Karas, V., Yazici, S., Shahzamanian, B., Sabha, N., Saalfeld, R., Smajic, S., Grellmann, R., Moser, L., Horrobin, M., Borkar, A., García-Marín, M., Dovčiak, M., Kunneriath, D., Karssen, G. D., Bursa, M., Straubmeier, C. and Bushouse, H. (2015), Monitoring the Dusty S-cluster Object (DSO/G2) on its Orbit toward the Galactic Center Black Hole, *ApJ*, **800**, 125, arXiv: 1410.8731.

Wang, Q. D., Nowak, M. A., Markoff, S. B., Baganoff, F. K., Nayakshin, S., Yuan, F., Cuadra, J., Davis, J., Dexter, J., Fabian, A. C., Grosso, N., Haggard, D., Houck, J., Ji, L., Li, Z., Neilsen, J., Porquet, D., Ripple, F. and Shcherbakov, R. V. (2013), Dissecting X-ray-Emitting Gas Around the Center of Our Galaxy, *Science*, **341**, pp. 981–983, arXiv: 1307.5845.

Wilkin, F. P. (1996), Exact Analytic Solutions for Stellar Wind Bow Shocks, *ApJL*, **459**, p. L31.

Wilkin, F. P., Canto, J. and Raga, A. C. (1997), On the Energetics and Momentum Distribution of Bow Shocks and Colliding Winds, in B. Reipurth and C. Bertout, editors, *Herbig-Haro Flows and the Birth of Stars*, volume 182 of *IAU Symposium*, pp. 343–352.

Witzel, G., Ghez, A. M., Morris, M. R., Sitarski, B. N., Boehle, A., Naoz, S., Campbell, R., Becklin, E. E., Canalizo, G., Chappell, S., Do, T., Lu, J. R., Matthews, K., Meyer, L., Stockton, A., Wizinowich, P. and Yelda, S. (2014), Detection of Galactic Center Source G2 at 3.8 μm during Periapse Passage, *ApJL*, **796**, L8, arXiv: 1410.1884.

Yuan, F. and Narayan, R. (2014), Hot Accretion Flows Around Black Holes, *ARA&A*, **52**, pp. 529–588, arXiv: 1401.0586.

Zajaček, M., Britzen, S., Eckart, A., Shahzamanian, B., Busch, G., Karas, V., Parsa, M., Peissker, F., Dovčiak, M., Subroweit, M., Dinnbier, F. and Zensus, J. A. (2017), Nature of the Galactic centre NIR-excess sources. I. What can we learn from the continuum observations of the DSO/G2 source?, *A&A*, **602**, A121, arXiv: 1704.03699.

Zajaček, M., Eckart, A., Karas, V., Kunneriath, D., Shahzamanian, B., Sabha, N., Mužić, K. and Valencia-S., M. (2016), Effect of an isotropic outflow from the Galactic Centre on the bow-shock evolution along the orbit, *MNRAS*, **455**, pp. 1257–1274, arXiv: 1510.02285.

Zhang, Q. and Zheng, X. (1997), The Role of Bow Shocks in Bipolar Molecular Outflows, *ApJ*, **474**, pp. 719–723.

Proceedings of *RAGtime 17–19, 17–19/23–26 Oct., 1–5 Nov., 2015/2016/2017, Opava, Czech Republic*
Z. Stuchlík, G. Török and V. Karas, editors, Silesian University in Opava, 2017, pp. 253–260

Chaotic motion in the Johannsen-Psaltis spacetime

Ondřej Zelenka[1,2,a] and Georgios Lukes-Gerakopoulos[1,b]

[1] Astronomical Institute of the Academy of Sciences of the Czech Republic, Boční II 1401/1a, CZ-141 31 Prague, Czech Republic
[2] Institute of Theoretical Physics, Faculty of Mathematics and Physics, Charles University, CZ-180 00 Prague, Czech Republic
[a] ondrzel@gmail.com, [b] gglukes@gmail.com

ABSTRACT
The Johannsen-Psaltis spacetime is a perturbation of the Kerr spacetime designed to avoid pathologies like naked singularities and closed timelike curves. This spacetime depends not only on the mass and the spin of the compact object, but also on extra parameters, making the spacetime deviate from Kerr; in this work we consider only the lowest order physically meaningful extra parameter. We use numerical examples to show that geodesic motion in this spacetime can exhibit chaotic behavior. We study the corresponding phase space by using Poincaré sections and rotation numbers to show chaotic behavior, and we use Lyapunov exponents to directly estimate the sensitivity to initial conditions for chaotic orbits.

Keywords: chaos – geodesic motion – black holes

1 INTRODUCTION

We study the geodesic motion in a family of spacetimes constructed by (Johannsen and Psaltis, 2011). The corresponding metric is characterized by an infinite number of parameters, i.e. the mass M, the spin a and a series of deviation parameters ϵ_k, where $k \in \mathbb{N}_0$. However, in this work we constrain ourselves to the lowest order of the unconstrained parameters, which is ϵ_3.

The Johannsen-Psaltis (JP) metric was designed to be a perturbation of the Kerr spacetime, which is of great astrophysical interest. The so-called *no-hair theorem* (see, e.g., Carter, 1971) states that the class of uncharged black-hole exterior solutions which are axisymmetric and don't violate causality (i.e. no closed timelike curves) consists of a discrete set of continuous families, each depending on at least one and at most two independent parameters. No other externally observable parameters are required for this description. Typically, the Kerr spacetime is assumed to describe a black hole (Rico, 2013). Kerr black holes are parametrized by their mass M and their angular momentum a. However, there is yet to be a proof if black holes are indeed described by the Kerr paradigm. Therefore,

978-80-7510-257-7

it would be of great astrophysical interest to test this conjecture by observing black hole candidates through electromagnetic and gravitational wave signals.

The Kerr spacetime is axisymmetric and stationary, but one special feature of this spacetime is that it has an extra "hidden" symmetry that makes geodesic motion in such a background correspond to an integrable system (Carter, 1968). There are spacetimes that deviate from Kerr by a deformation parameter, these spacetimes are called in the bibliography non-Kerr spacetimes (see, e.g., Bambi, 2017). These non-Kerr spacetimes do not usually possess the symmetry that the Kerr spacetime does, making geodesic motion correspond to a non-integrable system. As a result, geodesic motion in such spacetimes exhibits chaotic behavior, which is the topic of our study.

The organization of the article is as follows: in section 2 we describe the basics of geodesic motion, deterministic chaos in dynamical systems and some of the properties of the JP spacetime. In section 3 we use numerical examples to show that the JP metric doesn't correspond to an integrable system. Section 4 summarizes our main findings. Note that geometric units are employed throughout the article, $G = c = 1$. Greek letters denote the indices corresponding to spacetime and the metric signature is $(-,+,+,+)$.

2 GEODESIC MOTION AND CHAOS

The line element of a rapidly spinning black hole introduced in (Johannsen and Psaltis, 2011) reads in Boyer-Lindquist-like coordinates

$$\mathrm{d}s^2 = g_{tt}\mathrm{d}t^2 + g_{rr}\mathrm{d}r^2 + g_{\theta\theta}\mathrm{d}\theta^2 + g_{\phi\phi}\mathrm{d}\phi^2 + 2g_{t\phi}\mathrm{d}t\mathrm{d}\phi \quad , \tag{1}$$

where the metric components $g_{\mu\nu}$ (Johannsen and Psaltis, 2011) are

$$g_{tt} = -(1+h)\left(1 - \frac{2Mr}{\Sigma}\right) \quad , \tag{2a}$$

$$g_{t\phi} = -\frac{2aMr\sin^2\theta}{\Sigma}(1+h) \quad , \tag{2b}$$

$$g_{\phi\phi} = \frac{\Lambda\sin^2\theta}{\Sigma} + ha^2\left(1 + \frac{2Mr}{\Sigma}\right)\sin^4\theta \quad , \tag{2c}$$

$$g_{rr} = \frac{\Sigma(1+h)}{\Delta + a^2 h\sin^2\theta} \quad , \tag{2d}$$

$$g_{\theta\theta} = \Sigma \quad , \tag{2e}$$

and the metric functions are

$$\Sigma = r^2 + a^2 \cos^2\theta \quad , \tag{3a}$$

$$h = \sum_{k=0}^{\infty} \left(\epsilon_{2k} + \epsilon_{2k+1} \frac{Mr}{\Sigma}\right) \left(\frac{M^2}{\Sigma}\right)^k \quad , \tag{3b}$$

$$\Delta = r^2 + a^2 - 2Mr \quad , \tag{3c}$$

$$\omega^2 = r^2 + a^2 \quad , \tag{3d}$$

$$\Lambda = \omega^4 - a^2 \Delta \sin^2\theta \quad . \tag{3e}$$

The function $h(r,\theta)$ is what causes the deviation from the Kerr metric. Namely, setting $\epsilon_k = 0 \quad \forall k \in \mathbb{N}_0$ gives the Kerr metric. The parameters $(\epsilon_k)_{k=0}^{\infty}$ are, however, constrained. As explained in detail in (Johannsen and Psaltis, 2011), we have to set $\epsilon_0 = \epsilon_1 = 0$ and the parameter ϵ_2 is constrained by observational constraints on weak-field deviations from general relativity (Johannsen and Psaltis, 2011), i.e. $|\epsilon_2| \leq 4.6 \cdot 10^{-4}$. We therefore set $\epsilon_2 = 0$ as well and limit ourselves to the lowest order remaining parameter, which is ϵ_3, and set all the higher order parameters $\epsilon_k = 0 \quad \forall \quad k \geq 4$.

The proper time τ defined as $\mathrm{d}\tau^2 = -g_{\mu\nu}\mathrm{d}x^\mu \mathrm{d}x^\nu$ is employed as the evolution parameter. The geodesic motion of a free particle of rest mass m is then generated by the Lagrangian (see, e.g., Rindler, 2006)

$$\mathcal{L}(x^\mu, \dot{x}^\mu) = \frac{m}{2} g_{\mu\nu} \dot{x}^\mu \dot{x}^\nu \quad , \tag{4}$$

where dot denotes a derivative with respect to the proper time. Due to the preservation of the four-velocity $g_{\mu\nu}\dot{x}^\mu\dot{x}^\nu = -1$ along a geodesic orbit $\mathcal{L} = -m/2$ is a constant. The corresponding canonical momenta are

$$p_\mu = \frac{\partial \mathcal{L}}{\partial \dot{x}^\mu} = m g_{\mu\nu} \dot{x}^\nu \tag{5}$$

and performing the Legendre transform gives the Hamiltonian

$$\mathcal{H} = \frac{1}{2m} g^{\mu\nu} p_\mu p_\nu \quad . \tag{6}$$

The JP metric functions are independent of the parameters t and ϕ, i.e. it is stationary and axisymmetric, therefore the energy $E := -p_t$ and and the component of the angular momentum $L_z := p_\phi$ are integrals of motion. This allows us to restrict our study to the meridian plane generated by the polar-like coordinates (r,θ) and move to a simpler system of two degrees of freedom. Namely, one has to merely replace

$$\dot{t} = \frac{-g^{tt}E + g^{t\phi}L_z}{m}, \quad \dot{\phi} = \frac{-g^{t\phi}E + g^{\phi\phi}L_z}{m} \tag{7}$$

in the equations of motion to reduce the system. The motion in the resulting reduced system is characterized by the Newtonian-like two-dimensional effective potential

$$(p_r)^2 + \frac{g_{rr}}{g_{\theta\theta}} (p_\theta)^2 = -V_{\text{eff}} := -g_{rr} \left(1 + \frac{g_{\phi\phi}E^2 + g_{tt}L_z^2 + 2g_{t\phi}EL_z}{g_{tt}g_{\phi\phi} - g_{t\phi}^2}\right) \quad . \tag{8}$$

For $p_\theta = p_r = 0$ the roots of this effective potential $V_{\text{eff}} = 0$ form a curve in the meridian plane, which is called the *curve of zero velocity* (CZV).

In the Kerr case, an extra "hidden symmetry" exists[1], giving rise to the Carter constant $\mathcal{K}$ (Carter, 1968). This constant, along with E, L_z and $\mathcal{H}$, are independent and in involution, therefore geodesic motion in the Kerr spacetime background corresponds to an integrable system and trajectories of the reduced system lie on a family of two-dimensional *invariant tori*. These orbits oscillate in both degrees of freedom with their respective characteristic frequencies ω^r and ω^θ; their ratio $\omega = \omega^r/\omega^\theta$ is called the *rotation number* and it is useful for the classification of orbits. If ω is rational, the torus is called *resonant* and it hosts an infinite number of periodic orbits. If ω is irrational, the motion is called *quasiperiodic* and each orbit on the torus covers it densely.

When a perturbation is applied to such an integrable system, all the resonant tori are destroyed. According to the *KAM theorem* (Meiss, 1992), however, most of the non-resonant tori survive in the perturbed system for small perturbations; these are called KAM tori. According to the *Poincaré-Birkhoff theorem* (Lichtenberg and Lieberman, 1992), where there was a resonant torus, an even number of periodic trajectories survives in the perturbed system, half of them stable and half unstable. We use a Poincaré surface of section to display the phase space structure of the system. We define a surface in the phase space and plot the intersections of the orbits with the surface. Invariant tori correspond to circles in the surface of section. These form the *main island of stability* around a stable fixed point in the center.

Near the now destroyed resonant tori, quite a different structure arises. Around the stable periodic points (corresponding to surviving stable periodic orbits), smaller islands of stability arise, forming together with the unstable points (corresponding to surviving unstable periodic orbits) *Birkhoff chains*. These unstable periodic points lie between the aforementioned islands of stability. From the unstable points emanate asymptotic manifolds, there are stable and unstable branches. The branches of the same type cannot cross each other, which results in very complicated structures in the phase space. These complicated structures are the driving engines of deterministic chaos.

An effective tool to analyze types of motion on a Poincaré section of a non-integrable system of two degrees of freedom is the angular moment ν_ϑ, known in the literature as the rotation number (see, e.g, Voglis and Efthymiopoulos, 1998; Voglis et al., 1999). We denote the central fixed point of the main island of stability u_c and the n-th crossing of the surface of section by the orbit u_n. We define rotation angles

$$\vartheta_n := \text{ang}\,[u_{n+1} - u_c, u_n - u_c] \tag{9}$$

and the angular moment as

$$\nu_\vartheta = \lim_{N\to\infty} \frac{1}{2\pi N} \sum_{n=1}^{N} \vartheta_n \quad . \tag{10}$$

The dependence of this angular moment on the distance of the initial condition from the central fixed point is called the *rotation curve*. In an integrable system, such as the Kerr

[1] For more details on this symmetry see (Markakis, 2014) and references therein.

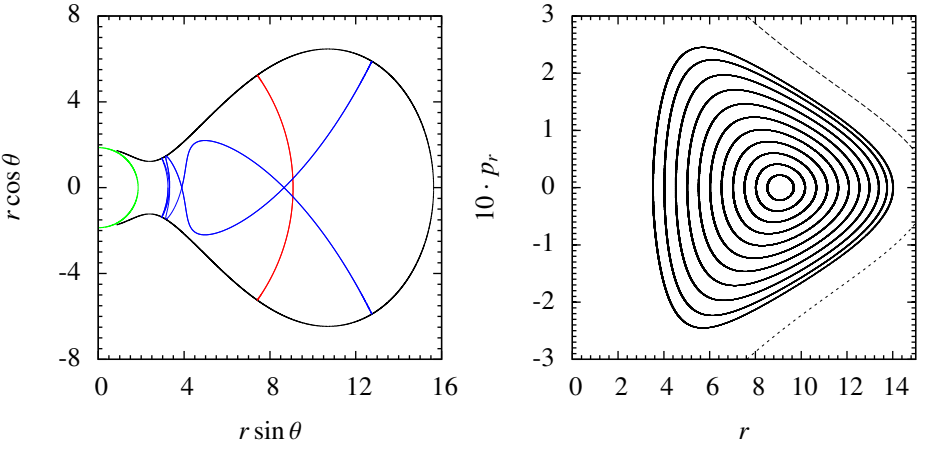

Figure 1. Left panel: projections of orbits on the meridian plane - the period-1 orbit (red), the 5/7 periodic orbit (blue), the event horizon (green), the CZV (black). Right panel: The main island of stability on the Poincaré section $\theta = \frac{\pi}{2}$.

spacetime, the rotation curve is strictly monotonous, but in a non-integrable system, it has non-monotonic variations when passing through chaotic zones, and plateaus when passing through islands of stability.

In order to quantify sensitivity to initial conditions, which is a property of chaotic systems by definition (Devaney, 1989), it is useful to define the *deviation vector* as a point of the tangent bundle of the phase space and interpret it as connecting two infinitesimally close trajectories. This vector evolves through the geodesic deviation equation

$$\ddot{\xi}^{\mu} + \frac{\partial \Gamma^{\mu}{}_{\kappa\lambda}}{\partial x^{\nu}} \dot{x}^{\kappa} \dot{x}^{\lambda} \xi^{\nu} + 2\Gamma^{\mu}{}_{\kappa\lambda} \dot{x}^{\kappa} \dot{\xi}^{\lambda} = 0 \quad . \tag{11}$$

As a measure of the deviation vector in a curved spacetime (see, e.g., Lukes-Gerakopoulos, 2014) we use

$$\Xi^2 := g_{\mu\nu} \xi^{\mu} \xi^{\nu} \quad . \tag{12}$$

Typically, the deviation vector follows one of two behaviors - a linear one for regular trajectories and an exponential one for chaotic trajectories. These behaviors can be detected by the *maximal Lyapunov characteristic exponent*

$$\mathrm{mLCE} := \lim_{\tau \to \infty} \frac{1}{\tau} \log \left[\frac{\Xi(\tau)}{\Xi(0)} \right] \quad , \tag{13}$$

which gives the inverse of a characteristic deviation time scale for chaotic trajectories. In the case of regular trajectories, it behaves as $\sim \tau^{-1}$ for large τ, so in a plot in logarithmic scale it appears as a line of slope -1.

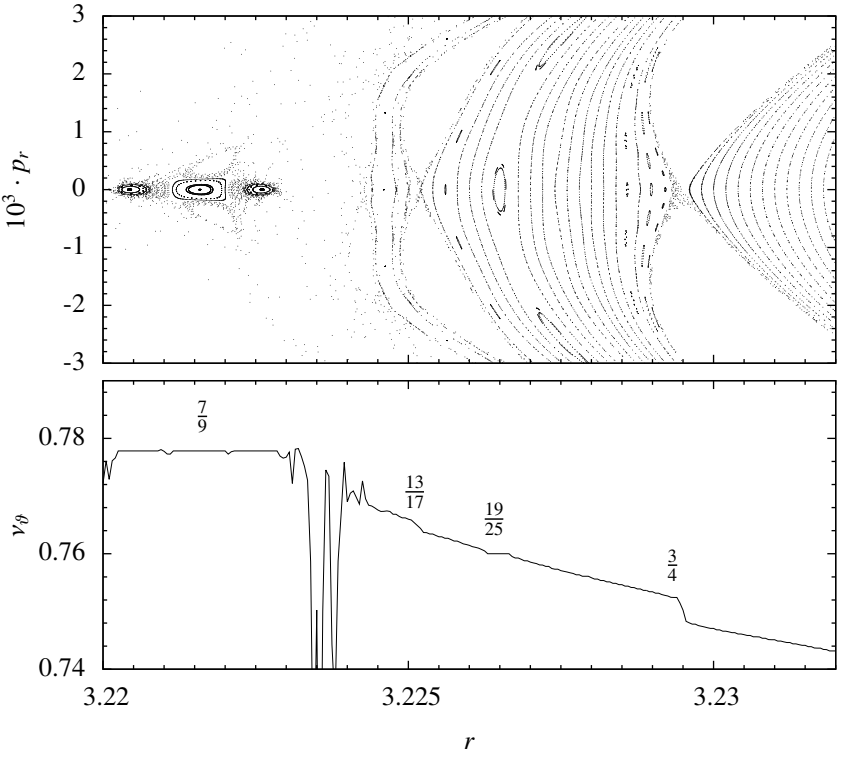

Figure 2. Top panel: Detail of the left tip of the main island of stability. Bottom panel: The rotation curve plotted for the $p_r = 0$ line of the top panel. The resonance plateaus along the curve are denoted by the respective fractions.

3 NUMERICAL EXAMPLES

All figures shown are plotted using the parameter values $M = m = 1$, $a = 0.5$, $\epsilon_3 = 0.3$, $E = 0.95$, $L_z = 2.85$. In the left panel of Fig. 1 are shown projections of two periodic orbits on the meridian plane are shown, bounded by the CZV. In the right panel, the main island of stability in the Poincaré section is shown. The equatorial plane $\theta = \pi/2$ with $\dot{\theta} > 0$ is taken as the surface of section. We notice no difference from an integrable system, as the chaotic behavior is not prominent at this broad scale depiction. This difference becomes, however, clearly visible in top panel of Fig. 2, which focuses on the left tip of the main island of stability shown in the right panel of Fig. 1. In particular, in the top panel of Fig. 2, alongside with KAM curves, appear islands of stability belonging to Birkhoff chains (ellipsoid-like structures) and chaotic zones (scattered points). Under the panel containing this detail of the surface of section, the corresponding rotation curve is plotted. The rotation curve exhibits non-monotonic variations in a chaotic zone and

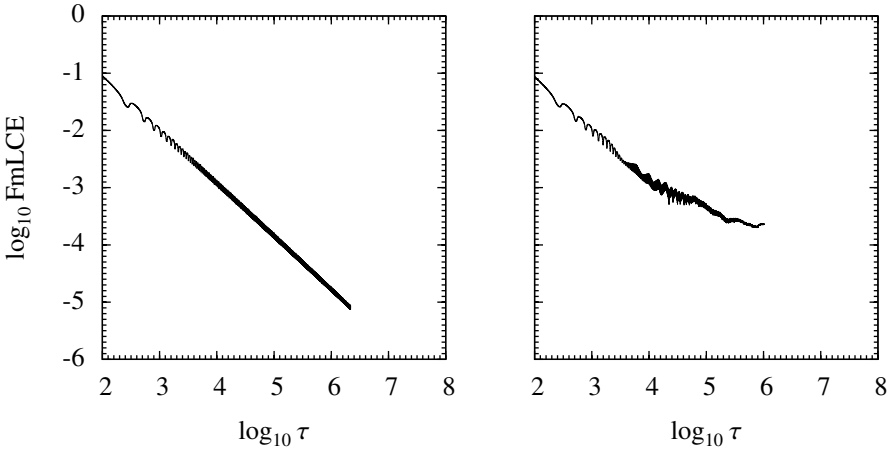

Figure 3. Convergence of mLCE for a regular orbit (left panel) with a chaotic orbit (right panel). Both orbits starting with $p_r = 0$ on the surface of section shown in Fig. 2, the regular from $r = 3.226$ and the chaotic from $r = 3.2294$.

plateaus (denoted by the corresponding fraction) along islands of stability. Thus, Fig. 2 indicates that the JP spacetime corresponds to a non-integrable system.

To directly estimate the sensitivity to initial conditions, we have calculated the mLCE. Fig. 3 shows the convergence of the mLCE for one regular (left panel) and one chaotic orbit (right panel). For the regular orbit indeed the mLCE convergence follows the -1 slope, while for the chaotic orbit the mLCE converges to a positive value.

4 CONCLUSION

We have shown by numerical examples that geodesic motion in the JP spacetime background corresponds to a non-integrable system, since chaos was detected. The astrophysical implication is that if the spacetime around black holes is not described by the Kerr metric, then one should expect imprints of chaos in electromagnetic and gravitational wave signals coming from systems like extreme mass ratio inspirals.

ACKNOWLEDGEMENTS

O.Z. and G.L-G are supported by Grant No. GACR-17-06962Y of the Czech Science Foundation. We thank Petra Suková and Ondřej Kopáček for useful discussions.

REFERENCES

Bambi, C. (2017), *Black holes : a laboratory for testing strong gravity*, Springer, Singapore, ISBN 978-981-10-4524-0.

Carter, B. (1968), Global structure of the kerr family of gravitational fields, *Phys. Rev.*, **174**, pp. 1559–1571, URL https://link.aps.org/doi/10.1103/PhysRev.174.1559.

Carter, B. (1971), Axisymmetric black hole has only two degrees of freedom, *Phys. Rev. Lett.*, **26**, pp. 331–333, URL https://link.aps.org/doi/10.1103/PhysRevLett.26.331.

Devaney, R. (1989), *An Introduction to Chaotic Dynamical Systems*, Addison-Wesley advanced book program, Addison-Wesley, ISBN 9780201130461, URL https://books.google.cz/books?id=elPvAAAAMAAJ.

Johannsen, T. and Psaltis, D. (2011), Metric for rapidly spinning black holes suitable for strong-field tests of the no-hair theorem, *Phys. Rev. D*, **83**, p. 124015, URL https://link.aps.org/doi/10.1103/PhysRevD.83.124015.

Lichtenberg, A. and Lieberman, M. (1992), *Regular and Chaotic Dynamics*, Second Edition, Springer-Verlag, New York, ISBN 0-387-97745-7.

Lukes-Gerakopoulos, G. (2014), Adjusting chaotic indicators to curved spacetimes, *Phys. Rev. D*, **89**, p. 043002, URL https://link.aps.org/doi/10.1103/PhysRevD.89.043002.

Markakis, C. (2014), Constants of motion in stationary axisymmetric gravitational fields, *Monthly Notices of the Royal Astronomical Society*, **441**, pp. 2974–2985, arXiv: 1202.5228.

Meiss, J. D. (1992), Symplectic maps, variational principles, and transport, *Rev. Mod. Phys.*, **64**, pp. 795–848, URL https://link.aps.org/doi/10.1103/RevModPhys.64.795.

Rico, J. M. A. (2013), *The Kerr black hole hypothesis: a review of methods and results*, Master's thesis, Lisbon, CENTRA, URL https://fenix.tecnico.ulisboa.pt/downloadFile/395145712687/dissertacao.pdf.

Rindler, W. (2006), *Relativity: special, general, and cosmological*, Oxford Univ. Press, 2 edition.

Voglis, N., Contopoulos, G. and Efthymiopoulos, C. (1999), Detection of ordered and chaotic motion using the dynamical spectra, *Celestial Mechanics and Dynamical Astronomy*, **73**(1), pp. 211–220, ISSN 1572-9478, URL http://dx.doi.org/10.1023/A:1008307332442.

Voglis, N. and Efthymiopoulos, C. (1998), Angular dynamical spectra. a new method for determining frequencies, weak chaos and cantori, *Journal of Physics A: Mathematical and General*, **31**(12), p. 2913, URL http://stacks.iop.org/0305-4470/31/i=12/a=015.

Title: **Proceedings of RAGtime 17–19:**
Workshops on black holes and neutron stars,
17–19/23–26 Oct., 1–5 Nov. 2015/2016/2017, Opava, Czech Republic

Published by: Silesian University in Opava
Faculty of Philosophy and Science
Institute of Physics
Bezručovo nám. 13
CZ-746 01 Opava, Czech Republic

Editors: Z. Stuchlík, G. Török and V. Karas

Cover design: Otakar Karlas

1st edition

Printed by : X-media servis,
U cementárny 1171/11,
CZ-703 00 Ostrava Vítkovice, Czech Republic

Published in December 2017

INVESTMENTS IN EDUCATION DEVELOPMENT

The publication was supported by the INTER-EXCELLENCE project No. LTI17018 and the internal grant of the Silesian University in Opava No. 07/2015-FPF.

ISBN 978-80-7510-256-0 (Print)
ISBN 978-80-7510-257-7 (Online)
ISSN 2336-5668 (Print)
ISSN 2336-5676 (Online)

Typeset in LaTeX

Název: **Proceedings of RAGtime 17–19:**
Workshops on black holes and neutron stars,
17–19/23–26 Oct., 1–5 Nov. 2015/2016/2017, Opava, Czech Republic

Nakladatel: Slezská univerzita v Opavě
Filozoficko–přírodovědecká fakulta v Opavě
Ústav fyziky
Bezručovo nám. 13
CZ-746 01Opava, Česká republika

Editoři: Z. Stuchlík, G. Török a V. Karas

Obálka: Otakar Karlas

První vydání

Tisk: X-media servis,
U cementárny 1171/11
CZ-703 00 Ostrava Vítkovice
Česká republika

Vydáno v prosinci 2017

INVESTMENTS IN EDUCATION DEVELOPMENT

The publication was supported by the INTER-EXCELLENCE project No. LTI17018 and the internal grant of the Silesian University in Opava No. 07/2015-FPF.

ISBN 978-80-7510-256-0 (Print)
ISBN 978-80-7510-257-7 (Online)
ISSN 2336-5668 (Print)
ISSN 2336-5676 (Online)

Vysázeno systémem LaTeX